Doctoral Dissertation

Development of metal-coordinated aminosilica networks for highly permeable and selective membrane separation

(金属配位アミノシリカ膜の開発と高透過性・高選択性分離)

UFAFA ANGGARINI

Department of Chemical Engineering,

Graduate school of Engineering, Hiroshima University

（広島大学大学院工学研究科 化学工学専攻）

September 2022

Hiroshima University Doctoral Dissertation

-- --

Abstract of dissertation

Membrane processes and technology are considered energy efficient for the separation of gas and liquid systems. Over the past decades, organosilica membranes have attracted high attention due to high thermal and chemical stability with no swelling, high flux, high separation performance, and adjustable pore sizes. The primary goal of this dissertation was to fabricate and optimize a hybrid thin film of metal-coordinated aminosilica membranes based on sol-gel processing followed by coordination reaction and investigate their performance in the separation of gas and liquid mixtures via pervaporation. The best performance of metal coordinated-organosilica based membranes was achieved by optimizing four parameters including the affinity of transition metal as Lewis-acid molecules, the affinity of the ligand as Lewis-base molecules, the mole ratio of metal/amine groups, and the existence of metal in a different phase to facilitate the transport of permeating molecules. At each step of optimization, the fixed variable was selected and applied, and the investigation proceeded to the next step.

In the first stage of modification of metal coordinated-organosilica membranes, the effect of metal doping was evaluated using a single gas permeation system. Values for surface area and pore volume of the metal-doped bis[3-(trimethoxysilyl) propyl] amine (BTPA) at metal/amine mole ratio of 0.25 mol mol^{-1} were both expanded by increasing metal coordination affinity on the order of Ni-BTPA (214 m^2 g^{-1}) > Cu-BTPA (75.7 m^2 g^{-1}) > Ag-BTPA (20.1 m^2 g^{-1}) > BTPA (2.36 m^2 g^{-1}). In line with material characterization, gas permeation was also increased in the same order, which corresponds to a higher affinity for metal coordination. Ni-BTPA membrane with the highest affinity for coordination achieved high levels of both permeance of N$_2$ and N$_2$/SF$_6$ at 3.75×10^{-7} mol m^{-2} s^{-1} Pa^{-1} and 1,900, respectively.

In the second stage, the optimization of coordination was examined by employing the incorporation of different amounts of nickel dopant (mole ratio of nickel/amine) into BTPA structure that ranged from 0.125 to 0.50 mol mol^{-1}. Higher nickel content increased the rigidity and resulted in a porous membrane structure with a high specific surface area that beneficially showed high performance for the pervaporation organic mixture of methanol/toluene on the order of Ni-BTPA 0.50 > Ni-BTPA 0.25 > Ni-BTPA 0.125 > BTPA. Ni-BTPA 0.50 has been found to exhibit superior performance with a

----

high level of flux at 2.8 kg m^{-2} h^{-1} and a separation factor higher than 900 in a 10 wt% methanol feed solution at 50 ^{o}C. In that work, Ni-BTPA 0.50 shows an attractive performance due to the balance between the formation of microporosity that was induced by nickel-amine coordination and the excessive amount of nickel ions that facilitated the fast transport of methanol while restraining the transport of toluene.

To prove the concept of metal-coordinated aminosilica membranes, in the third investigation, the affinity of amine-functionalized organosilica as a ligand was evaluated via different types of precursors. Nickel doping restructured the aminosilica network via a coordination bond, which then increased both the rigidity of the organic chain and the surface area or resultant material on the order of nickel doped bis [3-(trimethoxysilyl) propyl] amine (Ni-BTPA) > nickel-doped 3-aminopropyl triethoxy silane (Ni-APTES) > nickel-doped trimethoxy[3-(methyl amino) propyl silane (Ni-MAPTS). The prepared hybrid nickel-composite membranes were used for the pervaporation of various types of organic mixtures with methanol 10 wt% at 50 ^{o}C in the feed solution. Ni-BTPA with the strongest affinity for coordination recorded the highest separation performance for the flux that reached as high as 1.42 kg m^{-2} h^{-1} with an optimum separation factor for methanol/toluene of 5,000. The enhancement for both membrane flux and the separation factor verifies the balance between higher levels of interconnected micropores from nickel-amine coordination and the existence of uncoordinated nickel acting as active sites for the diffusion of methanol.

Based on the previous investigation, two phases of metal can facilitate a specific transport of components while the coordinated network generates a high flux of membrane. In the fourth evaluation, we examine the fabrication of silver-doped BTPA for facilitating the transport of H$_2$. The evolution of silver in two phases as silver ions and nanoparticles successfully modify the membrane structure from dense into microporous, and silver-modified aminosilica membranes showed hydrogen permeance of 1.46 10^{-6} mol m^{-2} s^{-1} Pa^{-1} with excellent H$_2$/C$_3$H$_8$ selectivity of 1,500. Based on this result, it is evident that the proposed modification via the two-phase structural evolution of silver reorganized the organosilica framework and improve the separation performance of the membranes.

Hiroshima University Doctoral Dissertation

-- --

<div align="center">

CONTENTS

</div>

Hiroshima University Doctoral Dissertation

-- --

Hiroshima University Doctoral Dissertation

-- --

Chapter 1
General introduction

1.1 Membrane separation technology

Membranes were defined as the semipermeable barriers that allow the separation of one or more components with a higher permeation for one compound but hinder the transport of the other as illustrated in Fig. 1-1(a). The membrane separation barrier divided the feed stream into the retentate stream and permeate stream. The retentate stream is the stream that has been retained by the membrane containing both the materials that have been rejected by the membrane barrier and the material that has not been rejected by the semipermeable barrier but has not been allowed to pass through the membrane. On contrary, permeate stream was defined as a stream that contains smaller molecules than membrane pores that allow the compound to pass through.
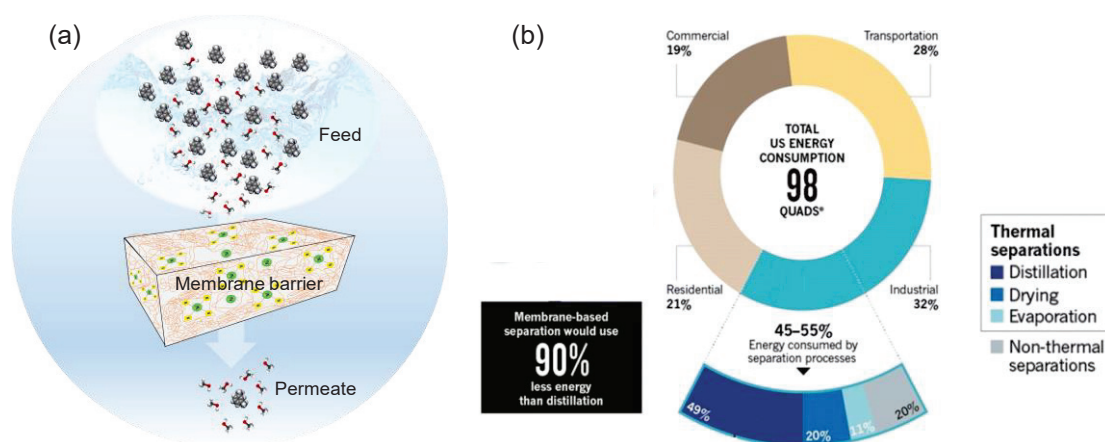
Fig. 1-1. The schematic image of membrane separation process (a), and the schematic representative of membrane technology reduce the energy cost in separation (b)

Starting at the end of the 1960s, membrane separation technology is considered to be a proficient competitive technique for industrial applications compared with conventional separation processes such as filtration, evaporation, crystallization, solvent extraction, or distillation, albeit with the consequence of high operational demand on energy [1]. Membrane separation processes have been proven to be clean, faster, more efficient, and more economical than conventional separation techniques (Fig. 1-1(b)) [2, 3]. In addition,

the separation processes could be performed at ambient temperatures, thus offering temperature-sensitive compounds to be treated without being chemically modified. The separation processes of components can be classified into several types, based on the phase species of components in both feed and permeate sides. In the case of liquid-phase separation, pressure-driven membrane processes were classified into four major categories based on the pore size of the membranes and the required transmembrane pressure as described in Fig. 1-2: microfiltration (MF), ultrafiltration (UF), nanofiltration (NF), and reverse osmosis (RO).

MF (0.1-5 µM, 1-10 bar)
- Suspended particles

UF (500-100,000 Da, 1-1,000 nm, 1-10 bar)
- Macromolecules

NF (100-500 Da, 0.5-10 nm, 10-30 bar)
- Divalent ions, organic molecules

RO (<0.5 nm, 35-100 bar)
- Monovalent ions

Water
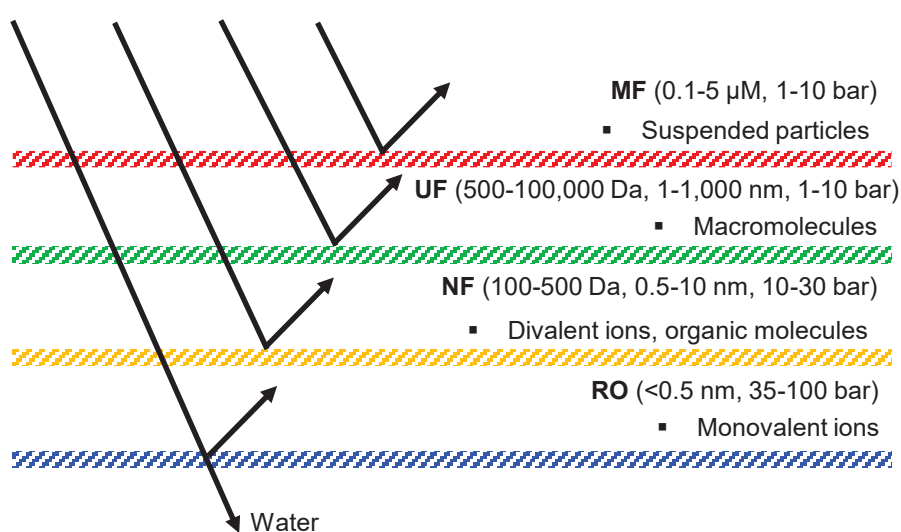
Fig. 1-2. Schematic images of different separation processes based on sizes

In addition, the pervaporation process (PV) is the membrane separation process with a typical pore size < 0.5 nm in which compounds are selectively transported from the liquid phase in the upper stream to the vapor phase in the lower stream, which enables better separation performance and lower levels of energy consumption [4]. The driving force for pervaporation is the vapor pressure difference between the feed and permeate sides; the pressure of the feed side is maintained at atmospheric levels while that of the permeate side is evacuated. On the other hand, the gas separation process (GS) corresponds to the separation where both feed and permeate streams are in the gaseous phase through the microporous or dense membrane network.

Pressure-driven membrane process could be operated in two different modes of dead-end and cross-flow operations as shown in Fig. 1-3 [5]. In the case of a dead-end module, the feed streams enter one side of the module and flow vertically towards the membrane

--- --

surface with the other streams for the permeate components leaving the module.
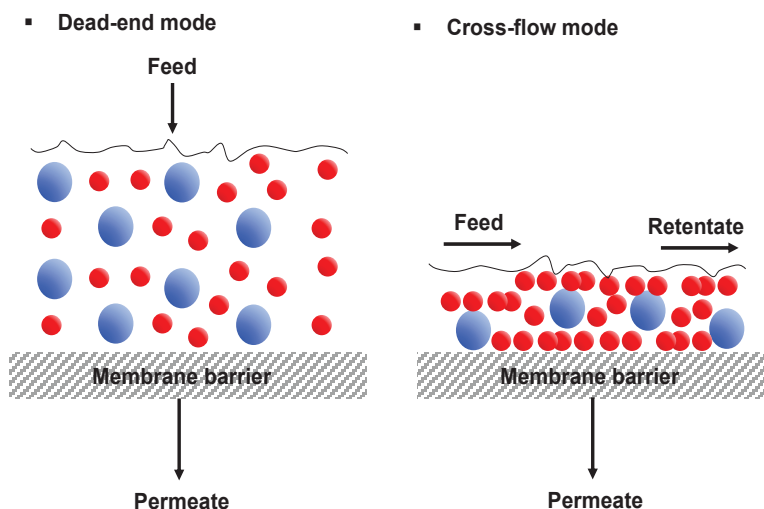
Fig. 1-3. Schematic diagrams of dead-end and cross-flow mode in pressure-driven membrane processes

However, the accumulation of the rejected particles is severe which results in impractical issues for this type of module. The other type of module was a cross-flow mode where the tangential flow could minimize the effect of accumulation of rejected species, limit the height of separated layered particles, and maintain the permeate flux.

1.2 Membrane gas separation

Membrane engineering has been growing during the last decades with several membrane operations that are dominant technologies in various areas such as in desalination of seawater, wastewater treatment, the concentration of vegetable and fruit juice, artificial organs, and gas separation. Membrane technology demonstrated lower energy consumption about 10 times lower compared with the thermal process. The use of a membrane in gas separation technology competes with the traditional thermal-based separation technologies, thus this method is recognized as the best available technology. However, several factors need to be considered to get the high performance of membranes for the real industrial application to be realized, which includes but is not limited to the design and development of new membrane materials with tailored structures for improved mass transport properties, the membrane's robustness in aggressive environments and ability of membrane materials to be operated in a wide range of operating condition. In

this section, an overview of the transport mechanism through different membrane structures and the interaction between permeating gases with the pore wall of the membrane, together with possible application in gas separation membrane technology is provided. Therefore, the important information from this discussion can be used to analyze and facilitate further optimization of materials design.

1.2.1 Transport mechanism: general introduction

Recently, an increased interest has been focused on the gas separation process, where the membrane performance can be tailor-made via the construction of the microstructure of the materials and the selection of membrane materials. Gas permeation (GP) is a separation process where membranes were used to separate gas mixtures without a phase change [6]. The separation performance of membrane-based gas separation is commonly correlated with permeability and selectivity. The permeation rate or flux of gas transported through the membrane was defined as the number of molecules that pass through in a unit area per unit time and it's proportional to the concentration gradient through the membrane as expressed in equation (1-1).

$$J = -D \frac{dc}{dx} \tag{1-1}$$

$$J = D \frac{C_2 - C_1}{L} \tag{1-2}$$

Where D is diffusivity, c is the concentration, and x is the position across the membrane. C_1 and C_2 are the downstream and upstream concentrations, respectively, and L is membrane thickness. Therefore, the permeability (P) of the membrane which represents the thickness-independent property that is related to flux (J) can be expressed in equation (1-3).

$$P = \frac{J L}{p_2 - p_1} = \left(\frac{C_2 - C_1}{p_2 - p_1} \right) D \tag{1-3}$$

When the upstream pressure is much larger than the downstream pressure, the permeability can be expressed as follows.

$$P = \left(\frac{C_2}{p_2} \right) D \tag{1-4}$$

The ratio of concentration over the pressure can be defined as the solubility coefficient (S) so that the permeability can be expressed.

$$P = S D \tag{1-5}$$

Permeance (P) is the product of the diffusivity (D) and solubility (S) of permeated molecules across the membrane barrier, where the diffusivity value is affected by the pore dimensions, and the solubility is affected by the dynamic parameter which describes the mobility of the compound and the interaction between membrane surface and permeated molecules [7-9]. The ideal separation factor of the mixture that contains A and B molecules can be expressed as the ratio of permeability of molecules A over molecule B, or express the separation factor as the ratio of diffusivity or solubility selectivity as follows.

$$\alpha_{A/B} = \frac{P(A)}{P(B)} = \frac{D(A)}{D(B)} = \frac{S(A)}{S(B)} \tag{1-6}$$

This equation is known as a solution-diffusion mechanism. Since the limiting stage of the mass transfer is overcoming the diffusion energy, the mechanism implies the activated diffusion and the temperature dependency of the diffusion coefficient and permeability coefficient can be expressed by the Arrhenius equation as follows.

$$D_A = D_A^* \exp\left(-\frac{\Delta E_a}{RT}\right) \tag{1-7}$$

$$S_A = S_A^* \exp\left(-\frac{\Delta H_a}{RT}\right) \tag{1-8}$$

Where $\Delta H_a < 0$ is the enthalpy of sorption, the equation (1-5) can be expressed as follows.

$$P_A = P_A^* \exp\left(-\frac{\Delta E_P}{RT}\right) \tag{1-9}$$

Where $\Delta E_P = \Delta E_a + \Delta H_a$. The transport mechanism of gases that diffuse within dense or porous membranes was different, depending on the pore size distribution of the membranes as shown in Fig. 1-4.
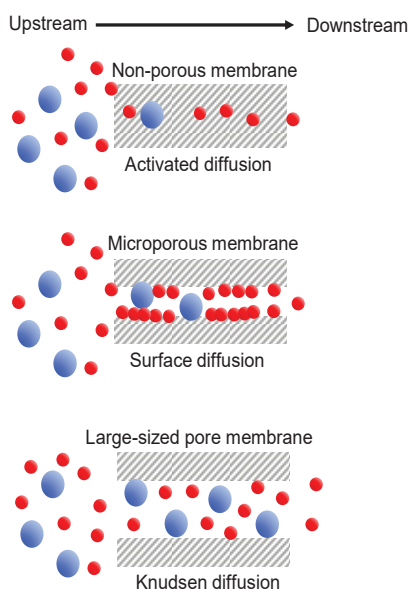
Fig. 1-4. The transport mechanism for the permeation of gases through membrane pore wall

In the case of dense membrane structure with narrow pore size, the molecular sieving

mechanism was considered as the activated diffusion process, while the larger pore size

of the membrane facilitates the surface diffusion and Knudsen diffusion mechanism. The

pore size modification of the membrane should be chosen based on the pore aperture size

of molecules that need to be separated, as shown in equation (1-10) [10].

$$d_i \; < \; d_p \; < \; d_j \hspace{4cm} (1\text{-}10)$$

Where d_i and d_j are the molecular size of the i and j gases, and d_p is the pore aperture

size of the membrane. Table 1-1 summarized the Lennard-Jones constant, molecular

weight, and the average velocities of several compounds.

Table 1-1 Molecular size, molecular weight, and the average velocities of permeated gases at room temperature [11]

Gas	σ (Å)	M_W (g mol^{-1})	$\bar{v}$ (m s^{-1})
He	2.60	4.00	1277
H$_2$	2.89	2.02	1800
CO$_2$	3.30	44.01	385
O$_2$	3.46	32.00	452
N$_2$	3.64	28.01	483
CO	3.69	25.01	476
Ar	3.54	39.95	399
CH$_4$	3.87	16.04	638
n-C$_5$H$_{12}$	5.78	72.15	297
C$_2$H$_6$	4.44	30.07	455
SF$_6$	5.13	146.06	209

1.2.2 Membrane transport mechanism through different structures

Solid membranes were classified into 2 main categories based on morphology or

structure: isotropic (symmetric) and anisotropic (asymmetric) membranes. Symmetric

membranes are further divided into two subclasses dense (non-porous) and porous

----

membranes, while the asymmetric membranes can be divided into anisotropic asymmetric and composites membranes [12]. The schematic images of membrane structure morphology as shown in Fig. 1-5.

Symmetric membranes

Dense membrane   Porous membrane

Asymmetric membranes

                                  Composite membrane
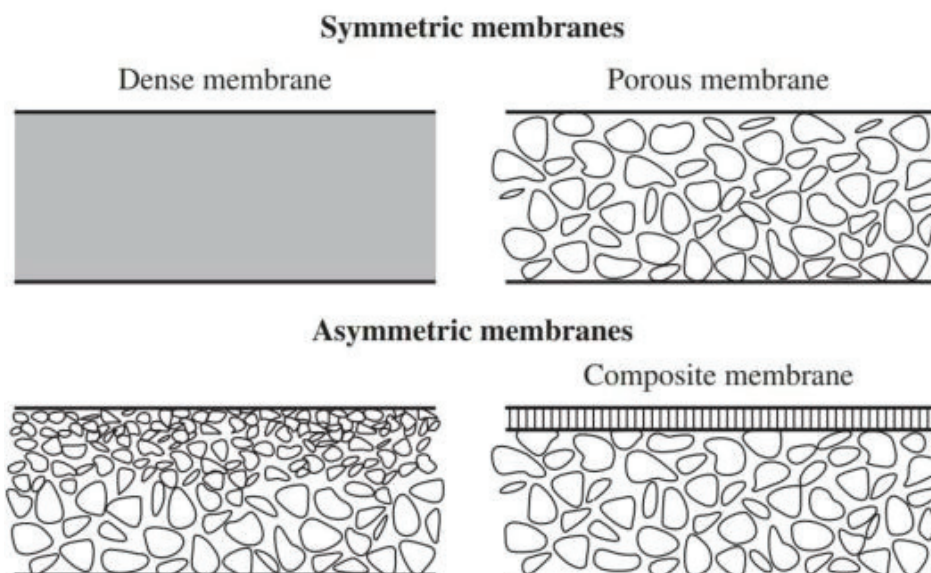
Fig. 1-5. Schematic representative of different membrane structures [13]

1.2.2.1   Dense membrane

A dense or non-porous membrane consists of a dense thin film layer through which permeated gases are transported via the solution-diffusion mechanism under the driving force of pressure, electrical, and concentration potential gradient. The solution-diffusion model assumes the pressure within the membrane is uniform and the chemical potential gradient across the membrane is only expressed as a concentration gradient [14]. As consequence, when pressure is applied to the system, the pressure everywhere within the membrane is constant at a high-pressure value. In this membrane structure, the penetrating molecules dissolve in the membrane matrix from the feed side, then diffuse through the membrane down a concentration gradient. The gas transport through a dense membrane involves three processes: the adsorption at the upstream boundaries, activated diffusion through the membrane, and desorption on the permeate stream. The separation of the different components in a mixture was directly related to the relative transport rate within the membrane, which was determined by the diffusivity (D) and the solubility (S) in the membrane material.

--- --

$$P = S \times D \qquad\qquad (1\text{-}11)$$

The permeability coefficient (P_i^G) can be expressed as follows [14].

$$P_i^G = \frac{D_i \gamma_i}{\gamma_{i(m)} P_{i\,sat}} \qquad\qquad (1\text{-}12)$$

Where D_i is diffusion coefficient, γ_i is permeating gas activity coefficient, $\gamma_{i(m)}$ is the affinity of membrane material, and $P_{i\,sat}$ is the saturation vapor pressure. The value of permeant's saturation vapor pressure and diffusion coefficient decreased with increasing molecular weight, competing effects on permeability coefficient. This means the permeability of the component decreased significantly as the molecular weight of the component increased.

Dense membranes structure such as those found in perovskite, metal, polymeric, glassy, and organosilica ceramic materials were used in membrane reactors for different applications such as methane conversion, hydrogen production, toxic gas treatment, and CO_2 separations [15]. However, the commercialization of dense membranes is seriously hindered by several challenges, which show a low permeating flux with high selectivity due to the thickness and small pore sizes of the membranes. Yu, et al [9] developed amine-silica membranes that were synthesized from different organosilica precursors of 3-(triethoxysilyl) propylamine (PA-Si), 3-(triethoxysilyl)-N-methyl propane-1-amine (SA-Si), and 3-(triethoxysilyl)-N, N-dimethyl propane-1-amine (TA-Si). Based on N_2 sorption characterization as shown in Fig. 1-6(a), all amine-silica membranes show low surface area ($<$ 1 m^2 g^{-1}) with negligible pore volume, which suggested the formation of dense or non-porous structure. Moreover, all amine-silica membrane shows low permeance for big-sized gases such as N_2 and exhibit high separation performance for CO_2/N_2 as high as 22 at 35 $^\circ$C (Fig. 1-6(b)). Better membrane structure will continue to be a focus research area for improving the separation performance of targeted compounds in a mixture.
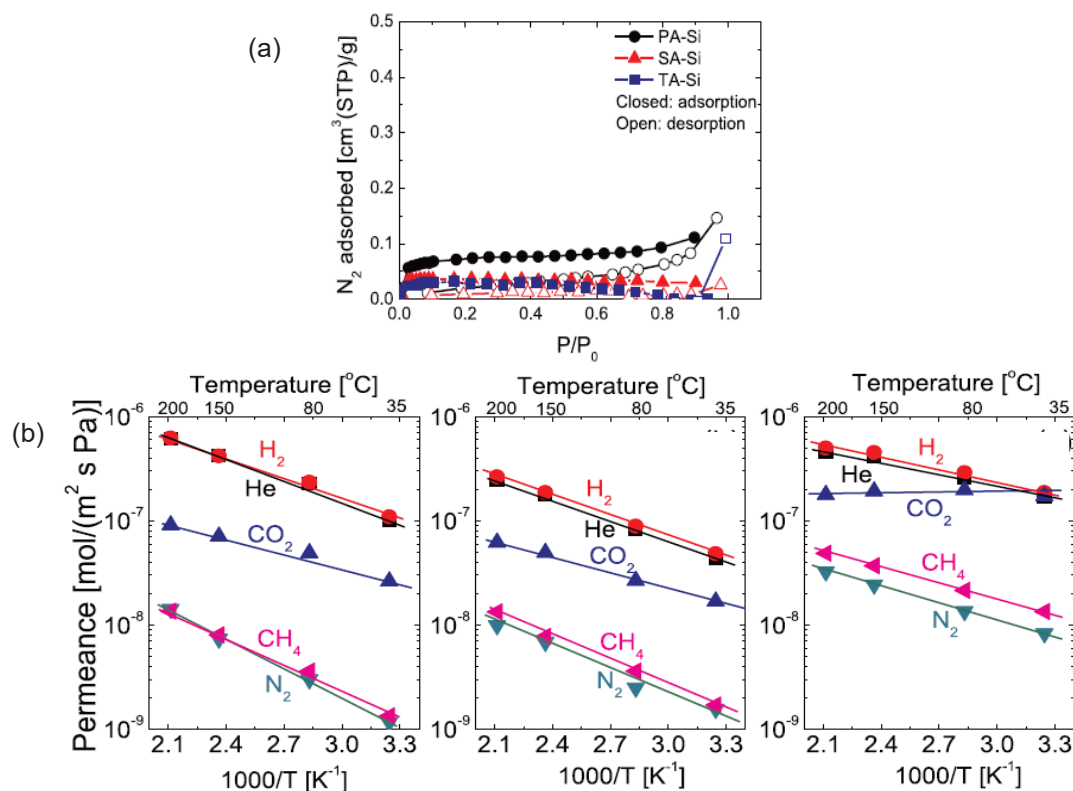
Fig. 1-6. N_2 sorption isotherms at -196 °C (a), and the permeance of permeating gases as a function of temperature dependence (b) for PA-Si, SA-Si, and Ta-Si xerogel powder calcined at 250 °C [9].

Plisko et al. [16] reported the surface morphology modification of polysulfone (PSF) based membranes modified with different content of poly(ethylene glycol)-b-poly (propylene glycol)-b- poly(ethylene glycol) (Pluronic F127) as shown in Fig. 1-7. The SEM images of PSF-Pluronic F127 hybrid membranes show the transformation from a dense membrane structure to a porous sponge-like (the pore size, pore quantity, and the polydispersity were increased) by increasing the Pluronic F127 content. At zero loading of Pluronic F127, the selective membrane barrier shows no pores that were detected (Fig. 1-7(a)). Higher porosity on PSF-Pluronic membranes was expected to improve the flux and the separation ability of the ethyl acetate-water mixture.
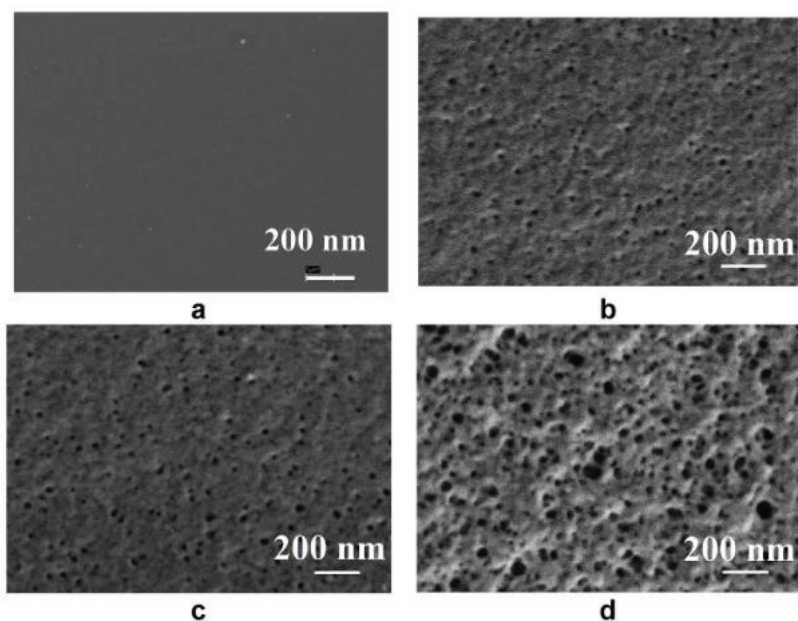
Fig. 1-7. The SEM images of the membrane surface for hybrid PSF-Pluronic F127 flat sheet membrane at different Pluronic content (wt.%) of 0 (a), 5 (b), 7 (c), and 10 (d) [16]

1.2.2.2   Porous membrane

Porous membranes consist of a solid matrix with defined pores diameters ranging from less than 10 nm to more than 50 nm [3]. Generally, these membranes have a rigid structure with highly pores that were randomly distributed and interconnected pores. The gas transport mechanism through porous membranes was achieved via a molecular sieving mechanism with the pores and molecular size of penetrating molecules being the determination parameter. Based on IUPAC classification, the pore size of the membranes could be classified based on the diameter size and the gas transport that dominated that structure, as shown in Table 1-2 [17].

Table 1-2. Membrane classification is based on pore size and gas transport mechanism inside pores

Type of membrane	Pore size [nm]	Transport mechanism	
Macroporous membranes	> 50 nm	Viscous flow	
		Molecular diffusion	

		Knudsen diffusion	
Mesoporous membranes	2 – 50 nm		
		Surface diffusion	
Microporous membranes	< 2 nm	Capillary condensation and pore filling	
		Micropore diffusion	
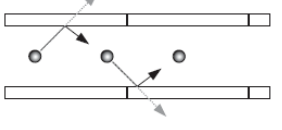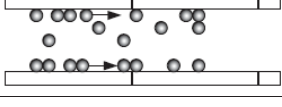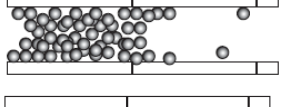
Viscous flow is predominant occurs for the porous membrane with a pore size larger compared to the mean free path of molecules or on the pore size larger than 50 nm [18]. The overall gas transport is mainly decided by the collisions of the gas species in the bulk phase and non-selective among different types of components. The permeance (P) of gases through a macroporous membrane can be calculated using equation (1-13).

$$P = P_K + \beta P_m \tag{1-13}$$

Where P_K represent the contribution of Knudsen flow and the second term related to the viscous flow contribution. The constant β is related to the area of porosity (ε), tortuosity factor (τ), thickness (L), the average pore sizes of the membranes (r), the viscosity of permeating molecule (μ), and temperature (T).

$$\beta = \left(\frac{1}{8}\right)\left(\frac{\varepsilon}{\tau L}\right) r^2 (\mu RT)^{-1} \tag{1-14}$$

The Knudsen permeance related to the gas diffusivity in the membrane pores can be estimated as follows.

$$P_K = \left(\frac{\varepsilon}{\tau}\right)\left(\frac{1}{L}\right)\left(\frac{1}{RT}\right) D \tag{1-15}$$

In this membrane structure, the gas diffusion (D) is governed by the Knudsen mechanism, so that D_K can be obtained from the data of pore structure with an average radius of and the molecular weight of permeating molecule (M) as follows.

$$D_K = \left(\frac{2}{3}\right)\left(\frac{8RT}{\pi M}\right)^{1/2} r \tag{1-16}$$

By combining equation (1-15) and (1-16), gives:

$$P_K = 1.06 \left(\frac{1}{L}\right)\left(\frac{\varepsilon}{\tau}\right) r (RTM)^{-1/2} \tag{1-17}$$

Mi et al. [19] investigated the permeation mechanism of helium (He), hydrogen (H2), and

nitrogen (N_2) through a multi-walled carbon nanotube (CNT) membrane with porous α-alumina support as shown in Fig. 1-8.
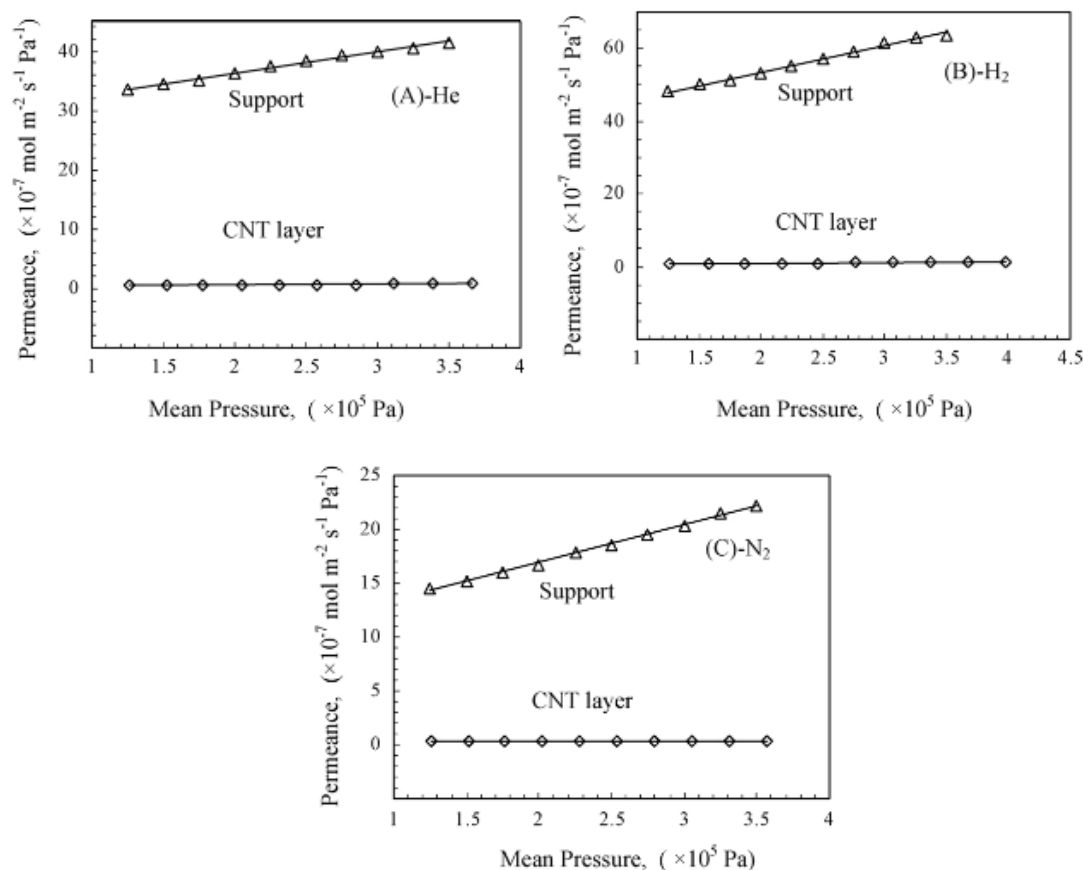
Fig. 1-8. Gas permeance of He, H_2, and N_2 through alumina support and CNT separation layer at 30 ℃ [19]

Gas permeance through the porous support suggested an inversely proportional value to the squared root of the molecular weight of permeating molecule. Moreover, the permeance of gases increases with the mean transmembrane pressure (Fig. 1-8) which indicated a significant contribution to the viscous flow with a large pore size of approximately around 0.3 μm.

Knudsen diffusion occurs depending on the gas pressure system and the mean free path in the gas phase (λ) applies to the intermediate pore size (r) between 10 Å and 500 Å, specifically, $r/\lambda \ll 1$. In this region, the collision was dominated between gas species and the pore wall, rather than between gas molecules in the bulk phase [18].It's common to use the Knudsen number (K_n) to characterize the regime of permeation

----

through membrane pore structure (d) as follows.

$$K_n = \frac{\lambda}{d} \qquad (1\text{-}18)$$

When $K_n \ll 1$, the viscous flow mechanism is operated, $K_n \gg 1$ the Knudsen diffusion was operative, and an intermediate regime is realized when $K_n \approx 1$.

The Knudsen diffusion coefficient (D_k) can be expressed as follows.

$$D_k = \frac{d}{3\tau}\bar{u} \qquad (1\text{-}19)$$

Where τ is pore tortuosity and $\bar{u}$ is the average velocity of permeating molecules which depends on the molecular mass of the component (m). The average velocity of the component can be calculated using the Maxwell speed distribution, as follows.

$$\bar{u} = \sqrt{\frac{8RT}{\pi m}} \qquad (1\text{-}20)$$

Hence the Knudsen diffusion coefficient (D_k) and the flux (J) of the membranes in the Knudsen regimes can be calculated as follows.

$$D_k = \left(d/3\tau\right)\left(8RT/\pi m\right)^{1/2} \qquad (1\text{-}21)$$

$$J = n\pi d^2 \Delta p D_k / 4RTL \qquad (1\text{-}22)$$

Where n is the surface concentration of the pores with the diameter d, Δp is the pressure drop across the membrane and L is the membrane thickness. By substituting equation (1-21) to (1-22), the flux and the permeability coefficient can be expressed as follows [20].

$$J = \left(n\pi^{1/2}d^3\Delta p/6\tau L\right)\left(2/mRT\right)^{1/2} \qquad (1\text{-}23)$$

$$P = \left(n\pi^{1/2}d^3/6\tau\right)\left(2/mRT\right)^{1/2} \qquad (1\text{-}24)$$

The gas transport via Knudsen diffusion occurs in the gaseous phase where the adsorption of components and the interaction between permeating molecules and membrane pore wall is negligible, thus the Knudsen permeance (P_k) equation can be simplified as follows [18].

$$P_k = \frac{\varepsilon d}{\tau L}\left(\frac{8}{9\pi mRT}\right)^{1/2} \qquad (1\text{-}25)$$

Where ε is the porosity of the membrane, R is the gas constant, and T is the absolute temperature. The ideal selectivity of two components in the Knudsen regime is expressed in the square root of molecular weight as shown in the following equation.

$$\alpha_{ij} = \left(M_j/M_i\right)^{1/2} \qquad (1\text{-}26)$$

The separation factor between two components of Knudsen diffusion is small due to the back diffusion, concentration polarization on the feed or permeate side, the occurrence of viscous flow on larger pores, and non-separative diffusion [21] as shown in Table 1-3.

Table 1-3. The calculated value for Knudsen selectivity

Gas mixture system	Knudsen selectivity [-]
H_2/N_2	3.74
H_2/CO_2	4.70
H_2/H_2S	4.11
H_2/SO_2	5.64
CO_2/N_2	0.80
N_2/O_2	1.07
CO_2/CH_4	0.60
O_2/CO_2	1.17
H_2/SF_6	8.50

Ren et al. [22] reported the gas permeation mechanism for bis(triethoxysilyl)ethane (BTESE) and bis(triethoxysilyl)octane (BTESO) membranes coated on silica zirconia (SiO_2-ZrO_2) and methyltrimethoxysilane-tetraethoxysilane (Me-SiO_2) intermediate layer at 200 ºC under dry conditions as shown in Fig. 1-9. Both SiO_2-ZrO_2 and Me-SiO_2 layers show high gas permeability, but low selectivity. The large pore size from the intermediate layers failed to separate specific gas pairs, and the gas transport mechanism was dominated by Knudsen diffusion. After the deposition of the selective membrane layer of BTESE and BTESO, the permeance of the membrane decrease with an improvement in membrane selectivity.
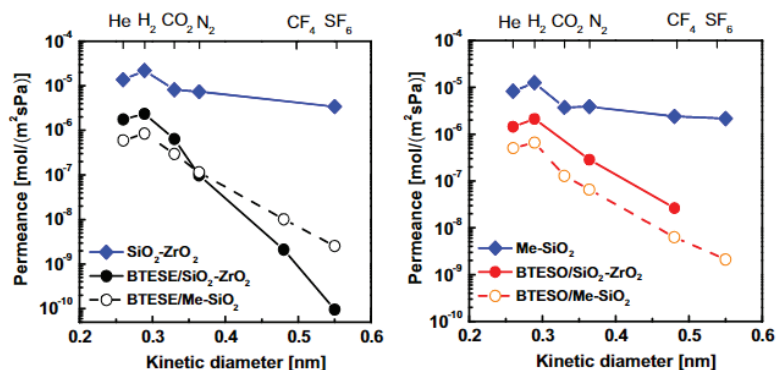
Fig. 1-9. The permeance of several gases as a function of the kinetic diameter of permeating molecules through SiO_2-ZrO_2 and Me-SiO_2 intermediate layer together with BTESE and BTESO membrane top layer [22].

Surface diffusion is the diffusion mechanism that occurs when the membrane pore size in the region between activated diffusion and Knudsen diffusion [20]. The surface diffusion mechanism occurred especially at low temperatures when the permeating molecules failed to escape from the surface potential field due to the interaction between the inner membrane pore wall and the gas species becoming strong compared to their kinetic energy [18]. Gas molecules adsorb on the surface of the membrane at the pore entrance, diffuse through the membrane, and desorp at the pore exit. This process generally takes place below monolayer adsorption, which is related to the Langmuir adsorption model. Since surface diffusion is also a form of activated diffusion, the energy barrier of ΔE_S is required for the penetrating molecules to jump from one adsorption site to another across the surface of pores. The energy barrier is proportional to the enthalpy of adsorption so the equation for the surface diffusion coefficient was expressed in (1-27).

$$D_S = D_S^* \exp\left(\frac{-aq}{RT}\right) \tag{1-27}$$

Where D_S^* is a pre-exponential factor and q ($q > 0$) is the heat of adsorption and a is a proportionally constant ($0 < a < 1$). It should be noted that more strongly adsorbed components are less mobile than weakly adsorbed ones. In this transport, the concentration of gas was described by Henry's law.

$$c = Kp \tag{1-28}$$

Where K is a temperature-dependent Henry law coefficient of $K = K_0 \exp\left(q/RT\right)$. Since solubility is the ratio of the equilibrium concentration over the pressure, the solubility can be expressed as follows.

$$S_S = K_0 \exp\left(\frac{-aq}{RT}\right) \tag{1-29}$$

The permeance is the product of diffusivity and the solubility as shown in equation (1-30).

$$P_S = P_S^* \exp\left(\frac{-aq}{RT}\right) \tag{1-30}$$

P_S^* is a constant and since the value of a is in the range of $0 < a < 1$, the total permeability will decrease with increased temperature which means that the increase of diffusivity is correlated with a decrease in surface concentration. The permeance in the surface diffusion model can also be expressed as follows.

$$P_S = P_0 exp\left(\frac{-\Delta H_a - \Delta E_S}{RT}\right) \tag{1-31}$$

Where the value of $-\Delta H_a - \Delta E_S$ being the energy barrier for diffusing molecules to permeate through the membrane, which shows a simple Arrhenius equation. Since the heat of adsorption is a positive quantity, and if this value is larger than the activation energy, the overall component becomes positive. Thus, the permeance of component decrease with increasing temperature.

Wei et al. prepared Pd-doped organosilica (POS) membranes by controlling the calcination atmosphere (Air, N_2, H_2, and H_2/N_2) to tailor and improve membrane separation performance. Fig. 1-10 shows the Arrhenius plot of H_2 and CO_2 permeance as a function of temperature dependency, where the slopes of each graph were equal to $-\Delta E$ (kJ mol^{-1}). Based on the result, H_2 molecules show positive activation energy, which means the transport of activated diffusion. On contrary to that, CO_2 permeance shows a decreased value at higher temperatures and exhibits negative apparent activation energies, which suggested the transport of CO_2 is dominated by the surface diffusion mechanism and exhibited strong adsorption capacity for CO_2.
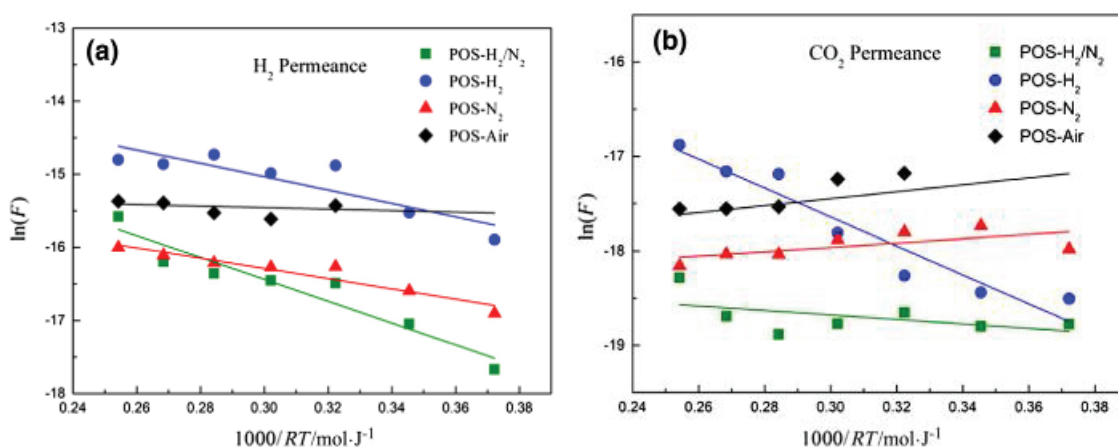
Fig. 1-10. Temperature dependence on H_2 (a) and CO_2 (b) permeance for POS-Air, POS-N_2, Pos-H_2, and POS-H_2/N_2 membranes.

The **molecular sieving mechanism** occurs when the pore apertures of the membranes approach the molecular dimension of the diffusing gas molecules. In this mechanism, the interaction energy between the molecules and membrane materials was comprised of both dispersive and repulsive interaction. When the pore opening was sufficiently small relative to the size of permeating molecules, the repulsive force was dominated, and the molecules require activation energy to pass through this constriction. In this region of activated diffusion, molecules with a slight kinetic diameter size can be

effectively separated through a molecular sieving mechanism [23]. The pore size of the membrane in the range of 0.7-2.0 nm provides the adsorption sites that would responsible for the surface diffusion, while the narrow ultra micropores (pores smaller than 0.7 nm) are enabled for molecular sieving mechanism, which makes the membrane show high permeance and selectivity for small-sized gases and restricts the diffusion of larger molecules [24]. Rungta et al. [25] reported the pore structure and bimodal distribution of carbon molecular sieve (CMS) which consist of micropores and ultra micropores as shown in Fig. 1-11. The critical ultra micropores window restricts diffusion, allowing effective discrimination between similar-sized gases via a molecular sieving effect. The existence of ultra micropores provides the separation ability under different conditions.
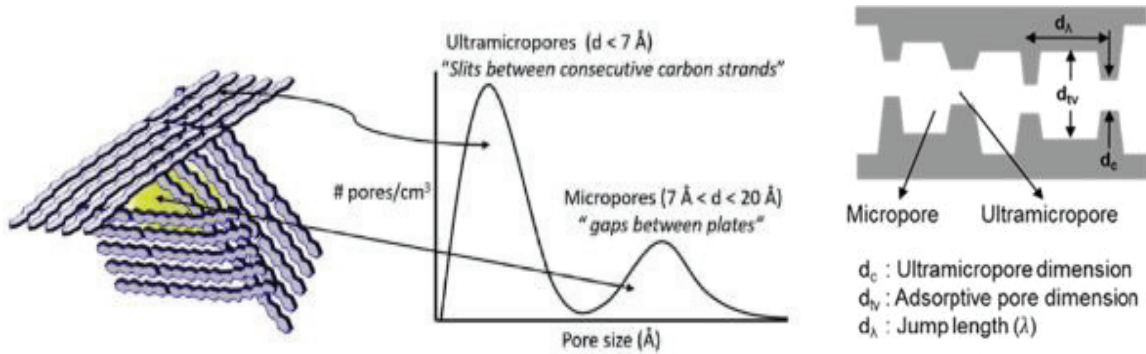
Fig. 1-11. The pore structure of CMS with a bimodal distribution of micropores and ultra micropores [25]

1.2.2.3   Gas Translation model (GT)

The gas translational (GT) model or best known as activated Knudsen diffusion was proposed based on the combination of the Knudsen diffusion model and the surface diffusion when the diffusing gas species have enough kinetic energy to escape the surface potential but cannot readily do because of the presence of membrane pore wall on the other side. The permeance can be expressed as follows [26].

$$P_{GT} = \frac{\varepsilon d_P \rho}{\tau L} \left(\frac{8}{\pi MRT} \right)^{1/2} \tag{1-32}$$

Where ε is the porosity of the membrane, d_P is the pore size of the membrane, τ is tortuosity, L is membrane thickness, M is the molecular weight of permeating molecules, R is a gas constant, T is the absolute temperature and ρ is the probability that consists of pre-exponential factor, ρ_g, and the kinetic energy to overcome the diffusion barrier.

$$\rho = \rho_g \, exp\left(-\frac{\Delta E}{RT}\right) \tag{1-33}$$

By substituting equation (1-33) into (1-32), the permeance of single gases can be expressed as follows.

$$P_{GT} = \frac{\varepsilon d_P \rho_g}{\tau L}\left(\frac{8}{\pi MRT}\right)^{1/2} exp\left(-\frac{\Delta E}{RT}\right) \tag{1-34}$$

The permeation equation on the GT model assumes the diameter of permeating molecules was smaller compared to the membrane pore diameter, and there is no physical pore blockage effect [18].

1.2.2.4   Modified-Gas Translation model (m-GT)

The Gas translation (GT) model was originally proposed by Shelekhin et al in 1995 [26]. In 2011, the Tsuru research group proposed the modified GT (m-GT) models to predict the gas permeation behavior through microporous membranes [8, 27, 28]. In the m-GT model, micropore permeation of a molecule with molecular size d_k through a cylindrical pore (pore size: d_p, length: L, tortuosity: τ_i) was formulated as follows. Using probability, ρ, which indicates the probability of diffusion through the micropore, and further expressed with the pre-exponential, ρ_g, and the kinetic energy, E_p, to overcome the diffusion barrier.

$$P_i = \varepsilon_i d_{p,i} \rho_i \sqrt{\frac{8RT}{\pi M_i}} \frac{1}{RT\tau_i L_i} \tag{1-35}$$

$$P_i = \varepsilon_i d_{p,i} \rho_{g,i} \sqrt{\frac{8RT}{\pi M_i}} \frac{1}{RT\tau_i L_i} \exp\left(-\frac{E_{p,i}}{RT}\right) \tag{1-36}$$

By considering the molecular size of a permeating gas ($d_{k,i}$) and the effective area for permeation, the modified GT model was obtained as shown in Equation (1-37).

$$P_{m-GT,i} = \frac{1}{3}\frac{\varepsilon}{\tau L}(d_p - d_i)\frac{(d_p-d_i)^2}{d_p^2}\sqrt{\frac{8}{\pi M_i RT}}\, exp\left(-\frac{E_{P,i}}{RT}\right) \tag{1-37}$$

$$= k_{0,i}\sqrt{\frac{1}{M_i RT}}\, exp\left(-\frac{E_{P,i}}{RT}\right) \tag{1-38}$$

where k_0 is the pre-exponential factor expressed by the configuration factors of a

----

membrane (porosity, tortuosity, membrane thickness, mean pore diameter) and permeating molecule (molecular size).

$$k_{0,i} = \frac{\varepsilon}{3\tau L} \frac{(d_p - d_i)^3}{d_p^2} \sqrt{\frac{8}{\pi}} \qquad (1\text{-}39)$$

The activation energy of permeating molecules $E_{P,i}$ and the pre-exponential factor of k_0 can be calculated via regression using equation (1-38) from the experimental measurement of temperature dependency of the single gas permeance result. The activation energy ($E_{P,i}$) can be expressed as the sum of the activation energy of diffusion ($E_{D,i}$) for the permeated molecules to surpass the potential energy barrier, and the energy of interaction or enthalpy of sorption ($-\Delta H_i$). In the case of small-sized micropores, the diffusion barrier act as the dominant factor for the permeation, the value of activation energy of permeating molecules is $E_{P,i} > 0$ and referred to as the activated diffusion (permeation of compounds increases with increasing temperature). For the permeation of molecules through large-sized micropores where the interactions between membrane matrix and permeated molecules are more dominant than the geometrical barrier, the apparent activation energy is $E_{P,i} < 0$ and referred to as surface diffusion (permeation of gases decreases with increasing temperature). On the other hand, when the permeation occurs through much larger micropores in which the Knudsen diffusion mechanism is more dominant, the value of activation energy is $E_{P,i} = 0$ (permeation of components constant with increasing temperatures).

The ideal selectivity for ith and jth components that need to be separated could be estimated from the ratio of permeances as follows.

$$\alpha_{i/j} = \frac{P_i}{P_j} = \sqrt{\frac{M_j}{M_i}} \frac{(d_p - d_i)^3}{(d_p - d_j)^3} exp\left(-\frac{E_{P,i} - E_{P,j}}{RT}\right) \qquad (1\text{-}40)$$

To simplify the equation (1-40), several assumptions were made such as all gases permeated through an identical size of pores, the micropores size of the membrane were justified in the range from several angstroms to 1 nm so that the difference in activation energy for permeation is negligible and independent from each gas species.

$$\alpha_{i/j} = \frac{P_i}{P_j} \approx \sqrt{\frac{M_j}{M_i}} \frac{(d_p - d_i)^3}{(d_p - d_j)^3} \qquad (1\text{-}41)$$

Based on equation (1-41), an ideal selectivity can be approximately calculated as a function of the mean pore diameter of the membrane (d_p) and the size of permeating molecules (d_i and d_j).

Pore size determination: normalized Knudsen permeance (NKP) and $k_{0,i}$ method

The normalized Knudsen-based permeance (NKP) method was calculated the ratio of an experimentally observed permeance of ith component to the ideal Knudsen permeance for each permeated gas (ith component) from the permeance of a standard gas (s component) such as Helium (He). NKP suggested the degree of permeance decrement from the ideal Knudsen permeance. The mean effective pore size of the membrane (d_P) less than 1 nm was qualitatively estimated based on the molecular size that caused the permeation mechanism to deviate from Knudsen to molecular sieving. The plot of NKP obtained from experimental research against the molecular size together with the NKP equation derived from the modified-gas translation (m-GT) model is as follows.

$$f_{NKP} = \frac{P_i}{P_S} \sqrt{\frac{M_i}{M_S}} = \frac{(d_P - d_i)^3}{(d_P - d_S)^3} \exp\left(-\frac{E_{P,i} - E_{P,S}}{RT}\right) \qquad (1\text{-}42)$$

In the case of gas permeation by the ideal Knudsen diffusion, $d_S = d_i = 0$; $E_{P,S} = E_{P,i} = 0$, and f_{NKP} is equal to unity. The equation in (1-42) can be simplified as follows.

$$f_{NKP} = \frac{P_i}{P_S} \sqrt{\frac{M_i}{M_S}} \approx \frac{\left(1 - \frac{d_i}{d_P}\right)^3}{\left(1 - \frac{d_S}{d_P}\right)^3} \qquad (1\text{-}43)$$

The experimentally obtained f_{NKP} at a certain permeation temperature of T (generally at the highest temperature is preferred) as a function of the kinetic diameter is fitted by equation (1-43), with d_P as a fitting parameter [8, 27, 28].

The pore sizes of the membranes can also be determined via the correlation between the cubic root of $k_{0,i}$ and the kinetic diameter of the ith component (d_i).

Meng et al. [29] reported the mixing of bis(triethoxysilyl) ethane-tetraethoxysilane (BTESE-TEOS) precursors to control the pore sizes of organosilica networks in hybrid membrane structure. The single-gas permeation results and the normalized Knudsen-based permeance (NKP) show the average pore size of the membrane (calculated based on equation (1-43)) was reduce in the order of BTESE (d_P= 0.51 nm) > BTESE-TEOS (d_P= 0.43 nm) > TEOS (d_P= 0.34 nm) as shown in Fig. 1-12. The modified BTESE-TEOS structure exhibited high O_2 permeance of 2.87×10^{-8} mol m^{-2} s^{-1} Pa^{-1}, with a high level of O_2/SO_2 permeance ratio of 7.3.
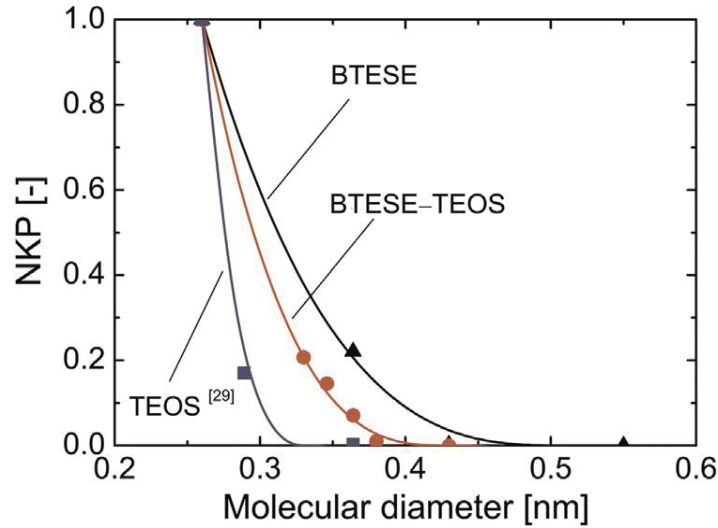
Fig. 1-12. NKP plot as a function of the kinetic diameter of permeating molecules at 200 °C for BTESE-, BTESE-TEOS-, and TEOS-derived membranes [29]

$k_{0,i}$ **method** was used for the determination of membrane pore size according to the equation (1-39). If a is defined as a constant that depends only on the structure of the membrane pores and is independent of the permeation molecules, as given by the following equation.

$$a = \frac{\varepsilon}{3\tau L d_P^2} \sqrt{\frac{8}{\pi}}$$
(1-44)

Thus, the following equation can be obtained.

$$k_{0,i} = a \left(d_p - d_i\right)^3$$
(1-45)

The cubic root of $k_{0,i}$ gives the linear correlation with d_i, with a slope of $-a^{1/3}$ and an intercept of $-a^{1/3}d_p$ as shown below.

$$\sqrt[3]{k_{0,i}} = \sqrt[3]{ad_p} - \sqrt[3]{ad_i} \qquad (1\text{-}46)$$

Based on that equation, from the plot of $k_{0,i}^{1/3}$ against d_i, the value of the mean effective pore size of the membrane can be estimated [28].

Nagasawa et al. [8] have shown that the cubic root of $k_{0,i}$ could be used for the pore sizes determination of BTESE-derived membranes synthesized with different water molar ratios as shown in Fig. 1-13. The plot between the cubic root of $k_{0,i}$ and kinetic diameter of permeated molecules giving a linear correlation, so that the pore size of the membrane (d_p) precisely estimated from the intercept of the x-axis based on equation (1-46). The pore size of the membrane was reduced as the water molar ratio increased in the order of BTESE-WR6 (d_p= 0.47 nm) > BTESE-WR120 (d_p= 0.44 nm) > BTESE-WR240 (d_p= 0.45 nm). The change in water molar ratio was sucessfully control the pore size of BTESE-derived membranes.
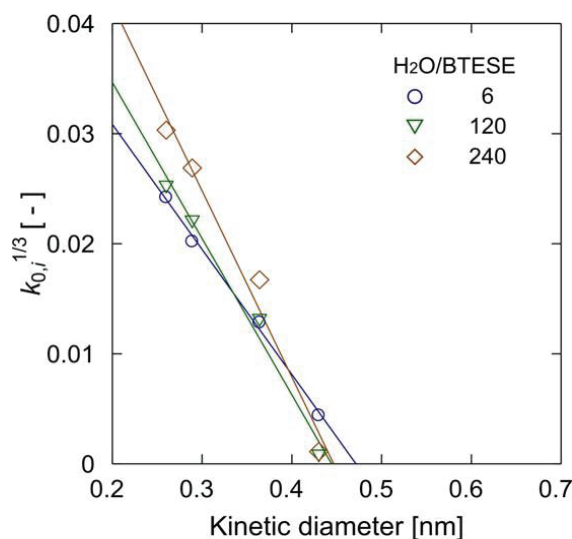
Fig. 1-13. The plot of $k_{0,i}^{1/3}$ as a function of kinetic diameter permeated gases for BTESE-derived membranes at different water molar ratios [8]

In another strategy to estimate the membrane pore size, the equation of (1-38) can be converted as follows.

$$\left(\sqrt{M_i}P_i\right)^{1/3} = \left(\frac{k_0}{\sqrt{RT}}exp\left(-\frac{E_{P,i}}{RT}\right)\right)^{1/3}(d_p - d_i) \qquad (1\text{-}47)$$

If the $E_{P,i}$ assumed to be constant to simplify the equation, the pore size of the membrane (d_p) of the membrane can be calculated by regressing $\left(\sqrt{M_i}P_i\right)^{1/3}$ to equation (1-47). The value of $\left(\sqrt{M_i}P_i\right)^{1/3}$ for each permeated gas is plotted as a function of the kinetic diameter of permeating molecules (d_i), and the intercept of molecular size at $\left(\sqrt{M_i}P_i\right)^{1/3} = 0$ reflects the pore size of the membrane.

Moriyama et al. [30] reported the pore size of BTESE-derived membranes that synthesized with different water and acid molar ratio could be determined via $\left(\sqrt{M_i}P_i\right)^{1/3}$ as a function of molecular size permeating gases as shown in Fig. 1-14. Two membranes refer to as M1 (WR=120, AR=1) and M2 (WR=240, AR=0.1) show different pore sizes of 0.58 and 0.42 nm, respectively. By changing the water and acid molar ratio, the H_2/N_2 permeance ratio was increased from 13 to 59, which then confirm the structure of the membranes was successfully controlled.
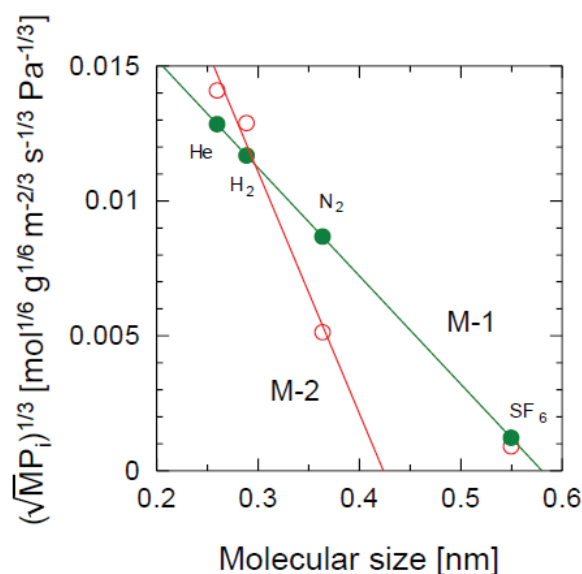
Fig. 1-14. The correlation between $\left(\sqrt{M_i}P_i\right)^{1/3}$ and molecular size of permeating gas for BTESE-derived membranes [30].

1.2.3 A recent application and development in gas separation by membrane technology

Nowadays, Gas permeation membrane technology gaining large attention in the chemical and petrochemical industry such as hydrogen recovery, air separation, CO_2 separation, recovery of organic from gas streams, natural gas dehydration, etc [31]. Table 1-4 presents the summary of industrial application for membrane gas separation-based process.

Table 1-4. Main industrial application of membrane gas separation

Separation	Process	Ref.
H_2/N_2	Ammonia purge gas	[31]
H_2/CO_2	Syngas ratio adjustment	[31]
H_2/hydrocarbon	Hydrogen recovery in refineries	[31], [1]
CO_2/N_2	Post-combustion carbon dioxide capture	[32]
O_2/N_2	Nitrogen generation, oxygen-enriched air production	[31]
CO_2/CH_4	Natural gas sweetening, landfill gas upgrading	[31], [1]
CO_2/Hydrocarbon	Natural gas liquid removal	[20]
N_2/CH_4	Nitrogen removal	[20]
N_2/SF_6	Gas-insulated equipment	[33]
H_2O/CH_4	Natural gas dehydration	[1]
He/Hydrocarbon	Helium separation	[31]
He/N_2	Helium recovery	[31]
Hydrocarbon/air	Hydrocarbon recovery, pollution control	[31]
Volatile organic species (e.g. ethylene, propylene)/ light gases (e.g. N_2)	Polyolefin purge gas purification, adsorption, refigeration and turboexpander plants	[20], [31]

The increased use of membrane technology is expected to reduce the environmental impact with a small footprint and costs of industrial processes. Gas separation properties largely depend on the membrane materials, membrane structure, thickness, membrane configuration, and membrane system design. Therefore, much research work is being addressed to evaluate and investigate new material that can develop a membrane with high performance including high

selectivity and permeability to specific gases.

Most membranes perform a trade-off between permeance (the ability to permeate molecules passing through the membrane barrier) and selectivity (the desired molecules are separated from the rest). Key design criteria for membranes have emerged with properly sized free-volume elements (pores), narrow free-volume or pore size distribution, a thin active layer, and highly tuned interaction between permeants of interest and the membrane [34]. Robeson in the 1990s reported the permeability data on several common gases such as He, H_2, O_2, N_2, CO_2, and CH_4 on polymeric membranes, and the trade-off relationship between permeability and selectivity was analyzed [35].

Several polymeric membranes show the highest selectivity at a certain permeability lay near a line, which is called the upper bound. More permeable polymers tend to have lower selectivity and vice versa. The result of the upper bound in 1991 was revisited in 2008 with a much larger database and notable advance in the search for more permeable and selective membranes [36]. Fig. 1-15 shows the trade-off for the different gas systems based on Robeson upper bound [36].
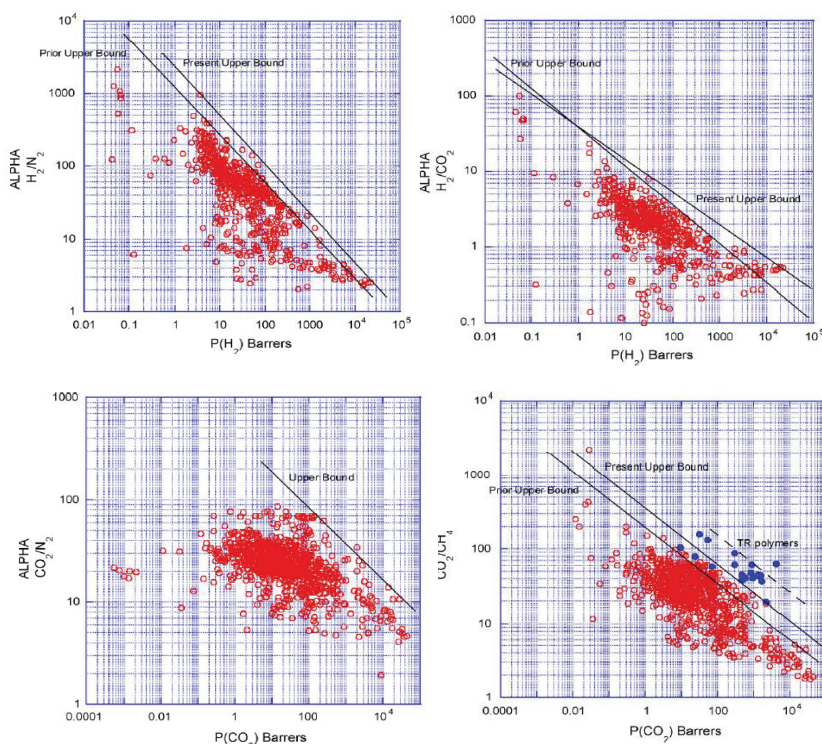
Fig. 1-15. Upper bound correlation for H_2/N_2 (a), H_2/CO_2 (b), CO_2/N_2 (c), and CO_2/CH_4 (d)

In general trend, most membranes show modest shifts in the upper bound that were studied between 1991 and 2008.

Various approaches have been explored to develop membrane materials that can exceed the upper bound, including surface modification, facilitated transport, hybrid membrane structure, and mix-matrix membrane. In principle, designing membrane structure to overcome the trade-off curve always encounter three common trends, as shown in Fig. 1-16.
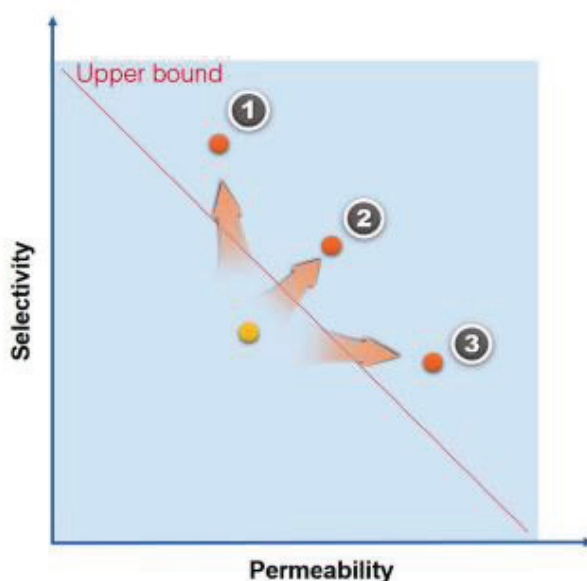
Fig. 1-16. Modification of membrane structure to overcome the upper bound line encountered with three common trends [34].

In the first case, the modification of the membrane with molecular sieving fillers such as carbon molecular sieving (CMS) and zeolites lead to enhances the selectivity of the membrane but decreases the permeability. The modification of pore structure for increasing the permeation rate often enhances the permeability of large-sized gases more than small-sized gases, resulting in increased permeance but decreased selectivity. In the second trend, the modification of molecular sieving filler with nano size or nanosheet shape can improve both permeability and selectivity. Membranes with very narrow pore size distribution or uniform pore sizes known as isoporous membranes could show both high permeability and selectivity due to the contribution of isoporous geometry with no tortuosity, precise, and uniform pore size. However, in the practical development of the membrane, isoporous structure was difficult to achieve and there is always a pore

size distribution in membrane structure. On the contrary, in the third case, the modification of the membrane with interfacial voids resulted in high permeability and lower selectivity.

Many studies focus on the development of membrane materials that show better permeability and/or better selectivity. Generally, high flux membranes can be obtained by using high-permeability materials and modifying the thickness of the membranes. Therefore, most of the current separating layers of the membranes are often less than 100 nm thick. Nagasawa et al. [37]reported the synthesis of microporous silica membrane with hexamethyldisiloxane (HMDSO) precursor via atmospheric-pressure, low-temperature plasma deposition. In that work, the thickness of the topmost layer was uniformly formed on the porous substrate with a thickness of 13 nm (Fig. 1-17). Plasma deposited layer simultaneously improves the membrane permeance for small-sized gas of $>10^{-6}$ mol m^{-2} s^{-1} Pa^{-1} with high selectivity for H_2/SF_6 of 6,300 which surpasses the trade-off line (Fig. 1-17(b)).
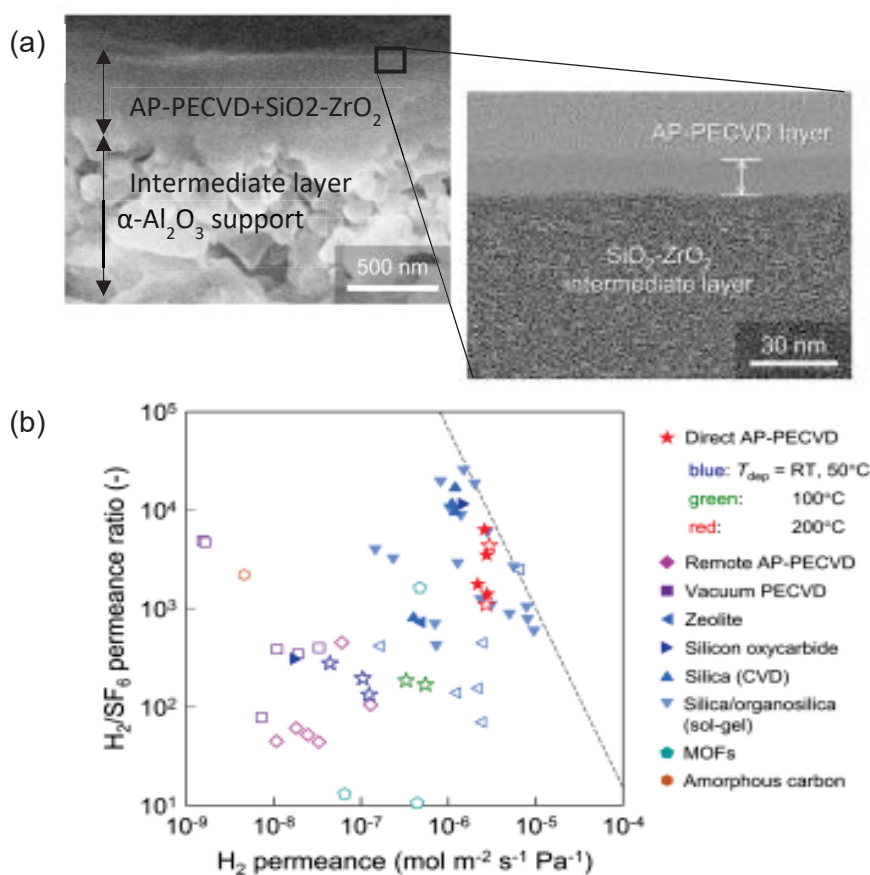
Fig. 1-17. The TEM cross-sectional images of the AP-PECVD membrane prepared at 200 °C (a), and the trade-off curve between H_2 permeance with H_2/SF_6 permeance ratio for different types of membranes.

In addition, the excellent transport properties must meet the criteria of mechanically robust, chemically, and thermally tolerant to operation conditions so that the membrane can survive manufacturing, installation, and long-term use.

1.3 Liquid phase separation processes

At present, membrane technology has been widely used for liquid phase separation including water treatment such as water production from seawater and surface water, and wastewater treatment. The common industrial application of membrane technology has shown an impressive growth in the wastewater treatment, biotechnology, pharmaceutics, chemical, and food industry which are categorized for the separation of liquid mixture. The use of membrane technology for the separation of liquid phase mixture has been recognized for the following advantages simplicity for the operational, low energy, high stability, easy control, large flexibility, and scale-up. In this section, the authors focus on the separation of liquid mixtures with microporous and dense membrane structures with a pore size smaller than 2 nm. Thus, the main feature of this section is an elaborate discussion of important and promising liquid phase separation techniques such as organic solvent nanofiltration (OSN), organic solvent reverse osmosis (OSRO), and pervaporation (PV). The general background of membrane separation for the liquid mixture containing organic solvents is provided and integrated with the application via different types of membrane materials for a comprehensive study. The interaction between solvent and membrane materials is then explained and related to process performance, i.e. permeability, flux, and separation factor.

1.3.1 Organic solvent nanofiltration (OSN)

Organic solvent nanofiltration (OSN) is a molecular separation technology based on membranes that allow the discrimination of dissolved species in an organic solvent on basis of size, shape, and the charge of molecules [38]. Based on the pressure required for the separation process, Mulder [39] classified the OSN as a process in which pressure from 5 to 20 or extended to 40 bar is applied. Most OSN membranes have a big pore size in the range of 0.7-2 nm. Stable OSN membranes with molecular weight cut-offs

(MWCOs) ranging from 200-1,000 g mol^{-1} have emerged for the separation of peptides, dyes, catalysts, and chemical intermediates [40]. However, the separation capability can not only be described by the MWCO only but the steric and electrostatic separation mechanism, typical environment of the solvent, structure, and properties of the solvent can be significantly affected. To predict the fluxes and the rejection through the porous and/or non-porous membranes, the transport mechanism between solutes and solvents has to be understood. Two main assumptions for the nanofiltration transport model were the pore-flow models and the solution-diffusion approach.

In **the pore-flow model**, stable porosity ($\boldsymbol{\varepsilon}$) is assumed to be present inside the membrane with the tortuosity of τ. The driving force for the transport is the pressure gradient across the membrane (∇_P), and the system was assumed at a constant temperature (Fig. (1-18)), so the equation can be written from the Stefan-Maxwell model as follows.

$$-x_{i(m)}\nabla_{T,P}\mu_i - x_{i(m)}\bar{V}_i\nabla_P = \sum_k \zeta_{i,k}\frac{x_{k(m)}N_i - x_{i(m)}N_k}{c_{t(m)}(\varepsilon/\tau)} + \zeta_{i,m}\frac{N_i}{c_{t(m)}(\varepsilon/\tau)} + \alpha_i'\frac{\zeta_{i,k}x_{i(m)}\beta_0}{\eta}\nabla_P \quad (1\text{-}48)$$

Where $x_{i(m)}$ is the molar fraction of ith component, $\nabla_{T,P}$ is the gradient at constant temperature and pressure, μ_i is the chemical potential, $\bar{V}_i$ is partial molar volume, $\zeta_{i,k}$ is friction coefficient, $c_{t(m)}$ is the molar concentration of component i, N_k is molar flux, α_i' is viscous flow parameter, η is viscosity, and β_0 is specific permeability and depends on the membrane structure. Since the contribution of the pressure gradient is much more significant than the activity gradient, equation (1-48) can be simplified as follows.
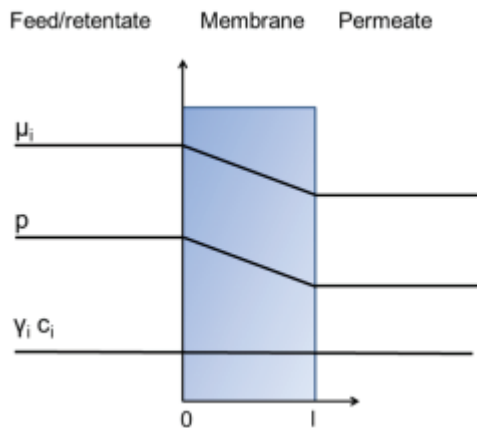
Fig. 1-18. The profile of chemical potential, pressure, and solvent activity characteristics of an organic component through a membrane barrier according to pore-flow transport

$$-x_{i(m)}\bar{V}_i\nabla_P - \alpha_i'\frac{\zeta_{i,m}x_{i(m)}\beta_0}{\eta}\nabla_P = \sum_k \zeta_{i,k}\frac{x_{k(m)}N_i - x_{i(m)}N_k}{c_{t(m)}(\varepsilon/\tau)} + \zeta_{i,m}\frac{N_i}{c_{t(m)}(\varepsilon/\tau)} \quad (1\text{-}49)$$

Considering the friction of chemical species with the membrane is much higher than the friction between species, the equation can be written as follows.

$$x_{i(m)}\bar{V}_i\nabla_P + \alpha_i' \frac{\zeta_{i,m}x_{i(m)}\beta_0}{\eta}\nabla_P = -\zeta_{i,m}\frac{N_i}{c_{t(m)}(\varepsilon/\tau)} \tag{1-50}$$

The first term on the left side is much lower compared to the second term, due to the small value of the species' partial molar volume, so the equation can be expressed as follows.

$$N_i = -\alpha_i'\frac{x_{i(m)}\beta_0}{\eta}\frac{\varepsilon}{\tau}\nabla_P \tag{1-51}$$

For small-sized permeating molecules concerning the pore size, the viscous selectivity is one, and the total volume flux (N_v) is expressed by.

$$N_v = -\frac{\beta_0}{\eta}\frac{\varepsilon}{\tau}\nabla_P \tag{1-52}$$

If the structure of the membranes contains more or less cylindrical pores, the Hagen-Poiseulle equation can be used.

$$N_v = -\frac{d_{pore}^2}{32\eta}\frac{\varepsilon}{\tau}\nabla_P \tag{1-53}$$

If the membrane consists of packed particles, the Carman-Kozeny can be used as follows.

$$N_v = -\frac{d_{particle}^2}{180(1-\varepsilon)^2\eta}\frac{\varepsilon}{\tau}\nabla_P \tag{1-54}$$

In **the solution-diffusion model**, it is assumed that each permeating molecule dissolved in the membrane matrix and diffuse through the membrane concentration gradient. In this model, there is no pressure gradient inside the membrane as shown in Fig. 1-19. The equation of Stefan-Maxwell can be expressed as follows.
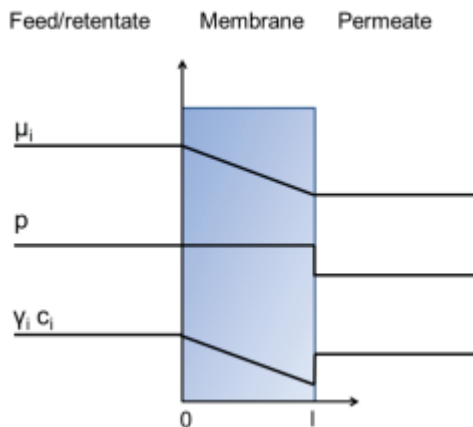
Fig. 1-19. The profile of chemical potential, pressure, and solvent activity characteristics of one component through a membrane via a solution-diffusion model

$$-x_{i(m)}\nabla_{T,P}\mu_i = \sum_k \zeta_{i,k}\frac{x_{k(m)}N_i - x_{i(m)}N_k}{c_{t(m)}} + \zeta_{i,m}\frac{x_m N_i}{c_{t(m)}} \qquad (1\text{-}55)$$

Considering the friction between components is smaller than the friction of species with the membrane matrix, the equation can be expressed as follows.

$$-x_{i(m)}\nabla_{T,P}\mu_i = \zeta_{i,m}\frac{x_m N_i}{c_{t(m)}} \qquad (1\text{-}56)$$

Kinetic coupling and the gradient of chemical potential with a molar fraction gradient were assumed to be negligible, the equation (1-56) can be written as follows.

$$N_i = -\frac{c_{i(m)}}{x_m \zeta_{i,m}}\nabla x_{i(m)} \qquad (1\text{-}57)$$

By assuming a constant value of x_m, and the activity coefficient for each penetrant inside the membrane remains constant, the equation (1-57) can be expressed as follows.

$$N_i = P_{i,m}^{molar}\left(x_{i,f} - \frac{\gamma_{i,p}}{\gamma_{i,f}}x_{i,p}exp\left(-\frac{\bar{V}_1\Delta P}{RT}\right)\right) \qquad (1\text{-}58)$$

The OSN process is much more complex compared to the aqueous filtration due to the contribution of all relevant component interactions such as solvent, solute, and membranes. Table 1-5 shows the viscosity (η), Hansen solubility parameter (δ), and the kinetic diameter (d_{kin}) of each type of solvent to analyze the effect of the physical properties of the component on the OSN performance. The viscosity of components was measured at 25 °C, and the total Hansen solubility parameter was used to reflect the polarity and the interaction strength between the solvent and membrane materials. The Hansen solubility parameter consists of dispersion, polarity, and hydrogen bonding parameter, which has been used to explain the membrane performance. The kinetic diameter of permeating molecules describes the size of molecules when passing through a membrane pore and reflects the smallest effective dimension of the molecules.

Table 1-5. The physical properties summary of selected solvents [41-43]

Solvent	η [mPa s]	δ [Mpa$^{1/2}$]	d_{kin} [nm]
Water (H$_2$O)	0.916	47.8	0.265
Methanol (MeOH)	0.539	29.6	0.38
Ethanol (EtOH)	1.081	26.5	0.44
Isopropanol (IPA)	2.058	23.5	0.47
Acetone (Ace)	0.316	19.94	0.47
Tetrahydrofuran (THF)	0.457	19.4	0.48

Dichloromethane (DMC)	0.414	20.3	0.49
Dimethylformamide (DMF)	0.816	24.8	0.5
Acetonitrile (AcN)	0.342	24.4	0.55
Toluene (Tol)	0.555	18.2	0.55
Methyl acetate (MA)	0.385	18.7	0.478
Methyl ethyl ketone (MEK)	0.410	19.05	0.504
Ethyl acetate (EtAc)	0.440	18.1	0.52
Isopropyl acetate (i-PAc)	0.490	17.6	0.57
Butyl acetate (BA)		17.41	0.585
Heptane (n-Hep)	0.400	15.3	N.a.
Hexane (n-Hex)	0.294	14.9	0.51
Butanol (BuOH)	2.60	23.2	0.505
Tertiary butanol (Tert-BuOH)	2.57	14.3	0.51

The industrial application of OSN can be found in the oil- and petrochemical, food, bioproduct industry, bulk chemistry, and the pharmaceutical industry. Table 1-6 gives an overview of OSN membrane application together with membrane materials. Higher OSN separation performance requires a membrane structure with high interconnected micropores and a thin membrane layer that shows higher permeance and permeating flux.

Table 1-6. OSN membrane application [38]

Solvent	Application	Membrane
Acetone	Vegetable oil deacidification	Polyamide (PA)
Chloroform/ toluene	Removing metals and carbon residue from heavy oil	Poly (vinylidene fluoride) (PVDF)
Cyclopentane	Fractionation of hydrocarbon oils	Polycarbonate
Dimethylformamide (DMF)	Pharmaceuticals, purification of polymers	Polydimethylsiloxane (PDMS)
Ethanol	Nutraceuticals, flavors, pigments, vegetable oil, protein, amino acids	Polysulfone (PSf), polyimide (PI)
n-heptane	Aromatics from heavy oil	Polypropylene
Hexane	Vegetable oil refining, regeneration of used lube oils	PDMS, PI, polyvinyl alcohol (PVA), ceramic membranes
Methanol	Refining vegetable oil, pharmaceuticals	Composites, ceramic membranes

----

Methyl esters	Biodiesel, vitamins	Composites membranes
Methyl ethyl ketone (MEK)	Removal of dewaxing solvents	Cellulose acetate (CA), PI
n-paraffins	Lube oil dewaxing	Polycarbonate
Propane	Oils from organic solvents	PI
Toluene/DMF/xylene	Removal of low molecular weight compounds in polymer manufacture	PI

1.3.2 Organic solvent reverse osmosis (OSRO)

Organic solvent reverse osmosis (OSRO) was developed for the separation of the smaller size of solute molecules in the different kinetic diameter range of 0.1-0.3 nm in liquid mixtures with the gradient of chemical potential across the membrane [44]. The membrane pore size that could be used for the OSRO process primarily provides a small size below 0.7 nm, and pressurizes the membrane feed to levels that exceed the transmembrane osmotic pressure is required before the permeation can occur [45]. Furthermore, OSRO membranes were responsive to the existence of defects that could induce pressure-driven diffusion and reduce the separation ability of the membranes. Properly high pressure for membrane operation was required to overcome the high osmotic pressure (generally higher than 30 bar) and enhance productivity, hence high stability of the membrane in organic media, high-pressure resistance, and favorable separation characteristics must be performed.

The transport mechanism of the permeated component through OSRO membranes generally follows the solution-diffusion mechanism where the molecules dissolved inside the membrane matrix and then diffuse through it as a permeate [46]. The separation of organic mixtures strongly depends on the sorption and diffusion behaviors of each component inside the membrane. The permeating molar flux (J) of one species is equal to its chemical potential gradient.

$$J = -\frac{DC_m x_m}{RT}\frac{d\mu}{dz} = -\frac{DC_m}{RT}\left(RT\frac{dx_m}{dz} + x_m v\frac{dp_m}{dz}\right) = -DC_m\frac{dx_m}{dz} \qquad (1\text{-}59)$$

Where v is the molar volume of one species, D is the diffusion coefficient, C_m is the total molar concentration, R is the gas constant, and T is the absolute temperature. The integration equation (1-59) is based on the membrane thickness from 0 to L, the flux of

the membrane can be expressed as follows.

$$J = \frac{DC_m}{L}(x_1^m - x_2^m) \tag{1-60}$$

The chemical potential equilibrium between the membrane surface and the solution was assumed to get the equation (1-61) and (1-62). On the feed side, it was assumed that $\mu_1^s = \mu_m^1$, while on the permeate side $\mu_2^s = \mu_2^m$.

Feed side: $\qquad \mu_0(p_1, T) + RT ln r_1^s x_1^s = \mu_0(p_1, T) + RT ln r^m x_1^m \tag{1-61}$

Permeate side: $\mu_0(p_2, T) + RT ln r_2^s x_2^s = \mu_0(p_2, T) + RT ln r^m x_2^m + v(p_1 - p_2) \tag{1-62}$

By substituting x_1^m and x_2^m into equation (1-60), and change the $\frac{DC_m}{Lr^m} = K$, so that the flux

(J) of the membrane can be expressed as follows.

$$J = K\left[r_1^s x_1^s - r_2^s x_2^s exp\frac{v(p_2-p_1)}{RT}\right] \tag{1-63}$$

The osmotic pressure can be defined as follows.

$$\pi = -\frac{RT}{v}\ln(rx) \tag{1-64}$$

By substituting equation (1-64), the flux of the membrane can be transformed into equation (1-64).

$$J = Kr_1^s x_1^s\left[1 - exp\left(\frac{v}{RT}(p_2 - p_1)\right) \times exp\left(\frac{v}{RT}(\pi_2 - \pi_1)\right)\right]$$

$$J = Kr_1^s x_1^s\left[1 - exp\left(\frac{-v}{RT}(\Delta p - \Delta \pi)\right)\right] \tag{1-65}$$

If we assumed $\frac{-v}{RT}(\Delta p - \Delta \pi) \approx 0$, the flux can be stated in equation (1-66)

$$J = \frac{Kr_1^s x_1^s v}{RT}(\Delta p - \Delta \pi) \tag{1-66}$$

The flux in the RO condition can be equally expressed to the molar fraction ratio in the permeate of components M and N, as shown below.

$$\frac{J_M}{J_N} = \frac{(x_2^s)_M}{(x_2^s)_N} = \frac{K_M\left[r_1^s x_1^s - r_2^s x_2^s exp\frac{v(p_2-p_1)}{RT}\right]_M}{K_N\left[r_1^s x_1^s - r_2^s x_2^s exp\frac{v(p_2-p_1)}{RT}\right]_N} \tag{1-67}$$

Thus, the permeation flux and the molar fraction of each component in the permeate can be calculated based on equations (1-63) and (1-67), respectively. The total flux (J_T) and the rejection (R) can be expressed below.

$$J_T = J_M + J_N \tag{1-68}$$

$$R = \left[1 - \frac{(x_2^s)_N}{(x_1^s)_N}\right] \times 100\% \tag{1-69}$$

Where $(x_1^s)_N$ and $(x_2^s)_N$ is the molar fraction of component N in the feed and on the

permeate side, respectively [47].

Presently, the industrial OSRO development is in the beginning stage, so the development of materials and the separation mechanism need to be further examined. Table 1-7 shows common separation systems of various binary mixtures and the appropriate membrane materials for each application.

Table 1-7. Organic mixtures separation performance via OSRO process

Membrane	System [molar ratio]	Pressure [Mpa]	Flux [kg m^{-2} h^{-1}]	Separation factor [-]	Ref.
SWC5	MeOH/Tol (96.3/3.7)	3.0	7.60	4.8	[48]
PK-PA	MeOH/Tol (90/10)	3.0	2.40	45	[46]
BTESA	MeOH/Tol (95/5)	2-18	0.24-3.98	19.7-240	[49]
BTESA	MeOH/MA (95/5)	12	2.20	8	[49]
BTESA	MeOH/DMC (95/5)	12	1.85	10	[49]
BTESA	MeOH/MTBE (95/5)	12	1.70	1,100	[49]
CAB	MeOH/Pentane (15/85)	3	N.a.	5.7	[50]
CA	MeOH/Pentane (15/85)	3	N.a.	15	[50]
Cellulose	MeOH/iso-BuOH (60/40)	15.5	3.20	1.7	[51]
PE	EtOH/Xylene (48.5/51.5)	6.9	0.15-0.23	36.7-61.8	[52]
CA	EtOH/Xylene (49/51)	6.9	0.54	2.7	[52]
PA	EtOH/P-Xylene (40/60)	1.7	N.a.	2.3	[53]
CA	EtOH/N-Heptane (67/33)	6.9	0.65	7.7	[52]
CAB	EtOH/N-Heptane (40/60)	5.2	0.42	2.3	[53]
PA	EtOH/N-Heptane (40/60)	5.2	0.10	8.5	[53]
AF2400/polyketone	EtOH/N-Hexane (40/60)	4	1.60	9.5	[54]
Glass	EtOH/Cyclohexane (45/55)	1.3	0.04	1.3	[55]
PE	N-heptane/Xylene (49.5/50.5)	6.9	0.59	1.1	[52]
CA	N-heptane/Xylene (49.5/50.5)	6.9	0.23	5.2	[52]

1.3.3 Pervaporation (PV)

1.3.3.1 Introduction: membrane transport properties of pervaporation

Pervaporation (PV) is a membrane-based separation process where the transport of components occurs through a dense membrane [56]. Membrane performance was determined by the chemical properties and the structure of the membrane matrix so that

the mass transport in pervaporation is based on permeated component-membrane interaction. Compounds are selectively transported from the liquid phase in the upper stream to the vapor phase in the lower stream, which enables better separation performance and lower levels of energy consumption [4, 57, 58]. These downstream operating conditions ensure the efficient removal of the component from the membrane downstream surface when maintaining the partial pressure of permeating component close to zero. The higher partial pressure of the feed stream can be achieved via a preheated process of the mixtures on the feed side (generally at a temperature close to that of its saturation temperature) [59]. In the pervaporation process, there is a mass transport and heat transfer across the membrane, including the change of physical state from the liquid in the feed stream to a vapor solution on permeate side with the enthalpy of vaporization. In most cases, the permeating compounds are recovered via the condensation process and the composition of permeate was evaluated with gas chromatography characterization as schematically shown in Fig. 1-20.
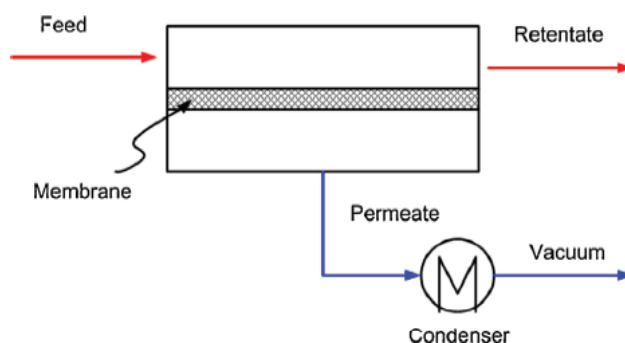
Fig. 1-20. Schematic diagram of vacuum pervaporation process [60]

The solution-diffusion model is frequently used for explaining mass transport through dense or non-porous membrane processes, particularly pervaporation (PV). The transport of components through a membrane consists of three main processes, including the sorption of the permeating component from the feed liquid into the membrane matrix, the diffusion of permeating component through the membrane, and the desorption of permeating component to the vapor phase on the downstream of the membrane as schematically describe in Fig. 1-21. In solution diffusion mode, several assumptions were made such as the membrane matrix is a homogeneous medium, an isothermal system, steady-state, no convection where the flux of the membrane is only diffusive, the first law

----

of Fick is valid, no coupling mass transport effect, interfacial equilibria where the chemical potential of separated compounds at the feed are the same and at the same pressure, and the chemical potentials of the component at the membrane or downstream interface are equal [56].

The driving force for the pervaporation was evaluated from the difference between the partial pressure in the feed and permeate streams so that the permeance of the i-th (P_i) component can be expressed as follows.

$$P_i = J_i \Big/ (p_{1,i} - p_{2,i}) \tag{1-70}$$

(i) Sorption

(ii) Diffusion

(iii) Desorption
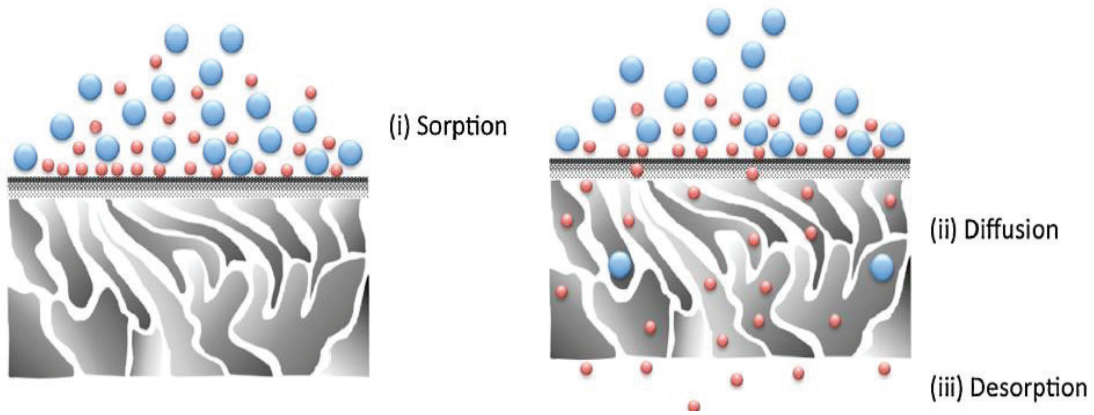
Fig. 1-21. Schematic image of the solution-diffusion process [60].

Where J_i is the molar flux of the i-th component, $p_{1,i}$ and $p_{2,i}$ are the feed partial pressure and the permeate partial pressure, respectively. The feed streams partial pressure of component i can be calculated as follows.

$$p_{1,i} = \gamma_i x_i p_{i,0} \tag{1-71}$$

$$\log p_{i,0} = A - B/(t[°C] + [C]) \tag{1-72}$$

Where $p_{i,0}$ is partial vapor pressure that is calculated based on the Antoine equation (Eq. 1-72), t is the temperature of the pervaporation system, x_i is the mole fraction of component i, and γ_i is activity coefficient that was determined by the Wilson equation. In this system, the permeate pressure ($p_{2,i}$) was assumed to be zero. The activity coefficient of each component can be calculated with Wilson parameters (Λ_{12} and Λ_{21}) based on equations (1-73) and (1-74) [4].

$$\ln \gamma_1 = -\ln(x_1 + \Lambda_{12}x_2) + x_2 \left[\frac{\Lambda_{12}}{x_1 + \Lambda_{12}x_2} - \frac{\Lambda_{12}}{\Lambda_{12}x_1 + x_2} \right] \tag{1-73}$$

$$\ln \gamma_2 = -\ln(x_2 + \Lambda_{21}x_1) + x_1 \left[\frac{\Lambda_{12}}{x_1 + \Lambda_{12}x_2} - \frac{\Lambda_{12}}{\Lambda_{21}x_1 + x_2} \right] \qquad (1\text{-}74)$$

The Wilson parameters for several methanol organic mixtures were summarized in Table 1-8.

In addition, a facilitated transport mechanism is possibly applied for the separation of liquid mixtures through a dense membrane structure where the accelerated transfer of targeted molecules occurs in addition to the normal Fickian diffusion.

Table 1-8. Kinetic diameter, Antoine coefficient, and Wilson parameter several organic compounds with methanol (MeOH) as compound 2 [61-63]

Compound 1	Molecular size [nm]	Antoine coefficient (Compound 1)			Antoine coefficient (Compound 2)			Wilson parameters	
		A	B	C	A	B	C	Λ_{12}	Λ_{21}
Ethanol (EtOH)	0.43	8.04494	1554.3	222.65	7.87863	1473.11	230	0.20397	2.30756
Isopropyl alcohol (IPA)	0.47	6.6604	813.055	132.93	7.87863	1473.11	230	1.24972	0.56621
Tertiary butanol (Tert-BuOH)	0.51	7.60203	1285.067	189.318	7.87863	1473.11	230	0.4825	2.2131
Methyl acetate (MA)	0.478	7.065	1157.63	-53.42	7.87863	1473.11	230	-99.919	452.06
Ethyl acetate (EA)	0.52	7.20211	1232.83	228	7.87863	1473.11	230	0.48274	0.50375
Butyl acetate (BA)	0.585	7.02845	1368.5	204	7.87863	1473.11	230	287.87	4182.56
Dimethyl carbonate (DMC)	0.53	6.4338	1413	-44.25	7.19736	1574.99	-34.3	0.7743	0.2836
Isopropyl acetate (i-PAc)	0.57	7.20211	1232.83	228	7.87863	1473.11	230	0.48274	0.50375
Toluene (Tol)	0.59	6.95464	1344.8	219.482	7.87863	1473.11	230	0.28838	0.121

The mobility of permeated components through facilitated transport can be classified into three classes, including a mobile carrier membrane, semi-mobile carrier membrane, and fixed-site carrier membrane as shown in Fig. 1-22 [64]. In mobile carrier membranes, the carriers can diffuse freely, while in semi-mobile carrier membranes the carrier can migrate otherwise it gains high energy to reach the state of activation. In the case of a fixed-site carrier membrane, the carrier can only oscillate within a nanoconfined space. The facilitated transport phenomena in pervaporation is dominated by the fixed-site carrier membrane, where a reversible reaction of A + B $\rightleftharpoons$ AB can take place between the carrier B and the permeating molecule A and lead to a preferential diffusion of component A

through the membrane matrix.

(a) Mobile carrier membrane   (b) Semi-mobile carrier membrane   (c) Fixed-site carrier membrane

• Target permeant   Carrier   —— Polymer chain   Liquid matrix   Polymer matrix
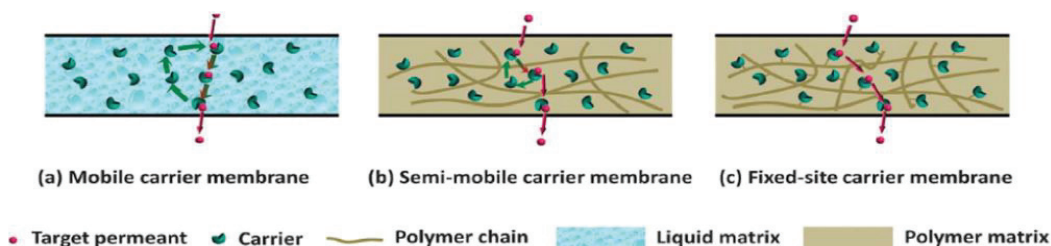
Fig. 1-22. Schematic image of the facilitated transport through mobile carrier membrane (a), semi-mobile carrier membrane (b), and fixed-site carrier membrane (c) [64].

Facilitated transport based on π-complexation has gained great attention in hybrid membranes for pervaporation. Some transition metal ions such as Ni^{2+}, Co^{2+}, Cu^{2+}, Ag^+, and Pd^{2+} can interact with specific components including pyrroles, thiophenes, pyridine, and aromatic species via π-complexation. Zhang et al. [65] reported the modification of $Co(HCOO)_2$-based hybrid membranes as schematically shown in Fig. 1-23 for the separation of benzene (aromatic) over cyclohexane and n-heptane (nonaromatic and aliphatic) via pervaporation. In that work, Cobalt formate has demonstrated a stable performance for facilitating the transport of aromatic compounds, resulting high permeating flux of 0.771 kg m^{-2} h^{-1} with a separation factor of 5.1.
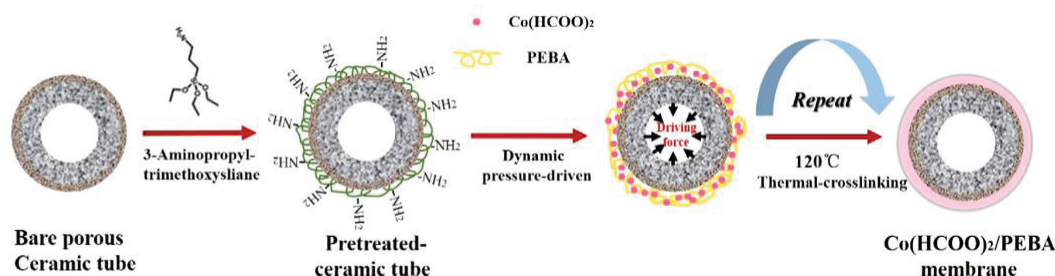
Fig. 1-23. Schematic synthesis concept of $Co(HCOO)_2$-PEBA membrane for facilitated transport of aromatic compound [65].

The separation factor on pervaporation performance was affected by the operating condition such as temperature, feed flow rate, and the feed concentration. Ma et al. [66] reported with an increase in temperature, the flux of permeated components such as water and ethanol was increased due to the increase of the vapor pressure that acts as the driving force of the permeation. Fig. 1-24 shows the correlation between the membrane permeance and the temperature dependence of water and ethanol. Permeation of the component was assumed to occur only by the diffusion following three consecutive steps: (1) the sorption onto the membrane, (2) diffusion of the adsorbed molecules through the

membrane, and (3) the desorption from the permeated side of the membrane.
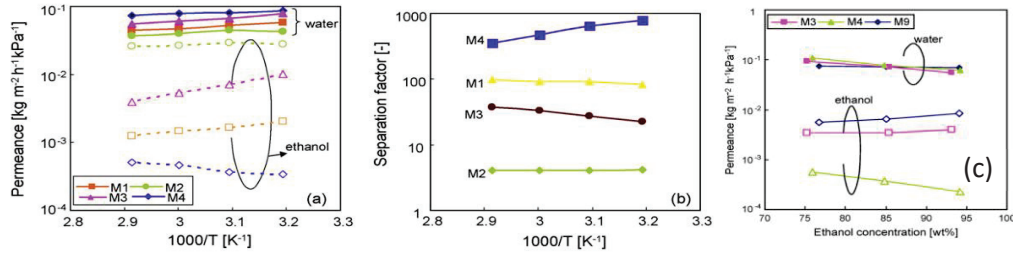
Fig. 1-24. Temperature dependence for permeance (a), the separation factor (b), and correlation between ethanol feed concentration with permeance for silica membranes (c) [66].

If it was assumed that the rate of adsorption and desorption are similar, adsorption is $S = S_0 exp(-\Delta H_S/RT)$, and the diffusivity is $D = D_0 exp(-E_D/RT)$, the permeance can be calculated as follows.

$$\frac{P_i}{l} = \frac{J_i}{\Delta P} = \frac{SD}{l} = \frac{S_0 D_0}{l} exp\left[\frac{-E_p}{RT}\right] \qquad (1-75)$$

The value of ΔP is equal to the feed partial vapor pressure for each component, S_0, D_0 are pre-exponential factors, E_D is the activation energy for diffusion, and ΔH_S is the heat of adsorption. Therefore, E_p is the total activation energy of the permeating molecule.

$$E_p = E_D - \Delta H_S \qquad (1-76)$$

A straight line in Fig. 1-24 was fitted based on the Arrhenius equation (1-75). The total activation energy of permeating component can be positive or negative, depending on the activation energy of diffusion exceeding the heat of adsorption. If $E_p > 0$, the energy of activated diffusion is greater than the heat of adsorption, hence, permeance increase with temperature, while the value of $E_p < 0$, the heat of adsorption is greater than the activation energy for diffusion, resulting in permeance that decreases as the temperature increases. Fig. 1-24(c) shows concentration dependence of the membrane, where water permeance remained nearly constant, while the ethanol permeance shows a different trend depending on the pore size of the membrane. Based on these results, the difference in partial vapor pressure as the main driving force and the interaction between membrane surface and permeating molecules could be taken into consideration.

The history of pervaporation was started in the 1910s by Kober who defined pervaporation as the permeation and evaporation after he evaluated water selective permeation through the membrane [67]. The first industrial pervaporation membrane was

launched by Gesellschaft fur Trenntechnik (GFT) using a composite membrane of crosslinked polyvinyl alcohol (PVA) on a porous poly(acrylonitrile) on non-woven support [68], followed by the installation of pervaporation plant for the dehydration of ethanol in Brazil [69]. Thereafter, the development of membrane material for the pervaporation process grew fast over the decades. Today, membrane research significantly increased from the aspect of the search for competitive membrane materials, the process, and its application in dehydration of organics and recovery of organic-organic separation.

1.3.3.2 Application of the pervaporation

a) Dehydration of alcohol

The separation of low molecular weight components such as alcohol and water has been one of the most challenging tasks due to the formation of azeotropic mixtures. The conventional separation process such as distillation requires high costs and energy consumption with low separation ability. In the case of solvent dehydration, where a small concentration of water content needs to be removed, hydrophilic membranes are generally used. The hydrophilic membrane can preferentially allow water to penetrate, resulting in high water content on permeate side and dehydrating the solvent in the retentate streams [70]. On contrary to that, hydrophobic membranes can be used to remove a small amount of the organic solvent from the systems that are dominated by water, leaving the water on the retentate side while admitting the solvent to penetrate.

Three main classes of membranes have recently been used for the dehydration of alcohol mixtures, including polymeric, inorganic membranes such as ceramic, zeolite, and organosilica, and composite membranes. Polymeric membranes are widely used in the solvent dehydration process due to their high-selective sorption and high-selective diffusion, which is capable to promote ion-dipole interaction, hydrogen bonding with water molecules, and preferential sorb water molecules. However, most polymeric membrane faces swelling problem during the operation process. At that time, the polymer chain is stretched and the pore size of the membranes was enlarged, resulting in higher membrane flux while decreasing selectivity as the large-sized molecules find it easier to pass through [59]. Ceramic membranes demonstrated high thermal and chemical stability

which could be able to operate in a wide range of pH conditions in any type of solvent. Ceramic class membranes such as silica-based membranes and zeolite were commonly used for this application. Zeolite materials with highly ordered well-defined structures exhibit micropores structure that can be varied ranging from 3 to 8 Å depending on the ratio of aluminum, oxygen, and silicon. The pervaporation of water and alcohol mixtures through zeolite membranes occurs by the capillary condensation of water molecules through the zeolitic and non-zeolitic pores, which reflect the formation of defect from the highly ordered crystalline structure was unavoidable [71]. The existence of defects gives rise to enhancing the greater flux while reducing the separation factor of the membranes.

To date, the development of mixed matrix membranes has been reported by several researchers for the application of pervaporation. The structure of mixed matrix membranes consists of inorganic materials that were dispersed into a polymeric base membrane as a matrix. Generally, the presence of inorganic filler could effectively strengthen the mechanical stability of the membrane and reduce the free volume in which large-sized molecules can diffuse. However, the combination of two different materials often generates interfacial voids that lead to reduced separation performance. Uragami et al. [72] reported the mixing of chitosan membrane with tetraethoxysilane (TEOS) up to 45 wt% effectively improved the selectivity of the chitosan membrane for the separation of water over ethanol. Despite that, a higher concentration of TEOS was found to further increase the swelling degree of the membrane during operation. The pervaporation performance of different types of membranes for the dehydration of alcohols is summarized in Table 1-9.

Table 1-9. Dehydration alcohol mixture via pervaporation through different types of membranes

Membrane	System	T_{PV} [ºC]	H_2O feed conc [wt%]	Total flux [kg m^{-2} h^{-1}]	Sep. factor [-]	Ref.
PVA, PSStSA-co-MA	H_2O/EtOH	30	4	0.43	190	[73]
PVA	H_2O/EtOH	60	4	0.12	10	[74]
Sericin	H_2O/EtOH	60	10	0.07	90	
PVA	H_2O/EtOH	60	10	0.12	115	[75]
Sericin/PVA (50/50)	H_2O/EtOH	60	10	0.07	130	
Chitosan/HEC	H_2O/EtOH	60	10	0.424	5,469	[76]
Alginate	H_2O/EtOH	50	4	0.095	202	[77]
PVA/Na-Alg	H_2O/EtOH	45	10	0.384	384	[78]

(80/20)						
Na-Alg/PVP (3/1)	H_2O/EtOH	30	4.6	0.09	364	[79]
PSF/PEG	H_2O/EtOH	25	10	0.6	325	[80]
PSF	H_2O/EtOH	25	10	0.7-0.9	600	[81]
Sodium sulfonate PSF	H_2O/EtOH	25	10	0.75	1,900	[82]
TGN/PSF (12.5/87.5)	H_2O/EtOH	25	10	0.44	680	[82]
Poly(amic methyl ester)	H_2O/EtOH	40	10	1.7	240	[83]
PSF hollow fiber	H_2O/EtOH	25	10	0.173	23.9	[84]
BAPP-Polyimide	H_2O/EtOH	25	10	0.27	22	[85]
PVA/SSA-Na^+	H_2O/EtOH	50	10	0.06	44	
PVA/SSA-Li^+	H_2O/EtOH	50	10	0.07	39	[86]
PVA/SSA-K^+	H_2O/EtOH	50	10	0.06	42	
PAA	H_2O/EtOH	24	10	0.175	4.9	
PAA-Li^+	H_2O/EtOH	24	10	0.160	8	
PAA-Na^+	H_2O/EtOH	24	10	0.215	6.3	
PAA-K^+	H_2O/EtOH	24	10	0.380	5.6	[87]
PAA-Ca^{2+}	H_2O/EtOH	24	10	0.220	5.5	
PAA-Al^{3+}	H_2O/EtOH	24	10	1.010	5	
PEI/PAA	H_2O/EtOH	70	5	0.314	604	[88]
PEI/PAA	H_2O/EtOH	40	5	0.140	1,207	[89]
PVA	H_2O/EtOH	30	10	0.095	77.3	
PVA/Pani (0.78/0.22)	H_2O/EtOH	30	10	0.035	18.6	
PVA/Pani (0.73/0.27)	H_2O/EtOH	30	10	0.061	514.3	[90]
PVA/Pani (0.52/0.48)	H_2O/EtOH	30	10	0.069	564.2	
PMDA-ODA	H_2O/EtOH	45	11.1	0.014	346	
PMDA-MDA	H_2O/EtOH	45	11.1	0.023	47	
BTDA-PDA	H_2O/EtOH	75	11.1	0.005	1594	[91]
BTDA-ODA	H_2O/EtOH	45	11.1	0.022	562	
BTDA-MDA	H_2O/EtOH	45	11.1	0.035	478	
PAN/SstSA, HEMA	H_2O/EtOH	30	50	0.65	212	[92]
Zeolite A	H_2O/EtOH	70	10.3	1.12	18,000	[93]
Zeolite T	H_2O/EtOH	70	10.1	0.91	1,000	
Zeolite A	H_2O/EtOH	45	5	0.86	54,000	[94]
Zeolite A	H_2O/EtOH	75	10	2.15	10,000	
Zeolite X	H_2O/EtOH	75	10	0.89	360	
Zeolite Y	H_2O/EtOH	75	10	1.59	130	[95]
Zeolite T	H_2O/EtOH	75	10	0.81	830	
ECN silica membrane	H_2O/EtOH	70	3.6	1.6	350	[96]
PAN	H_2O/EtOH	50	8	0.007	281	
PAN-Zeolite X (25 wt%)	H_2O/EtOH	50	8.7	0.054	35.9	
PAN-Zeolite X (32 wt%)	H_2O/EtOH	50	9	0.088	51.9	[97]
PAN-Zeolite X	H_2O/EtOH	50	7	0.369	3.2	

--- --

(40 wt%)						
PAN-Zeolite X (50 wt%)	H_2O/EtOH	50	8.5	0.277	7.1	
Chitosan	H_2O/EtOH	50	10	0.201	127	
Chitosan/Carboxyl	H_2O/EtOH	60	10	0.300	634	[98]
Chitosan/Carboxyl	H_2O/IPA	50	10	0.178	491	
PVA/Chitosan (80/20)	H_2O/IPA	60	10	0.644	900,000	[99]
PSSA-g-PTFE/Chitosan	H_2O/IPA	25	10	0.409	1,490	[100]
Na-Alginate	H_2O/IPA	30	10	0.012	356	
PVA	H_2O/IPA	30	10	0.041	21	
Na-Alg/PVA (25/75)	H_2O/IPA	30	10	0.024	195.5	
Na-Alg/PVA (50/50)	H_2O/IPA	30	10	0.034	119.6	[101]
Na-Alg/PVA (75/25)	H_2O/IPA	30	10	0.039	91	
PVA/Na-Alg (80/20)	H_2O/IPA	45	10	0.414	1,727	[78]
P84-Polyimide	H_2O/IPA	60	15	2.578	5	[102]
P84-copolyimide	H_2O/IPA	60	15	0.432	3,508	[103]
Zeolite A	H_2O/IPA	75	10.4	1.58	30,000	[93]
Zeolite T	H_2O/IPA	75	10.2	2,10	9,000	
ECN silica membrane	H_2O/IPA	80	4.5	1.9	1,150	[96]
Silica	H_2O/IPA	70	5	1.0	100	[104]
Silica	H_2O/IPA	80	10	0.65	73	
Silica-Zr 10 mol%	H_2O/IPA	80	10	0.86	300	
Silica-Zr 30 mol%	H_2O/IPA	80	10	0.67	27	
Silica-Ti 10 mol%	H_2O/IPA	80	10	0.78	400	[105]
Silica-Al 10 mol%	H_2O/IPA	80	10	0.08	210	
Silica-Al, Mg 10 mol%	H_2O/IPA	80	10	0.31	90	
Pervap SMS	H_2O/IPA	70	8.2	1.9	53	[106]
PVA-ZSM-5 (2 mass%)	H_2O/IPA	30	10	0.005	91.1	
PVA-ZSM-5 (4 mass%)	H_2O/IPA	30	10	0.003	141.1	[107]
PVA-ZSM-5 (6 mass%)	H_2O/IPA	30	10	0.003	216.2	
Silica	H_2O/n-BuOH	75	5	3.0	250	[104]
Silica	H_2O/n-BuOH	80	5	2.9	1,200	[108]
SMART NaA	H_2O/Tert-BuOH	60	10	1.5	1,600	[109]
Pervap SMS	H_2O/Tert-BuOH	60	10	3.5	144	

b) Isomer separation

The separation of isomer molecules offers several difficulties and is still very

challenging due to the similarity in size [110], similarity in physical and chemical properties, and similar volatility of the mixture pairs [111]. Compared to the conventional separation techniques such as distillation, low-temperature crystallization, chromatography, and extraction, the membrane-based process via pervaporation demonstrated numerous advantages including clean technology, environmentally friendly, and attractive energy efficiency. The Pervaporation process has become a necessary technology for the separation of azeotropic mixture with a close boiling point, where the separation performance of the membranes depends on the differences in solubility and the diffusivity of the permeated component [112]. However, the separation of organic mixture isomers based on the diffusivity through pervaporation is remain a challenging task. Therefore, the development of membrane materials that could determine the slight difference in the physical and chemical properties of the mixture must be considered. Table 1-10 shows the pervaporation performance of different types of membranes for the isomers separation.

Table 1-10. Pervaporation separation of organic liquid isomer via different types of membranes

Membrane	System	Feed composition [wt%]	T_{PV} [°C]	Total flux [kg m^{-2} h^{-1}]	Sep. factor [-]	Ref.
Polyamide-imide (PAI)	n-BuOH/tert-BuOH	50/50	60	0.008	1.11	[113]
Polyamide-imide (PAI)/ α-cyclodextrin (α-CD)	n-BuOH/tert-BuOH	50/50	60	0.003	1.34	
Polyamide-imide (PAI)/ β-cyclodextrin (β-CD)	n-BuOH/tert-BuOH	50/50	60	0.010	1.30	
Polyamide-imide (PAI)/ β-cyclodextrin (β-CD)	n-BuOH/tert-BuOH	50/50	60	0.022	1.13	
CD-grafted PAI	n-BuOH/tert-BuOH	50/50	60	0.0027	2.30	[114]
MFI ZSM-5	p-xylene/o-xylene	50/50	26-75	0.16	0.94-0.96	[115]
6FDA-6FpDA/4MPD	p-xylene/o-xylene	50/50	65	24.9	1.29	[110]
Polyurethane	p-xylene/o-xylene	50/50	25	0.30	1.37	[111]
Polyurethane/zeolite	p-xylene/o-xylene	50/50	25	0.31	1.89	
Silicalite (SS1)	p-xylene/o-xylene	50/50	50	0.271	21	[116]
Silicalite (SS1)	p-xylene/m-xylene	50/50	50	0.272	24	
Silicalite (SS2)	p-xylene/o-xylene	50/50	50	0.253	16	
Silicalite (SS2)	p-xylene/m-xylene	50/50	50	0.258	19	

MFI zeolite (templated)	p-dichlorobenzene (DCB)/o-DCB	50/50	60	0.40	2.3	[117]
MFI zeolite (template-free)	p-dichlorobenzene (DCB)/o-DCB	50/50	60	0.106	16.7	
Co(HCOO)$_2$/PEBA	Toluene/iso-octane	10/90	40	0.826	7.2	[65]
	Benzene/cyclohexane	10/90	40	0.760	4.6	
	Toluene/cyclohexane	10/90	40	0.685	4	
	Toluene/n-heptane	10/90	40	0.771	5.1	
APAF/3MPD-6FDA	Toluene/n-heptane	40/60	80	0.036	5.1	[118]
MOP-SO$_3$Na$_n$H$_m$	Benzene/cyclohexane	50/50	40	0.540	8.4	[119]
PU(0)-650	Benzene/cyclohexane	54/46	25	2.284	2.7	[120]

c) Polar/non-polar organic mixtures separation

The pervaporation of organic mixtures has been focused on polar/non-polar mixtures such as methanol/ methyl tert-butyl ethers (MeOH/ MTBE – azeotropic mixture with a ratio of 14/ 86 wt%), methanol/ dimethyl carbonate (MeOH/ DMC) – 70/30 wt%, and methanol/ toluene (MeOH/ Tol) – 73/27 wt% [121-123]. MeOH forms azeotropic mixtures during the separation process, which necessitates further methanol removal in order to acquire a highly pure solvent. The pervaporation for the separation of organic from organic mixtures performs a challenging task since most organic mixtures show similar physicochemical properties which enhance the difficulties to break them apart [45] and a strong interaction between molecules which leads to generating a high swelling degree for the membranes and rapidly reducing the pervaporation performance [124]. One approach to reducing the membrane swelling degree when the pervaporation of organic mixtures is to use a rigid backbone polymer or to use a copolymer consisting of the rigid segment that provides a strong network and softer segments to facilitate the transport of permeant [125]. Two main criteria for identifying the suitable membrane materials for pervaporation separation of given mixtures were affinity and the size sieving properties. The affinity is generally related to the interaction that is created between the membrane matrix and the penetrating solvent, while the size sieving effect could promote the diffusion selectivity of the small-sized component over a large-sized component. Table 1-11 shows the pervaporation performance of different types of membranes for the separation of the organic mixture.

Table 1-11. Pervaporation performance for different types of membranes in organic mixture separations

Membrane	System	Feed composition [wt%]	T_{PV} [°C]	Total flux [kg m^{-2} h^{-1}]	Sep. factor [-]	Ref.
Ppy-PF	MeOH/IPA	10/90	57.5	0.50	2	[126]
LPS/pDMAEMA/PAI	MeOH/IPA	15/85	50	3.39	9	[127]
HEMA	MeOH/cyclohexane	3.2/96.8	50	3.5	121	
PEGMA306	MeOH/cyclohexane	3.2/96.8	50	0.8	1,482	[128]
MePEG200MA/ PEGMA306	MeOH/cyclohexane	3.2/96.8	50	2.2	1,986	
Polyelectrolyte surfactant complex	MeOH/cyclohexane	12.1/87.9	50	1.08	2,415	[129]
	EtOH/cyclohexane	12.8/87.2	50	0.87	106	
NaY	MeOH/benzene	10/90	50	1.02	7,000	
NaY	EtOH/benzene	10/90	60	0.22	930	
NaY	EtOH/cyclohexane	10/90	60	0.27	1,000	[130]
NaY	MeOH/MTBE	10/90	50	1.70	5,300	
NaX	MeOH/MTBE	10/90	50	0.46	10,000	
ZIF-67	MeOH/MTBE	15/85	40	1.84	3,186	[131]
BTESA	MeOH/MTBE	6/94	40	1.54	8,050	[132]
PA-6/Al$_2$O$_3$	MeOH/MTBE	50/50	30	0.476	20	
PA-6/TiO$_2$	MeOH/MTBE	50/50	30	0.327	11	[133]
PA-6/ZrO$_2$	MeOH/MTBE	50/50	30	0.400	46	
GA-STA-CS	MeOH/DMC	50/50	10	1.03	91	[134]
PAA/PVA	MeOH/DMC	60/40	10	0.61	0.8	[135]
STA/CS	MeOH/DMC	50/50	10	1.16	67	[136]
Nafion	MeOH/DMC	40/60	10	0.93	11	[137]
BTESA	MeOH/DMC	50/50	10	3.13	118	[132]
BTESE	MeOH/DMC	50/50	10	0.45	235	[132]
Ppy-PF	MeOH/Tol	10/90	50	0.28	441	[126]
TiPCS	MeOH/Tol	10/90	50	0.64	410	[138]
Chitosan	MeOH/Tol	10/90	35	0.80	162	[139]
Cellulose acetate	MeOH/Tol	10/90	30	1.80	80	[140]
PA/UiO-66(NH$_2$)-EDTA/cellulose	MeOH/Tol	72/28	22	1.55	5	[141]
SPI	MeOH/Tol	10/90	50	0.79	49	[142]
TEOS-CS	MeOH/Tol	10/90	30	0.18	396	[143]

1.4 Membrane fabrication and materials

1.4.1 Membrane fabrication: introduction

The selection technique for membrane fabrication depends on the choice of materials, desired structure of membranes, and the final membrane application. The membrane fabrication technique can greatly affect the performance of the membranes.

Membranes can be classified into two classes based on material synthesis, including organic and inorganic membranes. Organic membranes generally include polymer materials such as polysulfone (PS), cellulose acetate (CA), polyethersulfone (PES), and polyvinylidene fluoride (PVDF), while the inorganic membrane includes ceramic materials such as zeolite, carbon molecular sieves (CMS), amorphous silica, etc. Table 1-12 presents the summary of the membrane fabrication method for different types of materials.

Table 1-12. Summary of commonly used membrane materials and the fabrication methods

Membrane type	Membrane material	Fabrication method	Application	Ref.
Organic membranes	Organic polymer	Phase inversion	MF, UF, NF, RO	[144]
		Sintering	MF	[144]
		Stretching	MF	[144]
		Track etching	MF	[144]
		Electrospinning	MD	[145]
Inorganic membranes	Metal membrane	Vacuum sputtering	GS	[146]
		Pyrolysis	GS	[147]
		Electroless plating	GS	[148]
		Bi-metal multi-layer deposition	GS	[149]
	Carbon molecular sieve (CMS)	Pyrolysis of polymer precursors (500 – 1000 ºC) under vacuum or inert gas	GS	[145]
	Metal oxide (TiO$_2$)	Slip-casting	UF	[145]
		Atomic layer deposition (ALD)	MF, UF, NF	[145]
	Zeolite	Hydrothermal	GS	[145]
		Hydrothermal	PV	[150]
		Hydrothermal-seeded growth	NF	[151]
	Metal-organic framework (MOF)	In situ growth	GS	[145]
		Seeded-assisted (secondary) growth	GS	
		Rapid thermal deposition	GS	
		Contra-diffusion	GS	
	Silica, organosilica, templated silica, metal oxide silica	Sol-gel	GS, PV	[145]
		Thermal chemical vapor deposition (CVD)	GS	[145]
		Plasma-enhanced chemical vapor deposition (PECVD)	GS, PV	[145]

*MF = microfiltration, UF = ultrafiltration, NF = nanofiltration, RO = reverse osmosis, PV = pervaporation, MD = membrane distillation

1.4.2 Permeation and physicochemical properties of the membranes

The separation performance of the membrane was determined by the selectivity and permeability of the membrane materials. The available range of membrane materials includes polymeric, carbon, organosilica, zeolite, MOF, and other ceramic materials. The porosity of the membrane is an important characteristic for determining separation efficiency. Based on permeating flux and selectivity, membranes can be classified into three categories porous, non-porous, and asymmetric [21]. A porous membrane was characterized by rigid, highly voided with randomly distributed interconnected pore structures. Porous membranes generally show very high levels of flux but low separation performance. Each type of membrane material has a different structure of pores as shown in Fig. 1-25. A membrane with permanent porosity has an immovable network of pores in which permeating molecules can travel, while most polymeric membranes with flexible porosity demonstrated a dynamic fluctuating pore that can move, shrink, expand and disappear. Non-porous membranes exhibited high separation performance but commonly show low permeability, where most permeated components are transported by the solution-diffusion mechanism. On the other hand, asymmetric membranes consist of two structurally distinct layers, one is a thin, dense selective layer, and the other is a porous substructure layer that provides support for the thin-topmost separation layer.
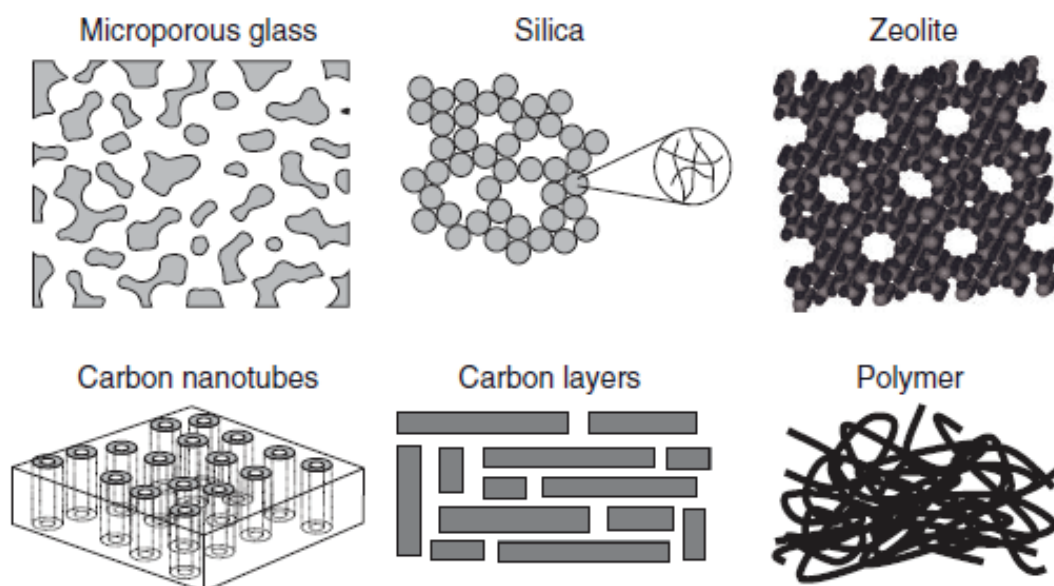
Fig. 1-25. Pore structure from different types of membranes [20]

The selection of membrane materials was expected to enhance the transport of molecules on the membrane surface, thus a microporous membrane material with a high surface area and interconnected pore structure or free volumes is more desirable. However, the adjustment of pore sizes must be made to improve the gas selectivity. Besides that, the chemical properties, the ease of fabrication, and the real-life performance can be used in the consideration for selecting membrane materials. For this reason, it is important to characterize the physicochemical properties of the material before evaluating the membrane performance. To be properly analyzed, Table 1-13 provides a summary of the experimental technique that can be used for membrane material characterization.

Table 1-13 Membrane physicochemical properties and corresponding characterization technique

Membrane property	Characterization technique	Ref.
Physical properties		
Hydrophilicity and hydrophobicity	Contact angle	[42]
Size distribution	Dynamic light scattering (DLS)	[152]
Porosity, surface area	N_2 sorption isotherms	[42]
Chemical properties		
Surface chemistry, ligand binding (surface-sensitive), electronic structure	Fourier transform infrared spectroscopy (FT-IR), X-ray photoelectron spectroscopy (XPS)	[42, 152]
Optical properties, electronic transition,	Ultraviolet-visible spectroscopy (UV-Vis)	[152]
Mass, composition, and thermal stabilities	Thermogravimetric analysis (TGA)	[152]
Order-disorder transformation, crystal structure, crystalline grain size	X-ray diffraction (XRD)	[152]
Structural properties		
Cross-section, surface roughness, the thickness of the topmost layer	Scanning electron microscope (SEM), transmission electron microscope (TEM)	[42]

1.4.3 Membrane Materials

1.4.3.1 Metal membranes

Dense metal-based membranes made of palladium, and its alloys such as silver, nickel, tantalum, vanadium, niobium, and zirconium show primary high selective separation for gas mixtures. Pd and its alloys membrane show specific characteristic to allow only hydrogen molecules to permeate, thus making these membranes possible to produce a pure stream up to 99.99% [153]. The development of metallic membrane was started in 1866 by Thomas Graham who observe unusually high adsorption capacity from the palladium-based membrane. The industrial commercialization of metallic membranes was started in the early 1960s by Johnson Matthey via palladium-silver alloy membrane for hydrogen purification [154].

The transport of metallic membranes occurs via charged particles or either surface-limited or diffusion-limited. Besides that, alloy-based membranes gained an increase of interest due to their improved performance including higher resistance, stability, decrease embrittlement tendency, and enhance hydrogen permeability. The abundance for each metal was plotted in Fig. 1-26 as a function of cost for the fabrication of metallic-based membranes.
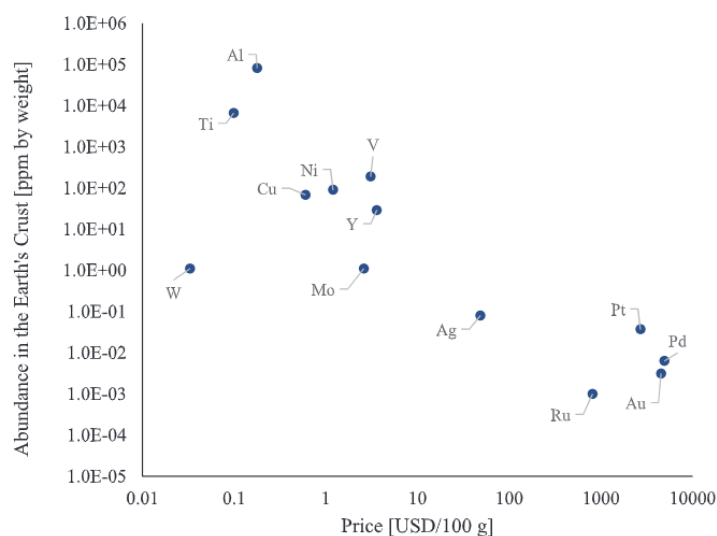
Fig. 1-26. The abundance and the cost of most commonly used metals for the preparation of Pd-based membranes (each price is referred to 2019) [155].

Pd77%Ag23% membrane shows 1.5-2 times higher permeability compared to pure Pd membrane and higher resistance against hydrogen embrittlement [156]. Pd-Cu and Pd-Pt

alloys have been found to have higher resistance against sulfur poisoning, thus to achieve higher permeability and resistance Pd alloy membranes were developed with more than two elements such as Pd-Ag-Au, Pd-Ag-Cu, and Pd-Au-Pt [157-159]. Other metals such as V, Nb, Ta, Zr, and Ni have been studied for highly permeable H_2 membranes as an alternative way to reduce the use of precious metals. Zr-Ni alloys have a reactive surface which can allow hydrogen dissociation and increase hydrogen solubility [160]. However, the high solubility of hydrogen led to generating hydrogen embrittlement and resulted in the precipitation of metal hydride. However, metal membranes have limitations on the very dense structure which led to low permeability. In addition, dense metallic-based membranes relatively show a high cost to be one to three orders of magnitude more expensive per unit surface area. The Pd-based membrane was reported to be incapable to produce high flow rates of hydrogen as high as 10,000-100,000 m^3 h^{-1} on an industrial large scale [161].

1.4.3.2 Polymeric membranes

Polymeric membranes are increasingly deal with interest for industrial applications due to their low-cost investment material, good processability, economic competitiveness, scalability, tuneability, and the easiness of large-scale manufacture. To achieve highly separation performance of the membrane, attention has been focused on modifications to the solution-diffusion properties in polymers. The modification of polymer structure could be conducted via crosslinking, grafting, blending, and copolymerization processes as presented in Fig. 1-27 [122]. The crosslinking method was generally performed to reduce the swelling degree and enhance the resistance of the polymeric membrane matrix in the feed mixture in order to derive higher stability and selectivity of the membranes. The crosslinking of polymer membranes was carried out by a chemical reaction, irradiation, and physical crosslinking [162]. On contrary to that, the optimize crosslinking process must be considered to avoid the formation of a brittle polymer with a loss in the dimensional stability. The grafting technique on polymer modification uses the oligomer chains that were attached as side chain branches irregularly to the polymer main chain by chemical reaction or irradiation. The molecules that are desired to be grafted must contain reactive functional groups which be able to

react with the functional groups of the polymer. The blending process of two polymers that are not covalently bonded can be done for creating hydrophilicity in the hydrophobic membranes. Two classes of polymer blends including homogeneous and heterogeneous blends, in which two polymers are miscible for all compositions and the other one is not totally miscible, respectively. However, the heterogeneous blends of polymers will not give enough mechanical strength to the thin membrane structure. Copolymerization can be implemented for two different polymers structure which is covalently bonded to increase the mechanical strength of the membrane.
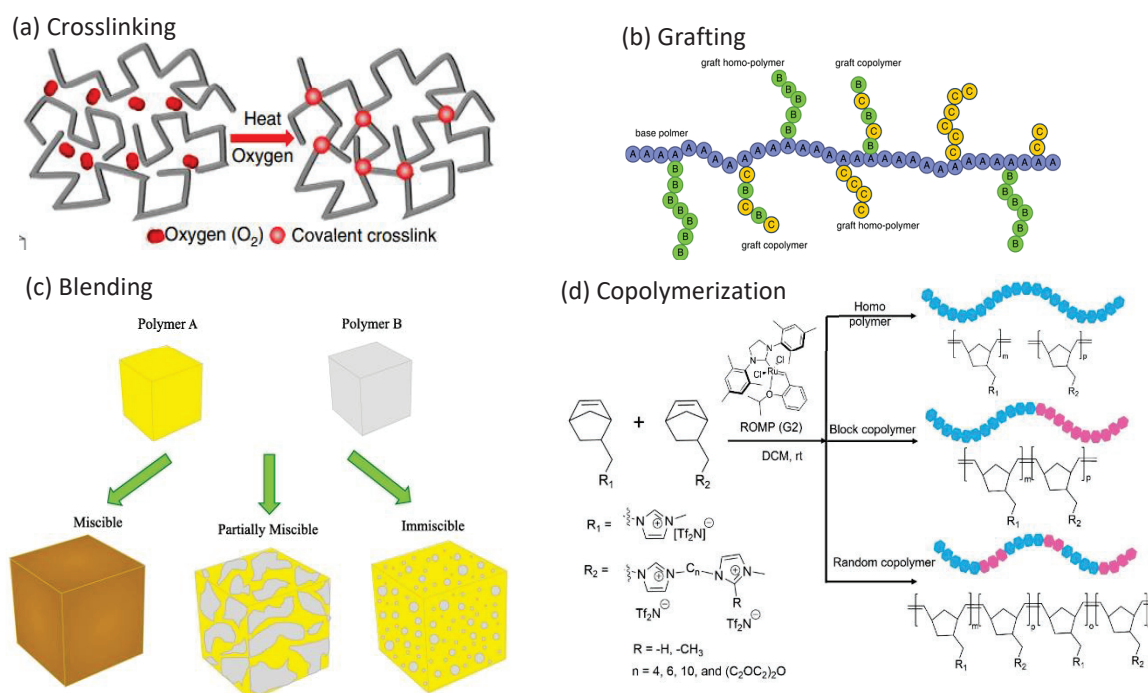
Fig. 1-27. Schematic concept of polymer membrane modification via crosslinking [163] (a), grafting [164] (b), blending [165] (c), and copolymerization [166] (d).

The gas separation process using polymeric membranes was first commercially applied in 1979 with prism separators from Monsanto with a modular design for the separation of hydrogen from the product stream of ammonia synthesis [167]. Polymeric materials are commonly used because it has film-forming ability, processability, and good mechanical properties. Most polymeric membranes show a trade-off effect, i.e. highly permeable membranes generate lower selectivity and vice versa [36]. Moreover, membrane plasticization and aging effects are commonly present which led to unstable and deteriorated separation performance in industrial applications. Plasticization refers to membrane dilating in the presence of condensable gas such as CO_2, which enhances

polymer chain mobility, and gives rise to higher permeability and lower separation factor. The dilation polymer matrix by CO_2 results in higher permeability for other gases and reduces overall separation performance. Consequently, concerted efforts have been devoted to modifying the properties of polymer membrane which can exhibit both high permeability and selectivity such as creating a hybrid polymer-inorganic structure, fabricating an active thin separation layer, and facilitating transport mechanism through the incorporation of appropriate carrier fillers with specific functional groups into the polymer matrix [168].

The utilization of polymeric membranes for pervaporation application is particularly based on the preferential absorption of polymer towards the components and the diffusion through the free volumes or pore structure of the polymers. The affinity between membrane materials and the permeating component becomes the most important parameter to select the appropriate membrane materials for pervaporation. The size determination effect from the free volume cavities provides an additional contribution to the permeation of the small-sized component over the large-sized ones [169]. In accordance with affinity, hydrophilic polymers were used to develop membranes for water or polar selective permeation, while hydrophobic (organophilic) polymers were operated for organic or non-polar selective permeation. Examples of hydrophilic membranes include a large number of polymers such as poly (vinyl alcohol) (PVA), polyamide (PA), Polyimide (PI), and polyelectrolyte complex (PEC). By contrast, a limited number of hydrophobic polymer membrane is available such as polydimethylsiloxane (PDMS) and poly (ether-block-amide) (PEBA). PEBA is an organophilic polymer consisting of polyamide (PA) and polyether (PE). The rigid properties of PA provide mechanical strength whereas the PE provides affinity for organic compounds. PEBA membranes generally show higher hydrophobicity compared to PDMS membranes which are favorable for the phenol/water separation or selective permeation of organics with large molecular size [170].

The other challenge to using polymeric membranes in organic/organic mixtures is the much larger swelling of the polymer matrix in the pure organic solvent which could reduce the size determination ability and stability of the membrane. Thus membrane surface modifications were used to solve this problem such as by introducing bulky fluorine groups into the PI structure to increase the free volume of PI membranes and

crosslinking is proposed to enhance the swelling resistance of PI membrane towards the organic solvents [171]. Copolymerization modification such as using PEBA and polyurethane (PU) to tune the soft/hard segments for achieving comprehensive separation performance and reducing the swelling degree of the membranes [120, 172].

1.4.3.3 Carbon molecular sieving membranes

Carbon membranes were fabricated via thermal conversion of polymer layers with pyrolysis or carbonization at high temperatures (generally 400-900 °C) in an inert atmosphere (Fig. 1-28(a)) [173]. At high temperatures, many polymer structures will thermally rearrange, crosslinked, and begin to carbonize. The predominant transport mechanism for most carbon membranes is the molecular sieving mechanism. Fig. 1-28(b) shows the comparison of surface morphology for carbon hollow fiber membrane with polymeric hollow fiber membrane. CMS membranes are considered porous materials where the permeates could penetrate through the pore system, while polymeric membranes consist of a dense active layer where the permeation is dominated by the solution-diffusion process [173].
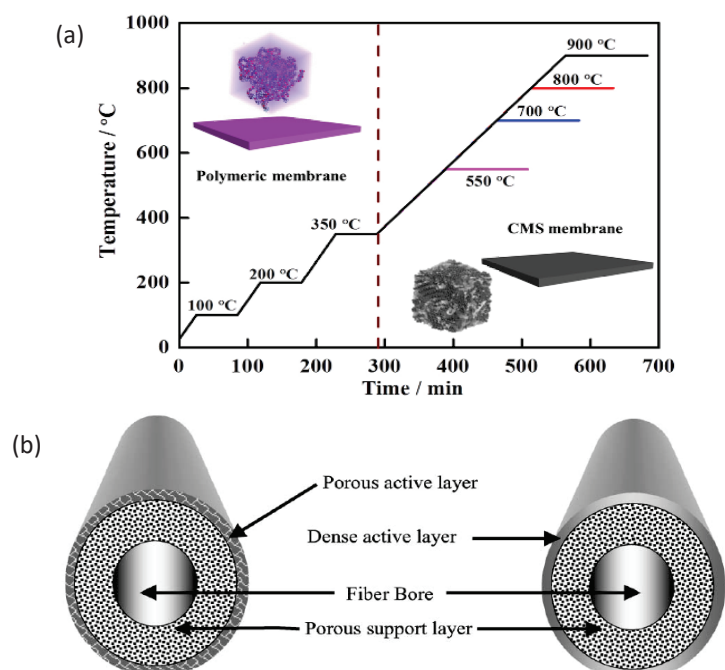
Fig. 1-28. Pyrolysis protocol of polymeric precursor for the development of CMS membranes [174] (a), and membrane surface comparison for CMS and polymeric hollow fiber membranes (b) [173].

Carbon membranes contain constrictions in the matrix that approach the size of permeated molecules, thus these materials can effectively determine the gas species of similar size. The separation occurred via size discrimination, where small-sized molecules can pass through the membrane pore structure while larger-sized molecules are obstructed. Permeation through the carbon matrix is related to the pore structure of the membrane. The pore structure of the carbon membrane consists of a relatively wide opening with narrow constrictions, where the opening pore contributed to the free volume and is responsible for the adsorption capacity. On the other hand, the constrictions are responsible for the discrimination of penetrated molecules, hence the diffusivity of a component depends on the size and shape of the molecule because the carbon molecular sieving membrane has a pore size that is close to the dimension of penetrated molecules. In these constrictions, the interaction energy between molecules and carbon matrix is involved both in dispersive and repulsive interaction. If the pore opening of the membranes becomes small relative to the size of penetrating molecules, the repulsive interaction was predominant and the molecules require higher activation energy to pass through the constriction. Therefore, molecules with slight differences in size can be effectively separated through molecular sieving. The permeation mechanism on carbon molecular sieve membranes is determined by the internal surface area, the dimension of pores, and the surface properties of the membrane matrix [23].

The permeation characteristics of CMS membranes can be varied by changing several synthesis parameters such as organic precursors, carbonization temperatures, and the chemistry of pyrolysis. CMS membranes can be obtained from the pyrolysis of different types of thermosetting polymers such as poly (vinylidene chloride) (PVDC), poly (furfuryl alcohol) (PFA), cellulose, polyacrylonitrile (PAN), phenol-formaldehyde and various coal. Xu et al. [175] reported the fabrication of CMS membrane from phenolphthalein-based cardo poly(arylene ether ketone) (PEK-C) that were carbonized at different temperatures with ultrahigh permeability for hydrogen purification. The result of that work shows that the H_2 permeability was decreased as the pyrolysis temperature increased due to the formation of dense and ordered carbon structure and the separation performance of H_2/CH_4 reach 1,1152 for CMS membrane calcined at 900 ºC. In addition, CMS membrane could be applied for liquid-phase separation via reverse osmosis. Koh et al. [176] reported the fabrication of CMS membrane (Fig. 1-29) for the separation of

xylene isomers via organic solvent reverse osmosis (OSRO). CMS hollow fiber membranes calcined at 450 C exhibited the highest p-xylene permeance of 1.6×10^{-8} mol m^{-2} s^{-1} Pa^{-1} with the selectivity of p-xylene/o-xylene of 7, while at higher calcination temperature (550 ^oC) the membrane shows the highest separation of 30 but with low permeance of 3.8×10^{-10} mol m^{-2} s^{-1} Pa^{-1}.
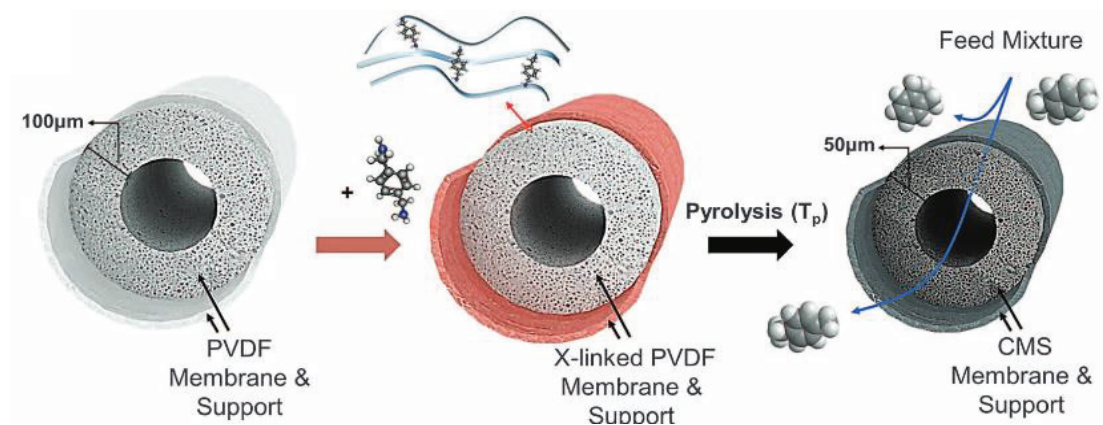
Fig. 1-29. The schematic image for the fabrication of CMS hollow fiber membranes at the pyrolysis temperature of 450-550 ^oC [176].

In contrast to the high separation performance of CMS membranes, most carbon membrane is brittle and fragile, and thus requires careful handling. In addition, the fabrication process of CMS membranes requires high thermal energy which led to generating difficulty and high-cost production. Pre-purifier step was required before membrane fabrication for removing traces of strongly adsorbing vapors which can clog up the pore system.

1.4.3.4 Zeolite membranes

Zeolite membranes are microporous aluminosilicate crystals with a pore size that was constructed by the TO_4 (T = Si, Al) tetrahedral unit framework with an oxygen atom that is shared between two adjacent atoms. Zeolites with 8- (e.g. LTA, CHA, DDR), 10- (MFI, FAU), and 12- (MOR) framework rings have different sizes of pore structure in the range of 0.38 to 0.74 nm as shown in Fig. 1-30.
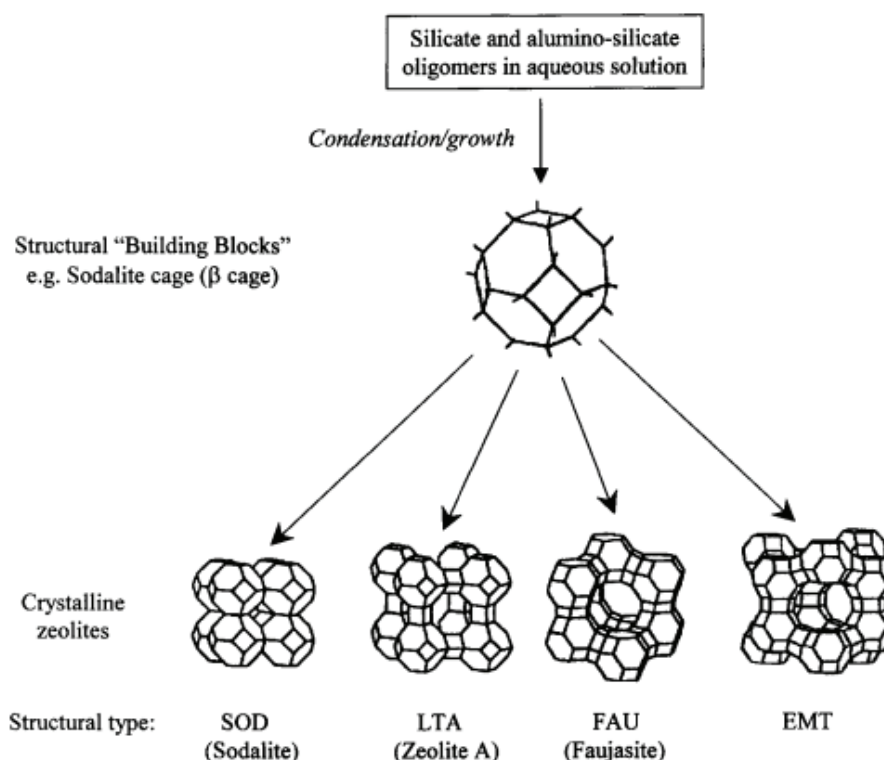
Fig. 1-30. Different zeolite structures are derived from oligomeric silicate and aluminosilicate species [177].

Zeolite membranes are commonly prepared by hydrothermal method via in-situ and secondary growth methods. In the case of in-situ growth, the surface of the substrate can be functionalized to enhance its interaction with zeolite crystals to generate a continuous membrane layer, while in the secondary growth method zeolite crystals were introduced as seeds on the substrate prior to hydrothermal synthesis. The secondary growth method shows a better process for controlling membrane integrity and thickness [178]. In addition, the properties of the seed layer including crystal size, thickness, and particle distribution are important to determine the properties of zeolite membranes. The membrane properties of zeolites are dependent on the ratio of Si/Al (Fig. 1-31), where a low Si/Al ratio exhibits high hydrophilicity but low acid resistance, while a higher Si/Al ratio generates a membrane with high acid stability but the pore size of the membranes were ranged from 0.56 to 0.74 nm which was too large for the separation of small-sized molecules [179].
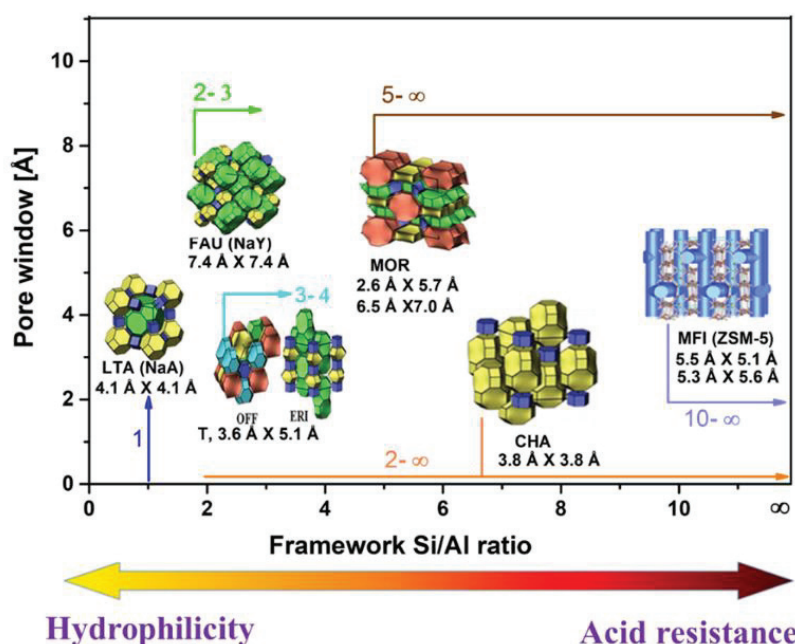
Fig. 1-31. The pore size, hydrophilicity, and the acid resistance properties of zeolite membranes as a function of the Si/Al ratio [180]

Several zeolite membranes are widely used in pervaporation applications, including water dehydration, organic/organic, and isomers separation. LTA (NaA) zeolite that was synthesized from a Si/Al ratio of 1 has an 8-membered oxygen ring that shows the pore diameter in the range of 0.23 and 0.42 nm [179]. The low Si/Al ratio of this membrane shows an extremely hydrophilic property, and the pore size of the membrane is close to the size of water molecules (kinetic diameter-KD = 0.29 nm), thus making LTA membranes appropriate for the application of dehydration of alcohol or other solvents. CHA zeolite membrane with a pore size of 0.38 nm shows a high flux of 13.3 kg m^{-2} h^{-1} with excellent separation of 6,000 for dehydration of ethanol/water mixture [181]. MFI membrane that was synthesized with a high Si/Al ratio showed defect-free quality with a high flux of 2.9 kg m^{-2} h^{-1} and achieved a separation factor of 160 for ethanol/water mixture at 25 ^{o}C [182]. Despite that, it was found that the performance of the MFI membrane declined after 177 hours of pervaporation at 100 C due to the loss of Silicon atoms from the zeolite framework and the further formation of silanol groups in the aqueous mixture [183, 184]. Moreover, the formation of a continuous and defect-free zeolite layer on porous support is quite challenging due to weak adhesion between microporous zeolite particles and macroporous support.

--- --

1.4.3.5 Porous coordination polymer or metal-organic frameworks (MOFs) membranes

Metal-organic frameworks (MOFs) have become an interest over the past decades due to their high crystallinity, porosity, modularity, and diverse functionality. MOFs are defined as hybrid materials where metal ions or small inorganic nanoclusters are linked into one-, two-, or three-dimensional networks via multifunctional organic linkers [185]. The crystallization of MOF structure in solution is based on the nucleation of secondary building units (SBUs) which are then joined together to form the final crystal structure as schematically depicted in Fig. 1-32. MOF as microporous crystalline materials shows an impressive performance for molecular sieving membranes with high permeability and selectivity compared to polymeric membranes due to their high microporosity and tunable channel structure. MOFs membrane was recently used for hydrogen purification, hydrocarbon separation, and CO_2 capture [186].
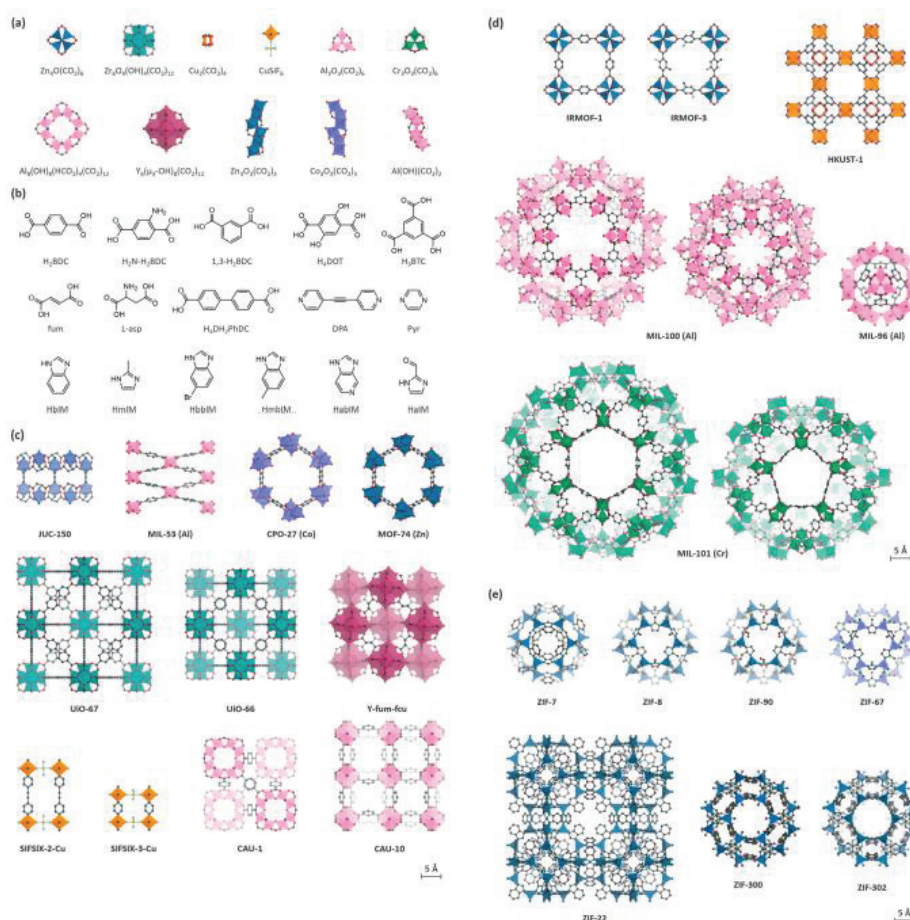
Fig. 1-32. Schematic images of inorganic secondary building units (SBUs) (a), organic linkers (b), and different structures of MOFs materials (c-e) [186]

Hiroshima University Doctoral Dissertation

Continuous MOF membrane is generally synthesized via precursors crystallization through hydrothermal, solvothermal, interfacial, and contra-diffusion synthesis. However, the different solubility between solvent and MOF precursors becomes the limitation for membrane synthesis. Li et al. [187] reported the sol-gel technique to synthesize ZIF-8 membranes with controllable thickness resulting in the precise synthesis of molecular sieves membrane. The sol-gel process was executed by gel coating for the dispersion of the precursor, then followed by thermal treatment for the crystallization process. The prepared ZIF-8 membrane shows impressive performance for C_3H_6/C_3H_8 separation with C_3H_6 permeance of 0.8×10^{-8} mol m^{-2} s^{-1} Pa^{-1} and selectivity of 200.

The other advantage of MOF structure after exceptional porosity is open metal sites (OMS) which could represent a major step forward in functional materials with special properties. HKUST-1 is one of the OMS structures which shows a high surface area of 1,800 m^2 g^{-1} after fully desolvated and is suggested used for new methane gas storage materials [188]. MOF-505 also demonstrated an extremely high surface area of 1830 m^2 g^{-1} and high hydrogen uptake of 2.47 wt% due to the existence of Cu metals as OMS in that structure [189]. The combination of high surface area that reflects permanent porosity and the occurrence of OMS contribute to the superior performance with respect to hydrogen, methane, and carbon dioxide sorption. Liu et al. [190] reported the effective enhancement of the structure of Cu-BTC via nitrogen-doping and lithium-doping as the open metal site (OMS). In that reported work, 3N-CuBTC shows higher methanol capacity due to the increased dispersive interaction caused by the lone pair electron of nitrogen atoms, while 3Li-3N-CuBTC exhibited higher methanol capacity due to the synergy effect from the lone pair electron of nitrogen atoms and the existence of metal in the cage structure of MOF that can significantly affect to the polarity and the preferential adsorption sites of the framework.

1.4.3.6 Mixed matrix membranes

The ceramic membrane such as CMS and zeolite are good in selectivity but are far too expensive for use on an industrial scale. To address this problem, membranes could be prepared from a material consisting of inorganic particles (e.g. zeolites, carbon

molecular sieves, silica) dispersed in a continuous polymer matrix, referred to as a mixed-matrix membrane as schematically shown in Fig. 1-33(a). Mixed-matrix membranes are supposed to combine the desired selectivity of inorganic membranes with low cost and the easiness of fabrication of polymer membranes.
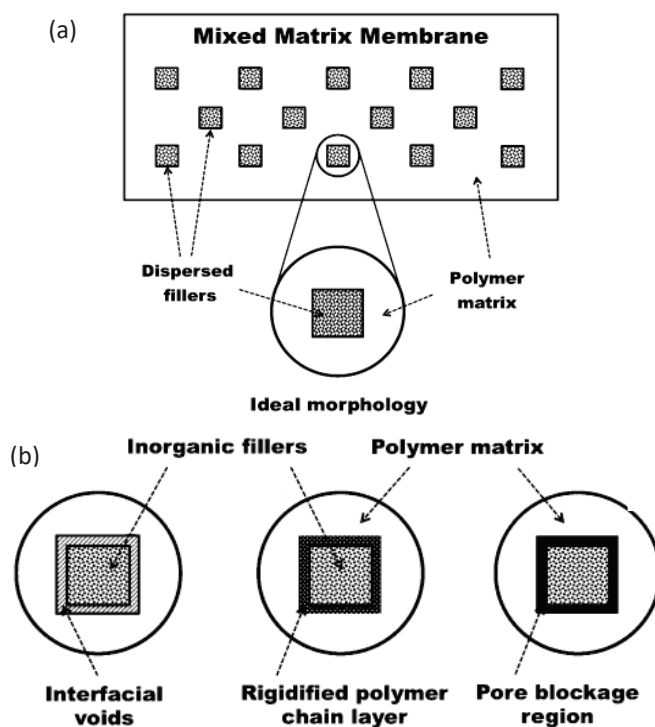
Fig. 1-33. The schematic representation of an ideal mixed-matrix membrane (a), and nonideal mixed matrix membrane morphology including interfacial voids, rigidified polymer chain layer, and pore blockage (b) [191]

The membrane properties of mixed-matrix structure depend on the particle size, particle pore size, dispersed load, polymer type, and polymer characteristics. The fabrication of ideal mixed-matrix membranes is very difficult because of the difference between the polymer and inorganic phase properties and weak polymer-particle adhesion, which results in the formation of organic-inorganic interface defects. Interface defects of mixed-matrix membranes are classified into three categories, including interface voids, rigidified polymer layer around particles filler, and particle pore blockage (Fig. 1-33(b)) [191]. The formation of interface voids is attributed to stresses after solvent evaporation and could occur from the nucleation of non-solvent or polymer lean phase around the inorganic phase during the phase separation process. Rigidified polymer layer related to uniform stress around particles filler after the removal of solvent, while pore blockage occurs for porous filler where particles clogged with the sorbent, solvent, contaminant, or minor

component in the feed gas or polymer chain in the fabrication step of the mixed-matrix membrane.

The inorganic materials used for the filler in mixed-matrix membranes could be classified into porous and non-porous types. Porous filler acts as a molecular sieving agent in the polymer matrix and discriminates permeated molecules based on their shape and sizes [192]. On the other hand, non-porous filler could improve the separation properties of the resultant membrane via increasing matrix tortuous pattern and limiting the diffusion of the large-sized component [193]. Vu et al. [194] reported the effect of carbon molecular sieves (CMS) as porous filler that was added into Matrimide 5218 as the polymer matrix. The addition of CMS 800-2 into Matrimide 5218 increased the permeability of the membrane from 10 to 44 barrier and the CO_2/CH_4 selectivity was increased from 35.3 to 200. In other work, Ahn et al. [195] reported the addition of 20 vol% nonporous silica particles into the polysulfone matrix led to an increase in the solubility and diffusivity coefficient, increasing the free volume of polymer membrane and enhancing CO_2 permeability from 6.3 to 19.7 Barrer. However, low permeances become one problem due to the difficulty of preparing a thin layer of the mixed-matrix membrane. In addition, the fabrication of mixed-matrix membranes usually involves a weak contact from the polymer particles matrix and poor distribution from the dispersed inorganic phase in the continuous polymer matrix.

1.4.3.7 Silica and organosilica-based membranes

1.4.3.7.1 Preparation technique for silica and organosilica membranes

Amorphous silica and organosilica-based membranes have been studied extensively for gas and liquid separation due to their chemical and physical stabilities. Tetraethylorthosilicate (TEOS) was generally used as silica precursors for the fabrication of silica membranes. On the other hand, organosilica membranes are derived from organic ligand silicon alkoxides which convert to organic/inorganic components after being fired in a N_2 atmosphere. In general, silica and organosilica-based membranes are prepared via CVD and sol-gel processes as discussed in this chapter.

--- --

a) Chemical Vapor Deposition (CVD)

Chemical vapor deposition (CVD) was commonly used to precisely control the pore size of inorganic membranes via thermal decomposition of a silicon-based precursor and the chemical reaction with an oxidant gas, resulting in the growth of the thin film layer [17]. The silica precursors that are mainly used for CVD reaction are tetraethylorthosilicate (TEOS) [196], tetramethoxysilane (TMOS) [197], silicon tetrachloride ($SiCl_4$) [198], and silane (SiH_4) [199] with oxidant gases such as air, O_2, O_3, N_2O, and water vapor. To fabricate a membrane on the porous substrate via the CVD method, two types of configurations can be used: counter-diffusion CVD where two reactants were supplied from the opposite side of substrates, and co-current CVD where precursors are supplied from one side of the substrate, while vacuumed on the other side of the system to obtain a defect-free membrane quality.

On the other hand, low-temperature CVD methods have been developed to minimize the cost of the high-temperature CVD process. Nagasawa et al. [200] reported a highly efficient gas separation membrane of hexamethyldisiloxane (HMDSO) was successfully synthesized via atmospheric-pressure plasma-enhanced chemical vapor deposition (AP-PECVD) with CO_2 permeance of 1.9×10^{-7} mol m^{-2} s^{-1} Pa^{-1} and a high level of CO_2/CH_4 selectivity of 166 at 50 °C. Plasma-enhanced CVD technique was capable to control the decomposition of converted gaseous precursors as a deposit hybrid thin films which have high thermal and chemical stability [17].

b) Sol-gel processes

Sol is a stable colloid suspension particle in a liquid, and a gel consists of a three-dimensionally continuous solid network surrounding a continuous liquid phase (wet gel). The formation of gels (gelation) is due to the formation of covalent bonds between the sol particles [201]. Gelation could induce by rapid evaporation of the solvent giving rise to capillary forces that cause shrinkage of the gel network producing an aerogel. The sol-gel processing of silica-based materials is to transform Si-OR and Si-OH species to siloxane (Si-O-Si) via a condensation reaction. A stable gel could be produced by maximizing the number of siloxane bonds and consequently minimizing the number of

----

silanol (Si-OH) and alkoxy (Si-OR) groups. The chemical reaction of silica-based materials during the sol-gel process can be described in the following equation.

Hydrolysis: $\qquad \equiv Si - OR + H_2O \rightarrow \equiv Si - OH + ROH$ (1-75)

Condensation: $\quad \equiv Si - OH + Si - OR \rightarrow \equiv Si - O - Si \equiv +ROH$ (1-76)

Condensation: $\quad \equiv Si - OH + Si - OH \rightarrow \equiv Si - O - Si \equiv + H_2O$ (1-77)
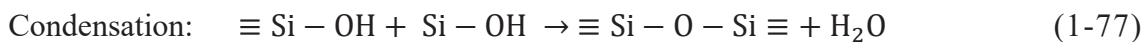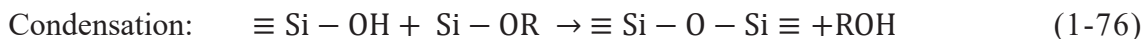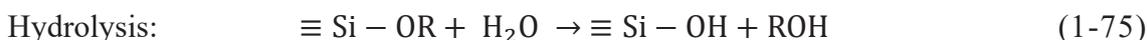
Hydrolysis reaction initiated in alkoxide precursors dissolved in alcohol system via the addition of water (hydrolysis agent) to generate Si-OH. Generally, the hydrolysis rate of precursors in water and alcohol is slow, therefore acid or base catalyst is necessary to improve the hydrolysis and condensation reaction rate. The most important parameter for the sol-gel reaction is the types of precursor, the pH condition that depends on acid or base catalyst, the ratio of alkoxy group to water content, the kind of solvent, temperature for synthesis, and the concentration of precursor. The reaction rate for hydrolysis and condensation has a pH dependence as shown in Fig. 1-34(a).
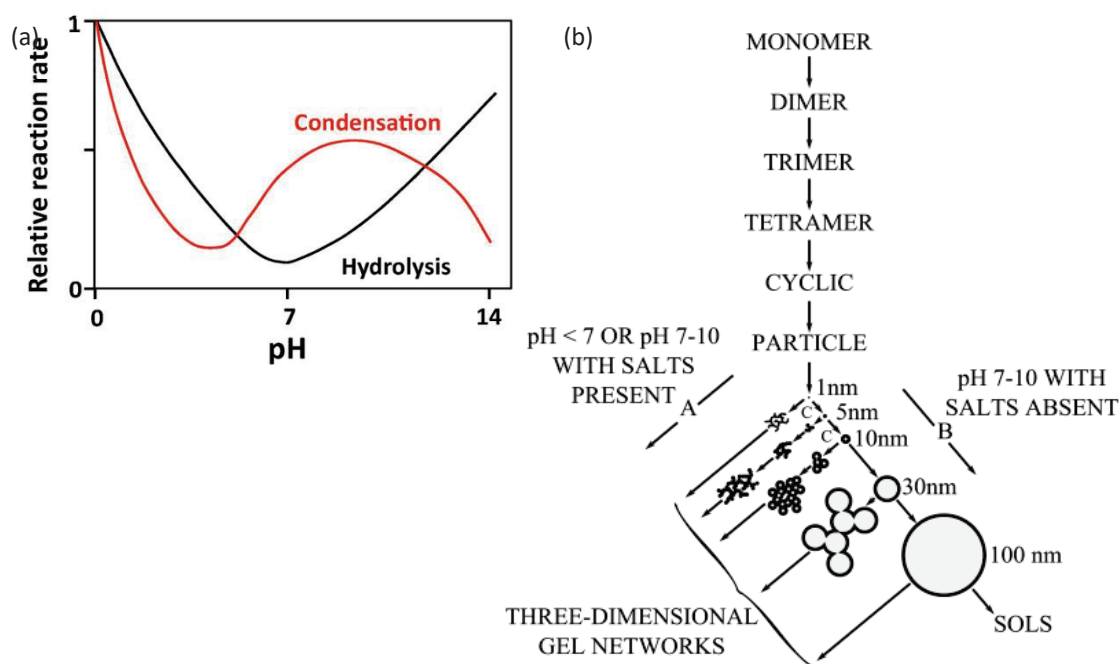
Fig. 1-34. The dependence of relative rates of Si(OR)4 hydrolysis and condensation towards pH condition [201] (a), Polymerization behavior of silica under different pH conditions [202]

The minimum reaction rate for hydrolysis is pH 7, while for condensation at pH 4.5. the hydrolysis of silicon alkoxide is faster than condensation in acid conditions. Most species are hydrolyzed at the beginning of the reaction and condensed to form a small oligomer.

On contrary to that, in basic conditions, the condensation rate is faster compared to the hydrolysis and the rate of hydrolytic cleavage of Si-O-Si bonds is higher than in acid conditions. Therefore, resulting in a network with a particulate character with big particle size and large pores. The schematic images for the structural development of silica gels under different pH as shown in Fig. 1-36(b).

1.4.3.7.2 Silica and types of organosilica membranes

Silica and organosilica membranes have been categorized as a class of inorganic membranes. Most pure silica membranes were fabricated from tetraethoxysilane (TEOS) showing a narrow pore size distribution in the range of 0.3-0.4 nm, which generally performed high selectivity for hydrogen separation. However, silica-based membranes presented low hydrothermal stability, small pore size distribution, and high transport resistance [203, 204]. On contrary to that, a different type of material derived from organoalkoxysilanes contains various organic functional groups in the inorganic Si-O-Si frameworks, which are known as organosilica material. Organosilica-based materials were characterized via covalent bonding between oxygen and hydrocarbons to silicon [205]. Hybrid organosilica membranes were getting great interest by using pendant-type precursors, then the appearance of bridged silica with stable and reliable performance become available for large-scale industrial application. The difference between both the pendant and bridge structure of organosilica precursors is shown in Fig. 1-35.
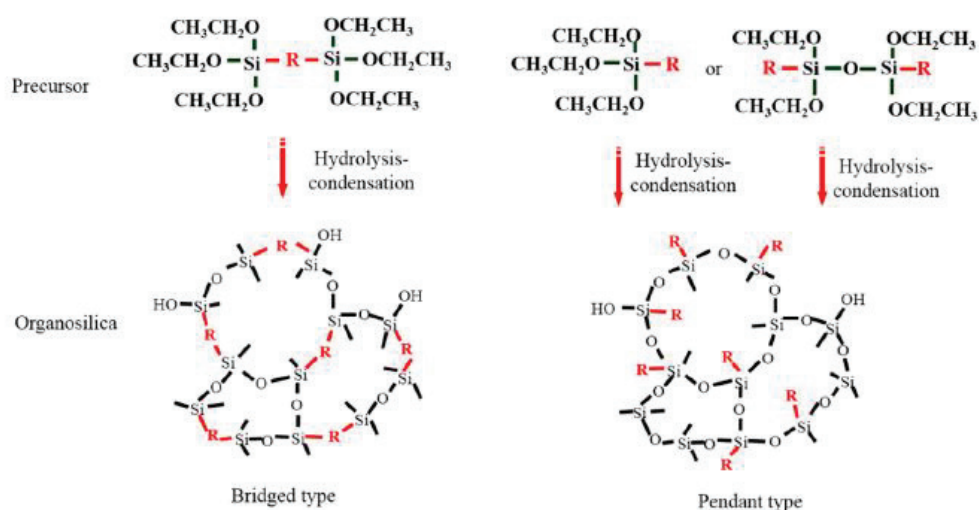
Fig. 1-35. The schematic images of the bridge- and pendant-type precursor of organosilica and their structure after hydrolysis and condensation reaction [204].

-- --

The bridge-type precursor contains organic groups that are located between two silicon atoms (as the linking unit O-Si-R-Si-O), and the pendant structure consists of organic groups that are connected with one silicon atom (Si-O-Si-R) [204]. A variety of organic groups can be used such as an alkane, alkene, alkyne, aromatic, and other functional moieties. Organosilica membranes are typically fabricated via sol-gel reaction which is finalized with a thermal treatment to consolidate the materials. A lower degree of calcination temperatures for the preparation of organosilica membranes results in functional membranes with lower performance including the separation factor and permeability.

These membranes exhibit high thermal and chemical stability with no swelling, high flux, high separation performance, and controllable pore size [206-208]. The separation ability of organosilica membranes depends mostly on the pore size and on the interaction between permeating molecules and the pore walls of membranes. Therefore, material modification is required to produce a highly porous material that can facilitate high permeability without sacrificing selectivity. However, the hydrothermal stability of organosilica membranes can be varied or even change at a high temperature and in a water vapor environment. Extreme operation conditions dramatically affect the microporous structure of silica membranes, where hydrophobic silicon-oxygen bonds from the siloxane network (Si-O-Si) tend to break and transform into hydrophilic silanol groups (Si-OH) [209].

$$\equiv Si - O - Si \equiv\ + H_2O \xrightarrow{Hydrolysis} 2 \equiv Si - OH \qquad (1\text{-}78)$$
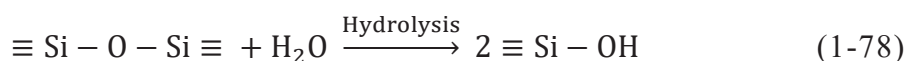
The existence of water molecules in hydrothermal conditions assists the breakage of the siloxane framework and the rehydration occurs on the silica surface via physisorption of H_2O molecules to a hydroxyl group, followed by the reaction with a nearby siloxane. In this condition, as more silanol groups were created, more sites for H_2O adsorption and the chain reaction of siloxane breakage occurs across the surface resulting in the localization of silanol groups and subsequently cross-pore condensation leading to smaller pore size as shown in Fig. 1-36(a).
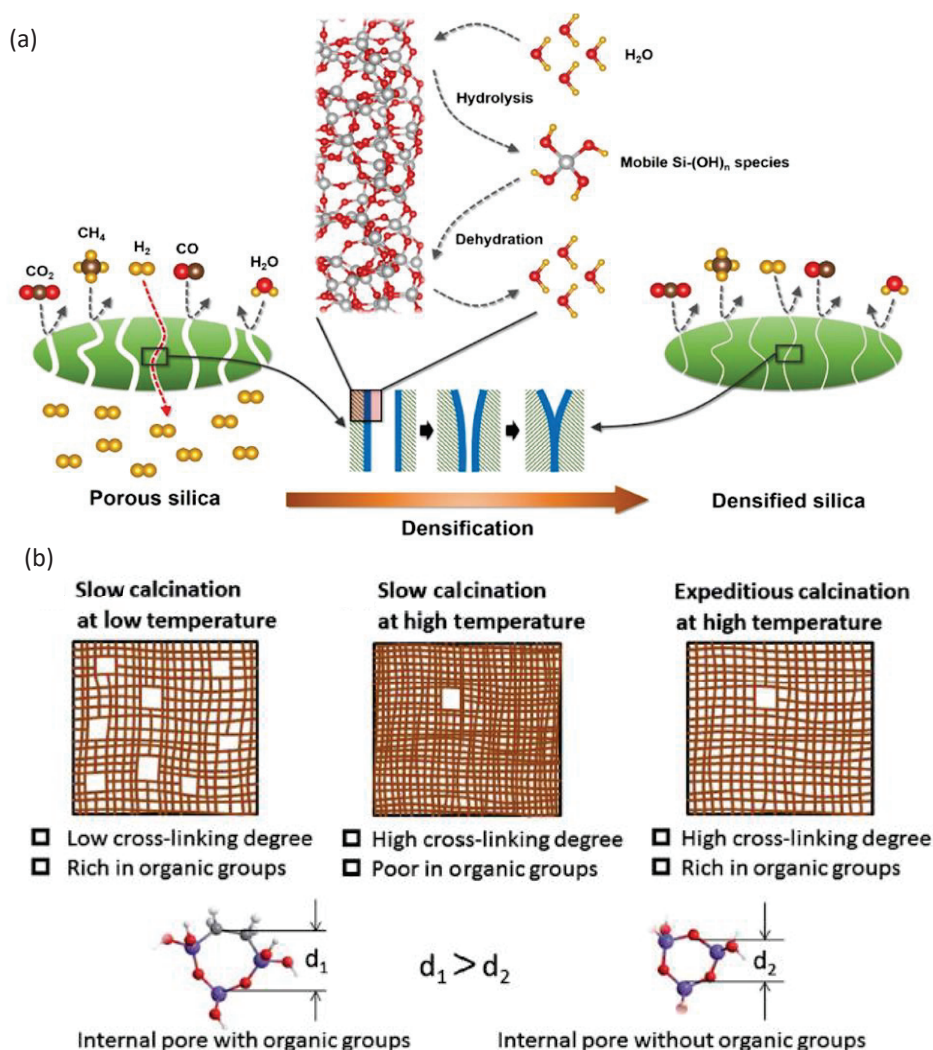
Fig. 1-36. The schematic mechanism of densification of the organosilica-based membrane at the hydrothermal condition [210] (a), and densification under different calcination conditions [211].

Song et al. [211] reported that BTESE-derived membrane calcined at 400 $^\circ$C shows a high surface area of 338 m^2 g^{-1}, while decreased at a higher calcination temperature of 600 $^\circ$C (S_{BET} = 122 m^2 g^{-1}). This result indicated that the organosilica membranes show a denser structure after calcination at higher temperatures as schematically depicted in Fig. 1-36(b). At low calcination temperature, a low crosslinking degree, and a high amount of organic linking unit can be retained. Slow calcination at high temperature resulting in a high cross-linking with the destruction of organic groups leads to the formation of a denser structure. On contrary to that, expeditious calcination results in a high crosslinking degree and less decomposition of organic groups.

To solve this problem, several modifications to the organosilica structure can be

made, especially for controlling the movement or regeneration of silanol groups including modification of silica matrix with methyl ($-CH_3$) groups [212], use of organically bridged bi-silyl precursors [213], doping transition metals or metal oxides [210], and co-polymerization of precursors [214].

1.4.3.7.3 Tailoring pore structure of organosilica membranes for improved performance

a) Organic template method

One approach for the development of a membrane that shows both high permeability and separation performance is to introduce the organic ligand embedded in a dense inorganic matrix that serves as a template for the creation of porosity. Raman and Brinker [215] reported the organic template approach which shows the densification of the inorganic matrix in the first stage and the establishment of micropores after the removal of the organic template via pyrolysis. The schematic image of the synthesis method of the inorganic membrane through the organic template method is presented in Fig. 1-37.
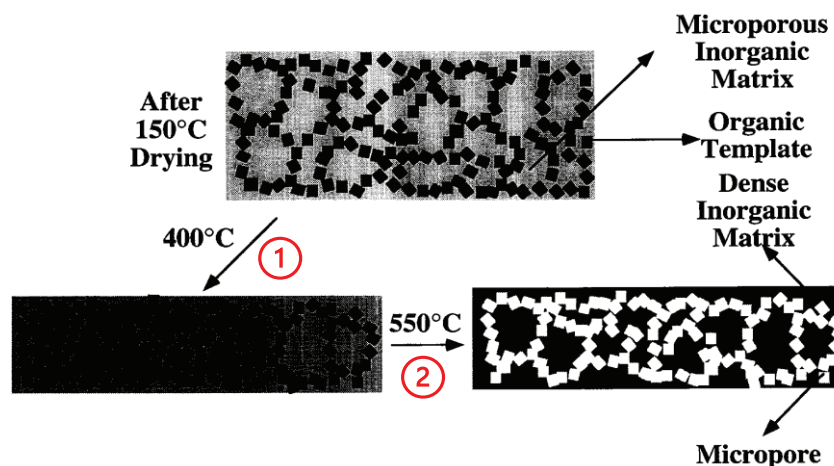
Fig. 1-37. The schematic image of the organic template method for the fabrication of porous inorganic membrane [215].

In general, the successful transcriptive synthesis of the inorganic membrane must be followed the criteria of the use of organic ligand that can homogeneously be incorporated into the inorganic matrix without the formation of phase separation, the synthesis

conditions give rise to the arrangement of the dense matrix so that pores will only be created via organic template removal process, and high durability of the matrix must be maintained without the collapse of the original network after the template removal process [216]. Li et al. [217] prepared an organic-inorganic hybrid silica membrane by using two different precursors of methyltriethoxysilane (MTES) and phenyltriethoxysilane (PhTES). In that work, both types of precursors show dense structure at the calcination temperature of 400 °C, but the N_2 adsorption capacity shows a significant increase after 550 °C which suggested the creation of pores after the pyrolysis of terminal organic groups in MTES-, and PhTES-derived xerogel powders (Fig. 1-38). At higher firing temperature, the H_2 permeance increased from 4.1×10^{-7} to 5.8×10^{-7} mol Pa^{-1} m^{-2} s^{-1} with a decrease in selectivity from 1300 to 77 due to the formation more loose structure.
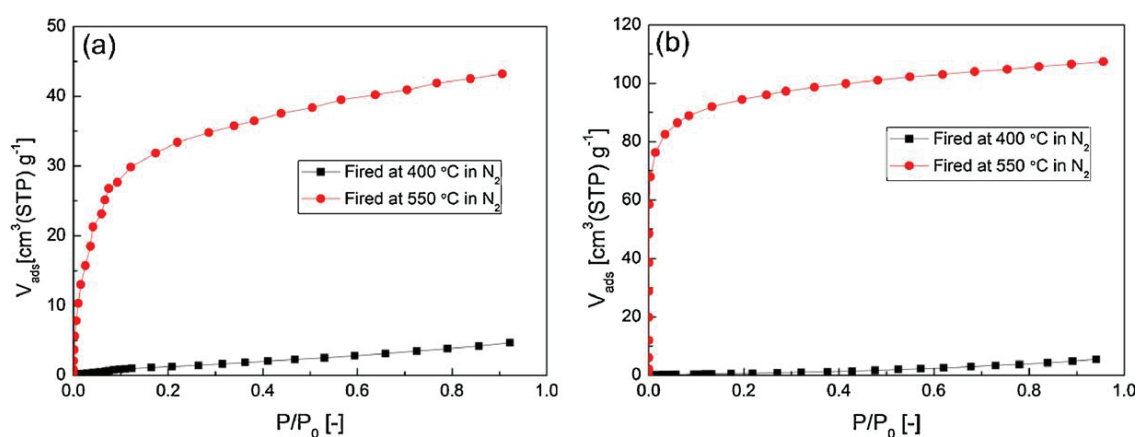
Fig. 1-38 N_2 adsorption isothermal of MTES (a) and PhTES (b) -derived gel powders calcined at different temperatures [217]

b) Spacer method

A spacer method is frequently prescribed for tailoring the microporosity by choosing bi-silyl precursors with different structures that produce organosilica-based materials with an optimum membrane pore size [218]. The utilization of a short and rigid linking chain between silicon atoms generates a porous structure, whereas the increase in the carbon number and flexibility of the linking units tends to produce a denser structure that is inappropriate for the construction of a high-flux membrane. Kanezashi et al. [219] reported the development of organosilica membranes via different types of spacer units as shown in Fig. 1-39(a). A short and rigid structure of the spacer unit shows the formation

of porous structure (BTESM Si-CH$_2$-Si, BTESE Si-C$_2$H$_4$-Si, and BTESB Si-Ph-Si), while a long and flexible linking unit shows the formation of non-porous structure (BTESP Si-C$_3$H$_6$-Si, BTMSH Si-C$_6$H$_{12}$-Si, and BTESO Si-C$_8$H$_{16}$-Si) as confirmed via N$_2$ sorption isotherms characterization (Fig. 1-39(b)). In line with material characterization, membrane evaluation (Fig. 1- 39(c)) shows that short and rigid precursors such as BTESM and BTESE exhibited higher permeance for small-sized gases such as He and H$_2$ compared with flexible-types precursor. However, the BTESB membrane with a rigid linking unit shows smaller H$_2$ permeance which is probably related to the free movement of the organic chain at the permeation temperature of 200 ⁰C.
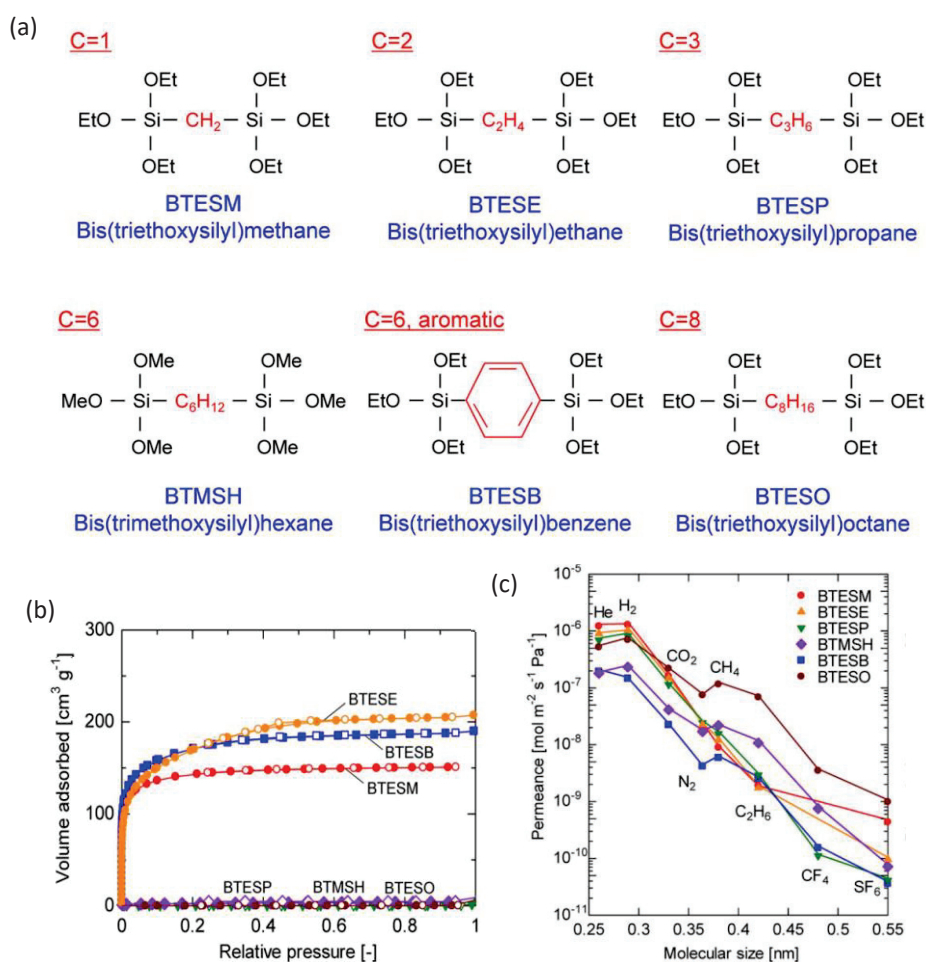
Fig. 1-39 Chemical structures of different types organosilica precursor (a), N$_2$ sorption isotherms for resulting xerogel powders calcined at 350 ⁰C (b), and single-gas permeation for different types of membranes at the measurement temperature of 200 ⁰C (c) [219]

Table 1-14 compares the effect of organic chain flexibility to the formation of porosity of the xerogel powder together with membrane performance. Organosilica

membrane with a long organic linking unit (carbon number higher than 3) shows the non-porous structure (negligible N_2 capacity) with low gas permeance and high selectivity.

Table 1-14 Organosilica-based membranes with different types of linking unit and their gas performance

Precursor	Chemical structure	T_C [°C]	S_{BET} [m²g⁻¹]	Permeance [10⁻⁷ mol m⁻² s⁻¹ Pa⁻¹]	Selectivity [-]	Ref.
BTESM	EtO–Si(OEt)₂–CH₂–Si(OEt)₂–OEt	350	~ 600	$H_2 = 10$	$H_2/N_2 = 70$	
BTESP	EtO–Si(OEt)₂–C₃H₆–Si(OEt)₂–OEt	350	0	$H_2 = 8$	$H_2/N_2 = 38$	[219]
BTMSH	EtO–Si(OEt)₂–C₆H₁₂–Si(OEt)₂–OEt	350	0	$H_2 = 3$	$H_2/N_2 = 15$	
BTESO	EtO–Si(OEt)₂–C₈H₁₆–Si(OEt)₂–OEt	350	0	$H_2 = 6$	$H_2/N_2 = 10$	
BTESE	EtO–Si(OEt)₂–C₂H₄–Si(OEt)₂–OEt	300	552	$H_2 = 9.5$	$H_2/N_2 = 22$	[220]
BTESEthy	EtO–Si(OEt)₂–CH=CH–Si(OEt)₂–OEt	300	763	$H_2 = 16.1$	$H_2/N_2 = 40$	
BTESA	EtO–Si(OEt)₂–C≡C–Si(OEt)₂–OEt	300	661	$H_2 = 26.8$	$H_2/N_2 = 10$	
BTESE	EtO–Si(OEt)₂–C₂H₄–Si(OEt)₂–OEt	300	476	$H_2 = 18$	$H_2/N_2 = 55$ $C_3H_6/C_3H_8 = 5$	
BTESEthy	EtO–Si(OEt)₂–CH=CH–Si(OEt)₂–OEt	300	556	$H_2 = 10$	$H_2/N_2 = 68$ $C_3H_6/C_3H_8 = 1.4$	[221]
BTESA	EtO–Si(OEt)₂–C≡C–Si(OEt)₂–OEt	300	594	$H_2 = 32$	$H_2/N_2 = 12$ $C_3H_6/C_3H_8 = 13$	
BTESE	EtO–Si(OEt)₂–C₂H₄–Si(OEt)₂–OEt	200	120	$H_2 = 12.9$	$H_2/N_2 = 16$ $CO_2/H_2 = 1$	
BTESBP	EtO–Si(OEt)₂–(C₆H₄)₂–Si(OEt)₂–OEt	200	77	$H_2 = 19.3$	$H_2/N_2 = 16$ $CO_2/H_2 = 2$	[218]
BTESO	EtO–Si(OEt)₂–C₈H₁₆–Si(OEt)₂–OEt	200	0	$H_2 = 23.2$	$H_2/N_2 = 5$ $CO_2/H_2 = 2$	
TTESPT-WR60	(triazine-based structure)	300	2	$H_2 = 19.7$	$H_2/N_2 = 9$	[222]
TTESPT-WR240	(triazine-based structure)	300	80	$H_2 = 14.6$ $C_3H_6 = 0.59$	$H_2/N_2 = 13$ $C_3H_6/C_3H_8 = 8$	

	Structure					
BTESA		300	594	$CO_2 = 25$	$CO_2/N_2 = 13$ $CO_2/CH_4 = 23$	
BTESA/ BTESB		300	565	$CO_2 = 20$	$CO_2/N_2 = 25$ $CO_2/CH_4 = 35$	[223]
BTESA/ BTESBP		300	783	$CO_2 = 30$	$CO_2/N_2 = 9$ $CO_2/CH_4 = 8$	
BTES-ED		300	373	$H_2 = 8.3$	$H_2/N_2 = 11$	[224]
BTES-MOU		300	155	$H_2 = 22.2$	$H_2/N_2 = 12$	[225]
BTES-POU		300	0	$H_2 = 6$	$H_2/N_2 = 19$	
BTMSN		300	336	$H_2 = 8.6$	$H_2/N_2 = 12$	[226]
BTPP-self-12		300	0	$H_2 = 5.32$	$H_2/N_2 = 19.8$	
BTPP-HCl-40		300	0	$H_2 = 3.02$	$H_2/N_2 = 32.8$	[227]
BTPP-HCl-240		300	0	$H_2 = 3.89$ $CO_2 = 0.34$	$H_2/N_2 = 20.4$ $CO_2/N_2 = 25$	
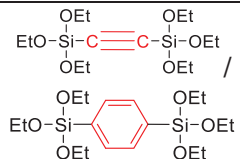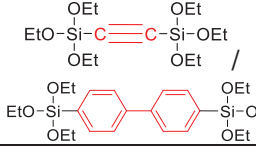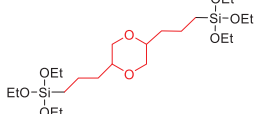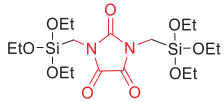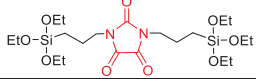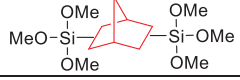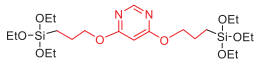
c) Metal doping

Silica and organosilica membranes could be doped with transition metals such as Ag [228], Al [229], Co [230], Zr [231], Fe [232], Nb [233], and Ni [234] to increase the stability characteristics of the membranes. Doping metal into silica structure presents functionalities that are not available for pure silica membranes. One of the specific functionalities that were developed via metal doping has been reported by Battersby et al. [235]. In that reported work, the structure of cobalt-doped tetraethylorthosilicate (Co-TEOS) was maintained microporous as H_2 selectivity was not affected by steam exposure for 200h of operation, while pure silica membrane shows the opening of larger pores resulting in mesoporous structure. Another specific functionality after the incorporation of metal-doping was reported by Kanezashi et al. [229]. Al doped bis (triethoxysilyl)

----

ethane (Al-BTESM) shows the densification structure with a lower surface area (S_{BET} = 507 m^2 g^{-1}) compared to pure BTESM xerogel powder (S_{BET} = 597 m^2 g^{-1}), but higher performance for C_3H_6/C_3H_8 separation was achieved for Al-BTESM with the highest permeance ratio of 40. Table 1-15 provides the summary metal-doped organosilica membranes for the separation in gas and liquid system.

Table 1-15. Performance comparison of the pristine and metal-doped silica and organosilica membranes

Metal-doped organosilica	Condition	T_C [ºC]	S_{BET} [m^2g^{-1}]	Permeance [10^{-7} mol m^{-2} s^{-1} Pa^{-1}]	Selectivity [-]	Ref.
TEOS	Si/Ni = 0	550	n.a.	H_2 = 0.89	H_2/H_2O = 13	
Ni-TEOS	Si/Ni = 4/1	550	n.a.	H_2 = 2.23	H_2/H_2O = 19	[234]
Ni-TEOS	Si/Ni = 2/1	550	n.a.	H_2 = 10.26	H_2/H_2O = 25	
BTESM	Si/Al = 0	200	597	C_3H_6 = 0.5	C_3H_6/C_3H_8 = 9	
Al-BTESM	Si/Al = 9.5/0.5	200	531	C_3H_6 = 0.1	C_3H_6/C_3H_8 = 10	[229]
Al-BTESM	Si/Al = 9/1	200	507	C_3H_6 = 0.08	C_3H_6/C_3H_8 = 20	
Al-BTESM	Si/Al = 8/2	200	387	C_3H_6 = 0.01	C_3H_6/C_3H_8 = 6	
	$T_{hydrothermal}$ = -	400	n.a.	H_2 = 1.8	H_2/CO_2 = 12	
	$T_{hydrothermal}$ = 100 ºC	400	n.a.	H_2 = 0.9	H_2/CO_2 = 17	
Zr-BTESE	$T_{hydrothermal}$ = 200 ºC	400	n.a.	H_2 = 1.0	H_2/CO_2 = 31	[231]
	$T_{hydrothermal}$ = 300 ºC	400	n.a.	H_2 = 0.8	H_2/CO_2 = 35	
BTESE	Si/Nb = 0	400	120	H_2 = 2	H_2/CO_2 = 2.8	
		300	119	H_2 = 2.25	H_2/CO_2 = 10.2	
Nb-BTESE	Si/Nb = 3/1	350	126	H_2 = 1.85	H_2/CO_2 = 10.9	[233]
		400	88.4	H_2 = 1.07	H_2/CO_2 = 56.3	
		450	26.8	H_2 = 0.97	H_2/CO_2 = 220	
BTESE	Metal/Si = 0/10	150	694	H_2O = 13.4	H_2O/IPA = 3,757	
Al-BTESE	Al/Si = 1/9	150	514	H_2O = 10.8	H_2O/IPA = 8,994	[236]
Zr-BTESE	Zr/Si = 1/9	150	395	H_2O = 17.0	H_2O/IPA = 14,205	
Pd-Nb-BTESE-0.05	Pd/Nb/Si = 0.05/0.33/1	400	233	H_2 = 1	H_2/CO_2 = 50	
Pd-Nb-BTESE-0.1	Pd/Nb/Si = 0.1/0.33/1	400	223	H_2 = 0.5	H_2/CO_2 = 62.5	[237]
Pd-Nb-BTESE-0.2	Pd/Nb/Si = 0.2/0.33/1	400	214	H_2 = 0.4	H_2/CO_2 = 57.4	
Pd-Nb-BTESE-0.4	Pd/Nb/Si = 0.4/0.33/1	400	177	H_2 = 1.5	H_2/CO_2 = 150	
Pd-BTESE (Pd/Si =	Calc. atm.= air	400	410	H_2 = 3	H_2/CO_2 = 8.91 H_2/CH_4 = 8.4	[238]

0.11/1)	Calc. atm.= N_2	400	547	$H_2 = 1$	$H_2/CO_2 = 8.6$ $H_2/CH_4 = 10.7$	
	Calc. atm.= H_2	400	507	$H_2 = 4$	$H_2/CO_2 = 8.0$ $H_2/CH_4 = 31.3$	
	Calc. atm.= H_2/N_2	400	540	$H_2 = 2$	$H_2/CO_2 = 15.0$ $H_2/CH_4 = 173$	
TEOS	Co = 0 mol%	500	390	$H_2 = 20$	$H_2/N_2 = 80$	
Co-TEOS	Co = 10 mol%	500	420	$H_2 = 50$	$H_2/N_2 = 200$	[239]
	Co = 30 mol%	500	200	$H_2 = 60$	$H_2/N_2 = 300$	
	Co = 50 mol%	500	195	$H_2 = 30$	$H_2/N_2 = 50$	
TEOS	Mg = 0 mol%	600	n.a.	$H_2 = 5.26$	$H_2/CO_2 = 9$	
Mg-TEOS	Mg = 10 mol%	600	n.a.	$H_2 = 2.10$	$H_2/CO_2 = 19$	[240]
	Mg = 15 mol%	600	n.a.	$H_2 = 2.20$	$H_2/CO_2 = 24$	
	Mg = 20 mol%	600	n.a.	$H_2 = 0.70$	$H_2/CO_2 = 350$	
BTESE	Metal = 0 mol%	300	n.a.	$H_2 = 3.12$	$H_2/CH_4 = 19.5$	
B-BTESE	B/(B+Si) = 20 mol%	300	n.a.	$H_2 = 4.98$	$H_2/CH_4 = 12.7$	[241]
Ta-BTESE	Ta/(Ta+Si) = 20 mol%	300	n.a.	$H_2 = 5.65$	$H_2/CH_4 = 12.3$	
Nb-BTESE	Nb/(Nb/Si) = 20 mol%	300	n.a.	$H_2 = 5.03$	$H_2/CH_4 = 12$	

Based on Table 1-15, most metal-doped organosilica membranes exhibit higher separation performance with lower permeance of components. Song et al. [242] reported that a pristine organosilica (1,2-bis(triethoxysilyl)ethane/BTESE) membrane has relatively large intra-particle pores and a loose network, while a metal-doped organosilica membrane shows a less porous structure as shown in Fig. 1-40.
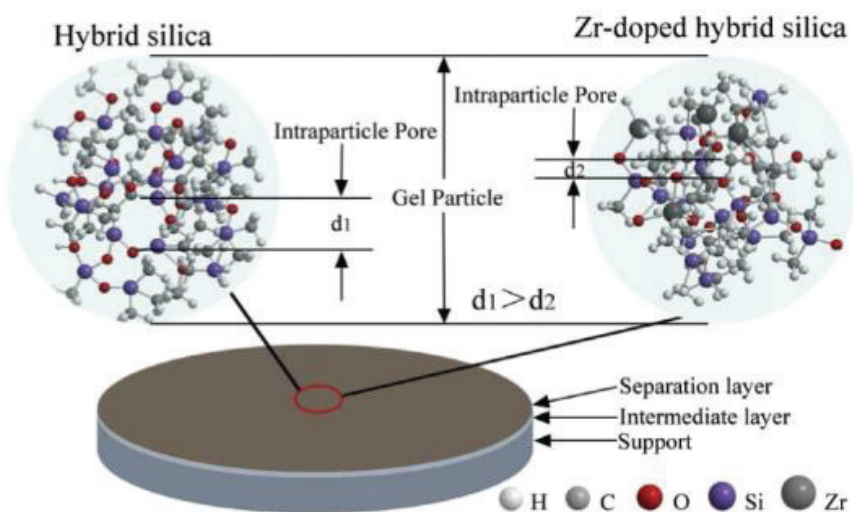
Fig. 1-40. The comparison of pore structure from pristine and metal-doped organosilica membranes [242].

1.5 Scope of this thesis

1.5.1 Proposal of organosilica-based coordination polymer

A coordination polymer composes of metal ions linked by the coordinated ligands in an infinite direction. The interconnected structural units have the potential to house nanometer-sized space. The infinite net structure is defined by the coordination bonds and molecular species linked by hydrogen bonding. Hence, a coordination polymer structure consists of metal and ligands or often includes guest and counterions [243]. The metal ions that act as connectors are commonly transition metals and/or lanthanoids with 2-6 coordination numbers. The coordination number of coordinated polymer structures can be varied depending on the metal and the oxidation state, which resulting different geometries and porosity. A transition metal easily forms complex due to the existence of empty d-orbitals, while alkali metal and rare earth ions tend to lose valence electrons and form cations with the positive charge which results in the ionic interaction. Ag(I) ions tend to form a linear chain with several linear linkers as a result of their preference for a coordination number of two [244]. The other metals such as Co(II) and Zn(II) show higher coordination numbers with higher dimensional network connectivity generated with ligands binding sites. The schematic presentation for the construction of coordinated polymers via different building blocks is shown in Fig. 1-41 [245].
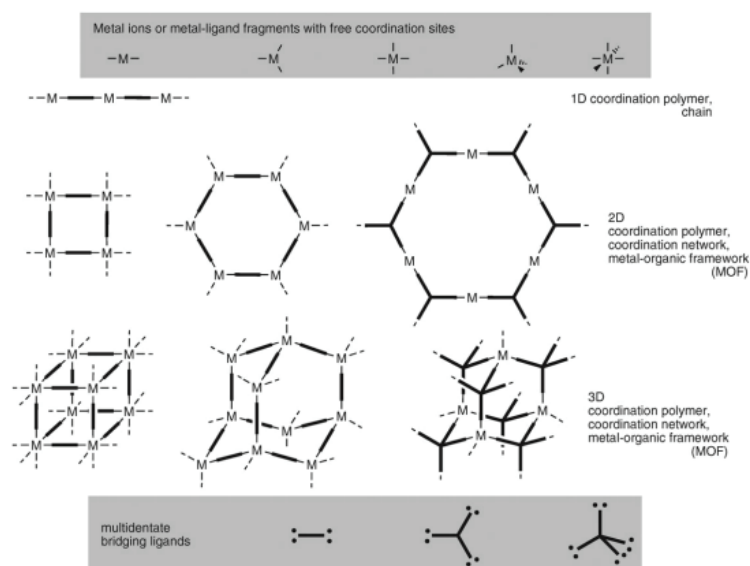
Fig. 1-41. Schematic images for the construction of coordination polymers with different building blocks [245].

A typical ligand or linker might have two or more coordination sites such as pyridyl, imidazole, nitrile, or carboxylate. Yang et al. [246] reported the formation of coordinated Cu^{2+} ions with the hydroxyl groups of cellulose polymer chain that could open the spacing between the molecule chain and create channels in cellulose nanofiber (CNF) that serve for ions conducting pathways as shown in Fig. 1-42.
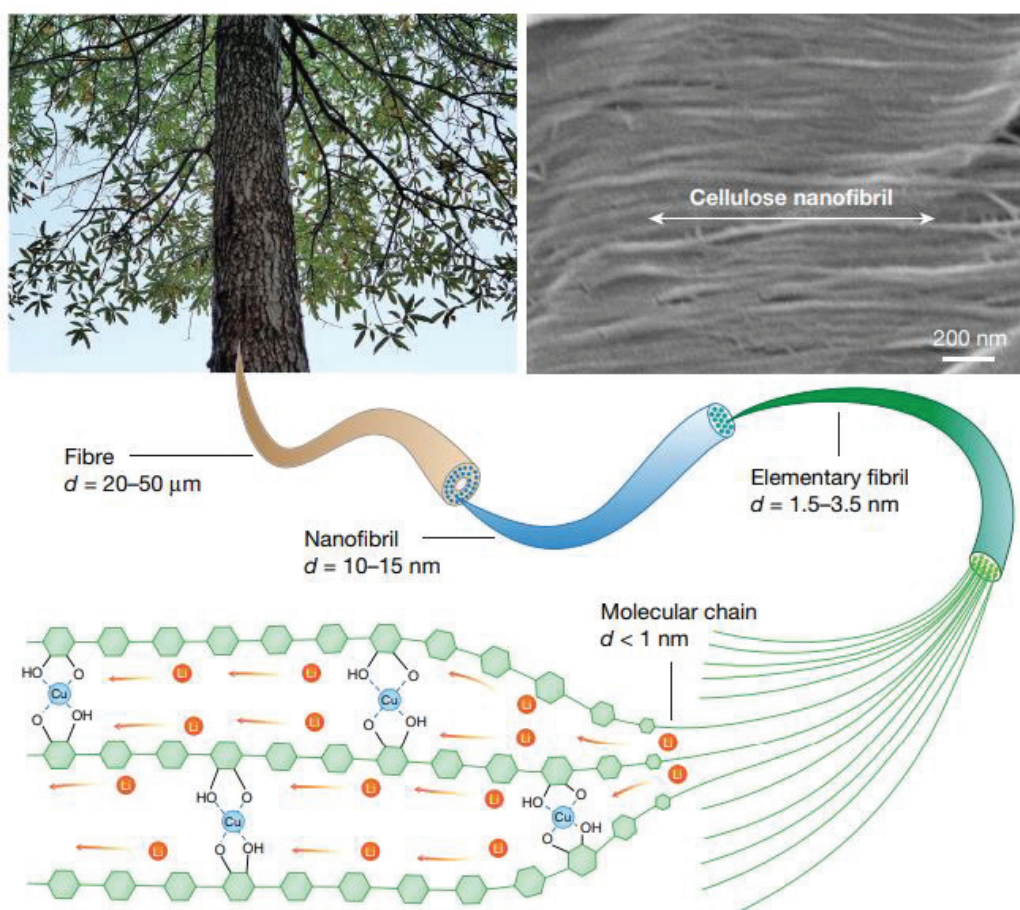
Fig. 1-42. The SEM image of cellulose nanofiber and the schematic structure of Cu^{2+} create coordination with hydroxyl groups opening channel structure for the transport of Li^+ ions [246].

In another work, Jia et al. [247] reported the formation of ZIF-8@cellulose nanofiber (ZIF-8@CNF) composite membranes that were prepared via electrostatic forces between Zn^{2+} and -COO^- from the CNF. After the formation of coordinated species (Zn^{2+}-COO^-), the 2-methylimidazole solution was poured into CNF-Zn^{2+} to facilitate the in situ growth of the ZIF-8@CNF composite membrane. The schematic concept of coordinated metal-polymer structure is shown in Fig. 1-42. Pristine CNF membrane shows a very dense structure where most permeating molecules are transported based on the solution-diffusion mechanism. After the in-situ growing of porous ZIF-8, connected-MOF

channels were constructed, increasing both CO_2 permeability and the selectivity for CO_2/N_2 of 566 Barrer and 45.6, respectively.
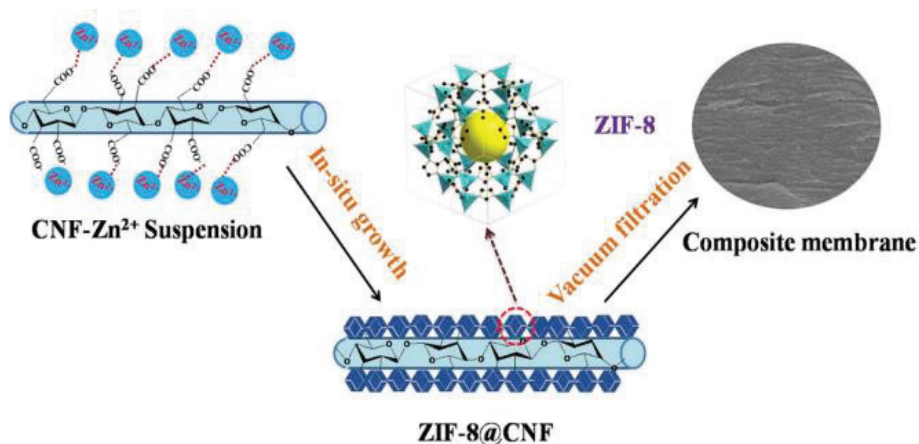
Fig. 1-43. Schematic image of the synthesis procedure for ZIF-8@CNF composite membranes [247].

Tanaka et al. [248] reported the hybridization of organosilica membranes connected with ZIF-8 networks for enhanced separation performance of C_3H_6/C_3H_8. The preparation of pristine ZIF-8 membrane shows a poor membrane adhesion with α-alumina support due to ZIF-8 cannot form a covalent bond with the surface OH from the support. In that work, they use 3-(2-imidazolin-1-yl) propyltriethoxysilane (IPTES) grafted on the surface of α-alumina support and promote the nucleation of ZIF-8 via coordination between IPTES-Zn-2 methylimidazole as schematically shown in Fig. 1-44. After the grafting of IPTES on the α-alumina support, the selectivity of C_3H_6/C_3H_8 increased to 36 with C_3H_6 permeance of 8.5×10^{-8} mol m^{-2} s^{-1} Pa^{-1}.
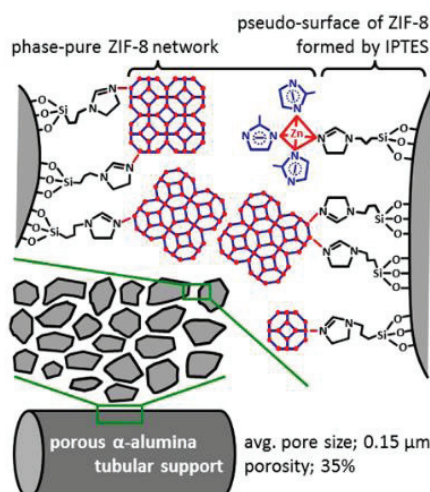
Fig. 1-44. Schematic image of IPTES grafted on α-alumina support followed by the nucleation of ZIF-8 structure [248]

Based on the reported works, it was possible to construct the coordination between transition metal (can act as Lewis-acid molecules) with polymer structure with specific functional groups such as amine moieties (can act as Lewis-base molecules or ligand). By following this concept, we firstly proposed the development of organosilica-based coordination polymers by adding a transition metal to change the flexibility of organic linking units of the precursors and improve the microporosity of the membrane while maintaining the amorphous nature of the silica networks. The concept of functionalized organosilica-based coordination polymer is shown in Fig. 1-45.
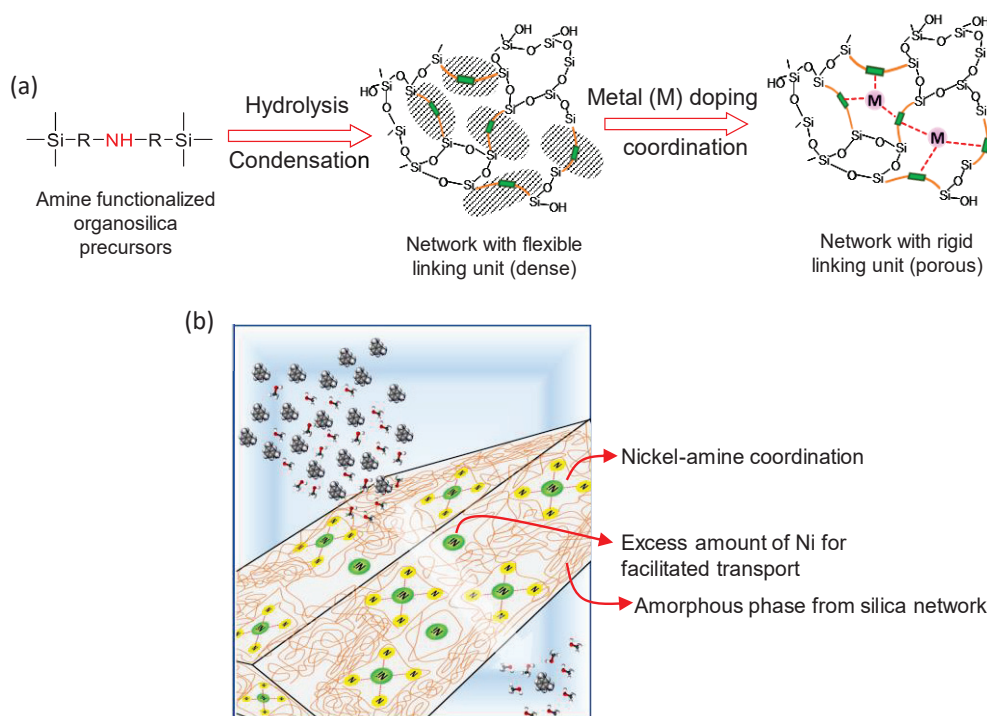
Fig. 1-45. Schematic image for the development of metal-coordinated amine-functionalized organosilica framework via hydrolysis and condensation followed by coordination (a), and the proposed membrane structure of hybrid organosilica-based coordination polymer

The varied structure of ligands from rigid to completely flexible was important to produce a definite structure of coordination polymer. When functional or non-functional organic groups are covalently linked to oxide networks, sol-gel coordinated materials are obtained. The strong interaction between metal and ligand produces a robust porosity, while weak coordination generates lining porosity. Based on the isothermal studies, the coordination-based polymer could provide permanent porosity through the linking of flexible moieties with a strong bond (between organic and inorganic components)

together with weaker bonds that show physical interaction such as van der walls or hydrogen bonding. When a weak bond increases the dimensionality of the framework into 2D or 3D, a higher dimensional structure shows a more robust nature. A new strategy of using metal-coordinated amine-functionalized organosilica precursors could control the microporosity of silica-based amorphous network. The addition of metal-generated subnanopores via the coordinated covalent bonds increased the crosslinking between network layers, which converted the texture of the membrane from a non-porous to a microporous entity. Fig. 1-46 shows the chemical structure of different types of N-functionalized organosilica precursors for the preparation of coordinated polymers as ligand connectors with a metal center. A hybrid network consisting of an ordered structure from coordinated polymers and an amorphous structure
 from the organosilica could be generating a membrane with both combinations of high permeating flux and selectivity.
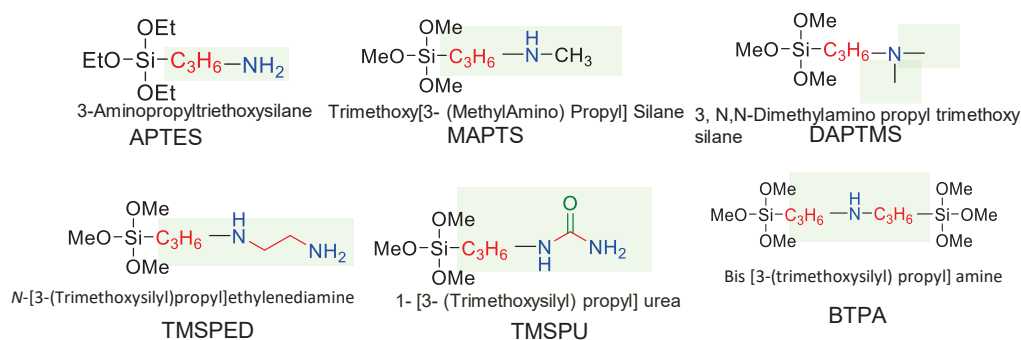
Fig. 1-46. The chemical structure of possible functionalized-organosilica precursors as the connector ligand for the formation of coordination polymer with metal center

Table 1-16 compares different types of membrane materials together with organosilica-based coordination polymer as one novel class of materials which provides a promising chance to approach high membrane performance. Organosilica-based coordination polymers can be constructed from coordination bonds (binding energy-BE = 20-50 kcal mol^{-1}), hydrogen and metal-metal bonds (BE = 1-30 kcal mol^{-1}), π-π stacking (BE = 0-12 kcal mol^{-1}), CH-π, electrostatic, and van der Waals interaction (BE = 0.1.5 kcal mol^{-1}), thus network with robust and rigid properties can be produced [244, 249].

Table 1-16. Comparison between the present proposed organosilica-based coordination polymer and conventional materials

Membrane materials	Building block	Fabrication method	Advantages	Disadvantages
Polymer	1. Organic monomer molecules	Phase inversion, interfacial polymerization, electrospinning	Low cost, easy to fabricate	Low permeability, swelling
Metal-organic framework (MOF)	1. Metal ions or inorganic nanocluster 2. Organic linker	In situ crystallization, seeded-assisted (secondary) growth, rapid thermal deposition, contra-diffusion	High permeability, high performance	Poor chemical and hydrothermal stabilities (lability of coordinate bonds)
MOF-Polymer	1. Metal ions or inorganic nanocluster 2. Organic linker 3. Organic monomer molecules	Solvent-casting method, spin coating,	Significantly enhance selectivity	Poor adhesion between the polymer phase and MOF particles, defects, and low separation capability
Organosilica-MOF	1. Organosilica precursor 2. Metal ions or inorganic nanocluster 3. Organic linker	Seeding free aqueous synthesis	Grafting the organosilica precursors can control the grain size of MOF particles, reduce the formation of defects	Lower permeability after grafting the organosilica precursor
Organosilica-based coordination polymer	1. Organosilica precursor 2. Metal ions	Sol-gel	High permeability, high selectivity, easy for fabrication	Low thermal stability due to the existence of amine organic linker
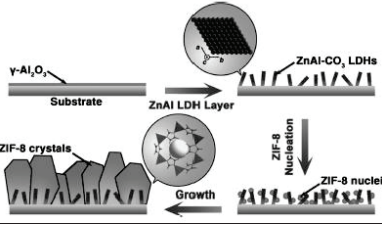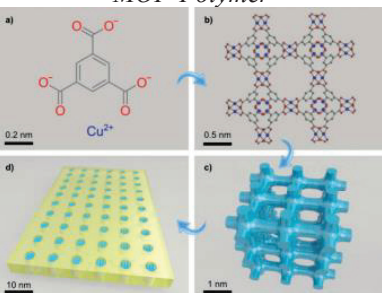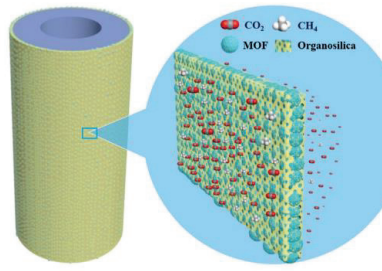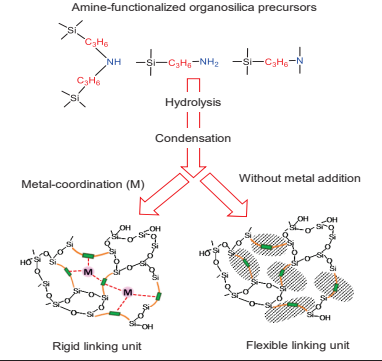
In addition, the sol-gel process for the synthesis of organosilica materials has the main advantages of its allowing an easy-preparation method, lower energy consumption, and applicability to a wide variety of materials with the different functional components in the structure of organosilica precursors.

1.5.2 Objectives and organization of this study

The overall objective of this dissertation research is to develop metal-coordinated amine-functionalized organosilica-induced microporosity for highly permeable membranes for both gas and liquid separation. By following the concept of metal-organic framework (MOF) where metal-linker interactions form nano spaces, in this dissertation, we attempted a novel synthesis strategy to control the pore size of amorphous amine-functionalized organosilica via sol-gel followed by coordination. Metal-doped aminosilica membranes are expected to generate subnanopores via the coordination of covalent bonds between aminosilica precursors as Lewis-base molecules (ligand) and the transition metal acted as Lewis-acid molecules. The crosslinking between metal and ligand was proposed to convert membrane texture from the non-porous entity into microporous ones via the development of more rigid linking units. The concept of metal-coordinated aminosilica membranes is schematically shown in Fig. 1-47. However, the research about organosilica-based coordination polymer was very limited, especially in the viewpoint of optimized conditions for the affinity of metal types, metal concentration, and the affinity of ligand.

Flexible linking units – non-porous   Rigid linking units - microporous
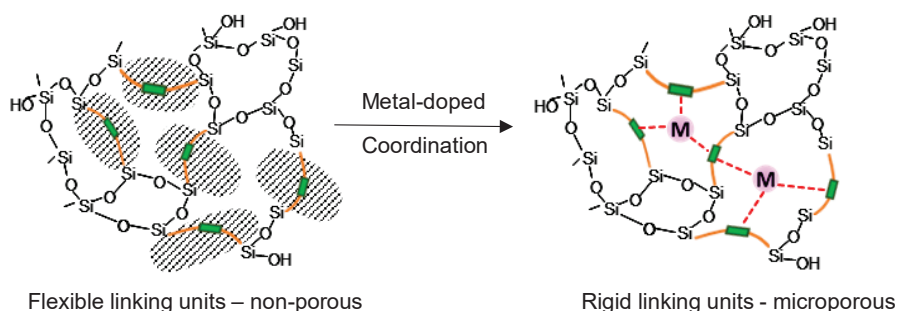
Fig. 1-47. The schematic image for the coordination mechanism between metal acceptors and amine donor electrons results in a rigid linking unit with a microporous structure

Therefore, this research has focused on the development of metal-coordinated aminosilica for highly permeable membranes, and the evaluation of their gas permeation properties

for the separation of specific gas mixtures and/or liquid systems via pervaporation. The main work of this study is as follows:

(i)   Synthesis, characterization, and membrane evaluation of different types of transition metals including silver (Ag), copper (Cu), and nickel (Ni) coordinated with bridge-type aminosilica precursor of bis [3-trimethoxysilyl) propyl] amine (BTPA);

(ii) Optimization of the formation microporosity of nickel-doped bis [3-trimethoxysilyl) propyl] amine (Ni-BTPA) at different nickel/amine (Ni/NH) mole ratios and the evaluation of membrane performance for the separation of azeotrope mixture via pervaporation;

(iii) Comparative studies on the formation of the coordinated network via different types of aminosilica ligand precursors including bis [3-(trimethoxysilyl) propyl] amine (BTPA), trimethoxy [3-(methylamino) propyl] silane (MAPTS) and 3-amino propyl triethoxysilane (APTES) and the separation performance of organic/organic mixtures via pervaporation;

(iv) The evaluation of the evolution of silver in two phases for facilitated transport on silver-doped BTPA membranes at different silver/amine mole ratios.

This thesis consists of 6 chapters, as follows:

Chapter 1 is the **"General introduction"**, which involves the research background and the purpose of this study.

Chapter 2 is **"Metal-induced microporous aminosilica creates a highly permeable gas-separation membrane"**. Hybrid microporous aminosilica membranes have been successfully synthesized via doping with Ag-, Cu- and Ni- into dense bis [3-(trimethoxysilyl) propyl] amine (BTPA) membranes, which creates micropores via the crosslinking between donor pairs of electrons in the amine moiety and electron acceptors in the empty "d" orbital of a transition metal. The formation of micropores within the coordinated covalently bonded compound was investigated via Ultraviolet-Visible spectroscopy (UV-Vis), Fourier Transform Infrared spectroscopy (FT-IR), X-ray Photoelectron Spectroscopy (XPS), X-ray Diffraction (XRD), Transmission Electron Microscopy (TEM), and the isotherms of N_2 and CO_2 sorption. Values for the surface area and pore volume of the metal-doped BTPA were both expanded by increasing the metal coordination affinity to 214 m^2 g^{-1} and 0.185 cm^3 g^{-1}, respectively. The effect of metal doping on the membrane separation performance was evaluated using a single-gas

permeation system and the activation energy of permeance was measured. Gas permeation was increased following the doping process due to the formation of a microporous structure on the order of Ni-BTPA > Cu-BTPA > Ag-BTPA > BTPA, which corresponds to a higher affinity for metal coordination. Permeation behavior was dominated by the molecular sieving effect that showed a high level of H_2 permeance at 4.45×10^{-6} mol m^{-2} s^{-1} Pa^{-1} with an H_2/SF_6 permeance ratio that reached 15,500, which is indicative of a defect-free membrane. By comparison with Cu-BTPA (14.8 kJ mol^{-1}), Ag-BTPA (19.5 kJ mol^{-1}), and BTPA (31.1 kJ mol^{-1}) membranes, the Ni-BTPA membrane showed the lowest value for CO_2 activation energy (8.9 kJ mol^{-1}), which can be ascribed to the microporosity that was formed by a higher coordination interaction. The nickel-doped BTPA achieved high levels of both permeance of N_2 and selectivity for N_2/SF_6 at 3.75×10^{-7} mol m^{-2} s^{-1} Pa^{-1} and 1,900, respectively.

Chapter 3 is **"Microporous nickel-coordinated aminosilica membranes for improved pervaporation performance of methanol/toluene separation"**. The nickel-doped bis [3-(trimethoxysilyl) propyl] amine (BTPA) derived membrane has a microporous coordinated network that offers high potential to be an ideal separation barrier for methanol-toluene azeotropic mixtures via the pervaporation process. Ni-BTPA membranes were modified by employing a nickel dopant over amine groups in mole ratios (mol mol^{-1}) that ranged from 0.125 to 0.50. The incorporation of different amounts of nickel dopant into flexible amine-rich organosilica precursors of BTPA increased the rigidity and resulted in a porous structure with a large specific surface area (increased from 2.36 up to 282 m^2 g^{-1}) and a high pore volume (from 0.024 up to 0.184 cm^3 g^{-1}). Methanol-toluene separation performance by the nickel-doped BTPA (Ni-BTPA) membranes was increased with increases in the nickel concentration. Ni-BTPA 0.50 showed separation performance that was superior to other types of membranes, along with a high level of flux at 2.8 kg m^{-2} h^{-1} and a separation factor higher than 900 in a 10 wt% methanol feed solution at 50 °C. These results suggest that the balance between the microporosity induced by amine-nickel coordination and an excessive amount of nickel-ion facilitates high levels of flux and separation of methanol.

Chapter 4 is **"Structural transformation of the nickel-coordination-induced subnanoporosity of aminosilica membranes for methanol-selective, high-flux pervaporation"**. A novel strategy to modify the dense framework of different types of

amine-functionalized organosilica membranes has been successfully applied via nickel coordination to induce the formation of microporous membranes. Prior to the nickel-coordination reaction, aminosilica sols were prepared via hydrolysis of several types of amine precursors: bis [3-(trimethoxysilyl) propyl] amine (BTPA), trimethoxy [3-(methyl amino) propyl] silane (MAPTS), and 3-aminopropyl triethoxy silane (APTES). The optimal nickel/amine mole ratio was established within a range from 0-0.50 mol mol^{-1}, and calcinations of the membranes were performed at 250, 300, and 350 ℃. We found that nickel doping restructured the aminosilica network via a coordination bond, which then increased both the rigidity of the organic chain and the surface area of the resultant materials on the order of nickel-doped bis [3-(trimethoxysilyl) propyl] amine (Ni-BTPA) > nickel-doped 3-aminopropyl triethoxy silane (Ni-APTES) > nickel-doped trimethoxy [3-(methyl amino) propyl] silane (Ni-MAPTS). Spectroscopy characterization studies such as Ultraviolet-visible (UV-vis), Fourier Transform Infrared (FT-IR), and X-ray Diffraction (XRD) along with micropore analysis of N$_2$ sorption isotherms revealed that the formation of a coordinated network could be sterically hindered by the existence of non-hydrolyzable methyl groups on the pendant chain. The prepared composite membranes were utilized for the pervaporation of various types of organic mixtures for a composition ratio of methanol/solvents of 10/90 wt% at 50 ℃. All nickel-composite membranes showed high flux and outstanding performance for the pervaporation of methanol/ dimethyl carbonate (MeOH/DMC) and methanol/ toluene (MeOH/Tol) mixtures. Ni-BTPA membranes with bridge-structured secondary-amine ligands recorded values for the flux that reached as high as 1.42 kg m^{-2} h^{-1} with an optimum separation factor for MeOH/Tol of 5,000.

Chapter 5 is **"Structural two-phase evolution of aminosilica-based silver-coordinated membranes for increased hydrogen separation"**. Hybrid organosilica membranes of silver-doped bis [3-(trimethoxysilyl) propyl] amine (BTPA) were prepared via sol-gel processing followed by coordination reactions to improve the permeability and separation performance. The evolution of silver in two phases as silver ions and as nanoparticles was observed during the modification of the aminosilica networks; the silver ions coordinated with amine moieties while the silver nanoparticles developed following reduction on the aminosilica surface. The silver/amine mole ratio was evaluated against the formation of coordinated and particulate species during modification in the

range of 0.1 to 0.5 mol mol^{-1}. The formation of microporosity was successfully developed from 2.36 to 115 m^2 g^{-1} by increasing the silver mole ratio. Furthermore, silver-modified aminosilica membranes showed hydrogen (H$_2$) permeance of 1.46×10^{-6} mol m^{-2} s^{-1} Pa^{-1}, which was 65-fold higher than pure BTPA with excellent selectivity for H$_2$/propane (C$_3$H$_8$) separation of 1,500. It is evident that the proposed modification method via the two-phase structural evolution of silver coordination and nanoparticles reorganized the organosilica framework and improved the separation in the dehydrogenation of propane.

Chapter 6 is **"Conclusions and recommendations"**. In this chapter, the main conclusions of this thesis are summarized and the recommendations are provided for further study.

References

[1] R.W. Baker, Future directions of membrane gas separation technology, Ind. Eng. Chem. Res., 41 (2002) 1393-1411.

[2] D.S. Sholl, R.P. Lively, Seven chemical separations to change the world, Nature, 532 (2016) 435-437.

[3] H. Strathmann, Membrane separation processes, J. Membr. Sci., 9 (1981) 121-189.

[4] N. Moriyama, H. Nagasawa, M. Kanezashi, T. Tsuru, Pervaporation dehydration of aqueous solutions of various types of molecules via organosilica membranes: Effect of membrane pore sizes and molecular sizes, Sep. Purif. Technol., 207 (2018) 108-115.

[5] Z. Cui, Y. Jiang, R. Field, Fundamentals of pressure-driven membrane separation processes, in: Membrane technology, Elsevier, 2010, pp. 1-18.

[6] K. Scott, R. Hughes, R. Hughes, Industrial membrane separation technology, Springer Science & Business Media, 1996.

[7] N. Moriyama, Y. Kawano, Q. Wang, R. Inoue, M. Guo, M. Yokoji, H. Nagasawa, M. Kanezashi, T. Tsuru, Pervaporation via silicon‐based membranes: Correlation and prediction of performance in pervaporation and gas permeation, AIChE J., 67 (2021) e17223.

[8] H. Nagasawa, T. Niimi, M. Kanezashi, T. Yoshioka, T. Tsuru, Modified gas‐translation model for prediction of gas permeation through microporous organosilica membranes, AIChE J., 60 (2014) 4199-4210.

[9] L. Yu, M. Kanezashi, H. Nagasawa, T. Tsuru, Fabrication and CO2 permeation properties of amine-silica membranes using a variety of amine types, J. Membr. Sci., 541 (2017) 447-456.

[10] V.M.A. Melgar, J. Kim, M.R. Othman, Zeolitic imidazolate framework membranes for gas separation: A review of synthesis methods and gas separation performance, Journal of Industrial and Engineering Chemistry, 28 (2015) 1-15.

[11] Y. Yampolskii, B. Freeman, Membrane gas separation, John Wiley & Sons, 2010.

[12] M.K. Purkait, M.K. Sinha, P. Mondal, R. Singh, Introduction to membranes, in: Interface science and technology, Elsevier, 2018, pp. 1-37.

Hiroshima University Doctoral Dissertation

----

[13] A.V. Mahenthiran, Z.A. Jawad, A Prospective Concept on the Fabrication of Blend PES/PEG/DMF/NMP Mixed Matrix Membranes with Functionalised Carbon Nanotubes for CO2/N2 Separation, Membranes, 11 (2021) 519.

[14] J.G. Wijmans, R.W. Baker, The solution-diffusion model: a review, J. Membr. Sci., 107 (1995) 1-21.

[15] X. Dong, W. Jin, N. Xu, K. Li, Dense ceramic catalytic membranes and membrane reactors for energy and environmental applications, Chem. Commun., 47 (2011) 10886-10902.

[16] T. Plisko, A. Penkova, K. Burts, A. Bildyukevich, M. Dmitrenko, G. Melnikova, R. Atta, A. Mazur, A. Zolotarev, A. Missyul, Effect of Pluronic F127 on porous and dense membrane structure formation via non-solvent induced and evaporation induced phase separation, J. Membr. Sci., 580 (2019) 336-349.

[17] A. Ayral, A. Julbe, V. Rouessac, S. Roualdes, J. Durand, Microporous silica membrane: basic principles and recent advances, Membrane science and technology, 13 (2008) 33-79.

[18] S.T. Oyama, M. Yamada, T. Sugawara, A. Takagaki, R. Kikuchi, Review on mechanisms of gas permeation through inorganic membranes, J. Jpn. Pet. Inst, 54 (2011) 298-309.

[19] W. Mi, Y. Lin, Y. Li, Vertically aligned carbon nanotube membranes on macroporous alumina supports, J. Membr. Sci., 304 (2007) 1-7.

[20] B. Freeman, Y. Yampolskii, Membrane gas separation, John Wiley & Sons, 2011.

[21] P. Pandey, R. Chauhan, Membranes for gas separation, Prog. Polym. Sci., 26 (2001) 853-893.

[22] X. Ren, M. Kanezashi, H. Nagasawa, T. Tsuru, Preparation of organosilica membranes on hydrophobic intermediate layers and evaluation of gas permeation in the presence of water vapor, J. Membr. Sci., 496 (2015) 156-164.

[23] C.W. Jones, W.J. Koros, Carbon molecular sieve gas separation membranes-I. Preparation and characterization based on polyimide precursors, Carbon, 32 (1994) 1419-1425.

[24] T. Araújo, G. Bernardo, A. Mendes, Cellulose-based carbon molecular sieve membranes for gas separation: a review, Molecules, 25 (2020) 3532.

[25] M. Rungta, G.B. Wenz, C. Zhang, L. Xu, W. Qiu, J.S. Adams, W.J. Koros, Carbon molecular sieve structure development and membrane performance relationships, Carbon, 115 (2017) 237-248.

[26] A. Shelekhin, A. Dixon, Y. Ma, Theory of gas diffusion and permeation in inorganic molecular‐sieve membranes, AlChE J., 41 (1995) 58-67.

[27] H.R. Lee, M. Kanezashi, Y. Shimomura, T. Yoshioka, T. Tsuru, Evaluation and fabrication of pore‐size‐tuned silica membranes with tetraethoxydimethyl disiloxane for gas separation, AlChE J., 57 (2011) 2755-2765.

[28] T. Yoshioka, M. Kanezashi, T. Tsuru, Micropore size estimation on gas separation membranes: A study in experimental and molecular dynamics, AlChE J., 59 (2013) 2179-2194.

[29] L. Meng, M. Kanezashi, J. Wang, T. Tsuru, Permeation properties of BTESE–TEOS organosilica membranes and application to O2/SO2 gas separation, J. Membr. Sci., 496 (2015) 211-218.

[30] N. Moriyama, H. Nagasawa, M. Kanezashi, T. Tsuru, Selective water vapor permeation from steam/non-condensable gas mixtures via organosilica membranes at moderate-to-high temperatures, J. Membr. Sci., 589 (2019) 117254.

[31] P. Bernardo, E. Drioli, G. Golemme, Membrane gas separation: a review/state of the art, Ind. Eng. Chem. Res., 48 (2009) 4638-4663.

[32] T.C. Merkel, H. Lin, X. Wei, R. Baker, Power plant post-combustion carbon dioxide capture: An opportunity for membranes, J. Membr. Sci., 359 (2010) 126-139.

[33] Y. Dai, Q. Li, X. Ruan, Y. Hou, X. Jiang, X. Yan, G. He, F. Meng, Z. Wang, Fabrication of defect-free Matrimid® asymmetric membranes and the elevated temperature application for N2/SF6 separation, J. Membr. Sci., 577 (2019) 258-265.

[34] H.B. Park, J. Kamcev, L.M. Robeson, M. Elimelech, B.D. Freeman, Maximizing the right stuff: The trade-off between membrane permeability and selectivity, Science, 356 (2017) eaab0530.

[35] L.M. Robeson, Correlation of separation factor versus permeability for polymeric membranes, J. Membr. Sci., 62 (1991) 165-185.

[36] L.M. Robeson, The upper bound revisited, J. Membr. Sci., 320 (2008) 390-400.

[37] H. Nagasawa, T. Kagawa, T. Noborio, M. Kanezashi, A. Ogata, T. Tsuru, Ultrafast synthesis of silica-based molecular sieve membranes in dielectric barrier discharge at low temperature and atmospheric pressure, J. Am. Chem. Soc., 143 (2020) 35-40.

[38] M. Priske, M. Lazar, C. Schnitzer, G. Baumgarten, Recent applications of organic solvent nanofiltration, Chem. Ing. Tech., 88 (2016) 39-49.

[39] M. Mulder, J. Mulder, Basic principles of membrane technology, Springer science & business media, 1996.

[40] P. Silva, S. Han, A.G. Livingston, Solvent transport in organic solvent nanofiltration membranes, J. Membr. Sci., 262 (2005) 49-59.

[41] A. Buekenhoudt, F. Bisignano, G. De Luca, P. Vandezande, M. Wouters, K. Verhulst, Unravelling the solvent flux behaviour of ceramic nanofiltration and ultrafiltration membranes, J. Membr. Sci., 439 (2013) 36-47.

[42] P. Marchetti, M.F. Jimenez Solomon, G. Szekely, A.G. Livingston, Molecular separation with organic solvent nanofiltration: a critical review, Chem. Rev., 114 (2014) 10735-10806.

[43] Y. Marcus, The sizes of molecules—revisited, J. Phys. Org. Chem., 16 (2003) 398-408.

[44] C. Liu, G. Dong, T. Tsuru, H. Matsuyama, Organic solvent reverse osmosis membranes for organic liquid mixture separation: A review, J. Membr. Sci., 620 (2021) 118882.

[45] R.P. Lively, D.S. Sholl, From water to organics in membrane separations, Nature materials, 16 (2017) 276-279.

[46] C. Liu, R. Takagi, D. Saeki, L. Cheng, T. Shintani, T. Yasui, H. Matsuyama, Highly improved organic solvent reverse osmosis (OSRO) membrane for organic liquid mixture separation by simple heat treatment, J. Membr. Sci., 618 (2021) 118710.

[47] G. Dong, H. Nagasawa, M. Kanezashi, T. Tsuru, Experimental study and modeling of organic solvent reverse osmosis separations through organosilica membranes, AIChE J., 66 (2020) e16283.

[48] C. Liu, R. Takagi, T. Shintani, L. Cheng, K.L. Tung, H. Matsuyama, Organic liquid mixture separation using an aliphatic polyketone-supported polyamide organic solvent reverse osmosis (OSRO) membrane, ACS Appl. Mater. Interfaces, 12 (2020) 7586-7594.

[49] G. Dong, H. Nagasawa, L. Yu, M. Guo, M. Kanezashi, T. Yoshioka, T. Tsuru, Energy-efficient separation of organic liquids using organosilica membranes via a reverse osmosis route, J. Membr. Sci., 597 (2020) 117758.

[50] B. Farnand, H. Sawatzky, Preferential Adsorption and Selective Permeation of Alcohol/Hydrocarbon Mixtures in Reverse Osmosis, Sep. Sci. Technol., 23 (1988) 1667-1681.

[51] W. Adam, B. Luke, P. Meares, The separation of mixtures of organic liquids by hyperfiltration, J. Membr. Sci., 13 (1983) 127-149.

[52] S. Sourirajan, Separation of hydrocarbon liquids by flow under pressure through porous membranes, in, NATIONAL RESEARCH COUNCIL OF CANADA OTTAWA (ONTARIO) DIV OF APPLIED CHEMISTRY, 1964.

[53] Y. Fang, S. Sourirajan, T. Matsuura, Reverse osmosis separation of binary organic mixtures using cellulose acetate butyrate and aromatic polyamide membranes, J. Appl. Polym. Sci., 44 (1992) 1959-1969.

[54] C. Liu, L. Cheng, T. Shintani, H. Matsuyama, AF2400/polyketone composite organic solvent reverse osmosis membrane for organic liquid separation, J. Membr. Sci., 628 (2021) 119270.

[55] K. Kammermeyer, D.H. Hagerbaumer, Membrane separations in the liquid phase, AlChE J., 1 (1955) 215-219.

[56] J. Crespo, C. Brazinha, Fundamentals of pervaporation, in: Pervaporation, Vapour Permeation and Membrane Distillation, Elsevier, 2015, pp. 3-17.

[57] T. Tsuru, A. Sasaki, M. Kanezashi, T. Yoshioka, Pervaporation of methanol/dimethyl carbonate using SiO2 membranes with nano‐tuned pore sizes and surface chemistry, AlChE J., 57 (2011) 2079-2089.

[58] S.-L. Wee, C.-T. Tye, S. Bhatia, Membrane Separation Process—Pervaporation through Zeolite Membrane, Sep. Purif. Technol., 63 (2008) 500-516.

[59] P.D. Chapman, T. Oliveira, A.G. Livingston, K. Li, Membranes for the dehydration of solvents by pervaporation, J. Membr. Sci., 318 (2008) 5-37.

[60] Y.K. Ong, G.M. Shi, N.L. Le, Y.P. Tang, J. Zuo, S.P. Nunes, T.-S. Chung, Recent membrane development for pervaporation processes, Prog. Polym. Sci., 57 (2016) 1-31.

[61] A. Fredenslund, Vapor-liquid equilibria using UNIFAC: a group-contribution method, Elsevier, 2012.

[62] H.-J. Liaw, C.-L. Tang, J.-S. Lai, A model for predicting the flash point of ternary flammable solutions of liquid, Combust. Flame, 138 (2004) 308-319.

[63] 小松弘昌, 山下泰宏, 平井千里馬, 田中豊志, 久木隆男, メタノール-tert-ブチルアルコール-tert-ブチルメチルエーテルおよび水からなる四組の大気圧下における三成分系気液平衡データと tert-ブチルメチルエーテル-水-メタノールまたは tert-ブチルアルコール三成分系の 303K における液液平衡データ, 化学工学論文集, 24 (1998) 116-122.

[64] Y. Li, S. Wang, G. He, H. Wu, F. Pan, Z. Jiang, Facilitated transport of small molecules and ions for energy-efficient membranes, Chem. Soc. Rev., 44 (2015) 103-118.

----

[65] Y. Zhang, N. Wang, C. Zhao, L. Wang, S. Ji, J.-R. Li, Co (HCOO) 2-based hybrid membranes for the pervaporation separation of aromatic/aliphatic hydrocarbon mixtures, J. Membr. Sci., 520 (2016) 646-656.

[66] Y. Ma, J. Wang, T. Tsuru, Pervaporation of water/ethanol mixtures through microporous silica membranes, Sep. Purif. Technol., 66 (2009) 479-485.

[67] P.A. Kober, PERVAPORATION, PERSTILLATION AND PERCRYSTALLIZATION, J. Am. Chem. Soc., 39 (1917) 944-948.

[68] G. Tusel, H. Brüschke, Use of pervaporation systems in the chemical industry, Desalination, 53 (1985) 327-338.

[69] S.P. Nunes, K.-V. Peinemann, Membrane technology, Wiley Online Library, 2001.

[70] S.I. Semenova, H. Ohya, K. Soontarapa, Hydrophilic membranes for pervaporation: an analytical review, Desalination, 110 (1997) 251-286.

[71] K.-i. Okamoto, H. Kita, K. Horii, K.T. Kondo, Zeolite NaA membrane: preparation, single-gas permeation, and pervaporation and vapor permeation of water/organic liquid mixtures, Ind. Eng. Chem. Res., 40 (2001) 163-175.

[72] T. Uragami, T. Katayama, T. Miyata, H. Tamura, T. Shiraiwa, A. Higuchi, Dehydration of an ethanol/water azeotrope by novel organic− inorganic hybrid membranes based on quaternized chitosan and tetraethoxysilane, Biomacromolecules, 5 (2004) 1567-1574.

[73] W.Y. Chiang, Y.H. Lin, Properties of modified poly (vinyl alcohol) membranes prepared by the grafting of new polyelectrolyte copolymers for water–ethanol mixture separation, J. Appl. Polym. Sci., 86 (2002) 2854-2859.

[74] M. Rafik, A. Mas, M.F. Guimon, C. Guimon, A. Elharfi, F. Schue, Plasma‐modified poly (vinyl alcohol) membranes for the dehydrationof ethanol, Polym. Int., 52 (2003) 1222-1229.

[75] M.L. Gimenes, L. Liu, X. Feng, Sericin/poly (vinyl alcohol) blend membranes for pervaporation separation of ethanol/water mixtures, J. Membr. Sci., 295 (2007) 71-79.

[76] R. Jiraratananon, A. Chanachai, R. Huang, D. Uttapap, Pervaporation dehydration of ethanol–water mixtures with chitosan/hydroxyethylcellulose (CS/HEC) composite membranes: I. Effect of operating conditions, J. Membr. Sci., 195 (2002) 143-151.

[77] R. Huang, R. Pal, G. Moon, Pervaporation dehydration of aqueous ethanol and isopropanol mixtures through alginate/chitosan two ply composite membranes supported by poly (vinylidene fluoride) porous membrane, J. Membr. Sci., 167 (2000) 275-289.

[78] Y. Dong, L. Zhang, J. Shen, M. Song, H. Chen, Preparation of poly (vinyl alcohol)-sodium alginate hollow-fiber composite membranes and pervaporation dehydration characterization of aqueous alcohol mixtures, Desalination, 193 (2006) 202-210.

[79] S. Kalyani, B. Smitha, S. Sridhar, A. Krishnaiah, Separation of ethanol− water mixtures by pervaporation using sodium alginate/poly (vinyl pyrrolidone) blend membrane crosslinked with phosphoric acid, Ind. Eng. Chem. Res., 45 (2006) 9088-9095.

[80] C.S. Hsu, R.M. Liou, S.H. Chen, M.Y. Hung, H.A. Tsia, J.Y. Lai, Pervaporation separation of a water–ethanol mixture by PSF–PEG membrane, J. Appl. Polym. Sci., 87 (2003) 2158-2164.

[81] S.-H. Chen, K.-C. Yu, S.-S. Lin, D.-J. Chang, R.M. Liou, Pervaporation separation of water/ethanol mixture by sulfonated polysulfone membrane, J. Membr. Sci., 183 (2001) 29-36.

[82] M.Y. Hung, S.H. Chen, R.M. Liou, C.S. Hsu, J.Y. Lai, Pervaporation separation of a water/ethanol mixture by a sodium sulfonate polysulfone membrane, J. Appl. Polym. Sci., 90 (2003) 3374-3383.

[83] J.-H. Kim, K.-H. Lee, S.Y. Kim, Pervaporation separation of water from ethanol through polyimide composite membranes, J. Membr. Sci., 169 (2000) 81-93.

[84] H. Tsai, M. Hong, G. Huang, Y. Wang, C. Li, K. Lee, J. Lai, Effect of DGDE additive on the morphology and pervaporation performances of asymmetric PSf hollow fiber membranes, J. Membr. Sci., 208 (2002) 233-245.

[85] Y. Wang, Y. Tsai, K. Lee, J. Lai, Preparation and pervaporation performance of 3, 3‐bis [4‐(4‐aminophenoxy) phenyl] phthalide based polyimide membranes, J. Appl. Polym. Sci., 96 (2005) 2046-2052.

[86] J.W. Rhim, S.W. Lee, Y.K. Kim, Pervaporation separation of water−ethanol mixtures using metal‐ion‐exchanged poly (vinyl alcohol)(PVA)/sulfosuccinic acid (SSA) membranes, J. Appl. Polym. Sci., 85 (2002) 1867-1873.

[87] Z.-K. Xu, Q.-W. Dai, Z.-M. Liu, R.-Q. Kou, Y.-Y. Xu, Microporous polypropylene hollow fiber membranes: Part II. Pervaporation separation of water/ethanol mixtures by the poly (acrylic acid) grafted membranes, J. Membr. Sci., 214 (2003) 71-81.

[88] G. Zhang, H. Yan, S. Ji, Z. Liu, Self-assembly of polyelectrolyte multilayer pervaporation membranes by a dynamic layer-by-layer technique on a hydrolyzed polyacrylonitrile ultrafiltration membrane, J. Membr. Sci., 292 (2007) 1-8.

[89] G. Zhang, W. Gu, S. Ji, Z. Liu, Y. Peng, Z. Wang, Preparation of polyelectrolyte multilayer membranes by dynamic layer-by-layer process for pervaporation separation of alcohol/water mixtures, J. Membr. Sci., 280 (2006) 727-733.

[90] B. Naidua, M. Sairam, K. Raju, T. Aminabhavi, Pervaporation separation of water plus isopropanol mixtures using novel nanocomposite membranes of poly (vinyl alcohol) and polyaniline, J. Membr. Sci., 260 (2005) 142-155.

[91] Y. Xu, C. Chen, J. Li, Experimental study on physical properties and pervaporation performances of polyimide membranes, Chem. Eng. Sci., 62 (2007) 2466-2473.

[92] W.Y. Chiang, Y.H. Lin, Properties of modified polyacrylonitrile membranes prepared by copolymerization with hydrophilic monomers for water–ethanol mixture separation, J. Appl. Polym. Sci., 90 (2003) 244-250.

[93] S. Sommer, T. Melin, Performance evaluation of microporous inorganic membranes in the dehydration of industrial solvents, Chemical Engineering and Processing: Process Intensification, 44 (2005) 1138-1156.

[94] A. Van den Berg, L. Gora, J. Jansen, M. Makkee, T. Maschmeyer, Zeolite A membranes synthesized on a UV-irradiated TiO2 coated metal support: the high pervaporation performance, J. Membr. Sci., 224 (2003) 29-37.

[95] K. Tanaka, R. Yoshikawa, C. Ying, H. Kita, K.-i. Okamoto, Application of zeolite membranes to esterification reactions, Catal. Today, 67 (2001) 121-125.

[96] H. Van Veen, Y. Van Delft, C. Engelen, P. Pex, Dewatering of organics by pervaporation with silica membranes, Sep. Purif. Technol., 22 (2001) 361-366.

[97] A. Kittur, S. Kulkarni, M. Aralaguppi, M. Kariduraganavar, Preparation and characterization of novel pervaporation membranes for the separation of water–

----

isopropanol mixtures using chitosan and NaY zeolite, J. Membr. Sci., 247 (2005) 75-86.

[98] W. Zhang, G. Li, Y. Fang, X. Wang, Maleic anhydride surface-modification of crosslinked chitosan membrane and its pervaporation performance, J. Membr. Sci., 295 (2007) 130-138.

[99] A. Svang-Ariyaskul, R. Huang, P. Douglas, R. Pal, X. Feng, P. Chen, L. Liu, Blended chitosan and polyvinyl alcohol membranes for the pervaporation dehydration of isopropanol, J. Membr. Sci., 280 (2006) 815-823.

[100] K.K. Rao, M. Subha, M. Sairam, N. Mallikarjuna, T. Aminabhavi, Blend membranes of chitosan and poly (vinyl alcohol) in pervaporation dehydration of isopropanol and tetrahydrofuran, J. Appl. Polym. Sci., 103 (2007) 1918-1926.

[101] M.D. Kurkuri, U.S. Toti, T.M. Aminabhavi, Syntheses and characterization of blend membranes of sodium alginate and poly (vinyl alcohol) for the pervaporation separation of water+ isopropanol mixtures, J. Appl. Polym. Sci., 86 (2002) 3642-3651.

[102] X. Qiao, T.S. Chung, Diamine modification of P84 polyimide membranes for pervaporation dehydration of isopropanol, AlChE J., 52 (2006) 3462-3472.

[103] X. Qiao, T.-S. Chung, K. Pramoda, Fabrication and characterization of BTDA-TDI/MDI (P84) co-polyimide membranes for the pervaporation dehydration of isopropanol, J. Membr. Sci., 264 (2005) 176-189.

[104] F.P. Cuperus, R.W. van Gemert, Dehydration using ceramic silica pervaporation membranes—the influence of hydrodynamic conditions, Sep. Purif. Technol., 27 (2002) 225-229.

[105] J. Sekulić, M. Luiten, J. Ten Elshof, N. Benes, K. Keizer, Microporous silica and doped silica membrane for alcohol dehydration by pervaporation, Desalination, 148 (2002) 19-23.

[106] T. Gallego-Lizon, Y.S. Ho, L.F. dos Santos, Comparative study of commercially available polymeric and microporous silica membranes for the dehydration of IPA/water mixtures by pervaporation/vapour permeation, Desalination, 149 (2002) 3-8.

[107] A. Kittur, M. Kariduraganavar, U. Toti, K. Ramesh, T. Aminabhavi, Pervaporation separation of water–isopropanol mixtures using ZSM‐5 zeolite incorporated poly (vinyl alcohol) membranes, J. Appl. Polym. Sci., 90 (2003) 2441-2448.

[108] T. Peters, J. Fontalvo, M. Vorstman, N. Benes, R. Van Dam, Z. Vroon, E. van Soest-Vercammen, J. Keurentjes, Hollow fibre microporous silica membranes for gas separation and pervaporation: synthesis, performance and stability, J. Membr. Sci., 248 (2005) 73-80.

[109] T. Gallego-Lizon, E. Edwards, G. Lobiundo, L.F. dos Santos, Dehydration of water/t-butanol mixtures by pervaporation: comparative study of commercially available polymeric, microporous silica and zeolite membranes, J. Membr. Sci., 197 (2002) 309-319.

[110] M. Schleiffelder, C. Staudt-Bickel, Crosslinkable copolyimides for the membrane-based separation of p-/o-xylene mixtures, React. Funct. Polym., 49 (2001) 205-213.

[111] S.J. Lue, T.-h. Liaw, Separation of xylene mixtures using polyurethane—zeolite composite membranes, Desalination, 193 (2006) 137-143.

[112] H.-M. Guan, T.-S. Chung, Z. Huang, M.L. Chng, S. Kulprathipanja, Poly (vinyl alcohol) multilayer mixed matrix membranes for the dehydration of ethanol–water mixture, J. Membr. Sci., 268 (2006) 113-122.

[113] Y. Wang, T.S. Chung, H. Wang, S.H. Goh, Butanol isomer separation using polyamide–imide/CD mixed matrix membranes via pervaporation, Chem. Eng. Sci., 64 (2009) 5198-5209.

[114] Y. Wang, T.S. Chung, H. Wang, Polyamide–imide membranes with surface immobilized cyclodextrin for butanol isomer separation via pervaporation, AlChE J., 57 (2011) 1470-1484.

[115] K. Wegner, J. Dong, Y. Lin, Polycrystalline MFI zeolite membranes: xylene pervaporation and its implication on membrane microstructure, J. Membr. Sci., 158 (1999) 17-27.

[116] W. Yuan, Y. Lin, W. Yang, Molecular sieving MFI-type zeolite membranes for pervaporation separation of xylene isomers, J. Am. Chem. Soc., 126 (2004) 4776-4777.

[117] Q.-P. He, Y. Zou, P.-F. Wang, X.-m. Dou, MFI-Type Zeolite Membranes for Pervaporation Separation of Dichlorobenzene Isomers, ACS omega, 6 (2021) 8456-8462.

[118] C.P. Ribeiro, B.D. Freeman, D.S. Kalika, S. Kalakkunnath, Aromatic polyimide and polybenzoxazole membranes for the fractionation of aromatic/aliphatic hydrocarbons by pervaporation, J. Membr. Sci., 390 (2012) 182-193.

[119] C. Zhao, N. Wang, L. Wang, S. Sheng, H. Fan, F. Yang, S. Ji, J.R. Li, J. Yu, Functionalized metal‐organic polyhedra hybrid membranes for aromatic hydrocarbons recovery, AlChE J., 62 (2016) 3706-3716.

[120] A. Wolińska-Grabczyk, Effect of the hard segment domains on the permeation and separation ability of the polyurethane-based membranes in benzene/cyclohexane separation by pervaporation, J. Membr. Sci., 282 (2006) 225-236.

[121] R. Castro-Muñoz, F. Galiano, O. de la Iglesia, V. Fíla, C. Téllez, J. Coronas, A. Figoli, Graphene oxide–Filled polyimide membranes in pervaporative separation of azeotropic methanol–MTBE mixtures, Sep. Purif. Technol., 224 (2019) 265-272.

[122] B. Smitha, D. Suhanya, S. Sridhar, M. Ramakrishna, Separation of organic–organic mixtures by pervaporation—a review, J. Membr. Sci., 241 (2004) 1-21.

[123] Q. Zhang, J. Peng, K. Zhang, Separation of an azeotropic mixture of dimethyl carbonate and methanol via partial heat integration pressure swing distillation, Asia‐Pacific Journal of Chemical Engineering, 12 (2017) 50-64.

[124] P. Shao, R. Huang, Polymeric membrane pervaporation, J. Membr. Sci., 287 (2007) 162-179.

[125] R.W. Baker, Membrane technology and applications, John Wiley & Sons, 2012.

[126] M. Zhou, M. Persin, J. Sarrazin, Methanol removal from organic mixtures by pervaporation using polypyrrole membranes, J. Membr. Sci., 117 (1996) 303-309.

[127] S.V. Kononova, Y.P. Kuznetsov, R. Apostel, D. Paul, H.H. Schwarz, New polymer multilayer pervaporation membrane, Die Angewandte Makromolekulare Chemie: Applied Macromolecular Chemistry and Physics, 237 (1996) 45-53.

[128] M. Ulbricht, H.-H. Schwarz, Novel high performance photo-graft composite membranes for separation of organic liquids by pervaporation, J. Membr. Sci., 136 (1997) 25-33.

[129] H.-H. Schwarz, R. Apostel, D. Paul, Membranes based on polyelectrolyte–surfactant complexes for methanol separation, J. Membr. Sci., 194 (2001) 91-102.

[130] H. Kita, K. Fuchida, T. Horita, H. Asamura, K. Okamoto, Preparation of Faujasite membranes and their permeation properties, Sep. Purif. Technol., 25 (2001) 261-268.

[131] P. Nian, C. Ma, H. Liu, J. Qiu, X. Zhang, High-performance Co-based ZIF-67 tubular membrane achieved by ZnO-induced synthesis for highly efficient pervaporation

----

separation of methanol/methyl tert-butyl ether mixture, Ind. Eng. Chem. Res., 58 (2019) 15297-15306.

[132] G. Dong, H. Nagasawa, L. Yu, Q. Wang, K. Yamamoto, J. Ohshita, M. Kanezashi, T. Tsuru, Pervaporation removal of methanol from methanol/organic azeotropes using organosilica membranes: Experimental and modeling, J. Membr. Sci., 610 (2020) 118284.

[133] R. Kopeć, M. Meller, W. Kujawski, J. Kujawa, Polyamide-6 based pervaporation membranes for organic–organic separation, Sep. Purif. Technol., 110 (2013) 63-73.

[134] J.H. Chen, X.F. Dong, Y.S. He, Investigation into glutaraldehyde crosslinked chitosan/cardo-poly-etherketone composite membrane for pervaporation separation of methanol and dimethyl carbonate mixtures, RSC advances, 6 (2016) 60765-60772.

[135] L. Wang, J. Li, Y. Lin, C. Chen, Separation of dimethyl carbonate/methanol mixtures by pervaporation with poly (acrylic acid)/poly (vinyl alcohol) blend membranes, J. Membr. Sci., 305 (2007) 238-246.

[136] J.H. Chen, Q.L. Liu, A.M. Zhu, Q.G. Zhang, J. Fang, Pervaporation separation of MeOH/DMC mixtures using STA/CS hybrid membranes, J. Membr. Sci., 315 (2008) 74-81.

[137] M. Kludský, O. Vopička, P. Matějka, Š. Hovorka, K. Friess, Nafion® modified with primary amines: chemical structure, sorption properties and pervaporative separation of methanol-dimethyl carbonate mixtures, Eur. Polym. J., 99 (2018) 268-276.

[138] Q. Wang, L. Yu, H. Nagasawa, M. Kanezashi, T. Tsuru, High‐performance molecular‐separation ceramic membranes derived from oxidative cross‐linked polytitanocarbosilane, J. Am. Ceram. Soc., 103 (2020) 4473-4488.

[139] R. Huang, G. Moon, R. Pal, N-acetylated chitosan membranes for the pervaporation separation of alcohol/toluene mixtures, J. Membr. Sci., 176 (2000) 223-231.

[140] A.A. Bhat, V.G. Pangarkar, Methanol-selective membranes for the pervaporative separation of methanol–toluene mixtures, J. Membr. Sci., 167 (2000) 187-201.

[141] A.V. Penkova, A.I. Kuzminova, M.E. Dmitrenko, V.A. Surkova, V.P. Liamin, D.A. Markelov, A.V. Komolkin, D.Y. Poloneeva, A.V. Laptenkova, A.A. Selyutin, Novel pervaporation mixed matrix membranes based on polyphenylene isophtalamide modified by metal–organic framework UiO-66 (NH2)-EDTA for highly efficient methanol isolation, Sep. Purif. Technol., 263 (2021) 118370.

[142] D. Sapegin, S. Kononova, G. Gubanova, E. Kruchinina, N. Saprykina, E. Popova, E. Vlasova, Selective facilitated fixed-site carrier transport of methanol through sulfonated copolyimide pervaporation membranes for the separation of methanol/toluene mixtures, Sep. Purif. Technol., 236 (2020) 116274.

[143] S. Moulik, V. Bukke, S.C. Sajja, S. Sridhar, Chitosan-polytetrafluoroethylene composite membranes for separation of methanol and toluene by pervaporation, Carbohydrate polymers, 193 (2018) 28-38.

[144] A. Bottino, G. Capannelli, A. Comite, F. Ferrari, R. Firpo, S. Venzano, Membrane technologies for water treatment and agroindustrial sectors, Comptes Rendus Chimie, 12 (2009) 882-888.

[145] S. Gray, T. Tsuru, Y. Cohen, W.-J. Lau, Advanced materials for membrane fabrication and modification, CRC Press, 2018.

[146] G. Saracco, V. Specchia, Catalytic inorganic-membrane reactors: present experience and future opportunities, Catalysis Reviews—Science and Engineering, 36 (1994) 305-384.

[147] Z.Y. Li, H. Maeda, K. Kusakabe, S. Morooka, H. Anzai, S. Akiyama, Preparation of palladium-silver alloy membranes for hydrogen separation by the spray pyrolysis method, J. Membr. Sci., 78 (1993) 247-254.

[148] M.E. Ayturk, Y.H. Ma, Electroless Pd and Ag deposition kinetics of the composite Pd and Pd/Ag membranes synthesized from agitated plating baths, J. Membr. Sci., 330 (2009) 233-245.

[149] M.E. Ayturk, I.P. Mardilovich, E.E. Engwall, Y.H. Ma, Synthesis of composite Pd-porous stainless steel (PSS) membranes with a Pd/Ag intermetallic diffusion barrier, J. Membr. Sci., 285 (2006) 385-394.

[150] K. Sato, T. Nakane, A high reproducible fabrication method for industrial production of high flux NaA zeolite membrane, J. Membr. Sci., 301 (2007) 151-161.

[151] Y. Wang, H. Rong, L. Sun, P. Zhang, Y. Yang, L. Jiang, S. Wu, G. Zhu, X. Zou, Fabrication and evaluation of effective zeolite membranes for water desalination, Desalination, 504 (2021) 114974.

[152] S. Mourdikoudis, R.M. Pallares, N.T. Thanh, Characterization techniques for nanoparticles: comparison and complementarity upon studying nanoparticle properties, Nanoscale, 10 (2018) 12871-12934.

[153] D. Mendes, A. Mendes, L. Madeira, A. Iulianelli, J. Sousa, A. Basile, The water‐gas shift reaction: from conventional catalytic systems to Pd‐based membrane reactors—a review, Asia‐Pacific Journal of Chemical Engineering, 5 (2010) 111-137.

[154] H. Hsieh, Inorganic membranes for separation and reaction, Elsevier, 1996.

[155] S. Liguori, K. Kian, N. Buggy, B.H. Anzelmo, J. Wilcox, Opportunities and challenges of low-carbon hydrogen via metallic membranes, Prog. Energy Combust. Sci., 80 (2020) 100851.

[156] T. Peters, M. Stange, H. Klette, R. Bredesen, High pressure performance of thin Pd–23% Ag/stainless steel composite membranes in water gas shift gas mixtures; influence of dilution, mass transfer and surface effects on the hydrogen flux, J. Membr. Sci., 316 (2008) 119-127.

[157] F. Braun, A.M. Tarditi, J.B. Miller, L.M. Cornaglia, Pd-based binary and ternary alloy membranes: Morphological and perm-selective characterization in the presence of H2S, J. Membr. Sci., 450 (2014) 299-307.

[158] K.E. Coulter, J.D. Way, S.K. Gade, S. Chaudhari, G.O. Alptekin, S.J. DeVoss, S.N. Paglieri, B. Pledger, Sulfur tolerant PdAu and PdAuPt alloy hydrogen separation membranes, J. Membr. Sci., 405 (2012) 11-19.

[159] S. Nayebossadri, J. Speight, D. Book, Effects of low Ag additions on the hydrogen permeability of Pd–Cu–Ag hydrogen separation membranes, J. Membr. Sci., 451 (2014) 216-225.

[160] S. Hara, K. Sakaki, N. Itoh, H.-M. Kimura, K. Asami, A. Inoue, An amorphous alloy membrane without noble metals for gaseous hydrogen separation, J. Membr. Sci., 164 (2000) 289-294.

[161] T. Rostrup-Nielsen, Manufacture of hydrogen, Catal. Today, 106 (2005) 293-296.

[162] J. Bitter, Effect of crystallinity and swelling on the permeability and selectivity of polymer membranes, Desalination, 51 (1984) 19-35.

[163] Q. Song, S. Cao, R.H. Pritchard, B. Ghalei, S.A. Al-Muhtaseb, E.M. Terentjev, A.K. Cheetham, E. Sivaniah, Controlled thermal oxidative crosslinking of polymers of intrinsic

microporosity towards tunable molecular sieve membranes, Nature communications, 5 (2014) 1-12.

[164] T.A. Sherazi, Graft Polymerization, in: E. Drioli, L. Giorno (Eds.) Encyclopedia of Membranes, Springer Berlin Heidelberg, Berlin, Heidelberg, 2016, pp. 886-887.

[165] W.F. Yong, H. Zhang, Recent advances in polymer blend membranes for gas separation and pervaporation, Prog. Mater Sci., 116 (2021) 100713.

[166] S. Ravula, K.E. O'Harra, K.A. Watson, J.E. Bara, Poly (ionic liquid) s with Dicationic Pendants as Gas Separation Membranes, Membranes, 12 (2022) 264.

[167] W.J. Koros, G. Fleming, Membrane-based gas separation, J. Membr. Sci., 83 (1993) 1-80.

[168] S. Wang, X. Li, H. Wu, Z. Tian, Q. Xin, G. He, D. Peng, S. Chen, Y. Yin, Z. Jiang, Advances in high permeability polymer-based membrane materials for CO 2 separations, Energy Environ. Sci., 9 (2016) 1863-1890.

[169] G. Liu, W. Jin, Pervaporation membrane materials: Recent trends and perspectives, J. Membr. Sci., 636 (2021) 119557.

[170] X. Cao, K. Wang, X. Feng, Removal of phenolic contaminants from water by pervaporation, J. Membr. Sci., 623 (2021) 119043.

[171] D. Katarzynski, C. Staudt, Temperature-dependent separation of naphthalene/n-decane mixtures using 6FDA–DABA-copolyimide membranes, J. Membr. Sci., 348 (2010) 84-90.

[172] T. Wu, N. Wang, J. Li, L. Wang, W. Zhang, G. Zhang, S. Ji, Tubular thermal crosslinked-PEBA/ceramic membrane for aromatic/aliphatic pervaporation, J. Membr. Sci., 486 (2015) 1-9.

[173] A.F. Ismail, L. David, A review on the latest development of carbon membranes for gas separation, J. Membr. Sci., 193 (2001) 1-18.

[174] M. Hou, W. Qi, L. Li, R. Xu, J. Xue, Y. Zhang, C. Song, T. Wang, Carbon molecular sieve membrane with tunable microstructure for CO2 separation: Effect of multiscale structures of polyimide precursors, J. Membr. Sci., 635 (2021) 119541.

[175] R. Xu, L. He, L. Li, M. Hou, Y. Wang, B. Zhang, C. Liang, T. Wang, Ultraselective carbon molecular sieve membrane for hydrogen purification, Journal of Energy Chemistry, 50 (2020) 16-24.

[176] D.-Y. Koh, B.A. McCool, H.W. Deckman, R.P. Lively, Reverse osmosis molecular differentiation of organic liquids using carbon molecular sieve membranes, Science, 353 (2016) 804-807.

[177] J. Ramsay, S. Kallus, Zeolite membranes, in: Membrane Science and Technology, Elsevier, 2000, pp. 373-395.

[178] N. Rangnekar, N. Mittal, B. Elyassi, J. Caro, M. Tsapatsis, Zeolite membranes–a review and comparison with MOFs, Chem. Soc. Rev., 44 (2015) 7128-7154.

[179] I.G. Wenten, P.T. Dharmawijaya, P.T.P. Aryanti, R.R. Mukti, Khoiruddin, LTA zeolite membranes: current progress and challenges in pervaporation, RSC Advances, 7 (2017) 29520-29539.

[180] W. Raza, J. Wang, J. Yang, T. Tsuru, Progress in pervaporation membranes for dehydration of acetic acid, Sep. Purif. Technol., 262 (2021) 118338.

[181] J. Jiang, L. Wang, L. Peng, C. Cai, C. Zhang, X. Wang, X. Gu, Preparation and characterization of high performance CHA zeolite membranes from clear solution, J. Membr. Sci., 527 (2017) 51-59.

[182] S.M. Mirfendereski, J.Y. Lin, High-performance MFI zeolite hollow fiber membranes synthesized by double-layer seeding with variable temperature secondary growth, J. Membr. Sci., 618 (2021) 118573.

[183] J. Kuhn, S. Sutanto, J. Gascon, J. Gross, F. Kapteijn, Performance and stability of multi-channel MFI zeolite membranes detemplated by calcination and ozonication in ethanol/water pervaporation, J. Membr. Sci., 339 (2009) 261-274.

[184] Z. Wu, C. Zhang, L. Peng, X. Wang, Q. Kong, X. Gu, Enhanced Stability of MFI Zeolite Membranes for Separation of Ethanol/Water by Eliminating Surface Si–OH Groups, ACS Appl. Mater. Interfaces, 10 (2018) 3175-3180.

[185] D. Buso, K.M. Nairn, M. Gimona, A.J. Hill, P. Falcaro, Fast synthesis of MOF-5 microcrystals using sol− gel SiO2 nanoparticles, Chem. Mater., 23 (2011) 929-934.

[186] Q. Qian, P.A. Asinger, M.J. Lee, G. Han, K. Mizrahi Rodriguez, S. Lin, F.M. Benedetti, A.X. Wu, W.S. Chi, Z.P. Smith, MOF-based membranes for gas separations, Chem. Rev., 120 (2020) 8161-8266.

[187] W. Li, W. Wu, Z. Li, J. Shi, Y. Xia, Sol–gel asynchronous crystallization of ultra-selective metal–organic framework membranes for gas separation, Journal of Materials Chemistry A, 6 (2018) 16333-16340.

[188] Y. Peng, V. Krungleviciute, I. Eryazici, J.T. Hupp, O.K. Farha, T. Yildirim, Methane storage in metal–organic frameworks: current records, surprise findings, and challenges, J. Am. Chem. Soc., 135 (2013) 11887-11894.

[189] B. Chen, N.W. Ockwig, A.R. Millward, D.S. Contreras, O.M. Yaghi, High H2 adsorption in a microporous metal–organic framework with open metal sites, Angew. Chem. Int. Ed., 44 (2005) 4745-4749.

[190] Z. Liu, K. Zhang, Y. Wu, H. Xi, Effective enhancement on methanol adsorption in Cu-BTC by combination of lithium-doping and nitrogen-doping functionalization, J. Mater. Sci., 53 (2018) 6080-6093.

[191] M. Aroon, A. Ismail, T. Matsuura, M. Montazer-Rahmati, Performance studies of mixed matrix membranes for gas separation: A review, Sep. Purif. Technol., 75 (2010) 229-242.

[192] C.V. Funk, D.R. Lloyd, Zeolite-filled microporous mixed matrix (ZeoTIPS) membranes: Prediction of gas separation performance, J. Membr. Sci., 313 (2008) 224-231.

[193] S. Bertelle, T. Gupta, D. Roizard, C. Vallières, E. Favre, Study of polymer-carbon mixed matrix membranes for CO2 separation from flue gas, Desalination, 199 (2006) 401-402.

[194] D.Q. Vu, W.J. Koros, S.J. Miller, Mixed matrix membranes using carbon molecular sieves: I. Preparation and experimental results, J. Membr. Sci., 211 (2003) 311-334.

[195] J. Ahn, W.-J. Chung, I. Pinnau, M.D. Guiver, Polysulfone/silica nanoparticle mixed-matrix membranes for gas separation, J. Membr. Sci., 314 (2008) 123-133.

[196] S.-i. Nakao, T. Suzuki, T. Sugawara, T. Tsuru, S. Kimura, Preparation of microporous membranes by TEOS/O3 CVD in the opposing reactants geometry, Microporous Mesoporous Mater., 37 (2000) 145-152.

[197] T. Yamaguchi, X. Ying, Y. Tokimasa, B.N. Nair, T. Sugawara, S.-i. Nakao, Reaction control of tetraethyl orthosilicate (TEOS)/O 3 and tetramethyl orthosilicate (TMOS)/O 3 counter diffusion chemical vapour deposition for preparation of molecular-sieve membranes, PCCP, 2 (2000) 4465-4469.

[198] S.M. Lee, N. Xu, S.S. Kim, A. Li, J.R. Grace, C.J. Lim, T. Boyd, S.-K. Ryi, A. Susdorf, A. Schaadt, Palladium/ruthenium composite membrane for hydrogen separation from the off-gas of solar cell production via chemical vapor deposition, J. Membr. Sci., 541 (2017) 1-8.

----

[199] L.-S. Hong, Z.-L. Liu, Gas-to-particle conversion mechanism in chemical vapor deposition of silicon carbide by SiH4 and C2H2, Ind. Eng. Chem. Res., 37 (1998) 3602-3609.

[200] H. Nagasawa, Y. Yamamoto, N. Tsuda, M. Kanezashi, T. Yoshioka, T. Tsuru, Atmospheric-pressure plasma-enhanced chemical vapor deposition of microporous silica membranes for gas separation, J. Membr. Sci., 524 (2017) 644-651.

[201] D. Levy, M. Zayat, The Sol-Gel Handbook, 3 Volume Set: Synthesis, Characterization, and Applications, John Wiley & Sons, 2015.

[202] A. Lazaro, N. Vilanova, L.D. Barreto Torres, G. Resoort, I.K. Voets, H. Brouwers, Synthesis, polymerization, and assembly of nanosilica particles below the isoelectric point, Langmuir, 33 (2017) 14618-14626.

[203] M. Asaeda, S. Yamasaki, Separation of inorganic/organic gas mixtures by porous silica membranes, Sep. Purif. Technol., 25 (2001) 151-159.

[204] X. Ren, T. Tsuru, Organosilica-based membranes in gas and liquid-phase separation, Membranes, 9 (2019) 107.

[205] I. Agirre, P.L. Arias, H.L. Castricum, M. Creatore, E. Johan, G.G. Paradis, P.H. Ngamou, H.M. van Veen, J.F. Vente, Hybrid organosilica membranes and processes: Status and outlook, Sep. Purif. Technol., 121 (2014) 2-12.

[206] K. Li, Ceramic Membranes for Separation and Reaction, John Wiley & Sons, 2007.

[207] T. Tsuru, Silica-Based Membranes with Molecular-Net-Sieving Properties: Development and Applications, J. Chem. Eng. Jpn., 51 (2018) 713-725.

[208] K. Yamamoto, J. Ohshita, Bridged Polysilsesquioxane Membranes for Water Desalination, Polym. J., 51 (2019) 1103-1116.

[209] M.C. Duke, J.D. Da Costa, D.D. Do, P.G. Gray, G.Q. Lu, Hydrothermally robust molecular sieve silica for wet gas separation, Adv. Funct. Mater., 16 (2006) 1215-1220.

[210] J. Yu, H.-K. Lim, S. Lee, Transition-Metal Softener for High-Durability Hydrogen Separation Silica Membranes, J. Phys. Chem. C, 123 (2019) 25761-25768.

[211] H. Song, Y. Wei, H. Qi, Tailoring pore structures to improve the permselectivity of organosilica membranes by tuning calcination parameters, Journal of Materials Chemistry A, 5 (2017) 24657-24666.

[212] J. Campaniello, C.W. Engelen, W.G. Haije, P.P. Pex, J.F. Vente, Long-term pervaporation performance of microporous methylated silica membranes, Chem. Commun., (2004) 834-835.

[213] R. Xu, J. Wang, M. Kanezashi, T. Yoshioka, T. Tsuru, Reverse osmosis performance of organosilica membranes and comparison with the pervaporation and gas permeation properties, AIChE J., 59 (2013) 1298-1307.

[214] H. Zhang, D. He, S. Niu, H. Qi, Tuning the microstructure of organosilica membranes with improved gas permselectivity via the co-polymerization of 1, 2-bis (triethoxysilyl) ethane and 1, 2-bis (triethoxysilyl) methane, Int. J. Hydrogen Energy, 46 (2021) 17221-17230.

[215] N. Raman, C. Brinker, Organic "template" approach to molecular sieving silica membranes, J. Membr. Sci., 105 (1995) 273-279.

[216] N.K. Raman, M.T. Anderson, C.J. Brinker, Template-based approaches to the preparation of amorphous, nanoporous silicas, Chem. Mater., 8 (1996) 1682-1701.

[217] G. Li, M. Kanezashi, T. Tsuru, Preparation of organic–inorganic hybrid silica membranes using organoalkoxysilanes: The effect of pendant groups, J. Membr. Sci., 379 (2011) 287-295.

[218] H.L. Castricum, G.G. Paradis, M.C. Mittelmeijer‐Hazeleger, R. Kreiter, J.F. Vente, J.E. Ten Elshof, Tailoring the separation behavior of hybrid organosilica membranes by adjusting the structure of the organic bridging group, Adv. Funct. Mater., 21 (2011) 2319-2329.

[219] M. Kanezashi, Y. Yoneda, H. Nagasawa, T. Tsuru, K. Yamamoto, J. Ohshita, Gas permeation properties for organosilica membranes with different Si/C ratios and evaluation of microporous structures, AlChE J., 63 (2017) 4491-4498.

[220] R. Xu, S.M. Ibrahim, M. Kanezashi, T. Yoshioka, K. Ito, J. Ohshita, T. Tsuru, New insights into the microstructure-separation properties of organosilica membranes with ethane, ethylene, and acetylene bridges, ACS Appl. Mater. Interfaces, 6 (2014) 9357-9364.

[221] M. Guo, M. Kanezashi, H. Nagasawa, L. Yu, K. Yamamoto, T. Gunji, J. Ohshita, T. Tsuru, Tailoring the microstructure and permeation properties of bridged organosilica membranes via control of the bond angles, J. Membr. Sci., 584 (2019) 56-65.

[222] S.M. Ibrahim, R. Xu, H. Nagasawa, A. Naka, J. Ohshita, T. Yoshioka, M. Kanezashi, T. Tsuru, Insight into the pore tuning of triazine-based nitrogen-rich organoalkoxysilane membranes for use in water desalination, RSC Advances, 4 (2014) 23759-23769.

[223] M. Guo, Y. Zhang, R. Xu, X. Ren, W. Huang, J. Zhong, T. Tsuru, M. Kanezashi, Ultrahigh permeation of CO2 capture using composite organosilica membranes, Sep. Purif. Technol., 282 (2022) 120061.

[224] K. Yamamoto, H. Muragishi, T. Mizumo, T. Gunji, M. Kanezashi, T. Tsuru, J. Ohshita, Diethylenedioxane-bridged microporous organosilica membrane for gas and water separation, Sep. Purif. Technol., 207 (2018) 370-376.

[225] T. Mizumo, H. Muragishi, K. Yamamoto, J. Ohshita, M. Kanezashi, T. Tsuru, Preparation and separation properties of oxalylurea‐bridged silica membranes, Appl. Organomet. Chem., 29 (2015) 433-438.

[226] J. Ohshita, H. Muragishi, K. Yamamoto, T. Mizumo, M. Kanezashi, T. Tsuru, Preparation and separation properties of porous norbornane-bridged silica membrane, J. Sol-Gel Sci. Technol., 73 (2015) 365-370.

[227] L. Yu, M. Kanezashi, H. Nagasawa, J. Ohshita, A. Naka, T. Tsuru, Fabrication and microstructure tuning of a pyrimidine-bridged organoalkoxysilane membrane for CO2 separation, Ind. Eng. Chem. Res., 56 (2017) 1316-1326.

[228] M. Kanezashi, S. Miyauchi, S. Hayakawa, H. Nagasawa, T. Yoshioka, T. Tsuru, Propylene/propane permeation properties of metal-doped organosilica membranes with controlled network sizes and adsorptive properties, J. Jpn. Pet. Inst, 59 (2016) 140-148.

[229] M. Kanezashi, S. Miyauchi, H. Nagasawa, T. Yoshioka, T. Tsuru, Gas permeation properties through Al-doped organosilica membranes with controlled network size, J. Membr. Sci., 466 (2014) 246-252.

[230] X. Yang, S. Sheridan, L. Ding, D.K. Wang, S. Smart, J.C.D. da Costa, A. Liubinas, M. Duke, Inter-layer free cobalt-doped silica membranes for pervaporation of ammonia solutions, J. Membr. Sci., 553 (2018) 111-116.

[231] M. ten Hove, M.W. Luiten-Olieman, C. Huiskes, A. Nijmeijer, L. Winnubst, Hydrothermal stability of silica, hybrid silica and Zr-doped hybrid silica membranes, Sep. Purif. Technol., 189 (2017) 48-53.

[232] A. Darmawan, J. Motuzas, S. Smart, A. Julbe, J.C.D. da Costa, Binary iron cobalt oxide silica membrane for gas separation, J. Membr. Sci., 474 (2015) 32-38.

----

[233] H. Qi, J. Han, N. Xu, Effect of calcination temperature on carbon dioxide separation properties of a novel microporous hybrid silica membrane, J. Membr. Sci., 382 (2011) 231-237.

[234] M. Kanezashi, M. Asaeda, Stability of H2-permeselective Ni-doped silica membranes in steam at high temperature, J. Chem. Eng. Jpn., 38 (2005) 908-912.

[235] S. Battersby, S. Smart, B. Ladewig, S. Liu, M.C. Duke, V. Rudolph, J.C.D. da Costa, Hydrothermal stability of cobalt silica membranes in a water gas shift membrane reactor, Sep. Purif. Technol., 66 (2009) 299-305.

[236] T. Terao, H. Nagasawa, M. Kanezashi, H. Yanagishita, T. Tsuru, Controlled organosilica networks via metal doping for improved dehydration membranes with layered hybrid structures, Sep. Purif. Technol., 278 (2021) 119561.

[237] H. Zhang, Y. Wei, H. Qi, Palladium-niobium bimetallic doped organosilica membranes for H2/CO2 separation, Microporous Mesoporous Mater., 305 (2020) 110279.

[238] Y. Wei, H. Zhang, J. Lei, H. Song, H. Qi, Controlling pore structures of Pd-doped organosilica membranes by calcination atmosphere for gas separation, Chin. J. Chem. Eng., 27 (2019) 3036-3042.

[239] R. Igi, T. Yoshioka, Y.H. Ikuhara, Y. Iwamoto, T. Tsuru, Characterization of Co‐doped silica for improved hydrothermal stability and application to hydrogen separation membranes at high temperatures, J. Am. Ceram. Soc., 91 (2008) 2975-2981.

[240] P. Karakiliç, C. Huiskes, M.W. Luiten-Olieman, A. Nijmeijer, L. Winnubst, Sol-gel processed magnesium-doped silica membranes with improved H2/CO2 separation, J. Membr. Sci., 543 (2017) 195-201.

[241] H.F. Qureshi, R. Besselink, J.E. ten Elshof, A. Nijmeijer, L. Winnubst, Doped microporous hybrid silica membranes for gas separation, J. Sol-Gel Sci. Technol., 75 (2015) 180-188.

[242] H. Song, S. Zhao, J. Chen, H. Qi, Hydrothermally stable Zr-doped organosilica membranes for H2/CO2 separation, Microporous Mesoporous Mater., 224 (2016) 277-284.

[243] S.R. Batten, S.M. Neville, D.R. Turner, Coordination polymers: design, analysis and application, Royal Society of Chemistry, 2008.

[244] S. Kitagawa, R. Kitaura, S.i. Noro, Functional porous coordination polymers, Angew. Chem. Int. Ed., 43 (2004) 2334-2375.

[245] C. Janiak, J.K. Vieth, MOFs, MILs and more: concepts, properties and applications for porous coordination networks (PCNs), New J. Chem., 34 (2010) 2366-2388.

[246] C. Yang, Q. Wu, W. Xie, X. Zhang, A. Brozena, J. Zheng, M.N. Garaga, B.H. Ko, Y. Mao, S. He, Copper-coordinated cellulose ion conductors for solid-state batteries, Nature, 598 (2021) 590-596.

[247] M. Jia, X.-F. Zhang, Y. Feng, Y. Zhou, J. Yao, In-situ growing ZIF-8 on cellulose nanofibers to form gas separation membrane for CO2 separation, J. Membr. Sci., 595 (2020) 117579.

[248] S. Tanaka, K. Okubo, K. Kida, M. Sugita, T. Takewaki, Grain size control of ZIF-8 membranes by seeding-free aqueous synthesis and their performances in propylene/propane separation, J. Membr. Sci., 544 (2017) 306-311.

[249] J.E. Lofgreen, G.A. Ozin, Controlling morphology and porosity to improve performance of molecularly imprinted sol–gel silica, Chem. Soc. Rev., 43 (2014) 911-933.

Chapter 2

Metal-induced microporous aminosilica creates a highly permeable gas-separation membrane

2.1 Introduction

Microporous inorganic membrane technology has shown great potential for producing molecular separation barriers that will be more economically competitive than conventional techniques such as filtration, evaporation, crystallization, solvent extraction, or distillation [1-3]. Over the past few years, gas separation has become one of the most widely used industrial applications of microporous membranes that offer high levels of permeability and separation. The transport system for gas separation in microporous inorganic membranes is dominated by molecular sieving via affinity, which places a premium on the control of pore size in order to create accessibility for guest molecules through the pores and determine the adsorptive properties of the membrane matrix that accomplishes separation [4]. Microporous silica membranes are a type of inorganic membrane with advantages that include controllable pore size, excellent mechanical strength, and high hydrothermal and chemical stability [5, 6].

Several methods such as the organic template and spacer method in the case of SiO_2-based polymers were developed to design as well as control the formation of micropores that would be suitable for gas separation [6-9]. The organic template method is generally used to create changes in pore size through the removal of the template during the calcination of organic functional groups [10]. Another method for porosity control has been developed using bi-silyl precursors (with a linking unit as a spacer) for the fabrication of microporous organosilica membranes, where the formation of the membrane network is strongly influenced by the introduction of spacers into an ordinary silica network [11-13]. A notable example of pore size control when using the spacer method was explained using several organosilica precursors with different numbers of carbon elements between bi-silyl bridges. Studies have shown that bis-(triethoxysilyl)-methane (BTESM), bis-

----

(triethoxysilyl)-ethane (BTESE), and bis-(triethoxysilyl)-benzene (BTESB) have a rigid linking chain ($Si-CH_2-Si$, $Si-C_2H_4-Si$, and $Si-Ph-Si$). By contrast, bis-(triethoxysilyl)-propane (BTESP), bis-(trimethoxysilyl)-hexane (BTMSH), and bis-(triethoxysilyl)-octane (BTESO) with carbon linking units of C_3, C_6, and C_8, respectively, form a dense structure related to network flexibility [14]. Spacer units serve as the minimum unit in the construction of a loose organosilica framework, and the increased flexibility of the linking unit chain tends to generate a denser structure that is not suitable for the creation of a highly permeable membrane.

Porous coordination polymers such as a metal organic framework (MOF) have recently been developed and can be characterized by the repeating coordination interactions that occur between metal receptors and ligands that form 1D, 2D, and 3D networks [7, 15, 16]. During the synthesis of coordination polymers, metal ions create interactions with ligands as crosslinkers, and form polymers with structures that feature a high-dimensional framework, a tailorable pore structure, and a large specific surface area. On the other hand, the higher dimensional structure of a porous coordinated polymer exhibits a more rigid framework that tends to form interfacial defects between the crystal structures, which results in a risk of reducing the selectivity of gas separation and makes it difficult to produce uniform film [17]. By following the concept of a MOF (metal–linker interactions form nanospaces), we attempted a novel process to control the pore size of amorphous amine-enriched silica via sol-gel processing followed by coordination.

Several studies on metal-doped organosilica have been carried out to increase membrane selectivity [18-21]. The mechanism for increasing selectivity involves the formation of covalent bonding with a siloxane network, which results in a denser membrane structure so that the separation factor between the different sizes of gases becomes higher. This was exemplified in experimental work undertaken by doping a porous BTESE precursor with zirconium, and the conclusion was that the addition of zirconium caused densification due to structural relaxation via limited diffusion [20]. The same result was reported in a study where the presence of doped cobalt caused decreased flux in a membrane when the metal content had been increased [21]. Even though the selectivity was increased due to

the small pore size, side effects included a decrease in the permeating flux and an increase in the activation energy. Apart from that, the amorphous nature of organosilica membranes confers great advantages in flexibility and produces fewer of the defects that are inevitable in membranes composed of crystalline materials such as zeolite and MOF. Therefore, organosilica membranes enable specific gas molecules to pass through while maintaining selectivity for gas separation.

Based on these observations, a hybrid framework consisting of an ordered structure from coordinated polymers and an amorphous structure from the organosilica network could be an alternative way to obtain both a higher permeating flux and selectivity for molecules with similar radii and properties [22]. In this study, we propose a new strategy of using metal-amine coordination to control the microporosity of silica-based amorphous networks. To the best of our knowledge, silica-based coordination polymers have not been reported. The amine groups in the linking units of bis [3-(trimethoxysilyl) propyl] amine (BTPA) were used as Lewis-base molecules (ligand) and transition metals acted as electron-pair acceptors, or Lewis acids. The addition of metal generated subnanopores via the coordination of covalent bonds increased the crosslinking between network layers, which converted the texture of the membrane from non-porous to a microporous aminosilica via the formation of more rigid linking units. In this research, silver, copper, and nickel were used as metal receptors with different coordination affinities that could form interactions with the secondary amine groups on BTPA molecules.

2.2 Experimental

2.2.1 Synthesis of bis [3-(trimethoxysilyl) propyl] amine (BTPA) and bis-(trimethoxysilyl)-hexane (BTMSH)

Aminosilica sol was prepared via the hydrolysis and condensation of aminosilica (BTPA) precursors in ethanol, and the reaction was catalyzed by exposure to nitric acid for 12 hours at room temperature. A mixture of water and nitric acid as a catalyst, was added into BTPA and ethanol under vigorous stirring.

The final molar ratio of BTPA/H_2O/HNO_3 was 1/300/1 and pure ethanol was used to adjust the BTPA concentration to 5 wt%. In this experiment, bis-(trimethoxysilyl)hexane (BTMSH) was used as a control group to confirm the formation of uncoordinated metal doping. As shown in Fig. 2-1, BTPA and BTMSH are similar in structure, and the only difference is the existence of the amine moieties in BTPA. BTMSH was synthezised in the manner of the preparation of BTPA sol, in order to achieve a clear comparison for both types of precursors.
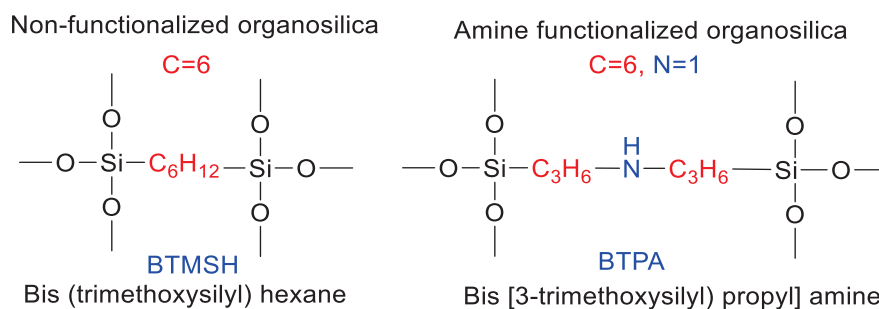
Fig. 2-1. The chemical structure of non-functionalized and amine-functionalized organoalkoxysilane precursors

2.2.2 Synthesis of metal-doped BTPA and BTMSH

$AgNO_3$, $Cu(NO_3)_2 \cdot 3H_2O$, and $Ni(NO_3)_2 \cdot 6H_2O$ were used as metal dopant to create different degrees of coordination with secondary aminosilica precursor. Metal-doped colloidal sols were prepared by adding dissolved metal salts into a BTPA sol with a stoichiometric metal/amine mole ratio of 0.25 (mol/mol) under vigorous stirring. The concentration of metal-doped BTPA sols was maintained at 5 wt% during preparation and was diluted at 0.1 wt% using pure water for membrane fabrication. Ni-BTMSH was also synthesized using the same parameters as metal-doped BTPA in order to obtain a comparative analysis of the coordinated components.

2.2.3 Characterization of metal-doped BTPA

The electronic interaction between metal receptors and amine donor electrons was examined using an Ultraviolet-visible spectrometer (UV-570,

JASCO, Japan). Functional groups of BTPA and metal-doped BTPA were identified using an FT-IR Spectrometer (FT/IR-4100, JASCO, Japan) with a wavenumber that ranged from 4000 – 500 cm^{-1}. Metal-doped aminosilica sols were coated onto KBr plates and then calcined at various temperatures under a N_2 atmosphere to evaluate the thermal stability of amines in coordination with metal prior to the decomposition of these moieties. X-ray photoelectron spectroscopy (JEOL RE series JES-RE1X ESR spectrometer) was used to investigate the different environments of amine sites after the addition of a transition metal, and to examine their bonding energy. All samples were prepared by coating the sols onto the surface of a silicon wafer via spin-coating (2,500 rpm), followed by calcination at 250 ⁰C under a N_2 atmosphere. The samples were kept in a dry vacuum oven overnight before the measurement.

Metal-doped aminosilica gel powder was prepared by drying at 50 ⁰C before thermal calcination at a different temperature under an inert atmosphere. The microstructure of the xerogel powder was characterized using an X-Ray diffraction D2 PHASER, (Bruker, Germany) with Cu-Kα radiation at a scanning range of 5⁰ to 80⁰. Morphology and different microstructure formations between coordinated and uncoordinated metal ions with amino moieties were characterized using a Transmission Electron Microscope (TEM JEOL2010 Ltd., Japan). A small amount of the sample powder was pulverized and transferred into a Cu microgrid. BTPA and metal-BTPA powder were calcined at 250 ⁰C under a N_2 atmosphere and thereafter evacuated at 150 ⁰C under vacuum conditions for 12 hours before the N_2 and CO_2 sorption measurement (BELMAX JAPAN Inc., Japan). Membranes cross-section morphology were characterized using Field Emission Scanning Electron Microscope (FE-SEM, JSM-7800F, JEOL).

2.2.4 Fabrication of metal-doped BTPA membranes and gas permeation measurement

Metal-doped aminosilica membranes were fabricated in a manner similar to that of organosilica membranes using porous α-alumina tubes as a membrane support with 50% porosity and an average pore size of 1 μm (length, 100 mm; inner

diameter, 8 mm; outer diameter, 10 mm), as supplied by Nikkato Corporation (Japan) [23, 24]. First, porous α-Al_2O_3 particle layers were developed from α-alumina particles mixed with 2 wt% SiO_2-ZrO_2 sol as a binder and subsequently calcined at 550 ⁰C under an air atmosphere for 15 minutes. The second porous layer had an average pore size of about 0.6 nm made by coating a 0.5 wt% SiO_2-ZrO_2 sol onto the surface of the particle layer and firing under an air atmosphere at 550 ⁰C as an intermediate layer. The topmost separation layer of metal-doped BTPA was formed with a wipe-coating of 0.1 wt% sol followed by calcination at 250 ⁰C under a N_2 atmosphere for 30-60 minutes.

Single-gas permeation measurement was conducted using the experimental setup schematically depicted in Fig. S2-1. High-purity gas such as He (kinetic diameter: 0.26 nm), H_2 (0.29 nm), CO_2 (0.33 nm), N_2 (0.36 nm), CH_4 (0.38 nm), CF_4 (0.48 nm), and SF_6 (0.55 nm) were fed to the outside of the membrane using an upstream pressure at 200- 400 kPa, while the permeate stream inside the system was maintained at atmospheric pressure (the pressure drop across the membrane was approximately 1 bar). The fresh membrane was pretreated at 200 ⁰C under a He flow of 50 cm^3 min^{-1} for at least 6 hours to remove any adsorbed molecules such as water from the surface of the membrane. The permeation test was conducted at temperatures ranging from 200 – 50 ⁰C and the permeation rate data were recorded when the membrane reached a steady state.

2.3 Results and Discussion

2.3.1 Metal addition and the effect on the physical and microstructure properties of aminosilica

In the present study, spectrometric data were collected and compiled to confirm the formation of coordinated interactions between transition metals and free electrons originating from the amine functionality of BTPA molecules. Fig. 2-2(a) shows that doping with metal ions shifted the highest absorption peak of approximately 212 nm to a higher wavelength, which corresponded to the different free-electron transitions of the amine groups (n → σ*) in the UV light range.

--- --
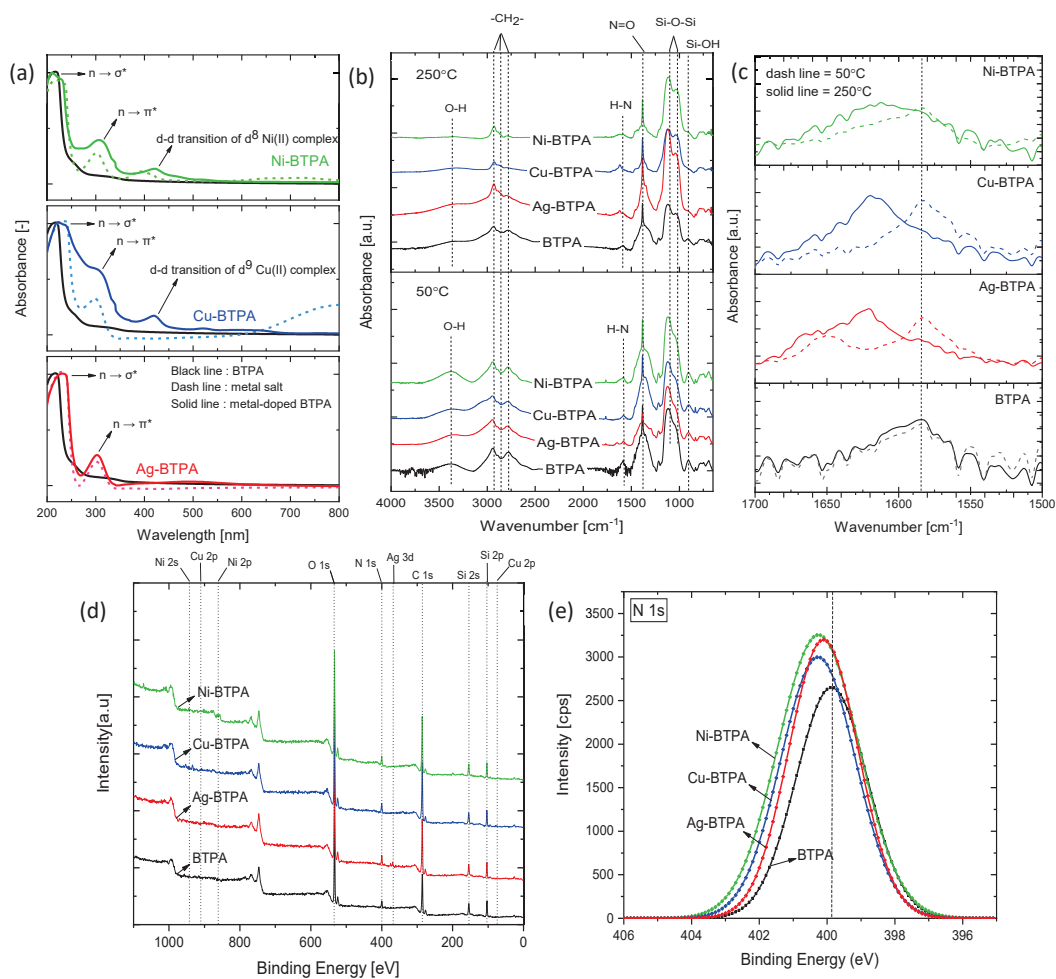
Fig. 2-2. UV-Vis absorption spectra of BTPA, metal salt and metal-doped BTPA (a). Infrared spectra in the range of $600 - 4000$ cm^{-1} for BTPA, Ag-BTPA, Cu-BTPA, Ni-BTPA at two stages of the calcination (b), higher magnification for NH deformation band in the range $1700 - 1500$ cm^{-1} (c). XPS spectra originating from BTPA and metal-doped BTPA wafer calcined at 250 ºC under inert atmosphere, survey spectra (d), and N (1s) high-resolution spectra (e).

Transition peaks that reflect coordination interactions between metals and ligands were observed in the range of visible light for Cu (d^9) and Ni (d^8) complexes through the presence of new peaks at a higher wavelength, but the Ag-(d^{10} = fully filled d orbital) complex showed no absorption peak at this range, because the resultant solution is colorless. NH (amine) groups are strong field ligands due to strong σ bond electron donor properties, and, therefore, it is easy to generate electrostatic interaction with metal-ion d orbitals [25, 26]. Cu and Ni generate coordinated covalent bonding to NH via a lone pair of electrons in the π electron system, and this type of electron delocalization weakens the donor properties of the ligand, which results in an appearance of the new absorption peak

at a higher wavelength (~420 nm), which can be attributed to the d-d transition of metal (II)-BTPA complexes [27, 28]. UV-Vis characterization has provided evidence that the metal-doping process forms crosslinks between metal and amine moieties that can be described as Lewis acid-base interactions.

Fig. 2-2(b) shows the FT-IR spectra of BTPA and metal-doped BTPA films that were coated onto the surface of KBr plates and calcined at different temperatures. All BTPA sols doped with different metals exhibited the vibration that is typical of functional groups that are similar to a pure BTPA sol. A higher calcination temperature increased the formation of siloxane bands (1,025-1,110 cm^{-1}) and decreased the silanol bands (909 cm^{-1}), which resulted in a higher level of siloxane connectivity [29]. In addition, the NH deformation band (1,591 cm^{-1}) of metal-doped BTPA was shifted to a higher wavenumber (~1,617 – 1,623 cm^{-1}) and the peak shape was broadened after calcination at a higher temperature of 250 °C (Fig. 2-2(c)). The shifting of the N-H band after calcination at 250 °C could be an indication of the coordination interaction between amine nitrogen atoms and metal ions, whereas the intensity of the N-H deformation band was changed after the formation of a metal complex [26, 30]. The coordination between a doped metal and the amine groups of BTPA molecules was observed more clearly after calcination temperature was raised to 250 °C probably due to reactions including hydrolysis, condensation, and coordination, which involved dynamic processes. Without calcination, reactions such as hydrolysis and condensation of the alkoxysilanes predominated because of the involvement of water and a nitric acid catalyst. Nevertheless, following calcination 250 °C, the coordination reaction became more dominant due to evaporation of the water and catalyst.

XPS characterization was conducted to examine the covalence bonding to the metal center in an aminosilica ligand binding environment [31]. Fig. 2-2(d) features the survey spectra for the sample before and after the metal doping process under a calcination temperature of 250 °C. The existence of metal peaks can be detected in certain orbitals, whereas the interaction of BTPA molecules with metals are apparent via the N (1s) orbital peak that reflects the contribution interaction of the amine moiety against metal receptors (Fig. 2-2(e)). A higher metal affinity generated an increase in the covalence bonding characteristics that led to an

increase in the density of the electrons on metal atoms but a decrease in the donor atoms of the ligand. Consequently, as the covalence interactions of donor-acceptor components increased, the peak of N (1s) that was attributed to an increase in the shift of donor atoms (ligand) to a higher binding energy (eV) [32, 33]. The electronic transition (UV-Vis), the upshifted frequency of NH deformation mode (FT-IR), and nitrogen N(1s) line analysis (XPS) all were consistent, which suggests coordination between organosilica-based NH (amino functional groups) and metal, as summarized in Table 2-1.

Table 2-1. UV-Vis electronic charge-transfer, FT-IR frequency of N-H deformation band, and N (1s) photoemission data that verified the formation of metal-amine interactions

Compound	UV-Visible		FTIR ν_{NH} [cm^{-1}]	XPS N (1s) Binding Energy [eV]
	Wavelength of absorption [nm]	Transition		
BTPA	212	n $\rightarrow$ σ^* (N-H)	1591	399.8
Ag-BTPA	234	n $\rightarrow$ σ^* (N-H)	1617	400.1
	303	n $\rightarrow$ π^* (N=O)		
Cu-BTPA	235	n $\rightarrow$ σ^* (N-H)	1618	400.3
	297	n $\rightarrow$ π^* (N=O)		
	420	d $\rightarrow$ d (d^9 Cu(II))		
Ni-BTPA	229	n $\rightarrow$ σ^* (N-H)	1623	400.5
	309	n $\rightarrow$ π^* (N=O)		
	421	d $\rightarrow$ d (d^8 Ni(II))		

In general, microporous silica membranes prepared using colloidal sols consist of a bimodal pore size distribution of both intraparticle and interparticle pores [9]. Intraparticle pores are formed as siloxane networks via interactions between atoms such as those in the Si-O-Si skeleton, whereas interparticle pores are the product of void spaces among the packed particles [34]. Therefore, it is necessary to optimize the formation of stable metal-amine coordination that is suitable for gas separation by avoiding the establishment of metallic nanoparticles that form gaps between BTPA-derived silica as interparticle spaces. Fig. 2-3(a) features X-Ray diffractograms of BTPA and metal-doped BTPA at a calcination

temperature of 250 °C under a N_2 atmosphere. Silver, copper, and nickel were used as metal dopants with low, moderate, and high affinities, respectively. Following the metal-doping process, calcination at higher temperatures can produce metal nanoparticles, which generally determines the formation of large pores (i.e., interparticle pores). At 250 °C, the silver (II) nitrate began to decompose, which resulted in the formation of silver nanoparticles and was confirmed by 2θ values of 38.5, 44.4, 64.6, and 77.6°.
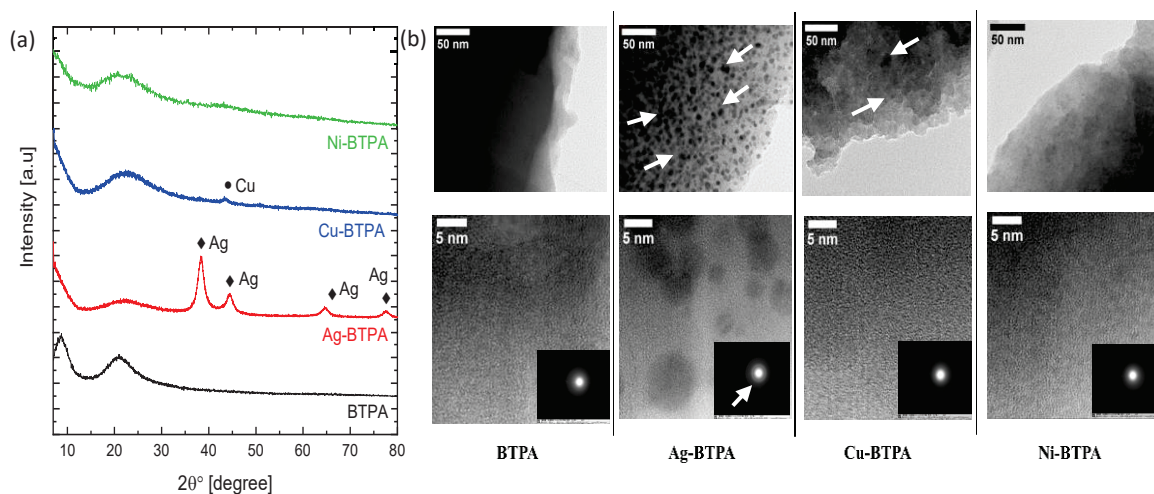
Fig. 2-3. XRD pattern of aminosilica xerogel powder calcined at 250 °C in N_2 atmosphere (a), and TEM photographs of BTPA and metal composite (b) (upper: low magnification at a scale of 50 nm, lower: higher magnification at a scale of 5 nm, insert: electron diffraction pattern).

The same result could be observed in Cu-BTPA, but the intensity of the copper nanoparticles was very small. On the other hand, Ni-BTPA showed different results—no nanoparticle peaks were observed, even though the calcination temperature was increased, as shown in Fig. 2-6(b). That figure shows only a broad peak that is similar to, or even broader than, that of a pure BTPA, which indicates the formation of a randomly oriented amorphous structure, suggesting that nickel was fully incorporated into the BTPA network and did not segregate into a crystalline structure that could be detected using X-ray Diffraction [35]. As the affinity of a metal dopant increases, a higher degree of coordination interaction develops and induces the formation of a stable compound in the metal-ion state. This result was observed in the amorphous Ni-BTPA structure when there is a high affinity for the metal-dopant, whereas a silver dopant with low affinity showed a

straightforward formation of nanoparticles, as characterized by a sharp crystalline peak.

TEM photographs describe the microstructure, dispersity, and aggregation characteristics [36]. As shown in Fig. 2-3(b), the TEM image of BTPA was transparent with a uniform surface and a halo electron diffraction pattern that reflected the formation of an amorphous phase in good agreement with the XRD results. By contrast, the addition of silver with a weak affinity to the amine group generated metal particles that were clearly visible as dark patches with a size of approximately 5 nm. The existence of uncoordinated silver tends to agglomerate and then generate a phase separation to form a crystalline structure following calcination at 250 ℃, which was also confirmed by a bright spot pattern with an additional white ring electron diffraction image. Cu-BTPA showed a homogenous distribution with a small number of dark spots, whereas Ni-BTPA showed no dark spots. In that case, a higher stabilization degree of Ni-doped BTPA sol was produced via electrostatic interaction between the metal ion with a higher affinity to the secondary amine group, which prohibited the formation of metal segregation. The evidence presented thus far supports the suggestion that an amorphous silica network had coordinated with metal via the amine moiety. Metals with a higher coordination affinity tend to generate a greater number of interactions that induce the reorganization of bridge amine chains so that the siloxane framework structurally rearranges to allow maximum coordination. Copper and nickel possibly form small clusters that give rise to a more rigid structure and higher levels of drying stress.

2.3.2 Pore textures induced by metal ion coordinated with amine sites

To confirm the formation of the permanent porosity that is generated by metal and amine coordination, gas sorption isotherms were performed. The microstructure properties of BTPA and metal-doped gel powder were evaluated via N_2 sorption isothermal testing at -196 ℃, as illustrated in Fig. 2-4(a). According to the IUPAC, BTPA powders are classified as an adsorption isotherm type II for non-porous material with a negligible amount of adsorbed N_2 (< 1 cc) [37]. These

results further suggest that BTPA is one of the organoalkoxysilane precursors that feature extremely flexible organic segments that fill the voids in a rigid Si-O-Si network following the sol-gel process, which consequently generates dense structure [14]. Following calcination at 250 ⁰C, the BTPA and metal-doped BTPA showed different types of adsorption curves. Following the addition of transition metal salts, the adsorption curves demonstrated types I- and IV microporous and mesoporous structures, respectively [37]. At very low relative pressure, the microporous structure exhibited a large capacity for nitrogen adsorption, while the mesoporous structure can be evaluated by the existence of a hysteresis loop at a higher relative pressure.
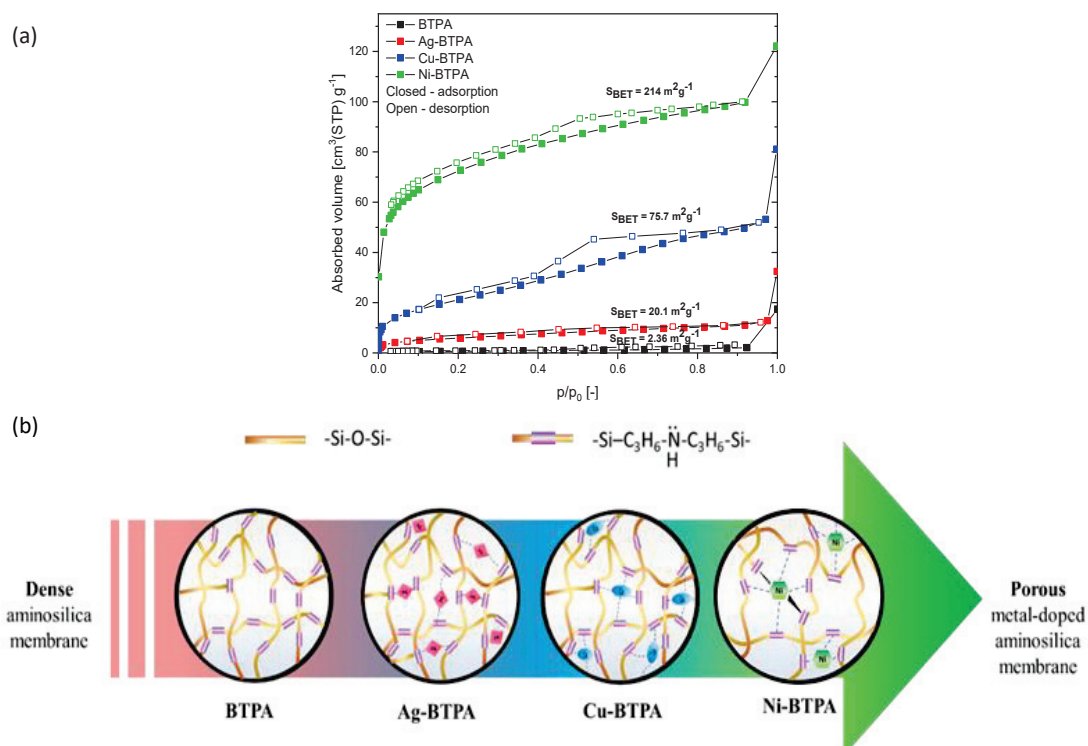
Fig. 2-4. N_2 adsorption-desorption isotherms for BTPA and metal-doped BTPA at -196 ⁰C, the xerogel powder was obtained at a calcination temperature of 250 ⁰C (a), and schematic image of the crosslink formation between metal receptor with a different coordination number and amine site as donor electron (b).

The Brunauer-Emmett-Teller (BET) surface area and total pore volume were determined from the N_2 sorption isothermal data, and t-plot analysis was used to determine the micropore volume of metal-doped BTPA. Based on the data shown in Table 2-2, the higher level of coordination by the transition metal generated a

greater amount of surface area and total pore volume. Based on XRD confirmation, at calcination temperatures of 250 ºC silver nanoparticles began to form, which suggested that an increase in surface area is also associated with the formation of interparticle pores. As expected, the percentage of micropores was increased with metal affinity, which confirmed an increase in the number of crosslinks and a microporous network. Ni-BTPA showed the greatest levels of surface area and total pore volume at 214 m^2 g^{-1} and 0.185 cm^3 g^{-1}, respectively.

Table 2-2 BET surface area and pore volume for BTPA and metal-doped BTPA

Metal doped-BTPA	S_{BET}[a] $(m^2\,g^{-1})$	Pore volume		% Microporosity
		V_{total}[b] $(cm^3\,g^{-1})$	V_{micro}[c] $(cm^3\,g^{-1})$	
BTPA	2.36	0.024	1.1×10^{-4}	0
Ag-BTPA	20.1	0.038	8.7×10^{-4}	2
Cu-BTPA	75.7	0.112	6.31×10^{-2}	56
Ni-BTPA	214	0.185	0.12	83

[a] The BET surface area; [b] the total pore volume; [c] the micropore volume

Porosity is believed to be created by the coordination between metal receptors and the donor electron pairs that originate from the amine groups inside BTPA molecules. As illustrated in Fig. 2-4(b), the higher metal affinity enables crosslinking via either the amine bridges or coordination of the neutral Lewis bases, which increases the number of interactions and generates arrangements that can be one-, two- or three-dimensional (Fig. 2-4(b)). Increased rigidity in the BTPA structure gives rise to a porous structure and a high surface area, which switches the gas transport mechanism from solution diffusion to molecular sieving, as will be discussed in 2.3.5 [38].

2.3.3 CO_2 adsorption of metal-doped BTPA

Fig. 2-5(a) compares the CO_2 sorption isotherms of pure BTPA and metal-doped BTPA dried gel powders measured at 25 ºC. In this measurement, dried gel powder was obtained at a calcination temperature of 250 ºC under an inert atmosphere. BTPA as a secondary aminosilica material exhibited a clear hysteresis

loop that correlated with the irreversible adsorption and desorption mechanisms of CO_2 gases inside free amine sites [39]. With a free amine as an adsorption site, the BTPA gel showed a higher level of CO_2 adsorption, that facilitated adsorption via a chemisorption mechanism by producing carbamate ions, as follows [40].

$$CO_2 + 2R_2NH \rightarrow R_2NCOO^- + RNH_2^+ \qquad (2\text{-}1)$$
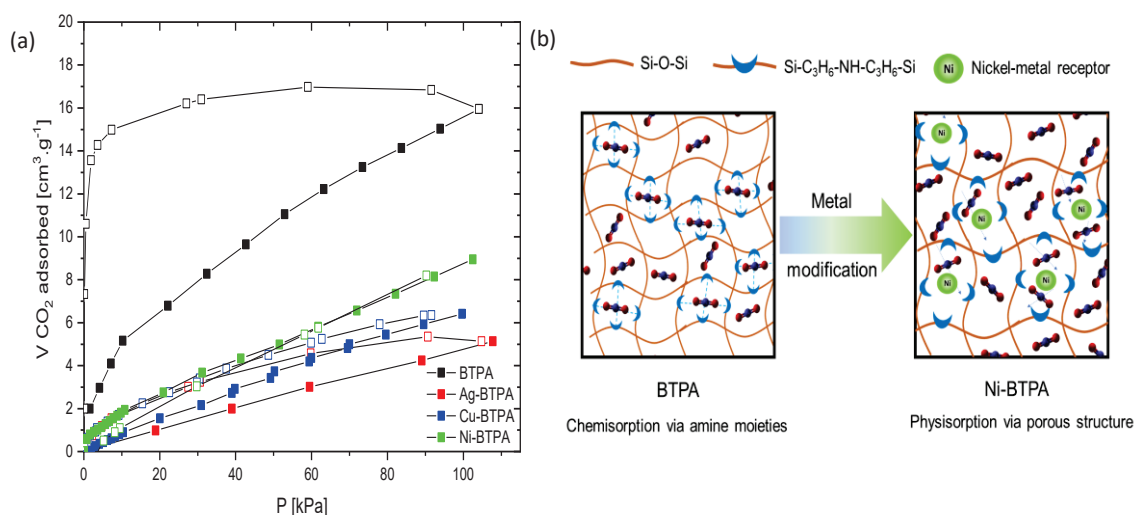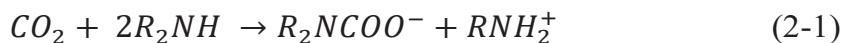
Fig. 2-5. CO_2 adsorption-desorption isotherms curve at 25 ⁰C for BTPA and metal-doped BTPA xerogel powder fired at 250 ⁰C under N_2 atmosphere (a), and schematic evolution of CO_2 transport inside BTPA and metal modified BTPA precursors with possible crosslink formation and their action of capturing CO_2 (b).

The stoichiometric mechanism of CO_2 transport by sterically hindered secondary amine groups is double that of the primary amine site, where one molecule of CO_2 can interact with two moles of an amine [41]. The isotherm curves for metal-doped BTPA show no saturation plateaus under high pressure and smaller loops or even no hysteresis for the order of Ag-BTPA > Cu-BTPA > Ni-BTPA, which indicates the complete removal of CO_2 as an adsorbed gas during the desorption process and tuning of the CO_2 adsorption mechanism to produce physical adsorption such as that seen in Henry sorption models [42, 43].

The CO_2 adsorption capacity was not only decided by an affinity for the material, but also by the existence of microporosity (pore volume and specific surface area) and the number of active adsorption sites (amine surface density). Even though Ag-BTPA shows the existence of a free amine site, the CO_2 adsorption exhibited the lowest level of capacity, and was associated with a weak coordination

interaction leading to the partial formation of coordination and nanoparticles as the temperature was increased to 250 ºC. As described, the CO_2 adsorption curve for Ni-BTPA and Cu-BTPA shows reversible and linear sorption isotherms, while a hysteresis loop could be observed for Ag-BTPA, indicating an irreversible adsorption-desorption mechanism on uncoordinated amines. So, it was reasonably suggested that Ag^+ partially existed in two different phases.

As schematically shown in Fig. 2-5(b), CO_2 gas transport inside the amine-modified silica matrix networks shows a chemical interaction whereas metal-doped BTPA exhibits physical adsorption. The coordination framework that was generated between the metal and amine groups induces transformation from a dense BTPA into a porous structure, which results in a CO_2 adsorption mechanism that is a reversible process. A large amount of energy is required for pure BTPA since the nucleophilic CO_2 gas attack via the free amine group leads to the formation of carbamate, which gives rise to a significant amount of additional operating costs [44]. However, the regeneration process for removing CO_2 at the surface of metal-doped aminosilica materials requires less consumption of energy.

2.3.4 Metal modification of amine- and non-functionalized organosilica precursors

Two types of organoalkoxysilane precursors were used to compare and analyze the different forms of coordination between amine and metal centers. BTMSH is a simple alkoxysilane that consists of a flexible organic bridge precursor without an amine functional group; like BTPA it has a very small N_2 adsorption capacity due to its flexible structure, as shown in Fig. 2-1 [14]. Both BTMSH and BTPA are type II, which indicates a non-porous structure (Fig.2-6(a)). Following the addition of metal, however, the surface area of a metal composite is increased, particularly for Ni-BTPA, while Ni-BTMSH displays only a small increase in the surface area, which likely is due to the formation of nickel nanoparticles. This argument was confirmed by the XRD pattern of Ni-BTMSH (Fig. 2-6(b)), which showed peaks for the formation of $Ni(OH)_2$, NiO, and Ni particles under higher calcination temperatures.
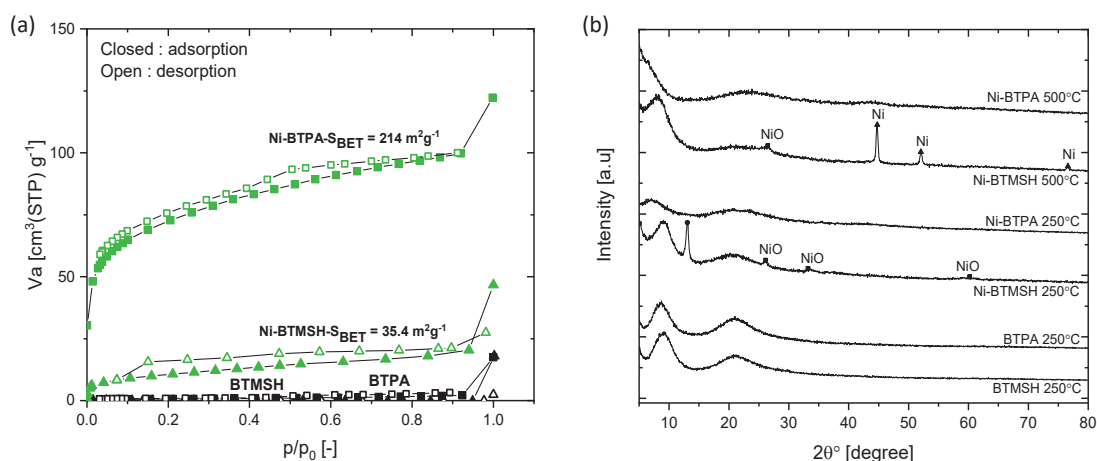
Fig. 2-6 N_2 sorption isotherms at -196 ℃ for non-functionalized organosilica (BTMSH), amine-functionalized organosilica precursors (BTPA) and Ni-doped silica gel fired at 250 ℃ (a), and XRD pattern of BTMSH, BTPA, and Nickel composite gel powder prepared at various calcination temperature (b).

The decomposition reaction of a nickel-metal salt is described by the following equations [45].

$$Ni(NO_3)_2 \cdot 6H_2O \rightarrow Ni(NO_3)_2 \cdot 3H_2O + 3H_2O \qquad (2\text{-}2)$$

$$Ni(NO_3)_2 \cdot 3H_2O \rightarrow Ni(NO_3)_2 \cdot 2H_2O + H_2O \qquad (2\text{-}3)$$

$$3Ni(NO_3)_2 \cdot 2H_2O \rightarrow Ni(OH)_2 \cdot Ni(NO_3)_2 \cdot 2H_2O + 2H_2O + 2HNO_3 \ (200℃) \qquad (2\text{-}4)$$

$$Ni(OH)_2 \cdot Ni(NO_3)_2 \cdot 2H_2O \rightarrow 3NiO + 3H_2O + 3O_2 + NO_2 \ (250℃) \qquad (2\text{-}5)$$

$$2NiO \rightarrow 2Ni + O_2 \ (500℃) \qquad (2\text{-}6)$$
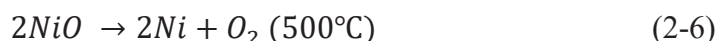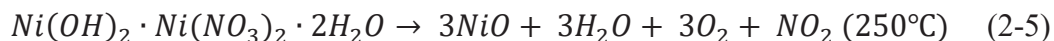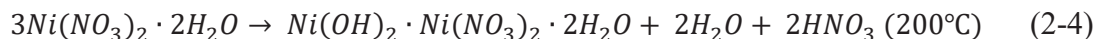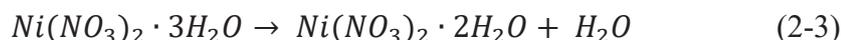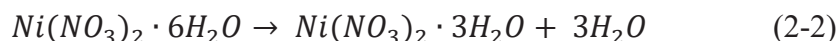
Ni-BTMSH is more likely to produce nickel nanoparticles, while the formation of nanoparticles has yet to be observed for Ni-BTPA at the same, or even higher temperature, which is further evidence of the coordination between BTPA and metal ions.

2.3.5 Gas permeation properties of metal-doped BTPA membranes

Fig. 2-7 shows the SEM cross-sectional images of thin-layer BTPA and Ni-BTPA membranes. Both membranes present a typical asymmetric structure consisting of an ultrathin top-most layer as a separation barrier conjoined with a SiO_2-ZrO_2 intermediate layer prepared on α-Al_2O_3 particles layer. Based on this SEM image, the thickness of the top-layer and intermediate layer were estimated to be approximately 235 – 275 nm without clear boundaries between the layers.

These results are similar to those reported by our research group, where the thickness of the combined layers was approximately 200 – 300 nm, and the separation layer was estimated to have a thickness that ranged from 13 to 50 nm [46, 47].
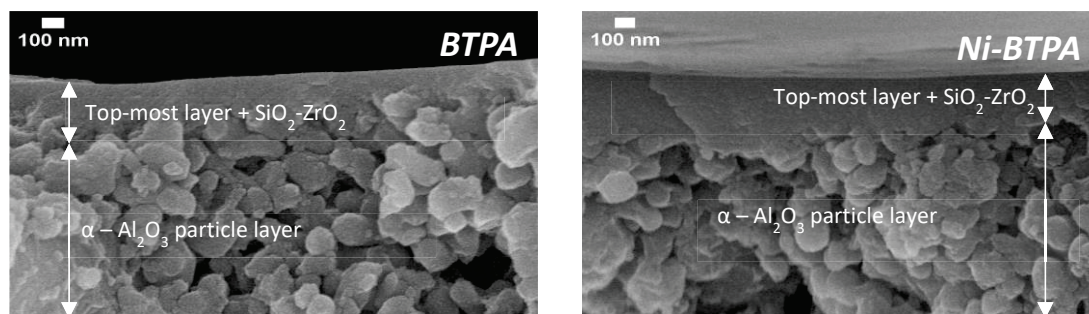
Fig. 2-7 The cross-sectional images for BTPA and Ni-BTPA consisting of a top-most layer as a separation barrier conjoined with a SiO_2-ZrO_2 intermediate layer with α-Al_2O_3 particles as a support layer.

Fig. 2-8 illustrates (a) single-gas permeance and (b) dimensionless permeance based on helium gas permeance at200 ℃ as a function of the molecular kinetic diameter. Fig. 2-8(c) illustrates the dependence of doped metals on gas permeance. All aminosilica membranes were fabricated at 250 ℃ under a N_2 atmosphere to avoid oxidation of the metal phase [48]. Single-gas permeance decreased as the molecular kinetic diameter increased, indicating a molecular sieving effect. Fig. 2-8(b) confirms that selectivity was much higher than that of Knudsen diffusion. As summarized in Fig. 2-8(c), following metal doping, the permeation of H_2 was increased from 7.13×10^{-7} mol m^{-2} s^{-1} Pa^{-1} (pure BTPA) to 4.45×10^{-6} mol m^{-2} s^{-1} Pa^{-1} (Ni-BTPA). Similar results were found for the permeance of gases such as He, CO_2, CH_4, and N_2. The increase in gas permeance can be ascribed to the formation of micropore structures on the order of Ni-BTPA > Cu-BTPA > Ag-BTPA > BTPA, which corresponds to the increased metal coordination affinity. The increase in metal affinity resulted in a greater degree of crosslinking with amine groups, a higher surface area of the metal-doped BTPA powders, and an enlarged network pore size that induce a higher rate of gas permeation in metal-doped BTPA membranes.
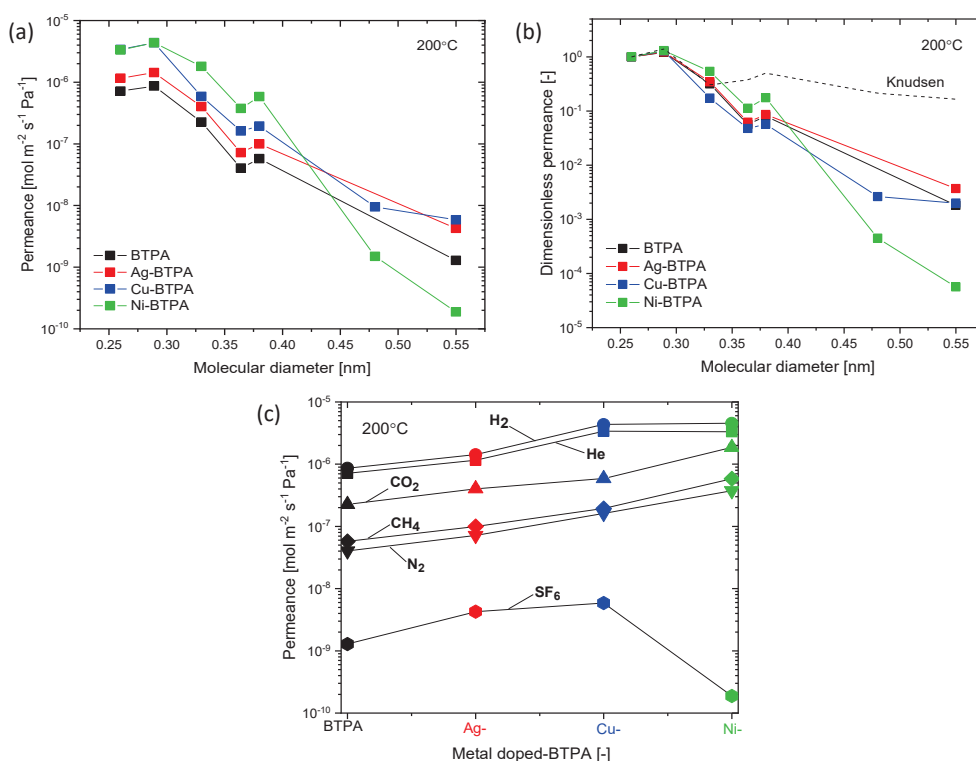
Fig. 2-8 Single gas permeance as a function of molecular size dependency (a), dimensionless permeance based on He permeance for BTPA and metal-doped BTPA measured at 200 ºC (b), and Gas permeance at 200 ºC as a function of metal affinity (c).

These findings indicate, and spectroscopy studies consistently show, a correlation between the structural properties of the materials and membrane performance. In contrast to the permeance of small gases, the permeance of SF_6 was sharply decreased after the addition of nickel-metal ions. This result suggests that the pore size distribution of nickel-doped BTPA is narrowly defined to within the range of the molecular sizes of N_2 (0.36 nm) and SF_6 (0.55 nm), and likely approximates that of SF_6 due to the high level of N_2 permeance. Ni-BTPA showed the most promising performance of H_2 and N_2 permeance at 4.45×10^{-6} and 3.75×10^{-7} mol $m^{-2} s^{-1} Pa^{-1}$ with higher selectivity for both H_2/SF_6 and N_2/SF_6 at 15,500 and 1,900, respectively. Ultrafine micropores are known to be induced by the crosslinking reactions among dense polyimide, which has resulted in gas separation performance that surpasses the trade-off lines [49]. The same concept was observed in this study as microporosity was created from a dense structure via crosslinking induced by the coordination of metals and electron-donor amines, resulting in higher porosity from the increase in membrane permeation.

Fig. 2-9 shows the correlation between the permeance ratio of He/SF_6 as a function of He/N_2 together with different types of microporous organosilica membranes such as BTESE, BTESA, and BTESB [4, 50, 51]. It should be noted that each plotted point corresponds to a different membrane indicating a reasonable reproducibility of permeation properties for metal-doped membranes. The solid curve illustrates the theoretical value that was calculated based on the modified gas translation (modified-GT model) equation for uniformly sized pores, as shown in Eq. (2-7) [4].
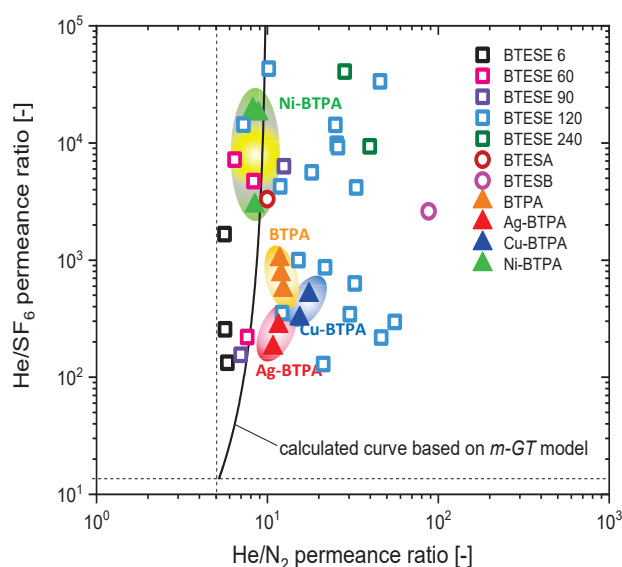
Fig. 2-9. The permeance ratio of He/SF_6 as a function of He/N_2 permeance ratio for different type of porous organosilica membranes (solid line : calculated curve that obtained based on modified gas translation model)

Microporous organosilica membranes generally show a comparatively scattered experimental relationship between the permeance ratio of He/N_2 and that of He/SF_6 due to the existence of micropores formed as network pores and larger pores that include defects from the grain boundaries. Ag-BTPA and Cu-BTPA both showed a lower permeance ratio of He/SF_6 and the corresponding He/N_2 ratio compared with the theoretical values. This can be ascribed to the possibility that after doping with low-affinity metals (Ag-, and Cu-), several larger pores were generated, which allowed SF_6 to permeate and resulted in a low permeance ratio for He/SF_6 and a broad pore-size distribution. Different results were observed for Ni-BTPA

----

membranes, which agreed well with the theoretical prediction curve at a high He/SF$_6$ ratio (He/SF$_6$ > 10,000). This result suggests that the formation of an ordered micropore framework from a fully coordinated amine-nickel interaction and the amorphous natural properties of organosilica generate a more uniform pore with a defect-free quality, which was also confirmed via both the m-GT model and the NLDFT analysis obtained by N$_2$ sorption calculation (Fig. S2-7 and S2-6 in the Supporting Information).

$$\alpha_{i/j} = \frac{P_i}{P_j} \approx \sqrt{\frac{M_j}{M_i}} \frac{(d_p - d_i)^3}{(d_p - d_i)^3} \tag{2-7}$$

$$P_{m-GT,i} = \frac{1}{3} \frac{\varepsilon}{\tau L} (d_p - d_i) \frac{(d_p - d_i)^2}{d_p^2} \sqrt{\frac{8}{\pi M_i RT}} \exp\left(-\frac{E_{P,i}}{RT}\right) \tag{2-8}$$

$$= \sqrt{\frac{k_{0,i}}{M_i RT}} \exp\left(-\frac{E_{P,i}}{RT}\right) \tag{2-9}$$

Fig. 2-10 shows the temperature dependence of single-gas permeance for metal-doped BTPA-derived membranes calcined at 250 ºC. The permeance of each gas is affected by the pore size distribution of the amorphous metal-doped aminosilica network [52]. The interaction between permeating molecules and the cylindrical microporous wall of the membranes was used to determine the activation energy based on the permeance equation of the modified gas translation model expressed in Eqs. (2-8) and (2-9) [53]. In that model, d_p, ε, τ, and L are membrane structural factors of the pore diameter, porosity, tortuosity, and thickness, respectively, while d_i is the kinetic diameter of permeating molecules, M_i is the molecular weight of the i component, R is the gas constant, and T is the absolute temperature. The activation energy for the permeating molecules ($E_{P,i}$) was obtained from the slope of the regression using Eq. 2-9 with the results of single-gas permeance measured at different temperatures [52, 54]. Most gas permeance values were increased when the temperature was elevated to a higher degree via the activated permeation mechanism. If there are defects in the structure of the membrane, the permeance of all gases larger than the defect sizes becomes high and follows Knudsen selectivity. The largest-sized permeating molecule of SF$_6$ was generally used to assess the existence of defects in the structure of the membrane. However, all metal-doped BTPA showed good

separation performance, particularly the Ni-BTPA version with H_2/SF_6 and N_2/SF_6 selectivities of 15,500 and 1,900, respectively, as an appropriate indicator of a defect-free membrane.
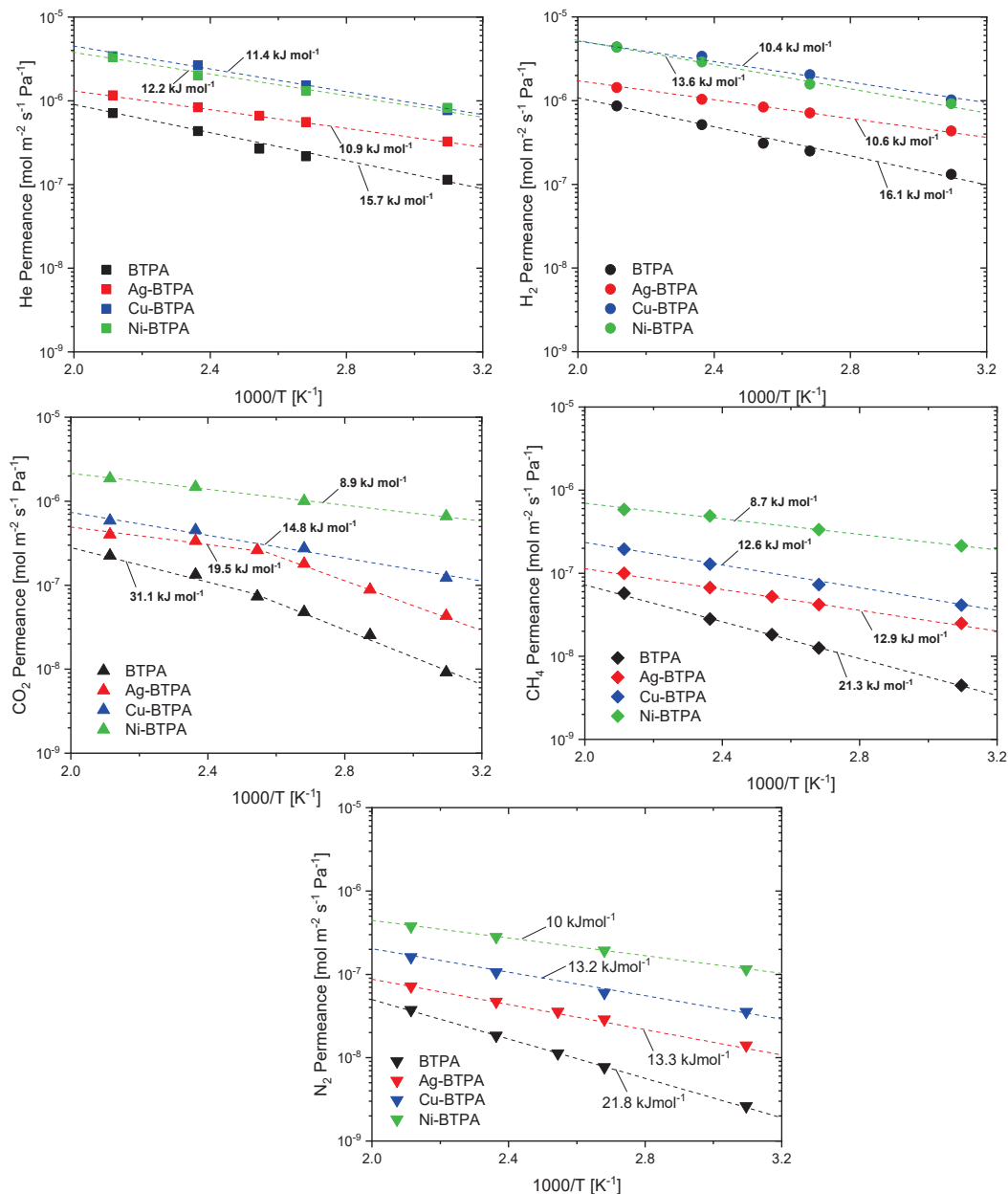
Fig. 2-10. Temperature dependence of gas permeance for BTPA and metal-doped BTPA membranes calcined at 250 ºC

What is interesting about the data in this experimental work is that a uniform and the defect-free thin layer was successfully deposited onto a porous substrate via a simple sol-gel process without sacrificing either high permeation or selectivity.

Compared with the results of most reported MOF membranes, where the formation of interfacial defects between intergrown MOF facilitates the rapid diffusion of most permeating gases resulting a significant decrease in selectivity [55-57].

The activation energy of each gas in the metal-doped aminosilica membrane is summarized in Table 2-3. The value of activation energy was obtained using the modified gas-translation approach to analyze the interaction between permeating molecules and the pore wall of the aminosilica membrane [14]. After the metal doping process, the permeance value for He, H_2, CO_2, N_2, and CH_4 were increased but the activation energy was decreased, which is associated with the increased pore sizes of metal-doped aminosilica membranes (estimated via NKP method, as shown in the supporting information Fig. S2-2). This translates to a smaller repulsive force being generated between gas molecules and the pore wall of the membrane. Moreover, when a metal has a higher coordination affinity, the connectivity formed via the amine-metal crosslinking is higher and pore space is enlarged by a coordinated metal so that the activation energy of small-to-medium sized gases becomes smaller and gas flux increases. The activation energies of He, H_2, N_2 and CH_4 were decreased with increases in the membrane pore size and in membrane network connectivity on the order of Ni-BTPA < Cu-BTPA < Ag-BTPA < BTPA.

Table 2-3. The estimated value of activation energy for BTPA and metal-doped BTPA derived aminosilica membrane

Gases	Ep [kJ mol^{-1}]			
	BTPA	Ag-BTPA	Cu-BTPA	Ni-BTPA
He	15.7	10.9	11.4	12.2
H_2	16.1	10.6	10.4	13.6
CO_2 (200º-120ºC)	20.2	11.3	-	-
CO_2 (120º-50ºC)	41.9	27.5	-	-
CO_2 (200º-50ºC)	31.1	19.5	14.8	8.9
N_2	21.8	13.3	13.2	10.0
CH_4	21.3	12.9	12.6	8.7

Interestingly, the CO_2 activation energy of BTPA and Ag-BTPA showed a very large value, particularly at low temperatures compared with other metal-doped forms of BTPA. Ag-BTPA showed a lower CO_2 activation energy than pure BTPA

Hiroshima University Doctoral Dissertation

----

but higher than Cu- and Ni-BTPA. This is because silver metals only established a low coordination affinity to the amine moiety. Free amine groups in pure BTPA and Ag-BTPA tend to form interactions with CO_2 resulting in the formation of carbamate, and the release of these species becomes more difficult, particularly at lower temperatures [58]. This trend is similar to a report by Yu et al., where the basicity of the secondary amine group in the organosilica precursor is higher than the sterically hindered amine group, and a greater level of energy is generated for the binding of CO_2 with the surface of the material, but the transport of CO_2 gas across membranes is then limited [14, 59]. In the work undertaken by Kim et al. and Wang et al., permeation behavior also showed that a strong interaction between CO_2 and amine moieties causes a decrease in the mobility and diffusivity of CO_2 that is associated with the formation of CO_2-induced amine crosslinking, leading to an enhancement of activation energy [60, 61].

2.3.6 H_2/N_2 and N_2/SF_6 separation through metal-doped aminosilica membranes compared with other types of membranes

Fig. 2-11(a) shows the trade-off between H_2 permeance and the selectivity of H_2 over N_2. Each point in the trade-off figures represents a different membrane, which again validates the reproducibility of BTPA metal-doped membranes with different metal variations. Membranes that are more gas-permeable show lower selectivity, and vice versa. Therefore, trade-off analysis is important in order to secure the best combination between permeability and selectivity. For comparison, the permeability data for mixed-matrix and polymeric membranes were compiled with an upper boundary that would reflect the highest selectivity of a polymer membrane for a given level of permeance. The upper boundary created by Robeson (membrane thickness around 1 μm) could be used as a comparison against permeance and selectivity for new and improved membrane materials [62, 63]. Ni-BTPA at 200 ºC exhibited H_2 permeance of 1.14×10^{-6}~4.45×10^{-6} mol m^{-2} s^{-1} Pa^{-1} with a H_2/N_2 permeance ratio of 10~28. Cu-BTPA also showed high permeance of 4.36×10^{-6} mol m^{-2} s^{-1} Pa^{-1} while demonstrating a moderate permeance ratio of 27. The H_2 permeance and H_2/N_2 permeance ratio for Ag-BTPA with a low metal

affinity are similar to those of BTPA. When compared with silica-based microporous membranes such as BTESE and TEOS, metal-doped BTPA membranes show a trend similar to that of porous membranes with high permeance and moderate selectivity for H_2/N_2 separation.
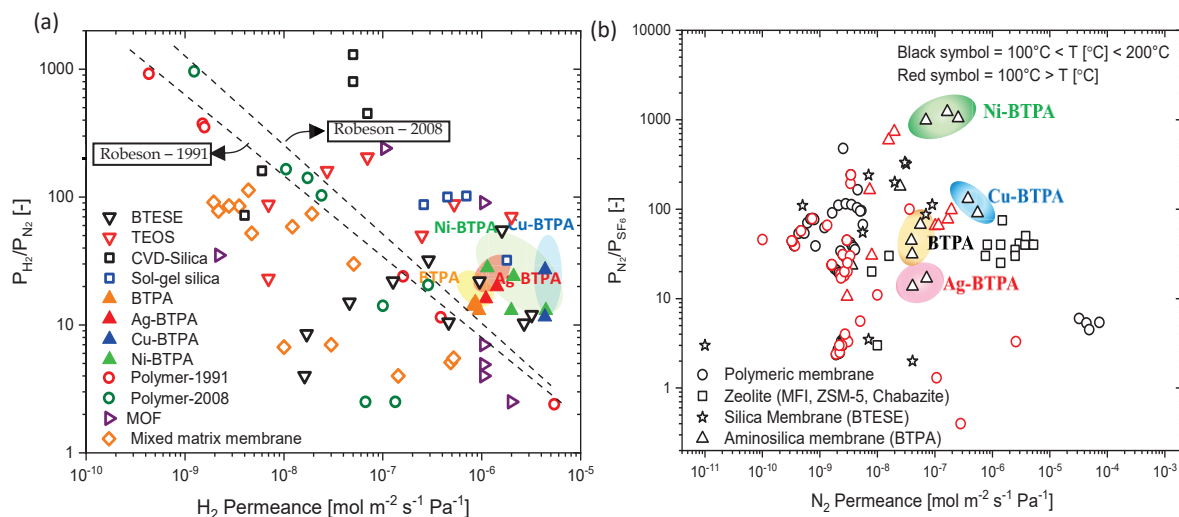
Fig. 2-11 H_2/N_2 permeance ratio as a function of H_2 permeance for a different type of hydrogen separation membranes (a), and correlation of N_2/SF_6 gas separation from various type of membranes as a function of N_2 permeance (b). Lines in (a) are calculated via Robeson upper bound 2008 and 1991

Fig. 2-11(b) compares the separation performance between N_2 and SF_6, which potentially is a larger contributor to global warming than CO_2 [64]. According to commercial applications in N_2-enriched discharge streams, the concentration of SF_6 should be reduced to less than 800 ppm, but high N_2 permeation must be maintained so that it can reach industrial separation levels with a large-scale project capacity of as much as 50 N m^3 h^{-1} [65, 66]. Several types of membranes have shown N_2/SF_6 selectivity up to 476, such as polymeric membranes, but with a low permeation rate for N_2 of approximately 1.61×10^{-8} mol m^{-2} s^{-1} Pa^{-1} [67]. Ni-BTPA has shown a promising separation factor of N_2/SF_6 at 1,900 with high N_2 permeance of 3.75×10^{-7} mol m^{-2} s^{-1} Pa^{-1} at 200 ºC. In order to focus on the durability and stability of Ni-BTPA as prime criteria for industrial applications, the time course of the single-gas permeation experiment was performed under different operation temperatures (Fig. S2-5 in the Supporting Information). The results showed stable performance where the permeance of gases was completely recovered to the initial measurement level at 200 ºC even

after the temperature of the operation was changed from 200 ⁰C to 50 ⁰C and then returned to 200 ⁰C. By comparison with other types of membranes, the modified dense BTPA structure produces a microporous metal-doped aminosilica membrane with both higher flux and selectivity, which represents a significant improvement in performance and is suitable for industrial separation applications.

2.4 Conclusions

The present research was focused on examining the affinity of different metals for the formation of coordinated compounds with the amine moiety of an amorphous silica matrix. The characterization of metal-doped BTPA has shown evidence of a metal-amine interaction that is induced by the reorganization of bridges in the amine-silsesquioxane network that allow maximum coordination to generate a more rigid structure. In this investigation, we found that the surface area and pore volume of a metal-doped BTPA composite was increased by increasing the metal coordination affinity on the order of Ni-BTPA > Cu-BTPA > Ag-BTPA > BTPA. An evaluation of single-gas permeance showed higher values for gas permeation, which corresponded to transformations in the membrane structure following the metal-doping process and simultaneously generated a defect-free membrane. The activation energy of permeated gas was decreased by increases in membrane pore size and in the network connectivity on the order of Ni-BTPA < Cu-BTPA < Ag-BTPA < BTPA. The Ni-BTPA membrane revealed excellent separation performance with permeance and selectivity of N_2 that reached 3.75×10^{-7} mol m^{-2} s^{-1} Pa^{-1} and 1,900, respectively.

References

[1] G. Crini, E. Lichtfouse, Advantages and disadvantages of techniques used for wastewater treatment, Environ. Chem. Lett., 17 (2019) 145-155.
[2] H. Strathmann, L. Giorno, E. Drioli, Introduction to membrane science and technology, Wiley-VCH Weinheim, 2011.
[3] P. Worsfold, A. Townshend, C.F. Poole, M. Miró, Encyclopedia of analytical science, Elsevier, 2019.
[4] M. Kanezashi, T. Sasaki, H. Tawarayama, H. Nagasawa, T. Yoshioka, K. Ito, T. Tsuru, Experimental and theoretical study on small gas permeation properties

through amorphous silica membranes fabricated at different temperatures, J. Phys. Chem. C, 118 (2014) 20323-20331.

[5] C. Kong, H. Du, L. Chen, B. Chen, Nanoscale MOF/organosilica membranes on tubular ceramic substrates for highly selective gas separation, Energy Environ. Sci., 10 (2017) 1812-1819.

[6] T. Tsuru, Nano/Subnano-Tuning of Porous Ceramic Membranes for Molecular Separation, J. Sol-Gel Sci. Technol., 46 (2008) 349-361.

[7] S. Kitagawa, R. Kitaura, S.i. Noro, Functional porous coordination polymers, Angew. Chem. Int. Ed., 43 (2004) 2334-2375.

[8] S.-i. Noro, R. Ochi, Y. Inubushi, K. Kubo, T. Nakamura, CH4/CO2 and CH4/C2H6 gas separation using a flexible one-dimensional copper (II) porous coordination polymer, Microporous Mesoporous Mater., 216 (2015) 92-96.

[9] T. Tsuru, Silica-Based Membranes with Molecular-Net-Sieving Properties: Development and Applications, J. Chem. Eng. Jpn., 51 (2018) 713-725.

[10] N. Raman, C. Brinker, Organic "template" approach to molecular sieving silica membranes, J. Membr. Sci., 105 (1995) 273-279.

[11] H.L. Castricum, G.G. Paradis, M.C. Mittelmeijer‐Hazeleger, R. Kreiter, J.F. Vente, J.E. Ten Elshof, Tailoring the separation behavior of hybrid organosilica membranes by adjusting the structure of the organic bridging group, Adv. Funct. Mater., 21 (2011) 2319-2329.

[12] H.L. Castricum, A. Sah, R. Kreiter, D.H. Blank, J.F. Vente, E. Johan, Hybrid ceramic nanosieves: stabilizing nanopores with organic links, Chem. Commun., (2008) 1103-1105.

[13] M. Kanezashi, Y. Yoneda, H. Nagasawa, T. Tsuru, K. Yamamoto, J. Ohshita, Gas Permeation Properties for Organosilica Membranes with Different Si/C Ratios and Evaluation of Microporous Structures, AlChE J., 63 (2017) 4491-4498.

[14] L. Yu, M. Kanezashi, H. Nagasawa, T. Tsuru, Fabrication and CO2 permeation properties of amine-silica membranes using a variety of amine types, J. Membr. Sci., 541 (2017) 447-456.

[15] S.R. Batten, N.R. Champness, X.-M. Chen, J. Garcia-Martinez, S. Kitagawa, L. Öhrström, M. O'Keeffe, M.P. Suh, J. Reedijk, Terminology Of Metal–Organic Frameworks And Coordination Polymers (Iupac Recommendations 2013), Pure Appl. Chem., 85 (2013) 1715-1724.

[16] H. Ting, H.-Y. Chi, C.H. Lam, K.-Y. Chan, D.-Y. Kang, High-permeance metal–organic framework-based membrane adsorber for the removal of dye molecules in aqueous phase, Environ.-Sci. Nano, 4 (2017) 2205-2214.

[17] J. Duan, W. Jin, S. Kitagawa, Water-resistant porous coordination polymers for gas separation, Coord. Chem. Rev., 332 (2017) 48-74.

[18] M. Kanezashi, S. Miyauchi, S. Hayakawa, H. Nagasawa, T. Yoshioka, T. Tsuru, Propylene/propane permeation properties of metal-doped organosilica membranes with controlled network sizes and adsorptive properties, J. Jpn. Pet. Inst, 59 (2016) 140-148.

[19] P. Karakiliç, C. Huiskes, M.W. Luiten-Olieman, A. Nijmeijer, L. Winnubst, Sol-gel processed magnesium-doped silica membranes with improved H2/CO2 separation, J. Membr. Sci., 543 (2017) 195-201.

[20] M. ten Hove, M.W. Luiten-Olieman, C. Huiskes, A. Nijmeijer, L. Winnubst, Hydrothermal stability of silica, hybrid silica and Zr-doped hybrid silica membranes, Sep. Purif. Technol., 189 (2017) 48-53.

[21] X. Yang, S. Sheridan, L. Ding, D.K. Wang, S. Smart, J.C.D. da Costa, A. Liubinas, M. Duke, Inter-layer free cobalt-doped silica membranes for pervaporation of ammonia solutions, J. Membr. Sci., 553 (2018) 111-116.

[22] M. Aroon, A. Ismail, T. Matsuura, M. Montazer-Rahmati, Performance Studies Of Mixed Matrix Membranes For Gas Separation: A Review, Sep. Purif. Technol., 75 (2010) 229-242.

[23] R. Igi, T. Yoshioka, Y.H. Ikuhara, Y. Iwamoto, T. Tsuru, Characterization of Co‐doped silica for improved hydrothermal stability and application to hydrogen separation membranes at high temperatures, J. Am. Ceram. Soc., 91 (2008) 2975-2981.

[24] W. Puthai, M. Kanezashi, H. Nagasawa, K. Wakamura, H. Ohnishi, T. Tsuru, Effect of Firing Temperature on The Water Permeability Of SiO_2–ZrO_2 Membranes for Nanofiltration, J. Membr. Sci., 497 (2016) 348-356.

[25] J.E. McMurry, Organic chemistry with biological applications, Cengage Learning, 2014.

[26] C.L. Phillips, T.Z. Regier, D. Peak, aqueous Cu (II)–organic complexation studied in situ using soft X-ray and vibrational spectroscopies, Environ. Sci. Technol., 47 (2013) 14290-14297.

[27] L. Li, C. Liu, A. Geng, C. Jiang, Y. Guo, C. Hu, Preparation, characterization and photocatalytic applications of amine-functionalized mesoporous silica impregnated with transition-metal-monosubstituted polyoxometalates, Mater. Res. Bull., 41 (2006) 319-332.

[28] E. Liarou, M. Staniforth, J.S. Town, A. Marathianos, M. Grypioti, Y. Li, Y. Chang, S. Efstathiou, E. Hancox, A.M. Wemyss, UV irradiation of Cu-based complexes with aliphatic amine ligands as used in living radical polymerization, Eur. Polym. J., 123 (2020) 109388.

[29] X. Ren, T. Tsuru, Organosilica-based membranes in gas and liquid-phase separation, Membranes, 9 (2019) 107.

[30] N. Zhang, J. Wang, H. Huo, L. Chen, W. Shi, C. Li, J. Wang, Iron, Cobalt and Nickel Complexes Bearing Hyperbranched Iminopyridyl Ligands: Synthesis, Characterization and Evaluation as Ethylene Oligomerization Catalysts, Inorg. Chim. Acta, 469 (2018) 209-216.

[31] Y. Liu, H. Liu, W. Huang, Y. Yu, X. Dai, Z. Shan, Self-assembly of hierarchical microsized hard carbon-supported Si encapsulated in nitrogen-doped carbon as anode for lithium-ion batteries, J. Mater. Sci., (2020) 1-12.

[32] T. Ivanova, A. Naumkin, A. Sidorov, M. Kiskin, V. Novotortsev, I. Eremenko, X-Ray Photoelectron Spectra and Structure of Polynuclear Nickel Complexes, Russ. J. Inorg. Chem., 52 (2007) 1781-1785.

[33] H. Konno, X-ray photoelectron spectroscopy, in: Materials Science and Engineering of Carbon, Elsevier, 2016, pp. 153-171.

[34] T. Tsuru, Development of Metal-Doped Silica Membranes for Increased Hydrothermal Stability and Their Applications to Membrane Reactors for Steam Reforming of Methane, J. Jpn. Pet. Inst, 54 (2011) 277-286.

[35] M. ten Hove, A. Nijmeijer, L. Winnubst, Facile synthesis of zirconia doped hybrid organic inorganic silica membranes, Sep. Purif. Technol., 147 (2015) 372-378.

[36] S. Mourdikoudis, R.M. Pallares, N.T. Thanh, Characterization techniques for nanoparticles: comparison and complementarity upon studying nanoparticle properties, Nanoscale, 10 (2018) 12871-12934.

[37] K.A. Cychosz, R. Guillet-Nicolas, J. García-Martínez, M. Thommes, Recent advances in the textural characterization of hierarchically structured nanoporous materials, Chem. Soc. Rev., 46 (2017) 389-414.

[38] A. Singh, W. Koros, Significance of entropic selectivity for advanced gas separation membranes, Ind. Eng. Chem. Res., 35 (1996) 1231-1234.

[39] R. Serna-Guerrero, Y. Belmabkhout, A. Sayari, Modeling CO2 adsorption on amine-functionalized mesoporous silica: 1. A semi-empirical equilibrium model, Chem. Eng. J., 161 (2010) 173-181.

[40] G. Sartori, D.W. Savage, Sterically hindered amines for carbon dioxide removal from gases, Ind. Eng. Chem. Fundam., 22 (1983) 239-249.

[41] R. Xing, W.W. Ho, Crosslinked polyvinylalcohol–polysiloxane/fumed silica mixed matrix membranes containing amines for CO2/H2 separation, J. Membr. Sci., 367 (2011) 91-102.

[42] N. Velikova, I. Spassova, Amine functionalized mesoporous hybrid materials: influence of KCl and xylene on the textural characteristics and CO 2 sorption, J. Sol-Gel Sci. Technol., 91 (2019) 374-384.

[43] L. Yu, M. Kanezashi, H. Nagasawa, N. Moriyama, T. Tsuru, K. Ito, Enhanced CO2 separation performance for tertiary amine‐silica membranes via thermally induced local liberation of CH3Cl, AlChE J., 64 (2018) 1528-1539.

[44] A.M. Varghese, G.N. Karanikolos, CO2 capture adsorbents functionalized by amine–bearing polymers: A review, Int. J. Greenh. Gas Control, 96 (2020) 103005.

[45] X.-y. Deng, Z.-k. Zhang, Mechanism and Non-isothermal Kinetics of Thermal Decomposition of Ni (NO_3) _2· 6H_2O [J], Journal of Qingdao University of Science and Technology (Natural Science Edition), 1 (2006).

[46] H. Nagasawa, T. Kagawa, T. Noborio, M. Kanezashi, A. Ogata, T. Tsuru, Ultrafast Synthesis of Silica-Based Molecular Sieve Membranes in Dielectric Barrier Discharge at Low Temperature and Atmospheric Pressure, J. Am. Chem. Soc., (2020).

[47] T. Tsuru, R. Igi, M. Kanezashi, T. Yoshioka, S. Fujisaki, Y. Iwamoto, Permeation properties of hydrogen and water vapor through porous silica membranes at high temperatures, AlChE J., 57 (2011) 618-629.

[48] H. Song, S. Zhao, J. Chen, H. Qi, Hydrothermally stable Zr-doped organosilica membranes for H2/CO2 separation, Microporous Mesoporous Mater., 224 (2016) 277-284.

[49] Y. Xiao, T.-S. Chung, Grafting thermally labile molecules on cross-linkable polyimide to design membrane materials for natural gas purification and CO 2 capture, Energy Environ. Sci., 4 (2011) 201-208.

[50] M. Guo, M. Kanezashi, H. Nagasawa, L. Yu, K. Yamamoto, T. Gunji, T. Tsuru, Fine‐tuned, molecular‐composite, organosilica membranes for highly efficient propylene/propane separation via suitable pore size, AlChE J., 66 (2020) e16850.

[51] R. Xu, S.M. Ibrahim, M. Kanezashi, T. Yoshioka, K. Ito, J. Ohshita, T. Tsuru, New insights into the microstructure-separation properties of organosilica membranes

with ethane, ethylene, and acetylene bridges, ACS Appl. Mater. Interfaces, 6 (2014) 9357-9364.

[52] M. Kanezashi, T. Shioda, T. Gunji, T. Tsuru, Gas permeation properties of silica membranes with uniform pore sizes derived from polyhedral oligomeric silsesquioxane, AIChE journal, 58 (2012) 1733-1743.

[53] B. Freeman, Y. Yampolskii, Membrane gas separation, John Wiley & Sons, 2011.

[54] H. Nagasawa, T. Niimi, M. Kanezashi, T. Yoshioka, T. Tsuru, Modified Gas‐Translation Model for Prediction of Gas Permeation Through Microporous Organosilica Membranes, AlChE J., 60 (2014) 4199-4210.

[55] D.S. Sholl, R.P. Lively, Defects in Metal–Organic Frameworks: Challenge or Opportunity?, J. Phys. Chem. Lett., 6 (2015) 3437-3444.

[56] A.W. Thornton, T. Hilder, A.J. Hill, J.M. Hill, Predicting gas diffusion regime within pores of different size, shape and composition, J. Membr. Sci., 336 (2009) 101-108.

[57] Y. Zhang, X. Feng, S. Yuan, J. Zhou, B. Wang, Challenges and recent advances in MOF–polymer composite membranes for gas separation, Inorg. Chem. Front., 3 (2016) 896-909.

[58] R.J. Oliveira, J.F. de Conto, M.R. Oliveira, S.M. Egues, G.R. Borges, C. Dariva, E. Franceschi, CO2/CH4 adsorption at high-pressure using silica-APTES aerogel as adsorbent and near infrared as a monitoring technique, J. CO2 Util., 32 (2019) 232-240.

[59] L. Yu, M. Kanezashi, H. Nagasawa, J. Oshita, A. Naka, T. Tsuru, Pyrimidine-bridged organoalkoxysilane membrane for high-efficiency CO2 transport via mild affinity, Sep. Purif. Technol., 178 (2017) 232-241.

[60] N. Wang, A. Mundstock, Y. Liu, A. Huang, J. Caro, Amine-modified Mg-MOF-74/CPO-27-Mg membrane with enhanced H2/CO2 separation, Chem. Eng. Sci., 124 (2015) 27-36.

[61] H.-J. Kim, W. Chaikittisilp, K.-S. Jang, S.A. Didas, J.R. Johnson, W.J. Koros, S. Nair, C.W. Jones, Aziridine-functionalized mesoporous silica membranes on polymeric hollow fibers: Synthesis and single-component CO2 and N2 permeation properties, Ind. Eng. Chem. Res., 54 (2015) 4407-4413.

[62] L.M. Robeson, Correlation of separation factor versus permeability for polymeric membranes, J. Membr. Sci., 62 (1991) 165-185.

[63] L.M. Robeson, The upper bound revisited, J. Membr. Sci., 320 (2008) 390-400.

[64] X. Li, H. Zhao, A.B. Murphy, SF6-alternative gases for application in gas-insulated switchgear, J. Phys. D: Appl. Phys., 51 (2018) 153001.

[65] Y. Dai, Q. Li, X. Ruan, Y. Hou, X. Jiang, X. Yan, G. He, F. Meng, Z. Wang, Fabrication of defect-free Matrimid® asymmetric membranes and the elevated temperature application for N2/SF6 separation, J. Membr. Sci., 577 (2019) 258-265.

[66] K. Inami, Y. Maeda, Y. Habuchi, M. Yoshimura, S. Hamano, H. Hama, Problems of the application of N2/SF6 mixtures to gas‐insulated bus, Electr. Eng. Jpn., 137 (2001) 25-31.

[67] A. Wolińska-Grabczyk, A. Jankowski, R. Sekuła, B. Kruczek, Separation of SF6 from binary mixtures with N2 using commercial poly (4-methyl-1-pentene) films, Sep. Sci. Technol., 46 (2011) 1231-1240.

Supporting Information

1. Gas cylinder
2. Pressure controller
3. Stop valve
4. Temperature controller
5. Furnace
6. Membrane module
7. Membrane
8. Pressure gauge
9. Back pressure valve
10. Three way valve
11. Vacuum pump
12. Soap film flow meter
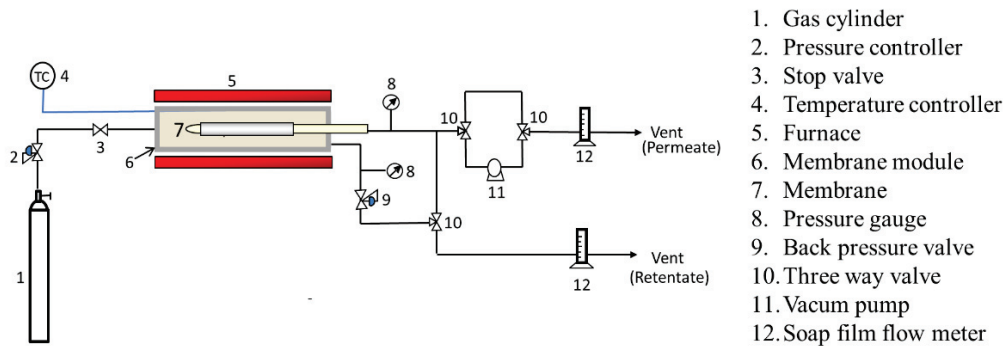
Fig. S2-1. Set up single gas permeation equipment
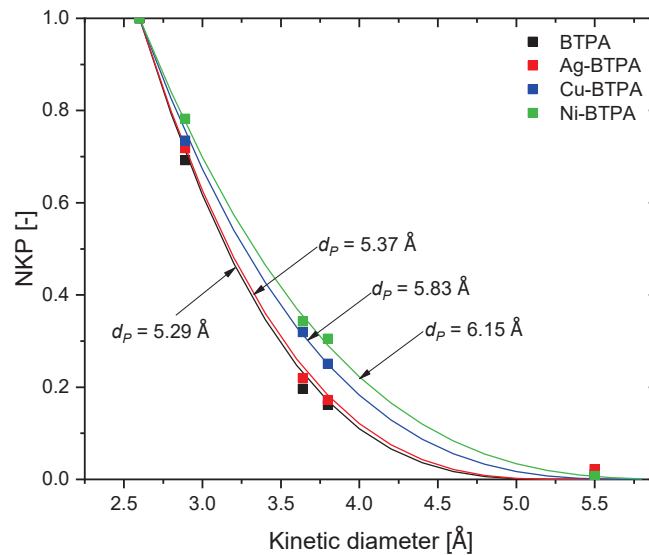
Fig. S2-2. Pore size prediction based on the NKP method of BTPA and metal-doped BTPA with different metals at 200 ⁰C
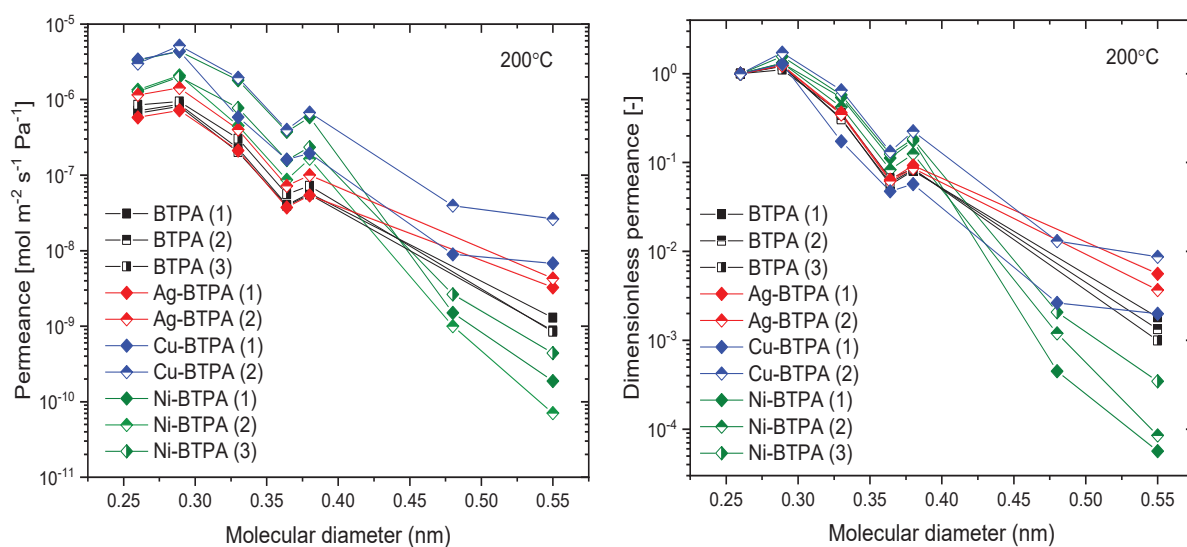
Fig. S2-3. Reproducible data of single gas permeance for Ni-BTPA as a function of kinetic diameter size of gases measured at 200 ºC
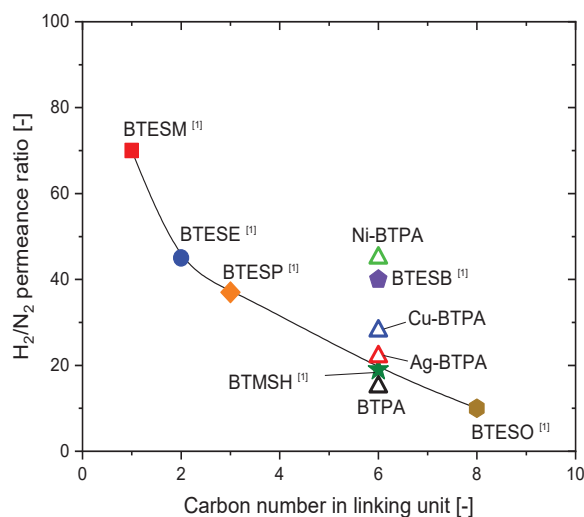
Fig. S2-4. permeance ratio of H_2/N_2 as a function of carbon number in linking unit of bi-silyl structure

Fig. S2-4. reveals that there has been a gradual decrease in the H_2/N_2 permeance ratio by increasing the number of carbon molecules between the bi-silyl bridges that give rise to higher flexibility in the linking unit. BTPA has a structure that is similar to that of BTMSH (six carbon atoms in a linking unit) and shows an H_2/N_2 permeance ratio of 15, which corresponds to the small pore size of the membranes. By contrast, after the addition of metal doping into the BTPA structure, a higher permeance ratio was achieved, which equates to an increase in membrane

----

connectivity and in the rigidity of the linking unit via amine-metal interactions. The linking unit structure transforms from flexible into rigid with increases in the metal affinity.
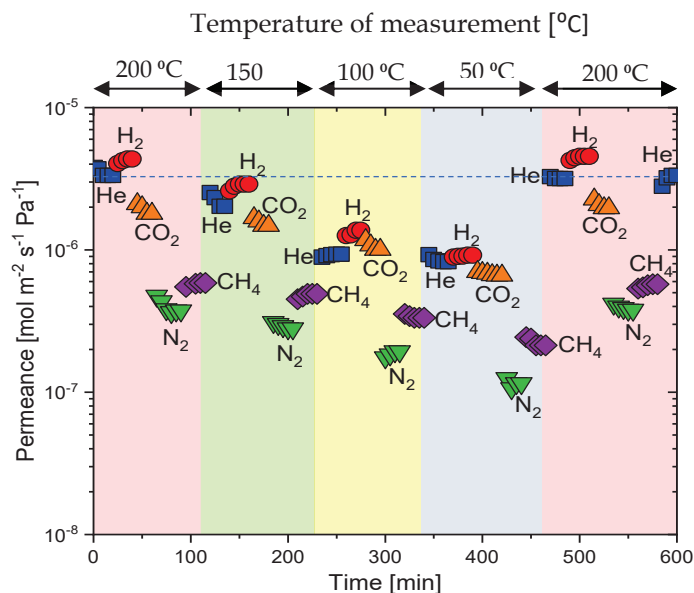
Fig. S2-5. Effective time courses for Ni-BTPA single-gas permeation performance at different operation temperatures (200 ºC → 150 ºC → 100 ºC → 50 ºC → 200 ºC)
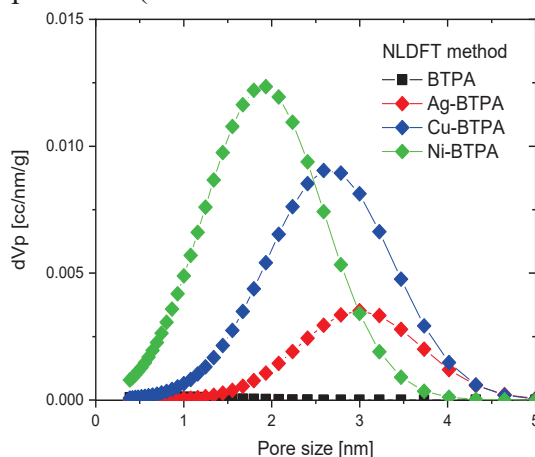
Fig. S2-6 NLDFT pore size distribution of amorphous aminosilica and metal-doped powder

According to the pore size distribution data in Fig. S2-6, as affinity for the metal-dopant increased, the pore size distribution narrowed as evident by a decrease in the full width at half maximum (FWHM) value in the NLDFT curve when fitted with a Gaussian function. In this case, the Ni-BTPA showed the most uniform pore size distribution while the BTPA and Ag-BTPA with highly maintained flexible amorphous material showed typically negligible and broad pore size distributions, respectively.
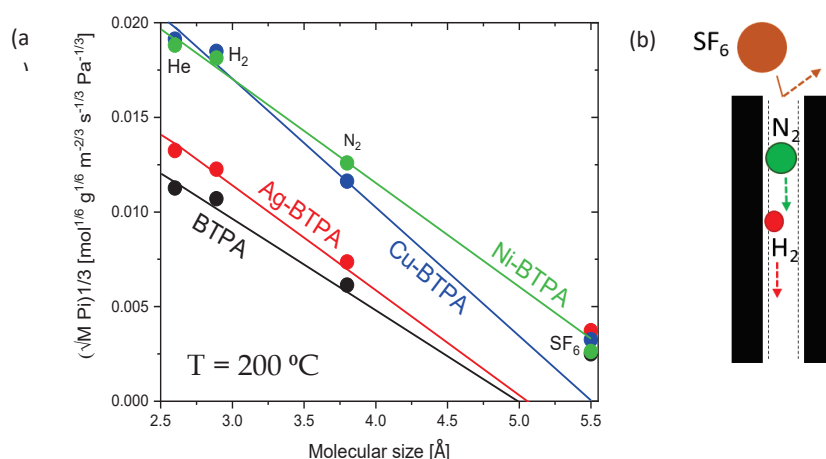
Fig. S2-7 The correlation of $\left(\sqrt{M_i}P_i\right)^{1/3}$ as a function of molecular size of permeating gases (points and lines are experimental and theoretically calculated, respectively) (a), and schematic gas transport for different gases in a cylindrical pore of Ni-BTPA (b).

The pore size of metal-doped BTPA-derived membranes was estimated by using modified-GT models, as shown in Eq. S.2-1, where the functions of $\left(\sqrt{M_i}P_i\right)^{1/3}$ for different permeating gases were plotted as the sizes of the permeating gases (d_i). As shown in Fig. S2-7(a), experimental permeation reveals that the membrane pore size was enlarged on the order of Ni-BTPA (6.10 nm) > Cu-BTPA (5.51 nm) > Ag-BTPA (5.06 nm) > BTPA (4.89 nm). Fig. S2-7(b) presents a schematic illustration of gas transport within cylindrically shaped pores of Ni-BTPA. H_2 and N_2 were accepted within the Ni-BTPA pores, whereas a large gas such as SF_6 was rejected by the repulsive forces between neighboring membrane pore walls. H_2 as a smaller molecule tends to perform at a higher level of potential energy compared with that N_2. On this occasion, the micropore diffusion rate was determined by the slower passage rate of N_2 through the membrane pore wall. As reported for most microporous organosilica membranes, the gas separation factor is typically at a moderate level for H_2/N_2 separation with a relatively high rate of permeation that relates to a thin topmost layer. More importantly, the $\left(\sqrt{M_i}P_i\right)^{1/3}$ of most gases has been the best fit for Ni-BTPA membranes, which indicate that Ni-BTPA consist of uniform pores. On the other hand, other metal-doped BTPA showed points that deviated from the calculated lines, which indicated that the pore sizes were not uniform.

$$\left(\sqrt{M_i}P_i\right)^{1/3} = \left(\frac{k_0}{\sqrt{RT}}exp\left(-\frac{E_{p,i}}{RT}\right)\right)^{1/3}(d_0 - d_i) \qquad \text{(S.2-1)}$$

Chapter 3

Microporous nickel-coordinated aminosilica membranes for improved pervaporation performance of methanol/toluene separation

3.1 Introduction

Methanol is one of the most commonly used solvents in industrial applications such as petroleum, pharmaceutical, electrochemical, petrochemical, fertilizer, textile, paint, cosmetics, etc [1-4]. One of the most challenging tasks in these industries is the separation of the organic mixture of methanol from toluene, which is associated with the formation of an azeotropic mixture with a composition of 27 wt% toluene under atmospheric pressure [5]. Extractive distillation and azeotropic distillation are frequently applied to separate mixtures with close boiling points [6-9]. In thermal-based separations such as distillation, the heat of evaporation is provided from the reboiler at the bottom stream and the heat of condensation is removed from the condenser at the upper stream and results in energy consumption estimated to be around 45 – 50% of the separation process [10]. Overcoming this expense, in a sustainable manner requires new technology.

Pervaporation has shown promise as a membrane-based separation technology for the separation of organic compounds with close boiling points, and azeotropic mixtures [1, 11]. With this technique liquid mixtures are separated via partial vaporization throughout the selective barrier of membranes. Compounds are selectively transported from the liquid phase in the upper stream to the vapor phase in the lower stream, which enables better separation performance and lower levels of energy consumption [12-14]. The driving force for pervaporation is the vapor pressure difference between the feed and permeate sides; the pressure of the feed side is maintained at atmospheric levels while that of the permeate side is evacuated. Polymeric and inorganic membranes are used for a wide variety of pervaporation applications [14, 15]. A considerable number of industrial pervaporation applications use polymeric membrane materials due to their relatively high flux and economical investment [16, 17]. Crosslinked poly(vinyl alcohol), poly(acrylic acid), highly hydrophilic chitosan, and polyacrylonitrile are frequently used in the preparation of highly permeable membranes that

----

are suitable for alcohol dehydration [18-23]. Nevertheless, a major problem of polymeric-based membranes is swelling that leads to instability and lower levels of selectivity.

Inorganic membranes, which are better known as ceramic membranes, are synthesized from organosilica-based materials. These membranes exhibit high thermal and chemical stability with no swelling, high flux, high separation performance, and controllable pore size [24-26]. The separation ability of organosilica membranes depends mostly on the pore size and on the interaction between permeating molecules and the pore walls of membranes. Therefore, material modification is required to produce a highly porous material that can facilitate high permeability without sacrificing selectivity. A spacer method is frequently prescribed for tailoring the microporosity by choosing bi-silyl precursors with different structures that produce organosilica-based materials with an optimum membrane pore size [27]. The utilization of a short and rigid linking chain between silicon atoms generates a porous structure, whereas the increase in the carbon number and flexibility of the linking units tends to produce a denser structure that is inappropriate for the construction of a high-flux membrane.

In the present study, we propose a new method to control the microporosity induced by crosslinking of the amine moieties in the linking units of bis [3-trimethoxysilyl) propyl] amine (BTPA) as a strong field ligand with electron donor properties (Lewis base) and nickel from transition metal groups as electron-pair acceptors (Lewis acid). The intercalation of metal-developed subnanopores through the coordination of covalent bonds expanded the amine crosslinking between network layers, which transformed the texture of the membrane from that of a flexible non-porous entity into a porous structure by means of the formation of more rigid linking units. We reported that hybrid microporous aminosilica membranes can be successfully synthesized via metal-amine coordination-induced microporosity with high-level improvements in both permeance and selectivity [28]. Nickel has a high coordination affinity to amine and was found to be fully incorporated into the amorphous BTPA framework. The nickel also induced the rearrangement of bridged amine chains into a more rigid structure with a high surface area and an increase in total pore volume. Therefore, it is necessary to investigate the effect that concentrations of nickel-doped BTPA (Ni-BTPA) exert on the formation of the microporosity of aminosilica-based coordination polymers.

The construction of silica-based amorphous microporous frameworks in Ni-BTPA could facilitate the diffusion selectivity of a smaller molecule such as methanol (kinetic diameter: 0.38 nm) rather than toluene (0.59 nm) [13, 29], while the nickel-amine coordination sites tend to generate a rigid segment via crosslinking among network layers that gives rise to a porous structure and may create an affinity with methanol. A high degree of metal doping

ensures the development of a high-flux membrane and a sorption selectivity that favors methanol (polarity index: 12.3 MPa$^{0.5}$) as a hydrophilic polar smaller-sized component, while the sorption of toluene (1.4 MPa$^{0.5}$) as a hydrophobic larger-sized compound would be limited [30]. In this study, an optimization experiment was performed via different mole ratios of nickel-metal against amine groups between bi-silyl precursors, and the textural properties of the resultant materials were characterized. The methanol/toluene pervaporation performance of each Ni-BTPA membrane was evaluated and discussed with respect to any effects of different nickel phases in the form of amorphous and nanoparticulated nickel.

3.2 Experimental

3.2.1 Preparation of a nickel-doped bis [3-(trimethoxysilyl) propyl] amine (Ni-BTPA) sol

Ni-BTPA coordinated sols were prepared via the hydrolysis and condensation of bis [3-(trimethoxysilyl) propyl] amine (BTPA) precursors with different mole ratios of Ni(NO$_3$)$_2 \cdot$6H$_2$O as metal dopants [28]. First, BTPA was dissolved into ethanol and a mixture of water and nitric acid as catalysts was added to the solutions under vigorous stirring. The mole ratio of BTPA/H$_2$O/HNO$_3$ was 1/300/1, and ethanol was used to adjust the concentration of BTPA to 5 wt%. The hydrolysis and condensation reactions were established at room temperature for 12 hours prior to the addition of a nickel-metal salt. Ni(NO$_3$)$_2 \cdot$6H$_2$O was added into the aminosilica sol in mole ratios (nickel/amine = mol/mol) of 0 (denoted as BTPA), 0.125 (Ni-BTPA 0.125), 0.25 (Ni-BTPA 0.25), and 0.50 (Ni-BTPA 0.50) to examine the effect that metal-doping exerts on the transformation of a dense BTPA structure. After the addition of dissolved nickel-metal salt, the mixtures were further stirred (550 rpm) at room temperature for 1 hour. In this study, Ni-BTPA with a ratio of 1.00 was also synthesized as a control group to facilitate analysis.

3.2.2 Characterization of nickel-doped aminosilica films and xerogels

Fourier transform infrared spectroscopy (FT/IR-4100, JASCO, Japan) was used to observe the evolution of the amine deformation band during the formation of coordinated interactions with a nickel-metal center. BTPA sols with different metal ratios were coated onto KBr plates and then calcined at 250 °C under a N$_2$ atmosphere. The binding energy and

environment of the amine sites were investigated via X-ray photoelectron spectroscopy (JEOL RE series JES-RE1X ESR spectrometer). Each nickel-doped BTPA film was coated onto a silicon wafer followed by calcination at 250 °C.

The Ni-BTPA sols were dried at 50 °C and then ground to obtain a fine powder, which was then calcined at 250 °C for 30 minutes under a nitrogen flow. The microstructures of the composites after the doping process were examined using X-ray diffraction (XRD D2 PHASER, Bruker, Germany) at a scanning range of 5° - 80°. A transmission electron microscope (TEM JEOL2010 Ltd., Japan) was used to confirm the microscopic morphology of coordinated nickel ions and nanoparticles. Textural properties of BTPA and Ni-BTPA were determined using a nitrogen sorption isotherm (BELMAX JAPAN Inc., Japan) at -196 °C. Methanol and toluene vapor sorption isotherms were measured to determine adsorption capacity, and the heats of adsorption for each of the organic solvents were evaluated at three different temperatures (25, 30, and 35 °C). Ni-BTPA powder with different mole ratios was pretreated at 200 °C under vacuum conditions for 12 hours before each measurement.

3.2.3 Fabrication of Ni-BTPA membranes and single-gas permeation measurements

Porous α-alumina tubes were used as membrane supports with 50% porosity and an average pore size of 1 μm (length 100 mm; inner diameter 8 mm; outer diameter 10 mm), as supplied by Nikkato Corporation (Japan) [31]. A Ni-BTPA membrane consists of a porous support layer (α-alumina particle and intermediate layer) with an ultrathin topmost layer acting as a specific separation barrier. First, porous particle layers were developed by coating α-alumina particles (average particle sizes 2 μm and 0.2 μm) that were dispersed into 2 wt% SiO_2-ZrO_2 sol as a binder and subsequently calcined at 550 °C under an air atmosphere for 15 minutes. The intermediate layer was constructed from 0.5 wt% SiO_2-ZrO_2 sol that was coated onto the surface of the particle layer and fired under an air atmosphere at 550 °C. These procedures were repeated several times until the average pore size of the support reached approximately 1 nm. Finally, the topmost layer was obtained by twice coating nickel-doped BTPA sols diluted to 0.1 wt% onto the intermediate layer followed by calcination at 250 °C under a flow of nitrogen for 30-60 minutes.

Before the measurements of single-gas permeation, a fresh membrane was pretreated at 200 ⁰C for 6 hours under a He flow to remove any adsorbed molecules. A single-gas permeation experiment was performed using high-purity He, H_2, CO_2, N_2, CH_4, CF_4, and SF_6. Each permeation gas was fed to the outside of the membrane with upstream pressures of 200 – 400 kPa, and the pressure inside the system was maintained at atmospheric levels. The gas permeation test was established at temperatures ranging from 200 – 50 ⁰C, and the flow rate of the permeate side was measured using a film flow meter (Horiba, Co. Ltd., Japan).

3.2.4 Pervaporation experiment

The separation of an organic-azeotropic mixture of methanol and toluene (Table 3-1) was performed using the pervaporation process. A schematic diagram of the pervaporation (PV) apparatus is shown in Fig. S3-2. The mixtures of methanol and toluene were circularized using a stirrer at 3,000 rpm to prevent a concentration polarization on the surface of the membrane. The pressure of the feed side was maintained at atmospheric levels, while the permeate side was evacuated to 0 – 2 kPa via the use of a vacuum pump. The temperatures of the feed solutions were maintained within a range of 30 – 50 ⁰C via the use of a thermocouple and a heating coil controller, while the concentrations of methanol in the feed solutions were varied from 10 to 50 wt%.

Table 3-1. Physical properties of organic solvents as azeotropic mixture

Penetrant	MW [g mol^{-1}]	Stokes diameter[29] [nm]	Boiling point [⁰C]	Polarity[32] [MPa$^{1/2}$]
MeOH	32.04	0.38	64.7	12.3
Toluene	92.14	0.59	110.6	1.40

The permeate vapor was collected using a glass trap cooled in a dewar vessel with liquid nitrogen for each time interval. The concentration of the feed solution was maintained constant during the measurement via the periodical addition of an appropriate amount of pure methanol. Each composition of the feed and permeate streams was determined via gas chromatography (GC-14B Shimadzu Cor., Japan).

Membrane flux (J) and the flux of each component (J_i) on the permeate side are described by equations (3-1) and (3-2), respectively.

$$J = \frac{w}{A \times t} \qquad \qquad (3\text{-}1)$$

$$J_i = J \times y_{i,p} \qquad \qquad (3\text{-}2)$$

J is the total permeated flux (kg m^{-2} h^{-1}), w is the permeate weight (kg), A is the membrane surface area (m^2), t is the permeating time (h), and $y_{i,p}$ is the weight fraction of component i in the permeate. The permeance of component i could be calculated from the molar flux (J_{Mi}) of the i component divided by the difference in the partial pressures of the feed ($p_{i,f}$) and permeate streams ($p_{i,p}$), as determined by the following equation.

$$P_i = {J_{Mi}} \Big/ {(p_{i,f} - p_{i,p})} \qquad \qquad (3\text{-}3)$$

The feed partial pressure of the ith component was calculated as $p_{i,f} = \gamma_i x_i p_i^0$, where γ_i is the activity coefficient according to the Wilson parameters, x_i is the mole fraction of the ith component, and p_i^0 is the vapor pressure according to the Antoine equation. On the other hand, the pressure in the permeate stream was presumed to be zero. The separation factor is defined as the ratios of the mole fractions in the permeate (y_{MeOH} and y_{Tol}) and feed (x_{MeOH} and x_{Tol}) streams, as follows.

$$\alpha = \left(\frac{y_{MeOH}}{y_{Tol}} \right) \Big/ \left(\frac{x_{MeOH}}{x_{Tol}} \right) \qquad \qquad (3\text{-}4)$$

3.3 Results and discussions

3.3.1 Optimization of the coordination driven by the nickel-metal mole ratio

The introduction of nickel into amine-containing organosilica precursor (BTPA) molecules was expected to increase the network dimensionality and convert the textural properties of the BTPA membrane from dense to porous. In order to clarify this idea, the spectroscopy characterization was collected for BTPA and Ni-BTPA sols and powders with different nickel ratios obtained via thermal treatment at 250 ⁰C.

Fig. 3-1(a) compares the UV-Vis spectral results for three Ni-BTPA sol solutions of different nickel content together with pure aminosilica precursors of BTPA and nickel nitrate. The absorption spectra of BTPA as an amine organosilica ligand (solid black line) presented one peak at 212 nm due to the amine electron intraligand transition (n → σ^*).
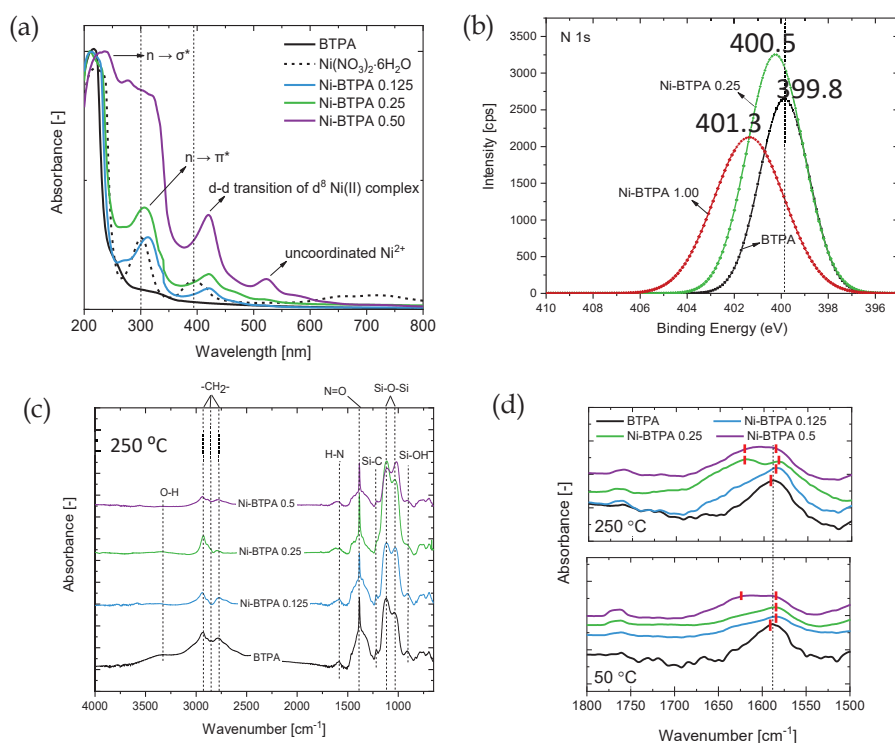
Fig. 3-1. UV-Vis spectra (200 – 800 nm) of BTPA, $Ni(NO_3)_2 \cdot 6H_2O$, and nickel-doped BTPA with different nickel content (a), N(1s) high-resolution spectra (b), infrared spectra in the range of 4,000 – 650 cm^{-1} (c), and higher magnification for NH deformation band in the range 1,700 – 1,500 cm^{-1} (d) originating from BTPA and Ni-BTPA wafer calcined at 250 ºC

The emitted absorbance for nickel-doped BTPA samples displayed three peaks at 227 - 241, 282 - 313, and 420 – 422 nm, which were related to the transitions of n → σ* (N-H), n → π* (N=O), and d→d (d^8 Ni^{2+}), respectively [28]. After the addition of a different amount of nickel, the ~212 nm peak gradually shifted to a higher wavelength, which was associated with a new environment of the free-electron transition of amine moieties [28]. Moreover, as an equivalent mole ratio (0.125 – 0.50) of nickel was added into the BTPA solution, peaks indicating coordination (300 nm and 420 nm) increased almost linearly to the nickel/amine mole ratio (Fig. S3-4). On the other hand, the new absorbance peak at ~395 nm, which was originally observed for $Ni(NO_3)_2 \cdot 6H_2O$, was gradually shifted to a higher wavenumber that was accompanied by a higher intensity due to a stronger d→d transition from lone pairs of electrons in the amine groups to the empty d orbitals of nickel [32, 33]. The high-resolution spectra of N1s of the XPS spectra confirmed the environment of nitrogen and its covalence binding interaction to nickel (Fig. 3-1(b)). The N1s binding energy for BTPA was centered at 399.8 eV, whereas Ni-BTPA containing nitrogen coordinated with nickel and showed a gradual shifting to a higher level of binding energy (400.5 to 401.3eV) that was ascribed to the highly coordinated donor atoms of nitrogen [34, 35].

Fig. 3-1(c) shows a wide range of FT-IR spectra, whereas Fig. 3-1(d) shows a narrow range of FT-IR spectra and exhibits a characteristic band at 1,550 – 1,650 cm^{-1}, which was assigned to N-H deformation from amine groups in the linking units of BTPA molecules, as summarized in Table 3-2. The formation of a coordination compound between amine groups and metal could be analyzed from this type of vibration. At low temperature, the N-H deformation band was shifted to a lower wavenumber due to the formation of a covalent coordination bond between the amine groups and nickel, which led to a stabilization of the Ni-BTPA structure [36]. Also, a broad N-H deformation band centered at 1,620 cm^{-1} was observed for a high nickel ratio of 0.50, which suggested the appearance of unreacted nickel after reaching the approximate saturation point, and led to the formation of a nickel agglomerate. In addition, the N-H deformation band become broader (1,610 – 1,620 cm^{-1}) and the intensity gradually increased when the calcination temperature was elevated to 250 ºC, suggesting the involvement of a dynamic process that include three different reactions: hydrolysis, condensation, and coordination [28]. The hydrolysis and condensation were controlled as the major reactions at low temperature due to the existence of water and nitric acid, while the coordination reaction was more predominant at higher temperatures after the removal of the water and the catalyst.

Table 3-2. FT-IR frequency of N-H deformation band

Compound	50 ºC	250 ºC
	ν N-H [cm^{-1}]	ν N-H [cm^{-1}]
BTPA	1588	1588
Ni-BTPA 0.125	1576	1579
Ni-BTPA 0.25	1580	1582 & 1620
Ni-BTPA 0.50	1583 & 1617	1587 & 1620

Fig. 3-2(a) compares the X-Ray diffractograms (XRD) of BTPA and Ni-BTPA powders at different amounts of nickel, which were fired under different calcination temperatures. All of the samples showed the main characteristics of amorphous properties, indicating that nickel ions were incorporated and dispersed well into the BTPA matrix. The formation of coordinated nickel and amine moieties generated coordination covalent bonds with lower energy levels, thereby increasing the stability of nickel to remain in an ionic phase. The ordered structure of the intermolecular periodic structure [37] at 2θ of 8º could be maintained at a lower concentration of nickel, but became more disordered and shifted to a lower degree of 2θ by increasing the metal ratio. Moreover, a wide diffraction peak of siloxane of near 2θ at 20º

showed that the intensity was both decreased and broadened by increasing the nickel/amine mole ratio, indicating the formation of a more amorphous structure [37, 38]. The excesses of nickel uncoordinated with amino groups easily formed metallic nickel and resulted in phase separation that was detected by the formation of crystalline nickel nanoparticles. High-temperature phase separation or metal segregation could be occurring from inhomogeneously distributed nickel. An optimized amount of nickel content generates a higher stabilization degree of coordinated Ni-BTPA sol and prohibits metal segregation. As a comparison, Fig. 3-2(b) presents the XRD patterns of Ni-BTPA xerogel powders with metal ratios ranging from 0 to 1.0 obtained at a calcination temperature of 250 °C. The slight conformation of metallic nickel nanoparticles at a 2θ of 45° was observed when the metal ratio was 0.50, which obviously was higher than 0.25. The intensity of nickel nanoparticles became stronger with increases in the metal concentrations. It should be noted that nickel is known to be theoretically coordinated with four amines in free solutions [39, 40], which seems appropriate for organosilica-based sol and gels.

In Fig. 3-2(c), the low-resolution TEM photographs (upper figures) and representative high resolution (lower figures) examples show a transparent surface for BTPA and Ni-BTPA with a low concentration of nickel (Ni/NH = 0.125, and 0.25), which means a uniform dispersion of nickel nanoparticles. Nickel nanoparticles could be observed at a metal ratio of 0.50, indicating that a nickel mole ratio higher than 0.25 tends to inhomogeneously distribute nickel [41], resulting in non-coordinating nickel that leads to the formation of phase separation. Similarly, diffraction pattern images also show diffusing halo patterns for pure materials and nickel-composites at low concentrations. The crystallization of nickel particles was observed from a clear ring pattern.

3.3.2 Metal-induced microporosity via nickel-amino interaction

The nitrogen sorption isotherms of BTPA and various Ni-BTPA xerogel powders at -196 °C are presented in Fig. 3-3(a), and the textural properties of each material are presented in Fig. 3-3(b) as a function of the nickel/amine mole ratio. BTPA showed a negligible amount of adsorbed N_2 indicating a non-porous structure. The addition of nickel-ion created a crosslink between the metal electron receptors and the amine electron donors, which produced intraparticle pores as a permanent porosity.
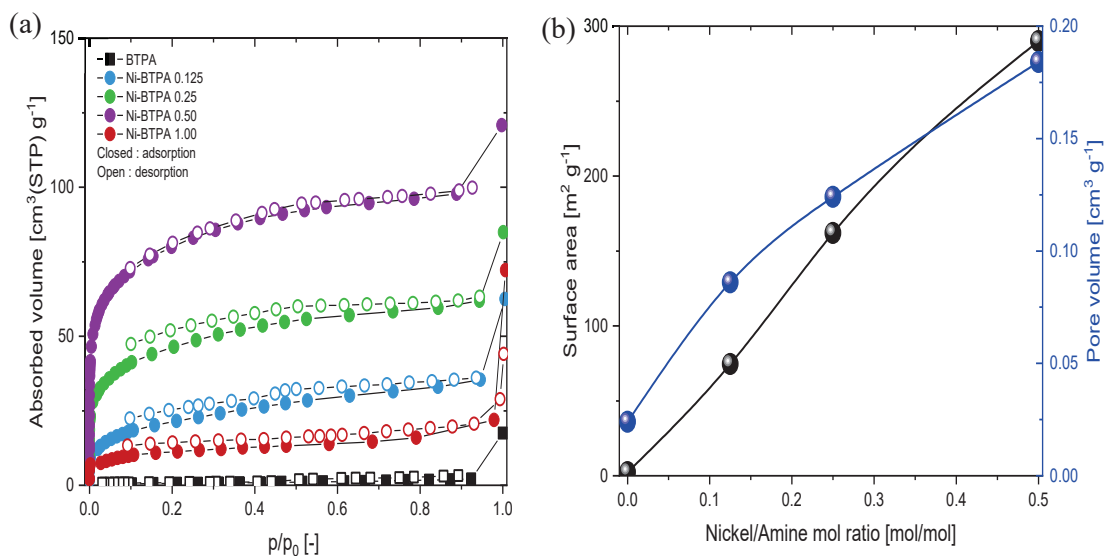
Fig. 3-3. N$_2$ isotherms (-196 ℃) for BTPA and different Ni-BTPA powders heat treated at 250 ℃ (a), and textural properties (surface area and pore volume) as a function of nickel mole ratio for nickel doped aminosilica xerogel powder obtained at the thermal treatment of 250 ℃ (b)

As summarized in Fig. 3-3(b), higher metal ratios produced higher surface areas on the order of Ni-BTPA 0.50 > Ni-BTPA 0.25 > Ni-BTPA 0.125 > BTPA. Although the theoretical coordination in free solutions is 0.25, nickel/amine mole ratios higher than 0.25 are also effective at forming a microstructure, as shown in Fig. 3-3(b). At an overly high nickel mole ratio of 1.00, the excess of nickel ions that were uncoordinated with the amine groups reduced the stability of coordination and led to the formation of nanoparticles resulting in a lowering of the surface area due to phase separation, as confirmed by XRD and TEM characterization (Fig. 3-3(a)).

Vapor-phase sorption isotherms were used to predict the separation performance and possible separation mechanism of Ni-BTPA. As shown in Fig. 3-4(a) and (b), the organic-vapor adsorption isotherm curves of microporous Ni-BTPA powders are preferable for the polar and smaller-sized methanol rather than the non-polar larger-sized toluene. The methanol adsorption capacity for Ni-BTPA was increased by small hysteresis loops following increases in the concentration of the nickel dopant, whereas BTPA showed a lower capacity and a large hysteresis loop. This finding implies that the nitrogen in the BTPA structure and the nickel-dopant both participate to enhance the methanol sorption capacity. The adsorbed organic vapor per the Ni-BTPA repeating unit appears in Fig. 3-4(c), and the undoped-BTPA showed a 0.24 mol mol^{-1} adsorption of methanol that confirmed the preferential adsorption of methanol into polar functional groups such as the amines in the BTPA structure.
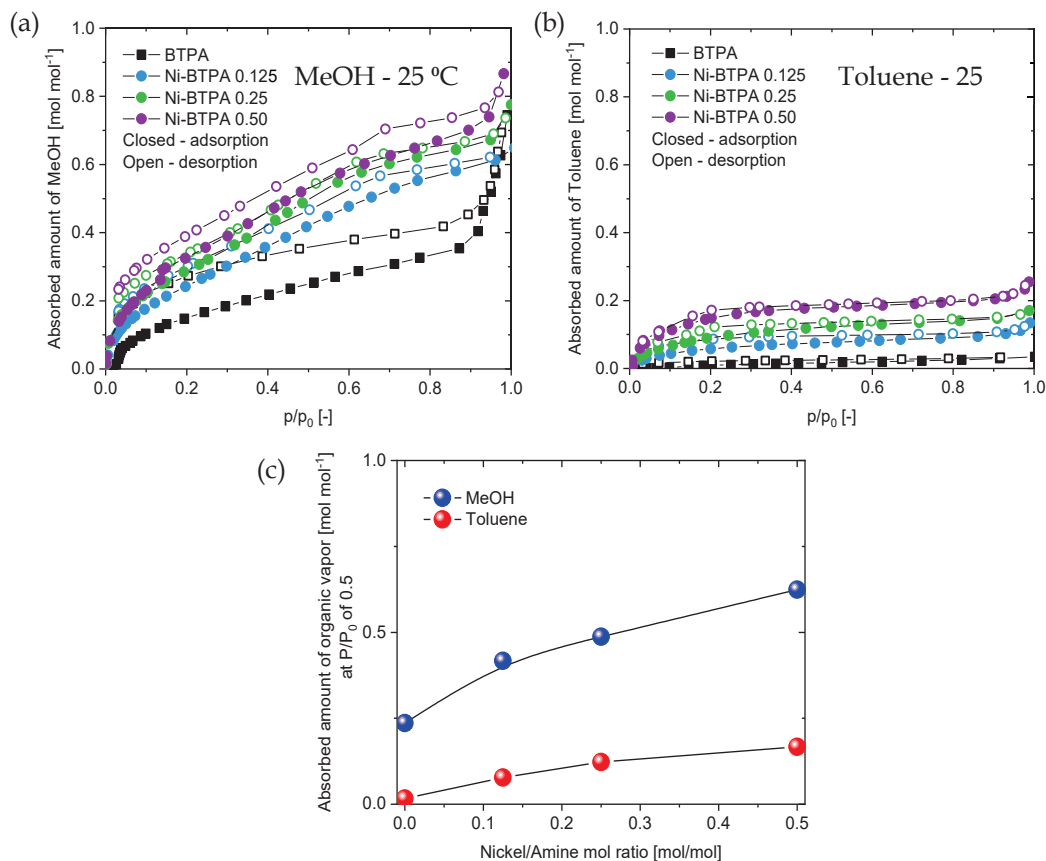
Fig. 3-4. Vapor sorption isotherms of methanol (a) and toluene (b) on Ni-BTPA xerogel powders with different metal mol ratio obtained at 25 ⁰C, and the absorbed amount of organic-vapor as a function of nickel/amine mol ratio at 25 ⁰C (c)

Thereafter, a significant enhancement of methanol sorption was observed approximately linear to the nickel content, and a Ni-BTPA of 0.50 showed the highest adsorption capacity of 0.57 mol mol^{-1}. In contrast, the low adsorption capacity of toluene as a less polar molecule provided plausible evidence of no specific interaction between toluene and the surface of materials. Toluene adsorption was slightly increased after the addition of nickel, which could be related to the higher microporosity of Ni-BTPA.

The specific active site of nitrogen was facilitated due to strong polarization for methanol [42], and the addition of nickel into the BTPA framework created a porous structure that contributed to higher methanol adsorption with a rapid diffusion rate. According to the work of Liu et al., the preferential adsorption of methanol onto a metal organic framework (MOF) structure was simulated via the grand canonical Monte Carlo method (GCMC) combined with density functional theory [43]. That observation shows a lone pair of electrons from the outer orbital of nitrogen molecules induced higher polarization onto methanol molecules, while the existence of a metal dopant firmly increased the specific interaction with methanol that led to

an enhancement of network polarity and multiplied the adsorption affinity [43, 44]. The favorable adsorption of methanol over toluene in Ni-BTPA and BTPA can be ascribed to an affinity with polar amine groups as well as to doped nickel and indicated the enhanced affinity associated to nickel filling pores. In this study, the modified framework was developed from a metal ion-amine crosslink to bring out the hydrophilic surface tendency, resulting in high separation for methanol as a polar component [45].

3.3.3 Tuning a membrane pore-structure via alterations in the nickel content

Single-gas permeance and dimensionless permeance based on He permeance are presented as a function of molecular sizes of the permeating gases in Fig. 3-5. An increase in the nickel mole ratio led to lower gas-transport resistance, and thus improved the permeance of gases on the order of Ni-BTPA 0.50 > Ni-BTPA 0.25 > Ni-BTPA 0.125 > BTPA. Ni-BTPA 1.00, which showed a loose structure with a Knudsen diffusion mechanism. This result could be explained as the generation of interparticle pores by nickel nanoparticles, which were unsuitable for gas separation [25, 46]. In this experiment, single-gas permeation of SiO_2-ZrO_2 as the intermediate layer was measured to compare Knudsen diffusion with Ni-BTPA 1.00 and to analyze the contribution of nickel nanoparticles to the pervaporation performance, as will be discussed in section 3.3.4.
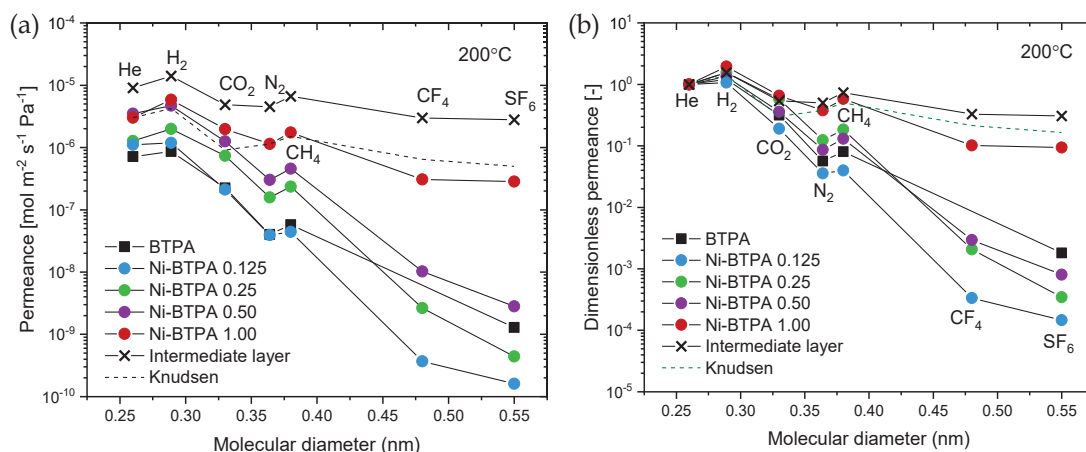
Fig. 3-5. Single-gas permeance as a function of gas molecule sizes (a), and dimensionless permeance based on He permeance (b) for BTPA and Ni-BTPA measured at 200 ºC

Fig. 3-6 shows the permeance and permeance ratios of H_2, N_2, and SF_6 as a function of the nickel/amine mole ratio of Ni-BTPA-derived membranes. The reproducibility of permeation properties has been confirmed since each point in Fig. 3-6 corresponds to a different

----

membrane. The permeance of H_2 and N_2 (Fig. 3-6a-lower figure) became higher with an increase in the nickel mole ratio, while their activation energy (Fig. 3-6b-upper figure) decreased with an increase in the concentration of nickel. The activation energy reflects the interaction between the pore wall of the membrane and permeating molecules [47, 48]; a lower magnitude of activation energy was equated with the generation of larger the pore sizes in the membranes. A general framework structure of organosilica networks originated from the hydrolysis and condensation of pure aminosilica precursors (BTPA), which allowed the formation of a broad pore size distribution and/or defects from grain boundaries. The Ni-BTPA 0.125 and 0.25 membranes showed smaller SF_6 permeance than pure BTPA (Fig. 3-6a-lower figure), which can be explained by the formation of more uniform micro-sized network pores and a defect-free thin layer through the involvement of metal-amine coordination.
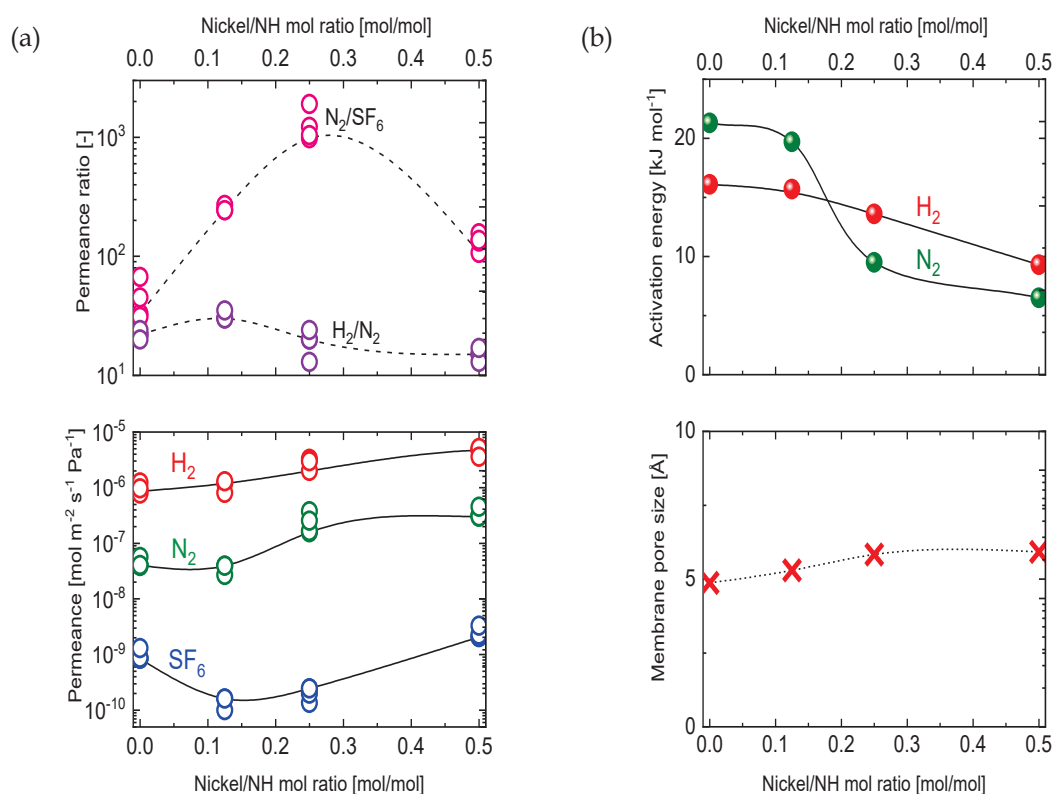
Fig. 3-6. Gas permeance (lower figure) with permeance ratio (upper figure) as a function of nickel mol ratio at 200 ºC (a), and membrane pore size (lower figure) with the activation energy (upper figure) of permeating gases as a function of nickel content (b)

Ni-doped BTPA-derived membranes showed moderate H_2/N_2 selectivity along with a decreasing trend (20 to 10) in the nickel/amine mole ratio, whereas the permeance ratios for N_2/SF_6 (Fig. 3-6a-upper figure) were higher than 100 and 1,000 for nickel/amine mole ratios of 0.50 and 0.25, respectively, which means the membrane pore size was controlled to less than

----

0.55 nm [49]. This finding indicates that a higher level of microporosity could be produced by increasing the nickel concentration, which would lead to an enlargement of the membrane pore size. The cross symbol (red color) in the lower portion of Fig. 3-6(b) shows the pore sizes of membranes that were calculated via a modified-gas translation (m-GT) model [50-52], which also confirms this idea (detailed calculation results are summarized in Fig. S3-10) in the Supporting Information). The pore sizes of the Ni-BTPA membrane gradually increased along with an increase in the nickel/amine mole ratio, which indicated that a higher nickel content tended to generate more crosslinking in the framework. As shown in Fig. 3-6(b), Ni-BTPA 0.25 showed the highest selectivity, which revealed the formation of uniform pores (Fig. S3-10). In contrast, BTPA, Ni-BTPA 0.125, and Ni-BTPA 0.50 showed lower selectivity for SF$_6$, which indicated the pore sizes were not uniform. This result is reasonably explained by a low concentration of nickel, which began the formation of a partially microporous structure that reached a saturation point at 0.25. At a metal ratio of 0.50, the excess amount of nickel tended to produce interparticle pores and gave rise to a wide distribution of pore sizes. Thus, it is clear that the pore size of Ni-BTPA membranes could be controlled by the concentration of nickel as an active site for coordination.
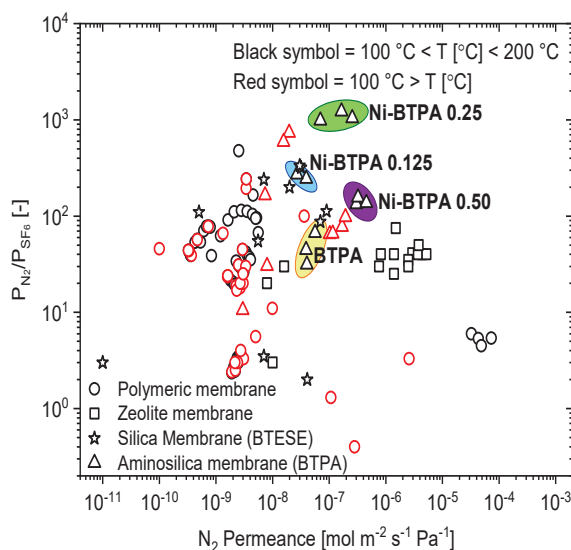
Fig. 3-7. Permeance ratio of N$_2$/SF$_6$ as a function of N$_2$ permeance for various type of membranes. Data plotted in this figure can be found in SI-18.

Fig. 3-7 summarizes the separation performance of N$_2$ over SF$_6$ for various types of membranes, including BTPA and Ni-BTPA membranes. As shown in the figure, microporous Ni-BTPA exhibited competitive performance with an excellent permeance ratio for N$_2$/SF$_6$ of higher than 100 – 1,000 and superior N$_2$ permeance of larger than 1.0×10^{-7} mol m^{-2} s^{-1} Pa^{-1}. Thus, Ni-BTPA membranes could be used for the prospective separation of molecules with a

critical kinetic diameter that ranges from 0.364 nm (N_2) $< d_{p_{Ni-BTPA}} < 0.55$ nm (SF_6). In a previous study, Moriyama et al. evaluate and observed a consistent correlation between single-gas permeation performance at 200 ℃ and pervaporation (PV) at 50 ℃ [53]. Therefore, by following a similar systematic approach, the tuning of membrane pore size in this study was focused on the separation of the methanol (0.38 nm)/toluene (0.59 nm) azeotropic mixture because both molecules have similar molecular sizes of N_2 (0.36 nm)/SF_6 (0.55 nm). Nickel doping was used to tailor the microporosity with an optimized pore size, which would allow methanol (0.38 nm) to pass through the membrane separation barrier, but would reject toluene molecules (0.59 nm) [29]. Based on single-gas permeance data, it was reasonable to expect the possible separation of methanol/toluene by Ni-BTPA membranes.

3.3.4 Ni-BTPA hybrid membranes for azeotropic organic separation by pervaporation

Fig. 3-8 shows the time courses for methanol/toluene pervaporation (PV) of BTPA and various Ni-BTPA membranes coated onto a SiO_2-ZrO_2 intermediate layer under a constant methanol feed concentration and temperature of 10 wt% and 50 ℃, respectively. For comparison, the PV performance of a SiO_2-ZrO_2 intermediate layer with an average pore size of 1 nm was also added to Fig. 3-8 [54]. Steady-state performance of membranes was observed after the first 200 minutes, which corresponds to the stabilization step reported by Yu et al., and this rate of performance continued for more than 10 hours [55]. The SiO_2-ZrO_2 membrane showed high flux and permeance of toluene as a major component in the feed solution, but, due to the large pore size, this membrane failed to separate methanol from a rich toluene mixture (separation factor = 1.9). After the deposition process of amino silica sol as a top-separation layer, the separation performance of the BTPA membrane improved (442), but the membrane flux declined to 0.04 kg m^{-2} h^{-1}. Nickel doping considerably enhanced both methanol flux and permeance, while maintaining a small flux of toluene. A higher flux of methanol could be obtained by increasing the concentration of the nickel dopant. BTPA, Ni-BTPA 0.125, and Ni-BTPA 0.25 showed low values for flux of 0.04 kg m^{-2} h^{-1}, 0.07 kg m^{-2} h^{-1}, and 0.14 kg m^{-2} h^{-1}, respectively. By contrast, Ni-BTPA 0.50 exhibited excellent performance in a stable manner for as long as 7 hours while maintaining a high-flux of 2.8 kg m^{-2} h^{-1} and the highest level of separation factor for methanol (larger than several hundred).
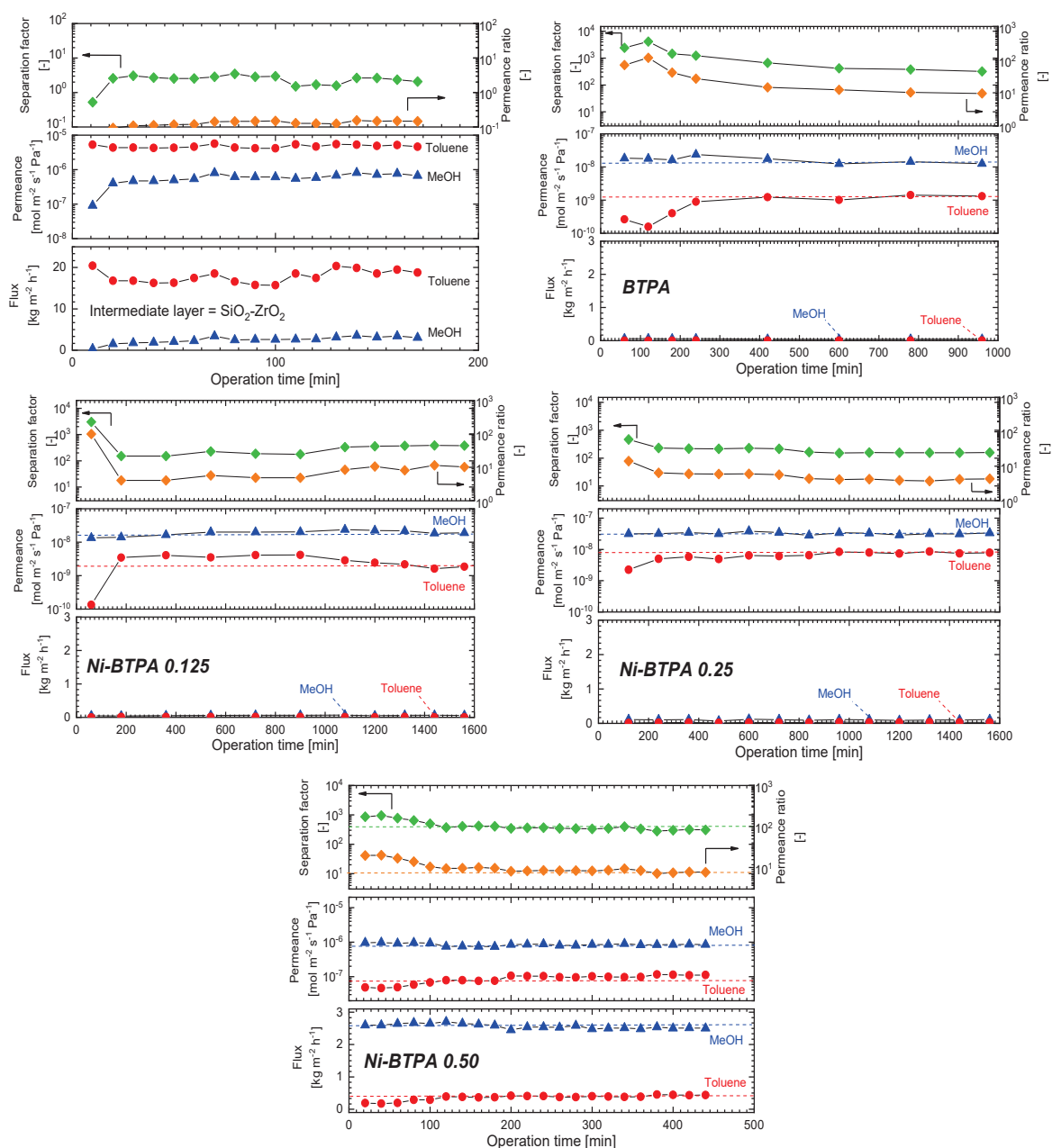
Fig. 3-8 Effective time courses for SiO_2-ZrO_2 layer, BTPA, and Ni-BTPA pervaporation performance in methanol/toluene (10 wt%/ 90 wt%) mixture

The enhancement of both methanol flux and permeance ratio could be ascribed to the specific interaction between uncoordinated nickel as a Lewis acid with a hydroxyl group from methanol as a Lewis-base and increased diffusivity of methanol via larger pore sizes. When the nickel mole ratio exceeds 1.00 (Fig. S3-13) the formation of phase separation tends to reduce the separation factor of the membrane, thus confirming the optimum mole ratio of nickel dopant at 0.50.

Pervaporation performances are summarized as a function of the nickel/amine mole ratio in Fig. 3-9(a), while Fig. 3-9(b) shows the trade-off relationship between total flux and methanol separation performance for comparison with other types of membranes. Ni-BTPA 0.125 and Ni-BTPA 0.25 showed higher total flux than pure BTPA membranes but with lower selectivity. This result revealed a trade-off where a more permeable membrane tends to show a lower level of selectivity [56]. Contrary to expectations, Ni-BTPA 0.50 showed a significant improvement in performance and reached methanol flux higher than 1 kg m^{-2} h^{-1}, which is about 70-fold higher than that of BTPA, while selectivity increased from 442 to 907. It should be noted that each point in Fig. 3-9(a) corresponds to one membrane, which confirmed the reproducibility of membrane fabrication. The Ni-BTPA 0.50 derived membrane showed attractive performance with a much-enhanced flux and separation factor by comparison with the other types of membranes (Fig. 3-9(b)), due to the balance between the formation of microporosity that was induced by amine-nickel coordination and the excessive amount of nickel ions that facilitated the fast transport of methanol while restraining the transport of toluene.
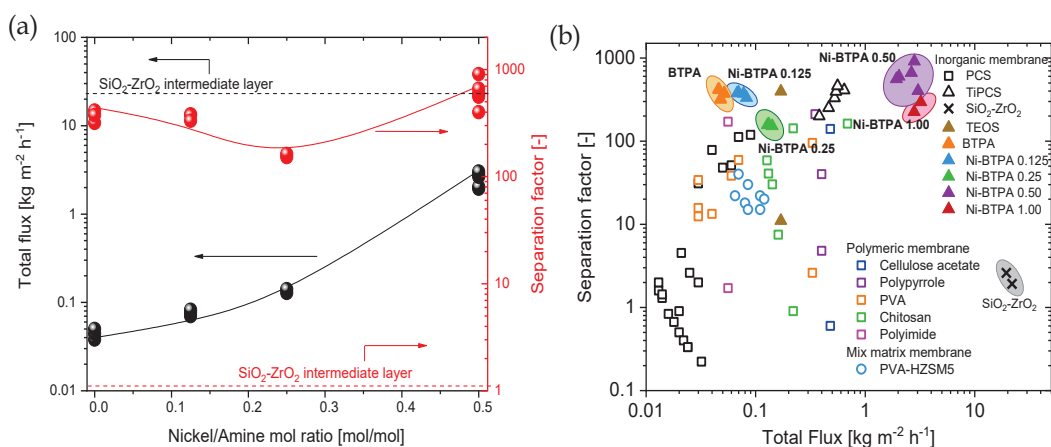
Fig. 3-9. The pervaporation performance of SiO$_2$-ZrO$_2$ as intermediate layer, BTPA, and Ni-BTPA membranes for methanol/toluene separation (10 wt%/ 90 wt%) at 50 ℃ (a), and the trade off between methanol/toluene separation factor as a function of total flux for a different type of membranes (b).

The effect of the methanol feed concentration on Ni-BTPA 0.50 pervaporation performance was studied for compositions ranging from 10 wt% to 50 wt% of methanol in feed solutions at a constant temperature of 50 ℃, as presented in Fig. 3-10. The flux of methanol was gradually increased, while the flux of toluene remained constant when the concentration of methanol in the feed solution was increased. Methanol and toluene permeance were approximately constant from 10 – 50 wt%, indicating an almost constant permeance ratio. It

should be noted that toluene permeance in the pure system was lower than that in the mixture, which could be ascribed to the preferential adsorption of methanol. The methanol permeance in a single component was higher than in the mixture, suggesting that toluene hindered the methanol permeation. This finding is consistent with that of Moriyama et al. who also found that, as a major component, an organic mixture blocks the permeation of minor compounds, resulting in lower permeance in a binary system [53]. In addition, methanol preferentially adsorbs at the surface of the membrane due to hydrophilic surface properties via crosslinked amine-nickel coordination, which leads to high performance in breaking the azeotropic balance.
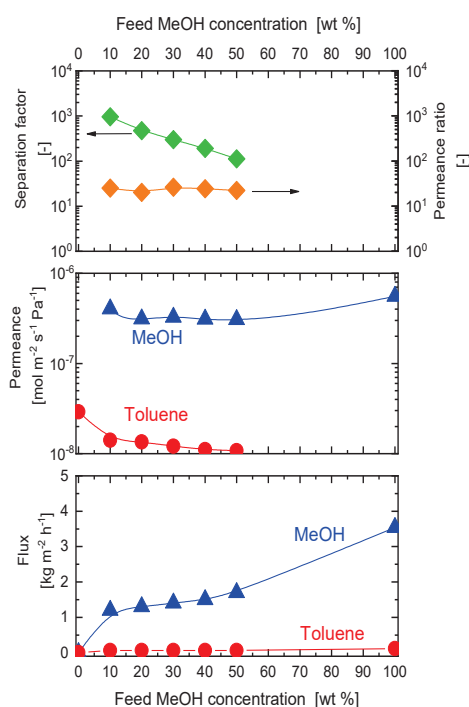
Fig. 3-10. The effect of methanol feed concentration (wt%) through Ni-BTPA 0.50 membrane pervaporation performance at 50 °C

A competitive level of adsorption was also observed even at low concentrations of methanol where the diffusion selectivity favors the smaller molecules (0.38 nm) of methanol compared with the larger size of toluene molecules (0.59 nm), which results in pore blockage for toluene.

Pervaporation performance for the Ni-BTPA 0.50 membrane was examined at temperatures ranging from 30 °C to 50 °C with a constant methanol concentration of 10 wt%, as shown in Fig. 3-11. Methanol flux was increased by increasing the temperature of measurement (0.76 to 1.52 kg m^{-2} h^{-1}), while the flux of toluene remained constant or slightly increased (0.04 to 0.05 kg m^{-2} h^{-1}), resulting in a higher separation factor at high temperature.

A higher operating temperature of pervaporation enhances the feed-side vapor pressure and as a driving force for the smaller molecules of methanol, which results in the enrichment of methanol in the micropores and prevents the entrance of toluene.
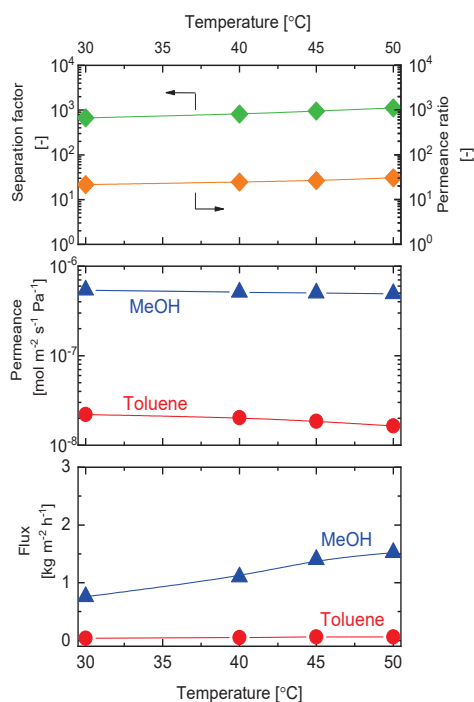
Fig. 3-11. Temperature dependency of Ni-BTPA 0.50 membrane on: flux, permeance, permeance ratio and separation factor for methanol/toluene (10/90 wt%)

Moreover, the higher operating temperature of the pervaporation process may lead to an enhancement of the framework structural mobility, which would create more free volume to be occupied by permeating molecules and would facilitate fast transport within the membrane network.

To deepen the understanding of molecular transport in the pervaporation process, the activation energy of permeance for each component was calculated using the Arrhenius equation, as shown in Eqns. (3-5) and (3-6), and summarized in Table 3-3.

$$P = P_0 exp\left(-\frac{\Delta E_p}{RT}\right) \tag{3-5}$$

$$\Delta E_p = \Delta E_d - \Delta H_s \tag{3-6}$$

In that equation, P, P_0, ΔE_p, R, and T are the permeance, the pre-exponential factor, the activation energy of permeation, the gas constant, and the absolute temperature, respectively, while ΔH_s is the heat of adsorption and ΔE_d is the activation energy for the diffusion process.

Table 3-3. The activation energy for methanol and toluene according to the Arrhenius equation

Compound	Ep [kJ mol^{-1}]
MeOH	-3.73
Toluene	-18.6

As with the previously described effect of the methanol feed-solution concentration, the adsorption-diffusion mechanism dominates the molecular transport behavior of the Ni-BTPA 0.50 membrane. The permeation of methanol and toluene proceeded from the adsorption process with the heat of ΔH_s (positive), followed by diffusion of E_D (positive), giving an activation energy for the permeating molecules of $\Delta E_p = \Delta E_d - \Delta H_s$. Larger ΔH_s and ΔE_d are achieved for more preferential adsorption and stronger steric hindrance, respectively. It is apparent from this table that both methanol and toluene have a negative activation energy ($E_p < 0$), which means the heat of adsorption is higher than the activation energy for diffusion [57]. The Ni-BTPA 0.50 membrane shows a negative value of E_p for both methanol and toluene, which means that the permeance of both molecules was decreased as the temperature of measurement increased. Interestingly, methanol showed a large E_p compared with toluene, which revealed that methanol permeance increased faster as the temperature increased. As discussed in Figure 3-4(c), ΔH_s for methanol would be larger than that for toluene due to a larger affinity to Ni-BTPA. Therefore, the ΔE_d for methanol should be larger than that for toluene. Although the ΔE_d of toluene should have been larger than that of methanol under molecular sieving, a lower ΔE_d for toluene than that for methanol suggests the permeation of methanol occurs primarily through small pores via activated diffusion while toluene could permeate only through a large pore via the surface diffusion process.

3.4 Conclusions

Ordered microporous nickel-doped BTPA membranes were fabricated via different nickel loadings to create coordination with nitrogen-enriched BTPA precursors. Spectroscopic characterization consistently showed a linear correlation between material properties and membrane performance, where a higher nickel content generated a higher surface area of Ni-BTPA powders on the order of Ni-BTPA 0.50 > Ni-BTPA 0.25 > Ni-BTPA 0.125 > BTPA. The pore size of the Ni-BTPA membranes also increased with Ni-doping with a higher gas flux of the membrane. Afterward, a higher nickel content (1.00) tended to generate phase separation

----

that reduced the separation factor of the membrane, thus further confirming that the optimal point for a nickel mole ratio is 0.50. Ni-BTPA exhibited superior performance for gas separation ($N_2/SF_6 > 100 – 1,000$, N_2 permeance $> 10^{-7}$ mol m^{-2} s^{-1} Pa^{-1}) and methanol/toluene separation with high flux and separation factors of 2.8 kg m^{-2} h^{-1} and 907, respectively, for a 10 wt% methanol concentration in the feed solution.

References

[1] R.W. Baker, Membrane Technology And Applications, John Wiley & Sons, 2012.

[2] G. Genduso, H. Farrokhzad, Y. Latré, S. Darvishmanesh, P. Luis, B. Van der Bruggen, Polyvinylidene Fluoride Dense Membrane For The Pervaporation Of Methyl Acetate–Methanol Mixtures, J. Membr. Sci., 482 (2015) 128-136.

[3] S. Moulik, V. Bukke, S.C. Sajja, S. Sridhar, Chitosan-Polytetrafluoroethylene Composite Membranes for Separation of Methanol and Toluene by Pervaporation, Carbohydrate polymers, 193 (2018) 28-38.

[4] R.D. Noble, S.A. Stern, Membrane Separations Technology: Principles and Applications, Elsevier, 1995.

[5] G. Dong, H. Nagasawa, L. Yu, M. Guo, M. Kanezashi, T. Yoshioka, T. Tsuru, Energy-Efficient Separation of Organic Liquids Using Organosilica Membranes via a Reverse Osmosis Route, J. Membr. Sci., 597 (2020) 117758.

[6] Z. Han, Y. Ren, H. Li, X. Li, X. Gao, Simultaneous Extractive And Azeotropic Distillation Separation Process For Production Of Poden From Formaldehyde And Methylal, Ind. Eng. Chem. Res., 58 (2019) 5252-5260.

[7] J.s.A. Jaime, G. Rodríguez, I.n.D. Gil, Control of an Optimal Extractive Distillation Process with Mixed-Solvents as Separating Agent, Ind. Eng. Chem. Res., 57 (2018) 9615-9626.

[8] K. Mishra, N. Kaistha, Synthesis, Design, and Control of an Azeotropic Distillation System for Methanol–Isopropyl Acetate Separation, Ind. Eng. Chem. Res., 58 (2018) 1229-1243.

[9] S. Sun, L. Lü, A. Yang, W. Shen, Extractive Distillation: Advances in Conceptual Design, Solvent Selection, and Separation Strategies, Chin. J. Chem. Eng., 27 (2019) 1247-1256.

[10] D.S. Sholl, R.P. Lively, Seven Chemical Separations to Change The World, Nature, 532 (2016) 435-437.

[11] Y.K. Ong, G.M. Shi, N.L. Le, Y.P. Tang, J. Zuo, S.P. Nunes, T.-S. Chung, Recent Membrane Development for Pervaporation Processes, Prog. Polym. Sci., 57 (2016) 1-31.

[12] N. Moriyama, H. Nagasawa, M. Kanezashi, T. Tsuru, Pervaporation Dehydration of Aqueous Solutions of Various Types of Molecules via Organosilica Membranes: Effect of Membrane Pore Sizes and Molecular Sizes, Sep. Purif. Technol., 207 (2018) 108-115.

[13] T. Tsuru, A. Sasaki, M. Kanezashi, T. Yoshioka, Pervaporation of Methanol/Dimethyl Carbonate Using SiO_2 Membranes with Nano‐Tuned Pore Sizes and Surface Chemistry, AlChE J., 57 (2011) 2079-2089.

[14] S.-L. Wee, C.-T. Tye, S. Bhatia, Membrane Separation Process—Pervaporation through Zeolite Membrane, Sep. Purif. Technol., 63 (2008) 500-516.

[15] P.D. Chapman, T. Oliveira, A.G. Livingston, K. Li, Membranes for The Dehydration of Solvents by Pervaporation, J. Membr. Sci., 318 (2008) 5-37.

[16] Y.-L. Liu, C.-H. Yu, K.-R. Lee, J.-Y. Lai, Chitosan/Poly (Tetrafluoroethylene) Composite Membranes Using in Pervaporation Dehydration Processes, J. Membr. Sci., 287 (2007) 230-236.

[17] V.V. Namboodiri, L.M. Vane, High Permeability Membranes for The Dehydration of Low Water Content Ethanol by Pervaporation, J. Membr. Sci., 306 (2007) 209-215.

[18] J.H. Chen, Q.L. Liu, J. Fang, A.M. Zhu, Q.G. Zhang, Composite Hybrid Membrane of Chitosan–Silica in Pervaporation Separation of MeOH/DMC Mixtures, J. Colloid Interface Sci., 316 (2007) 580-588.

[19] C. Hu, B. Li, R. Guo, H. Wu, Z. Jiang, Pervaporation Performance of Chitosan–Poly (Acrylic Acid) Polyelectrolyte Complex Membranes for Dehydration of Ethylene Glycol Aqueous Solution, Sep. Purif. Technol., 55 (2007) 327-334.

[20] M. Li, J. Wang, S. Zhou, A. Xue, F. Wu, Y. Zhao, Polyacrylonitrile-Supported Self-Aggregation Crosslinked Poly (Vinyl Alcohol) Pervaporation Membranes for Ethanol Dehydration, Eur. Polym. J., 122 (2020) 109359.

[21] L. Wang, J. Li, Y. Lin, C. Chen, Separation of Dimethyl Carbonate/Methanol Mixtures by Pervaporation with Poly (Acrylic Acid)/Poly (Vinyl Alcohol) Blend Membranes, J. Membr. Sci., 305 (2007) 238-246.

[22] L. Wang, J. Li, Y. Lin, C. Chen, Crosslinked Poly (Vinyl Alcohol) Membranes for Separation of Dimethyl Carbonate/Methanol Mixtures by Pervaporation, Chem. Eng. J., 146 (2009) 71-78.

[23] W. Zhang, Y. Fang, X. Wang, Structure Optimization of Water-Permselective Membrane Surfaces by Reconstruction, J. Membr. Sci., 303 (2007) 173-182.

[24] K. Li, Ceramic Membranes for Separation and Reaction, John Wiley & Sons, 2007.

[25] T. Tsuru, Silica-Based Membranes with Molecular-Net-Sieving Properties: Development and Applications, J. Chem. Eng. Jpn., 51 (2018) 713-725.

[26] K. Yamamoto, J. Ohshita, Bridged Polysilsesquioxane Membranes for Water Desalination, Polym. J., 51 (2019) 1103-1116.

[27] M. Kanezashi, Y. Yoneda, H. Nagasawa, T. Tsuru, K. Yamamoto, J. Ohshita, Gas Permeation Properties for Organosilica Membranes with Different Si/C Ratios and Evaluation of Microporous Structures, AlChE J., 63 (2017) 4491-4498.

[28] U. Anggarini, T. Tsuru, M. Kanezashi, H. Nagasawa, L. Yu, Metal-Induced Microporous Aminosilica Creates A Highly Permeable Gas-Separation Membrane, Mat. Chem. Front., (2021).

[29] M. Van Leeuwen, Derivation Of Stockmayer Potential Parameters For Polar Fluids, Fluid Phase Equilib., 99 (1994) 1-18.

[30] C.M. Hansen, Hansen Solubility Parameters: A User's Handbook, CRC press, 2007.

[31] W. Puthai, M. Kanezashi, H. Nagasawa, K. Wakamura, H. Ohnishi, T. Tsuru, Effect of Firing Temperature on The Water Permeability Of SiO_2–ZrO_2 Membranes for Nanofiltration, J. Membr. Sci., 497 (2016) 348-356.

[32] R. Haddad, E. Yousif, A. Ahmed, Synthesis And Characterization Of Transition Metal Complexes Of 4-Amino-5-Pyridyl-4h-1, 2, 4-Triazole-3-Thiol, Springerplus, 2 (2013) 1-6.

[33] C.-H. Lim, M. Kudisch, B. Liu, G.M. Miyake, C–N Cross-Coupling via Photoexcitation of Nickel–Amine Complexes, J. Am. Chem. Soc., 140 (2018) 7667-7673.

[34] T. Ivanova, A. Naumkin, A. Sidorov, M. Kiskin, V. Novotortsev, I. Eremenko, X-Ray Photoelectron Spectra and Structure of Polynuclear Nickel Complexes, Russ. J. Inorg. Chem., 52 (2007) 1781-1785.

[35] H. Konno, X-ray photoelectron spectroscopy, in: Materials Science and Engineering of Carbon, Elsevier, 2016, pp. 153-171.

----

[36] N. Zhang, J. Wang, H. Huo, L. Chen, W. Shi, C. Li, J. Wang, Iron, Cobalt and Nickel Complexes Bearing Hyperbranched Iminopyridyl Ligands: Synthesis, Characterization and Evaluation as Ethylene Oligomerization Catalysts, Inorg. Chim. Acta, 469 (2018) 209-216.

[37] S.S. Choi, A.S. Lee, H.S. Lee, H.Y. Jeon, K.Y. Baek, D.H. Choi, S.S. Hwang, Synthesis and Characterization of Uv‐Curable Ladder‐Like Polysilsesquioxane, J. Polym. Sci., Part A: Polym. Chem., 49 (2011) 5012-5018.

[38] Y. Kaneko, N. Iyi, T. Matsumoto, H. Usami, Synthesis of Water-Soluble Silicon Oxide Material by Sol-Gel Reaction in Tetraalkoxysilane-Aminoalkyltrialkoxysilane Binary System, J. Mater. Res., 20 (2005) 2199-2204.

[39] J.R. Hartman, R.W. Vachet, J.H. Callahan, Gas, Solution, and Solid State Coordination Environments for The Nickel (II) Complexes of a Series of Aminopyridine Ligands of Varying Coordination Number, Inorg. Chim. Acta, 297 (2000) 79-87.

[40] F. Wagner, E.K. Barefield, N-Alkylation of Macrocyclic Secondary Amine Complexes of Nickel (II), Inorg. Chem., 15 (1976) 408-417.

[41] K. Prasanth, M.C. Raj, H. Bajaj, T. Kim, R. Jasra, Hydrogen Sorption in Transition Metal Modified Mesoporous Materials, Int. J. Hydrogen Energy, 35 (2010) 2351-2360.

[42] X. Ma, L. Li, Z. Zeng, R. Chen, C. Wang, K. Zhou, C. Su, H. Li, Synthesis of Nitrogen-Rich Nanoporous Carbon Materials with C3n-Type from ZIF-8 for Methanol Adsorption, Chem. Eng. J., 363 (2019) 49-56.

[43] Z. Liu, K. Zhang, Y. Wu, H. Xi, Effective Enhancement on Methanol Adsorption in Cu-BTC by Combination of Lithium-Doping and Nitrogen-Doping Functionalization, J. Mater. Sci., 53 (2018) 6080-6093.

[44] Y. Wang, L. Yang, G. Luo, Y. Dai, Preparation of Cellulose Acetate Membrane Filled with Metal Oxide Particles for The Pervaporation Separation of Methanol/Methyl Tert-Butyl Ether Mixtures, Chem. Eng. J., 146 (2009) 6-10.

[45] L. Wang, X. Han, J. Li, X. Zhan, J. Chen, Hydrophobic Nano-Silica/Polydimethylsiloxane Membrane for Dimethylcarbonate–Methanol Separation via Pervaporation, Chem. Eng. J., 171 (2011) 1035-1044.

[46] T. Tsuru, Development of Metal-Doped Silica Membranes for Increased Hydrothermal Stability and Their Applications to Membrane Reactors for Steam Reforming of Methane, J. Jpn. Pet. Inst, 54 (2011) 277-286.

[47] H.R. Lee, M. Kanezashi, Y. Shimomura, T. Yoshioka, T. Tsuru, Evaluation and Fabrication of Pore‐Size‐Tuned Silica Membranes with Tetraethoxydimethyl Disiloxane for Gas Separation, AlChE J., 57 (2011) 2755-2765.

[48] A. Shelekhin, A. Dixon, Y. Ma, Theory of Gas Diffusion and Permeation in Inorganic Molecular‐Sieve Membranes, AlChE J., 41 (1995) 58-67.

[49] M. Kanezashi, T. Shioda, T. Gunji, T. Tsuru, Gas Permeation Properties of Silica Membranes with Uniform Pore Sizes Derived from Polyhedral Oligomeric Silsesquioxane, AlChE J., 58 (2012) 1733-1743.

[50] G. Li, H.R. Lee, H. Nagasawa, M. Kanezashi, T. Yoshioka, T. Tsuru, Pore‐Size Evaluation and Gas Transport Behaviors of Microporous Membranes: an Experimental and Theoretical Study, AlChE J., 61 (2015) 2268-2279.

[51] H. Nagasawa, T. Niimi, M. Kanezashi, T. Yoshioka, T. Tsuru, Modified Gas‐Translation Model for Prediction of Gas Permeation Through Microporous Organosilica Membranes, AlChE J., 60 (2014) 4199-4210.

[52] T. Yoshioka, M. Kanezashi, T. Tsuru, Micropore Size Estimation on Gas Separation Membranes: a Study in Experimental and Molecular Dynamics, AlChE J., 59 (2013) 2179-2194.

[53] N. Moriyama, Y. Kawano, Q. Wang, R. Inoue, M. Guo, M. Yokoji, H. Nagasawa, M. Kanezashi, T. Tsuru, Pervaporation via Silicon‐Based Membranes: Correlation and Prediction of Performance in Pervaporation and Gas Permeation, AlChE J., e17223.

[54] W. Puthai, M. Kanezashi, H. Nagasawa, T. Tsuru, Development and Permeation Properties of SiO_2-ZrO_2 Nanofiltration Membranes with a MWCO of< 200, J. Membr. Sci., 535 (2017) 331-341.

[55] L. Yu, D. Korelskiy, M. Grahn, J. Hedlund, Very High Flux MFI Membranes for Alcohol Recovery via Pervaporation at High Temperature and Pressure, Sep. Purif. Technol., 153 (2015) 138-145.

[56] H.B. Park, J. Kamcev, L.M. Robeson, M. Elimelech, B.D. Freeman, Maximizing The Right Stuff: The Trade-Off Between Membrane Permeability and Selectivity, Science, 356 (2017).

[57] Y. Ma, J. Wang, T. Tsuru, Pervaporation of Water/Ethanol Mixtures Through Microporous Silica Membranes, Sep. Purif. Technol., 66 (2009) 479-485.

Supporting Information

----------SI-(3-1)----------

1. Gas cylinder
2. Pressure controller
3. Stop valve
4. Temperature controller
5. Furnace
6. Membrane module
7. Membrane
8. Pressure gauge
9. Back pressure valve
10. Three way valve
11. Vacuum pump
12. Soap film flow meter
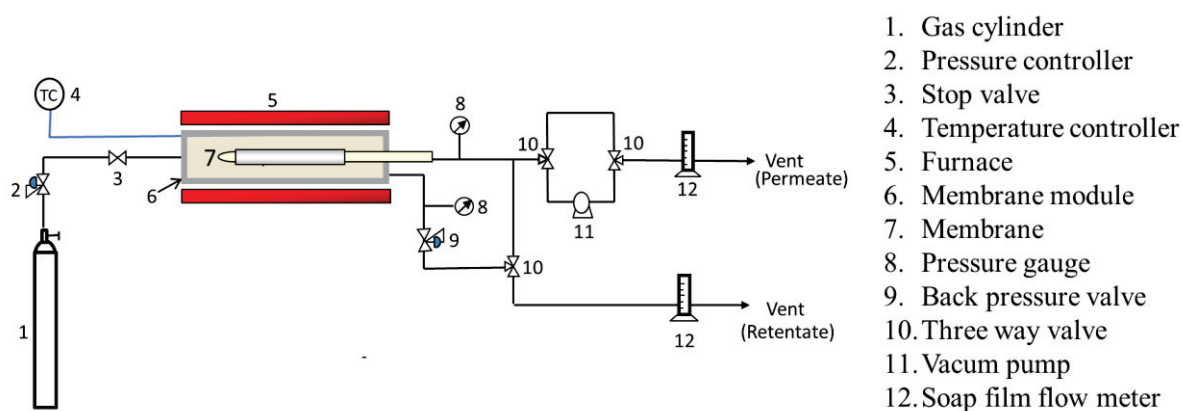
Fig. S3-2. Experimental single-gas permeation apparatus set-up

----

----------SI-(3-2)----------

1. Membrane
2. Heater
3. Screw
4. Cold trap
5. Thermocontroller
6. Thermocouple
7. Motor
8. Vacuum pump
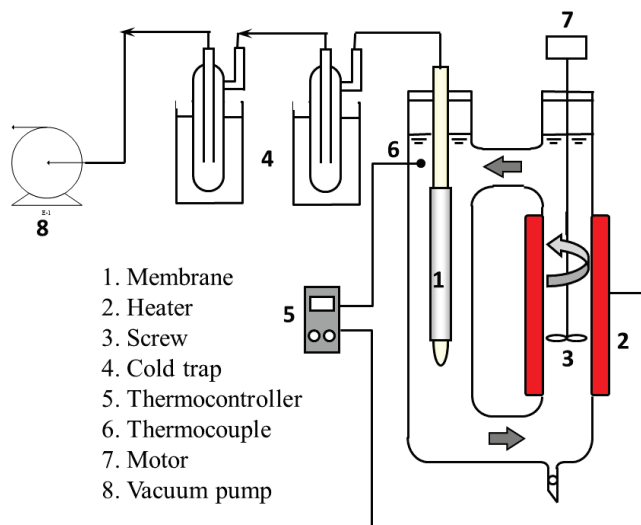
Fig. S3-3. Schematic design of pervaporation apparatus

----------SI-(3-3)----------
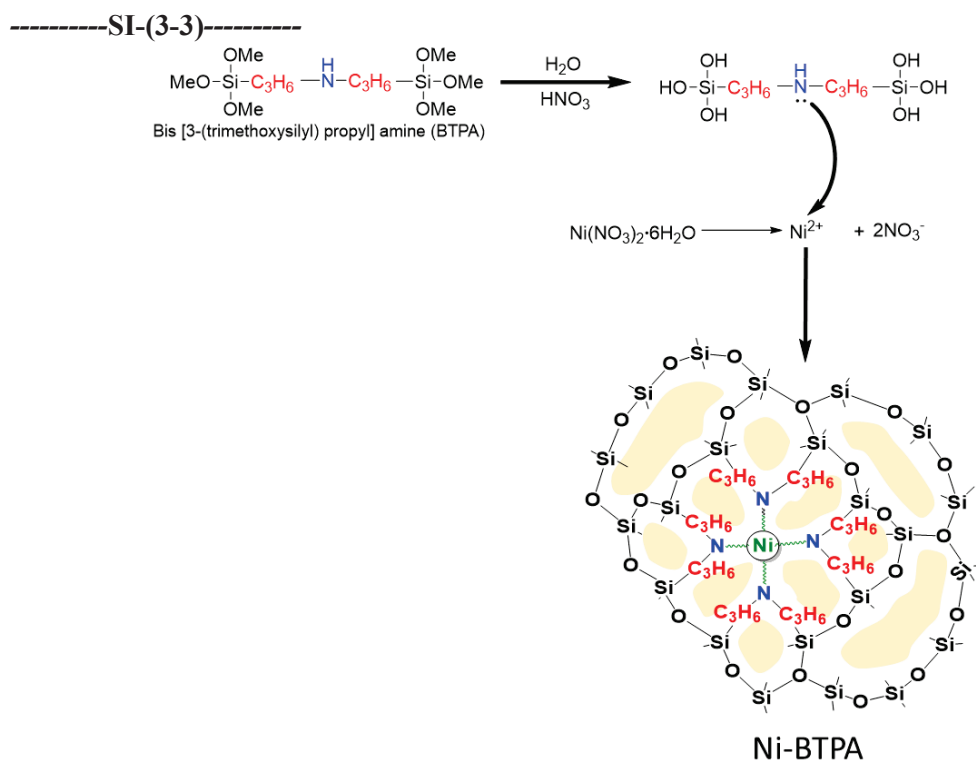
Fig. S3-3. A schematic illustration for the formation of pore structure in Ni-BTPA-derived membrane via hydrolysis and condensation of BTPA precursors, then coordination with nickel ion

Fig. S3-3. shows a possible mechanism for the formation of a coordinated network on Ni-BTPA-derived gels. Metal-doped amine-functionalized organosilica was synthesized via a two-step process that includes (1) hydrolysis and condensation of BTPA precursors in ethanol with nitric acid as an acid catalyst, followed by (2) the incorporation of metal ion (Ni^{2+}) to produce coordination that then induces the formation of a microporous framework. In this study, we assumed that all the methyl groups in the alkoxy chain were fully hydrolyzed and condensed, which was then followed by the conversion of the silanol groups into a siloxane network with calcination under a temperature of 250 ^{o}C (confirmed with FTIR characterization). The incorporation of transition metals such as nickel produced coordination with the amine groups on the linking unit of the BTPA chain so that it could control the rigidity of the BTPA chain to generate a three-dimensional porous network (marked with a colored area in the schematic Fig. S3-3.

----------**SI-(3-4)**----------
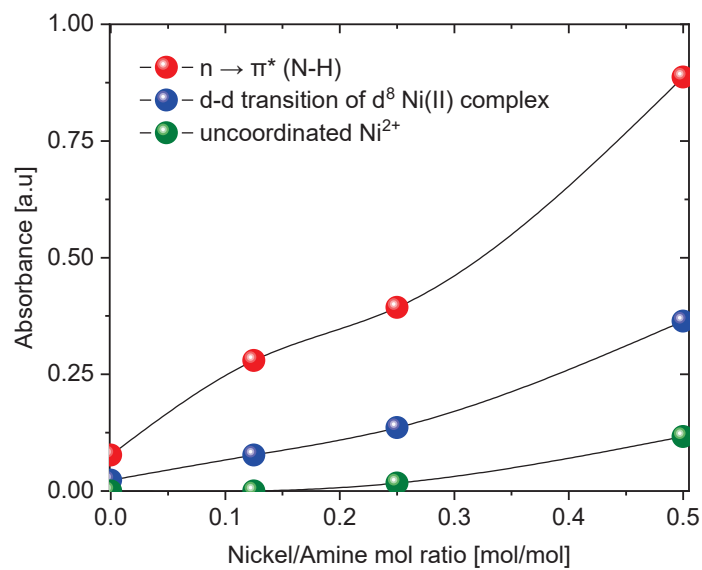
Fig. S3-4. UV-Vis spectral changes of Ni-BTPA as a function of nickel/amine mol ratio

----------**SI-(3-5)**----------
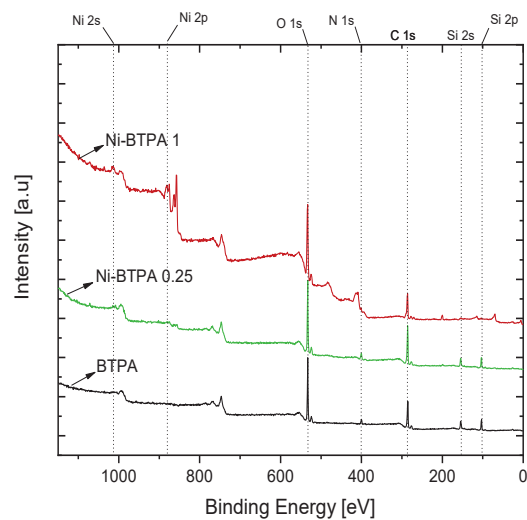
Fig. S3-5. The wide scan energy XPS spectra of BTPA and Ni-BTPA wafer calcined at 250 ⁰C

----------SI-(3-6)----------
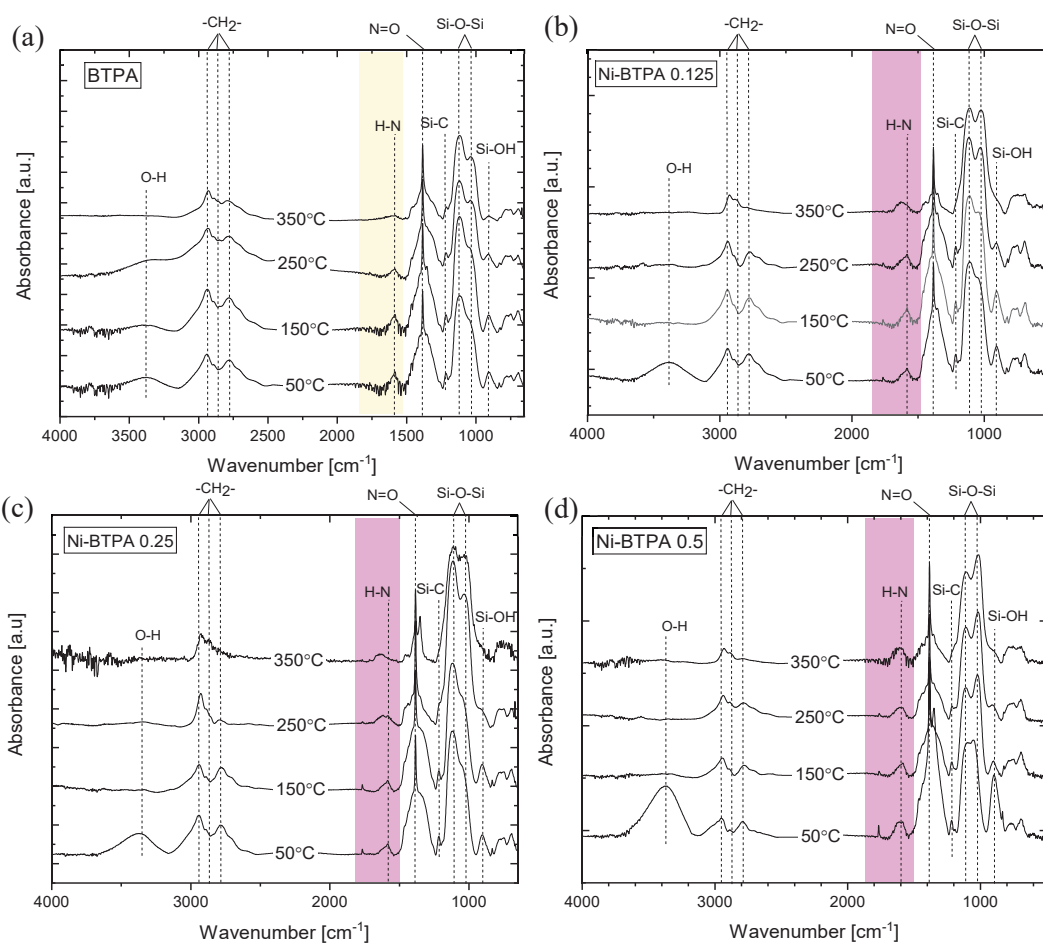
Fig. S3-6. Infrared spectra in the range of 4000-650 cm^{-1} for BTPA (a), Ni-BTPA 0.125 (b), Ni-BTPA 0.25 (c), and Ni-BTPA 0.50 (d) at different calcination temperatures

----------SI-(3-7)----------
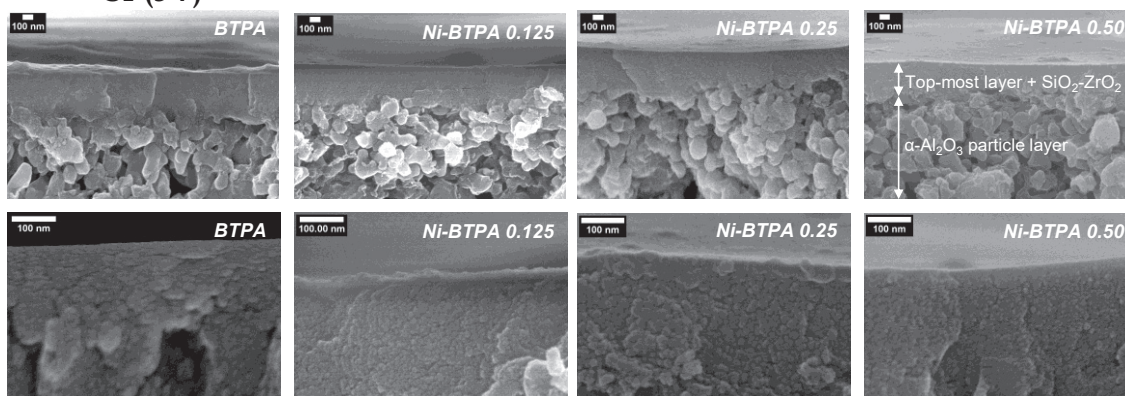
Fig. S3-7. The cross-sectional SEM images for BTPA and Ni-BTPA at different nickel content (upper: low magnification, lower: higher magnification)

-- --

----------SI-(3-8)----------
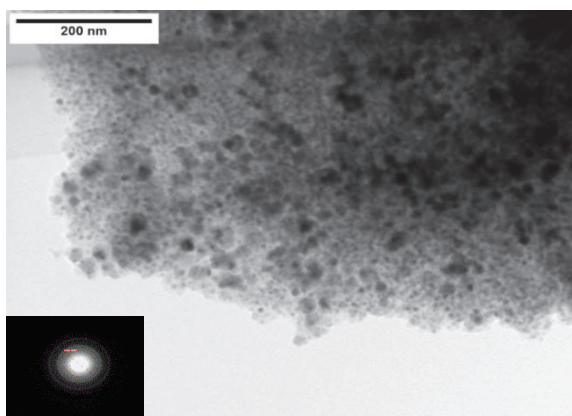
Fig. S3-8. TEM microphotograph of Ni-BTPA 1.00 (insert figure : Ni-BTPA selected-area diffraction pattern with additional white crystalline ring)

----------SI-(3-9)----------
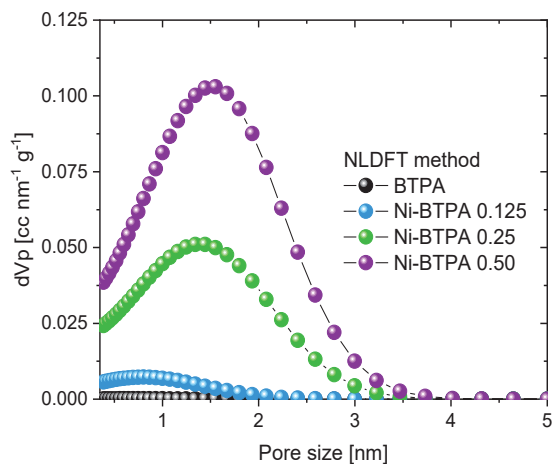
Fig. S3-9. NLDFT pore size distribution of BTPA and different Ni-BTPA powder calcined at 250 ⁰C

Fig. S3-9 reveals a gradual increase in the pore size of Ni-BTPA powder with increases in the metal ratio on the order of Ni-BTPA 0.50 > Ni-BTPA 0.25 > Ni-BTPA 0.125 > BTPA. At a high metal concentration of 0.50, an increasing number of BTPA molecules that act as amine ligands could be coordinated with nickel and result in higher porosity.

----------SI-(3-10)----------

The membrane pore size of BTPA and nickel-doped BTPA were estimated by the modified-gas translation (m-GT) model, as defined by the following equation.

$$\left(\sqrt{M_i}P_i\right)^{1/3} = \left(\frac{k_0}{\sqrt{RT}}exp\left(-\frac{E_{p,i}}{RT}\right)\right)^{1/3}(d_0 - d_i) \qquad (S.3-1)$$

P_i is the permeance of *i-th* gas, M_i is the molecular weight of permeating gas, k_0 is a constant that depends on the structure of the membrane and is independent of any permeating gases, $E_{p,i}$ is a constant for the sake of simplicity, $(d_0 - d_i)$ is the diffusion distance instead of d0 for the *i-th* component, R and T correspond to gas constant and temperature, respectively. The value of $\left(\sqrt{M_i}P_i\right)^{1/3}$ of different gases was plotted as a function of the molecular size of permeating gases (d_i), as presented in Fig. S3-10. The intercept of molecular size at $\left(\sqrt{M_i}P_i\right)^{1/3} = 0$ corresponds to the pore size of the membrane (d_0).
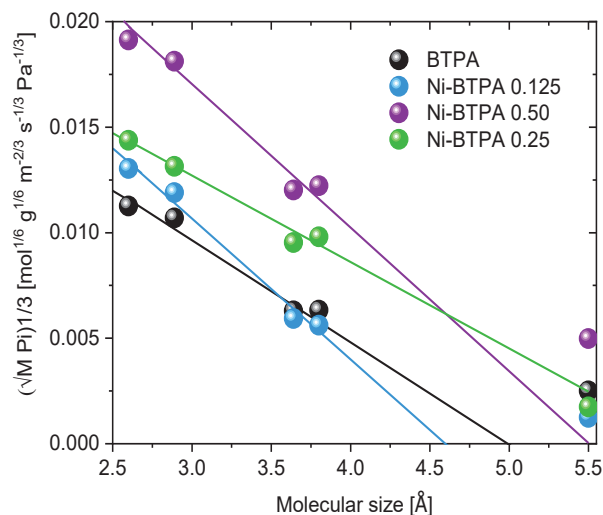
Fig. S3-10. Relationship between molecular size of permeating gases and $\left(\sqrt{M_i}P_i\right)^{1/3}$ for Ni-BTPA derived membranes (solid curves: theoritical value based on Eq (1), symbols: experimental result)

----------**SI-(3-11)**----------
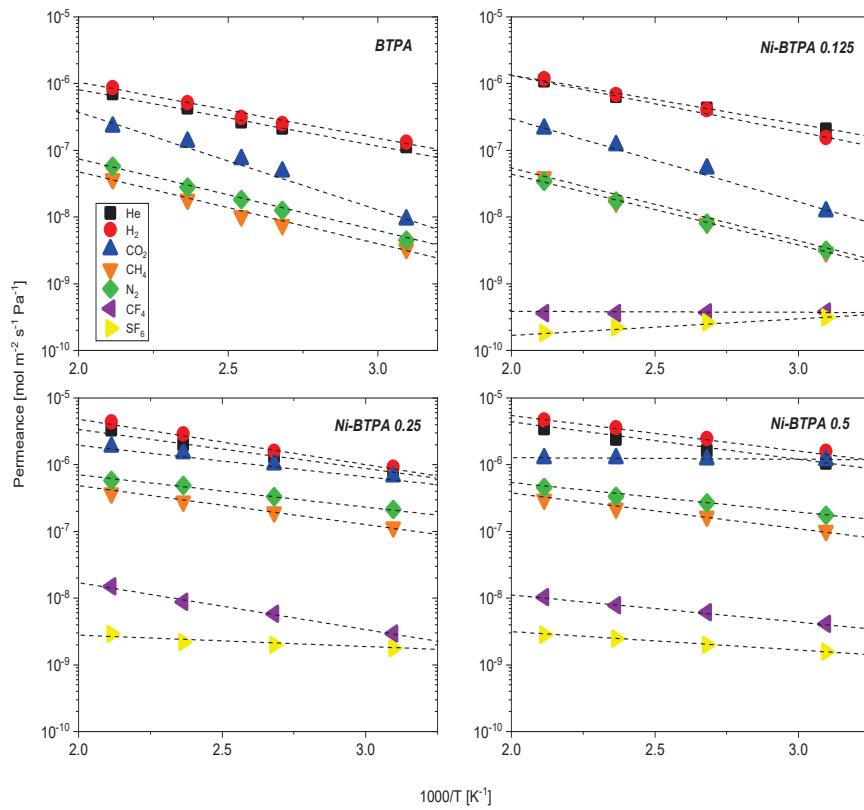
Fig. S3-11. Temperature dependence of gas permeance for BTPA and Ni-BTPA with different metal ratio at the temperature range between 50° to 200°C

----------**SI-(3-12)**----------
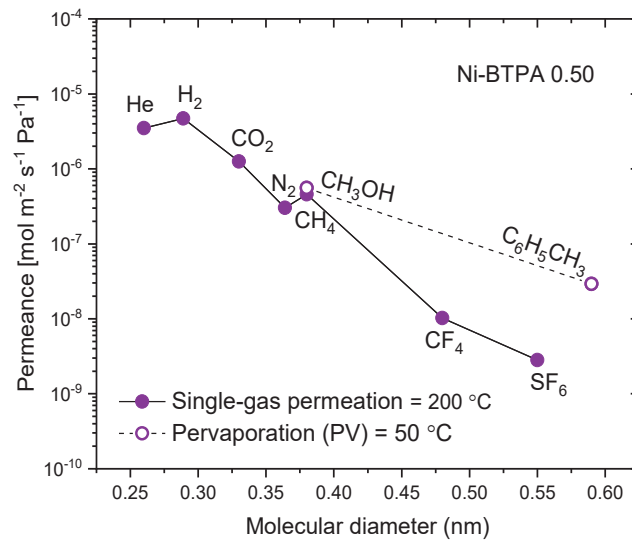
Fig. S3-12. Single gas permeance as a function of molecular diameter dependency (solid line) and pervaporation performance of methanol-toluene separation for Ni-BTPA 0.50

----------SI-(3-13)----------
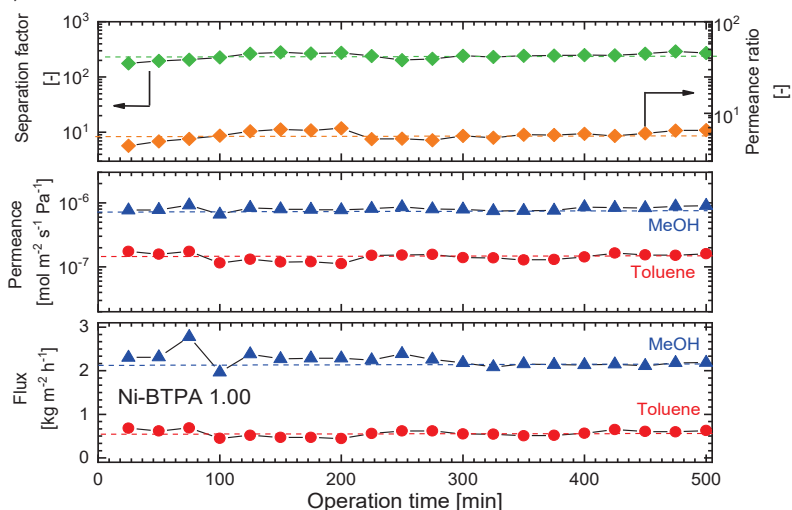
Fig. S3-13. Effective time courses for Ni-BTPA 1.00 pervaporation performance in methanol/toluene (10 wt%/ 90 wt%) mixture

----------SI-(3-14)----------
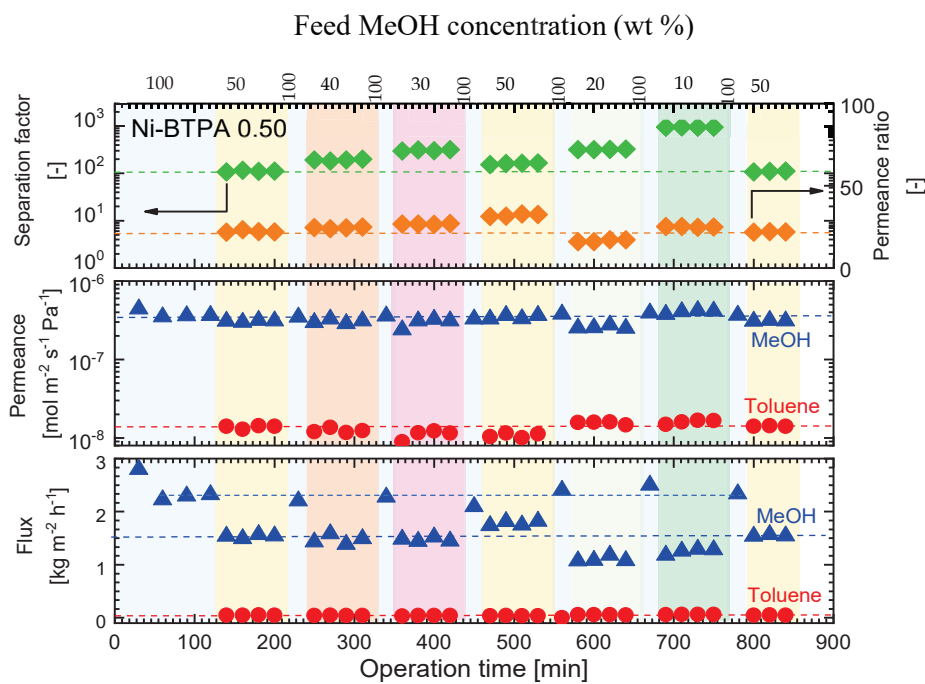
Fig. S3-14. Time course of separation performance at different methanol feed concentration for Ni-BTPA 0.50 membrane measured at 50 °C

----------SI-(3-15)----------
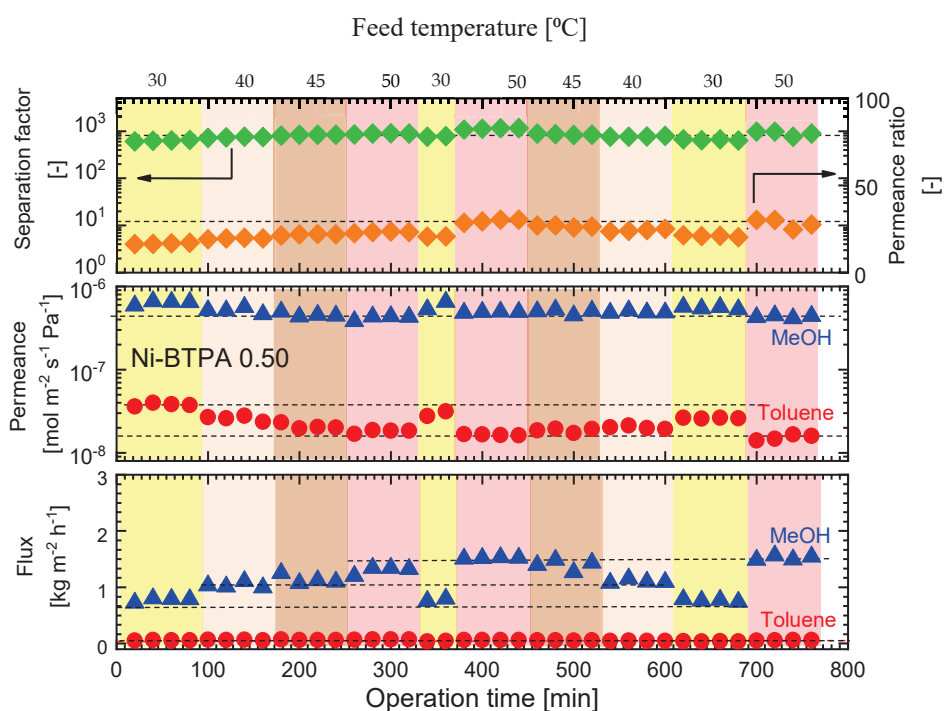
Fig. S3-15 Time course of pervaporation at different temperature through Ni-BTPA 0.50 membrane at feed composition of methanol/toluene mixture of 10 wt%/90 wt%

----------SI-16----------
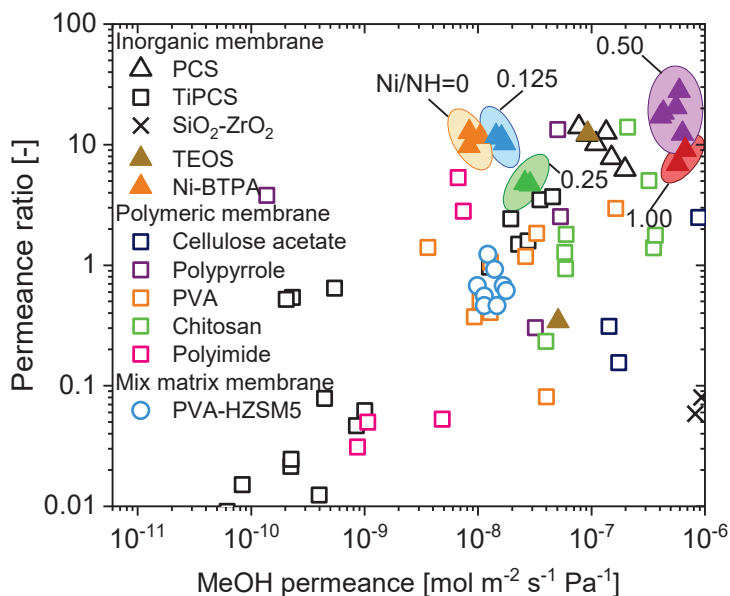
Fig. S3-16 The trade off between methanol/toluene permeance ratio as a function of methanol permeance for a different type of membranes.

--- --

----------SI-(3-17)----------

Table S3-1. Textural properties for BTPA and various Ni-BTPA xerogel powder obtained at the thermal treatment of 250 ºC

Metal doped-BTPA (Ni/NH=mol/mol)	Surface area ($m^2 g^{-1}$)	Pore volume ($cm^3 g^{-1}$)
BTPA	2.36	0.024
Ni-BTPA 0.125	74.6	0.086
Ni-BTPA 0.25	162	0.124
Ni-BTPA 0.50	282	0.184
Ni-BTPA 1.00	38.7	0.064

Hiroshima University Doctoral Dissertation

--- --

Chapter 4

Structural transformation of the nickel coordination-induced subnanoporosity of aminosilica membranes for methanol-selective, high-flux pervaporation

4.1 Introduction

Interest continues to grow for the use of pervaporation as an efficient membrane-based separation technology for the separation of azeotropic compounds, mixtures with close boiling points, mixtures with similar sizes of components, and heat-sensitive organic mixtures [1-4]. Pervaporation is considered a proficient competitive technique compared with conventional separation processes such as extractive distillation, azeotropic distillation, and pressure-swing distillation, albeit with the consequence of high operational demand on energy [5-9]. With pervaporation, feed liquid mixtures are selectively transported into the vapor phase at the permeate side after vaporization through a semi-permeable membrane via preferential sorption and diffusion processing [10]. This technique shows great performance and cost-effectiveness for the removal of trace volatile organic components from aqueous solutions, dehydration of aqueous-organic solvents, and the separation of organic-organic mixtures [11-16].

The pervaporation of organic mixtures has been focused on polar/non-polar mixtures such as methanol/ methyl tert-butyl ethers (MeOH/ MTBE – azeotropic mixture with a ratio of 14/ 86 wt%), methanol/ dimethyl carbonate (MeOH/ DMC) – 70/30 wt%, and methanol/ toluene (MeOH/ Tol) – 73/27 wt% [2, 17, 18]. Ethyl acetate (EA) mixed with MeOH is commonly used in the pharmaceutical industry to produce aminothioxime acid, gastrodin, etc. However, the separation of EA and MeOH is required in order to recycle and reduce pollution [19]. MTBE as a lead-free octane enhancer in gasoline fuel has been industrially produced from MeOH and isobutylene, but this additive faces a challenge in purification due to the formation of an azeotropic mixture [20]. DMC is an important chemical that is widely used as a gasoline additive due to an oxygen content that is higher than that of MTBE [21]. DMC is also used as a non-aqueous solvent for lithium batteries,

as a constituent in dimethyl sulfate, and as a phosphate substituent in methylation and carbonylation reactions [22, 23]. Toluene is another important solvent that is used extensively for many applications – particularly in the pharmaceutical, petrochemical, and textile industries. In the manufacturing industry, toluene is usually produced through the alkylation of benzene with methanol. However, the product streams contain a mixture of methanol and toluene that must be separated [24]. In addition, MeOH forms azeotropic mixtures during the separation process, which necessitates further methanol removal in order to acquire a highly pure solvent.

For industrial purposes, the development of pervaporation remains a challenging task — membrane materials with high permeance and flux that nonetheless are able to maintain adequate selectivity. The main polymeric membrane materials being considered include cellulose polymers, polyvinyl alcohol, chitosan, polyimide, and polyacrylonitrile [25-31]. These materials are considered to be versatile with simple fabrication methods that translate to a reasonably low-cost investment [32]. On the other hand, polymeric membranes additionally have issues with selective layer swelling, which significantly reduces the stability of membranes under harsh environments [2, 10]. Several studies have used zeolite and metal-organic frameworks (MOFs), which have exhibited chemical, thermal, and mechanical stability for the pervaporation of alcohol/organic solvents [33]. Chen et al. [34] prepared NaY zeolite membranes via fluoride-containing precursors, which provided high flux with a good separation factor for MeOH/DMC that reached 1.02 kg m^{-2} h^{-1} and 100, respectively. Msahel et al. investigated the pervaporation performance of Fe-MOF-MW with a total flux of 0.63 kg m^{-2} h^{-1} and a separation factor of 11 for the separation of MeOH/MTBE [35]. In contrast to such high-flux performance, zeolite and MOF membranes have shown stiff and brittle properties that can lead to the formation of intercrystalline defects during membrane fabrication, which reduces selectivity during operation [36].

An alternative to this has been the emergence of membranes that are robust, microporous, inorganic, and silica-based membranes. These membranes have relatively narrow pore sizes that are adjustable and tremendous levels of performance in terms of both permeance and selectivity; they do not swell in organic solvents; they are able to maintain chemical and thermal stability; and, they have an amorphous structure that gives

them flexibility [37-40]. Moriyama et al. [41] have reported promising pervaporation performance for microporous 1,2-bis(triethoxysilyl)ethane (BTESE $-CH_2-CH_2-$)-derived membranes in dehydration systems with flux as high as 1.1 kg m^{-2} h^{-1}. Dong et al. [14] also reported the utilization of microporous bis(triethoxysilyl)acetylene (BTESA $-C\equiv C-$) membranes with a separation factor as high as 120 and flux as high as 4 kg m^{-2} h^{-1} in the pervaporation of MeOH/DMC (10/90 wt%) mixtures at 50 ^{o}C. Currently, microporous organosilica membranes are commonly custom-tailored via the use of organic templates and spacers [42-44]. Ordered microporous silica is easily formed after the removal of the organic compounds that were introduced as a template into an inorganic matrix via thermal processing. Unfortunately, capillary stress and shrinkage are often involved during condensation reactions, which could result in network collapse and reduction in the pore volume of affected membranes [45]. The spacer method uses a bridged bis-silyl structure and is frequently used to modify the textural properties of organosilica precursors. Kanezashi et al. [46] have successfully developed loose amorphous networks by using high-permeance, defect-free BTESE. Nevertheless, the formation of microporosity has been limited to the use of short and rigid precursors, because an increase in the carbon number between silicon atoms creates high flexibility and has failed to develop a highly permeable network [43, 47].

More recently, we proposed a novel concept for sol formation and the following coordination reaction via the addition of metal ions to create crosslinking units with amine-functionalized organosilica precursors. In our previous studies, we examined the effect that metal affinity and metal mole ratios can exert on the formation of a microporous coordinated network [11, 48]. Nickel ion is known to generate outstanding properties of high microporosity compared with other transition metals such as silver and copper due to the high affinity of nickel ions, which theoretically creates four coordination numbers with amine moieties. In other experimental work, we also found that the microporosity was increased with increases in the nickel/amine mole ratio, which improved the surface area of materials from 2.36 to 282 m^2 g^{-1} [49]. The metamorphosis of dense to tailorable versions of microporous aminosilica has successfully improved the permeability of membranes, and the amorphous phase of the organosilica structure is responsible for maintaining the high selectivity of the membranes due to flexibility. Anggarini et al. [50] report that another attractive feature of this method is the evolution

of the use of metals in two different phases — as ions coordinated with amine moieties and as nanoparticles that confer both high microporosity and facilitate the transport of specific components. A membrane structure that could selectively separate methanol from organic solvents would be desirable for industrial applications, particularly one that preserves the high flux of methanol. A previous investigation by our group showed that the balance between the microporosity induced by amine-nickel coordination and the uniform distribution of an excessive amount of nickel ions in nickel-doped bis [3-(trimethoxysilyl) propyl] amine (Ni-BTPA) facilitates flux that reaches as high as of 2.8 kg m^{-2} h^{-1} with a MeOH/Tol separation factor as high as 900 at 50 $^{\circ}$C [49].

In accordance with previous findings based on one type of aminosilica (BTPA), the present study provides new insights for predicting the construction of microporous nickel coordinated aminosilica membranes via different types of amine precursors. Herein, we discuss three types of nickel-doped aminosilica precursors that were synthesized from bis[3-(trimethoxysilyl) propyl] amine (BTPA-bridge-type/secondary amine), trimethoxy [3-(methylamino) propyl] silane (MAPTS-pendant-type/ secondary amine), and 3-amino propyl triethoxy silane (APTES-pendant-type/ primary amine). The resultant materials were systematically studied for their effect on the formation of microporosity, and the structural phases of nickel were studied for their effect on the specific transport of methanol and on selective pervaporation under different types of solvents.

4.2 Experimental

4.2.1 Material synthesis: aminosilica and nickel-modified aminosilica sols

The set of pristine aminosilica precursors used in this experimental work consisted of bridge and pendant amines: bis [3-(trimethoxysilyl) propyl] amine (BTPA), trimethoxy [3-(methylamino) propyl] silane (MAPTS), and 3-amino propyl triethoxy silane (APTES). The chemical structures of these three types of aminosilica precursors appear in Fig. 4-1. Briefly, the sols of aminosilica precursors were synthesized via hydrolysis and condensation to achieve molar ratios of precursor/H_2O/HNO_3 of 1/300/1 and 1/150/1

for bridge and pendant types of precursors, respectively. Ethanol (C_2H_5OH) was used as the solvent to adjust the concentration of precursors to 5 wt%, and then the hydrolysis and condensation reactions were performed under vigorous stirring (550 rpm) at room temperature for 12 h.

Another set of nickel-doped samples was obtained via the addition of nickel nitrate ($Ni(NO_3)_2 \cdot 6H_2O$) as the metal dopant into aminosilica sols followed by a coordination reaction. The coordination reaction was facilitated via the addition of a stoichiometric amount of nickel-metal salts dissolved into the aminosilica precursors in nickel/amine (Ni/NH) mole ratios of 0, 0.25, and 0.5 mol mol^{-1}, followed by stirring for 1 h at ambient temperature. The obtained nickel-doped aminosilica samples are referenced according to the different amounts of nickel ions: Ni-BTPA 0.25, Ni-BTPA 0.50, Ni-MAPTS 0.25, Ni-MAPTS 0.50, Ni-APTES 0.25, and Ni-APTES 0.50. For the membrane preparation, the resultant nickel-doped aminosilica composite materials were diluted by 0.1 wt% using pure water.
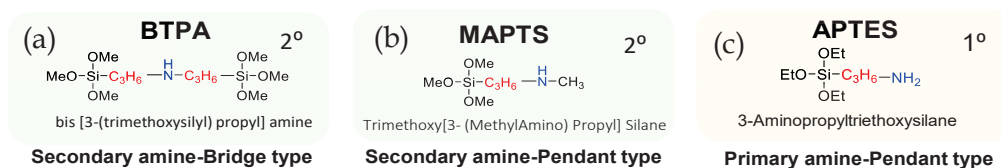
Fig. 4-1. The chemical structure of amine-functionalized alkoxysilanes utilized in this work: BTPA (a), MAPTS (b), and APTES (c).

4.2.2 Characterization of nickel-doped aminosilica films and xerogels

Both pristine and nickel-doped aminosilica gel powders were prepared via a slow solvent evaporation process at 50 °C under an air atmosphere [47]. The chemical structure of nickel-modified aminosilica was examined using Fourier Transform Infrared Spectroscopy (FT/IR-4100, JASCO, Japan) over a wavenumber range of from 500-4,000 cm^{-1}. The nickel-doped aminosilica-derived films were coated onto a potassium bromide (KBr) plate and then calcined at 250, 300, and 350 °C under a N_2 flow for 30 min to assess the thermal stability of amine moieties as the active site for coordination. The formation of the coordinated compound was verified using a UV-Vis diffuse reflectance spectrophotometer (Shimadzu UV-3600 plus) in a range of 200-1,000 nm. The thermal properties of the nickel-modified aminosilica powder were determined using a thermogravimetric mass spectrometer (TG-MS, TGA-DTA-PIMS 410/S, Rigaku, Japan).

A wide-angle powder D2 PHASER X-ray diffractometer (Bruker, Germany) that used Cu Kα radiation in a 2θ range of from 5-80° was used to evaluate the structural transformations of all composites, which included amorphous and crystalline structures ascribed to organosilica and uncoordinated nickel particles, respectively. The formation of nickel nanoparticles was confirmed using a transmission electron microscope (TEM JEOL 2010 Ltd., Japan). Textural characterization was performed using N_2 sorption isotherms at -196 ^{o}C and CO_2 adsorption-desorption isotherms at 25 ^{o}C in a BELMAX (BELJAPAN Inc.). The specific surface area was calculated based on the Brunauer-Emmett-Teller (BET) technique in a P/P_0 range of from 0.05-0.20. All samples were pretreated with heating at 200 ^{o}C under vacuum conditions for 12 hours prior to the adsorption-desorption measurement.

4.2.3 Fabrication of nickel-doped aminosilica membranes and single-gas permeation measurement

Porous α-alumina tubes with 50% porosity and average pore size of 1 μm (length, 100 mm; inner diameter, 8 mm; outer diameter, 10 mm) were used as membrane supports, as supplied by the Nikkato Corporation (Japan) [51]. The α-alumina tubes were connected to non-porous alumina (Al_2O_3) tubes before membrane preparation with glass joints via a heat treatment process at 950 ^{o}C under an air atmosphere [52]. The connection process was repeated two or three times to prevent gas leakage. α-Al_2O_3 particles with average particle sizes of 2 and 0.2 μm were dispersed into a silica-zirconia (SiO_2-ZrO_2) sol as a binder with a solid concentration of 10 wt% and were subsequently coated onto the outer surface of a porous α- Al_2O_3 support followed by calcination at 550 ^{o}C under an air atmosphere for 15 min. These procedures were repeated three times for each type of particle to smooth the surface of the membrane. The intermediate layer consisted of a 0.5 wt% SiO_2-ZrO_2 sol coated onto the surface of the particle layer with firing under an air atmosphere at 550 ^{o}C. These procedures were repeated several times until the average pore size of the support reached approximately 1 nm. Finally, the topmost layer was obtained by double coating 0.1 wt% nickel-doped aminosilica sols (Ni-BTPA, Ni-MAPTS, and Ni-APTES) onto the intermediate layer followed by calcination at 250-350

°C under a flow of N$_2$ for 30-60 min. The nickel-doped aminosilica-derived membranes are referenced by their calcination temperatures (250, 300, and 350 °C under a nitrogen (N$_2$) atmosphere): Ni-BTPA250, Ni-BTPA300, Ni-BTPA350, Ni-MAPTS250, Ni-MAPTS300, Ni-MAPTS350, Ni-APTES250, Ni-APTES300, and Ni-APTES350.

Single-gas permeation experiments were conducted using high-purity components (He, H$_2$, CO$_2$, N$_2$, CH$_4$, CF$_4$, and SF$_6$) under conventional constant pressure at 50-200 °C. Each permeation gas was fed to the outside of the membrane with an upstream pressure of 200 – 400 kPa. The pressure in the permeate was maintained at atmospheric levels, and the flow rate of the permeate was measured using a film flow meter (Horiba, Co. Ltd., Japan). The permeation measurement was recorded after the membrane reached a steady-state with respect to the pressure difference between the shell and the inner side of the membrane and flux. The permeate flow rate was evaluated with errors of less than 5 and 20% for permeance values larger than 10^{-7} and smaller than 10^{-7} mol m^{-2} s^{-1} Pa^{-1}, respectively. The permeance of each gas (P_i) and the ideal selectivity for the $i-th$ and $j-th$ components ($\alpha_{i/j}$) were calculated using the following equations.

$$P_i = {F_i}/{A\Delta p_i} \tag{4-1}$$

$$\alpha_{i/j} = \frac{P_i}{P_j} \tag{4-2}$$

where P_i is the permeance of the $i-th$ component (mol m^{-2} s^{-1} Pa^{-1}), F_i is the permeate molar flow rate of the ith component (mol s^{-1}), A is the effective cross-sectional area of the membrane (m^2), and Δp_i is the partial pressure difference of component i between the feed and the permeate of the membrane (Pa).

4.2.4 Pervaporation (PV) measurement

The separations of 7 types of binary organic mixtures containing methanol (MeOH) (10 wt%) in the feed solution were conducted via the pervaporation process at 50 °C. A schematic diagram of the pervaporation (PV) apparatus appears in the Supporting Information, Fig. S4-2. The physical properties of methanol and the 7 types of organic solvents are summarized in Table 4-1. The mixtures of methanol and organic solvents were circulated using a stirrer at 3,000 rpm to prevent concentration polarization on the surface of the membrane. The pressure of the feed side was maintained at

atmospheric levels, while the permeate side was evacuated to $0 - 2$ kPa (absolute) via the use of a vacuum pump. The permeate vapor was collected using a glass trap cooled in a dewar vessel with liquid nitrogen for each time interval. The concentration of the feed solution was maintained at a constant level during the measurement via the periodical addition of appropriate amounts of pure methanol.

Table 4-1. Physical properties of the selected organic solvents

Penetrant (abbreviation)	MW [g mol^{-1}]	Molecular size [nm]	Density [g cm^{-3}]	Boiling point [ºC]	Hansen solubility [MPa$^{1/2}$]
Methanol (MeOH)	32.04	0.38 [53]	0.791	64.7	29.6
Ethanol (EtOH)	46.07	0.43 [53]	0.789	78.37	26.5
Isopropyl alcohol (IPA)	60.11	0.47 [53]	0.786	82.6	23.6
Tertiary butanol (Tert-BuOH)	74.12	0.51 [53]	0.788	82.0	14.3
Ethyl acetate (EA)	88.12	0.52 [53]	0.895	77.2	18.2
Dimethyl carbonate (DMC)	90.07	0.53 [54]	1.069	90.0	18.7
Isopropyl acetate (i-Pac)	102.1	0.57 [55]	0.872	89.0	17.6
Toluene (Tol)	92.14	0.59 [53]	0.867	110.6	18.0

The compositions of the feed and permeate streams were determined via gas chromatography (GC-14B Shimadzu Cor., Japan). Membrane flux (J) and the flux of each component (J_i) on the permeate side are described by equations (4-3) and (4-4), respectively.

$$J = \frac{w}{A \times t} \tag{4-3}$$

$$J_i = J \times y_{w,i} \tag{4-4}$$

In equations (4-3) and (4-4), J is the total permeate flux (kg m^{-2} h^{-1}), w is the permeate weight (kg), A is the membrane surface area (m^2), t is the permeating time (h), and $y_{w,i}$ is the weight fraction of component i in the permeate. The permeance of component i could be calculated from the molar flux (J_{Mi}) of the i component divided by the difference in the partial pressures of the feed ($p_{i,f}$) and permeate streams ($p_{i,p}$), as determined using equation (4-5).

$$P_i = J_{Mi} \Big/ (p_{i,f} - p_{i,p}) \tag{4-5}$$

The feed partial pressure of the ith component was calculated as $p_{i,f} = \gamma_i x_i p_i^0$, where γ_i is the activity coefficient according to the Wilson parameters, x_i is the mole fraction of the ith component, and p_i^0 is the vapor pressure according to the Antoine equation. On the other hand, the pressure in the permeate stream was presumed to be zero. The separation factor is defined as the ratios of the mole fractions in the permeate (y_i and y_j) and feed (x_i and x_j) streams, as shown by equation (4-6).

$$\alpha = \left(\frac{y_i}{y_j}\right) \Big/ \left(\frac{x_i}{x_j}\right) \tag{4-6}$$

4.3 Results and discussion

4.3.1 The three-dimensional micropore network assembly of nickel-aminosilica via coordinated sol-gel reaction

The reactivity of different types of aminosilica precursors that developed via the nickel-amine coordination was examined using the nickel dopant as the corresponding metal connector at a nickel/amine (Ni/NH) mole ratio of 0.25 mol mol^{-1} with calcination at 250 °C. The UV-vis diffuse reflectance spectra of pristine materials and nickel-doped aminosilica xerogel powders prepared with different types of amine precursors appears in Fig. 4-2(a) along with the FT-IR of both materials.
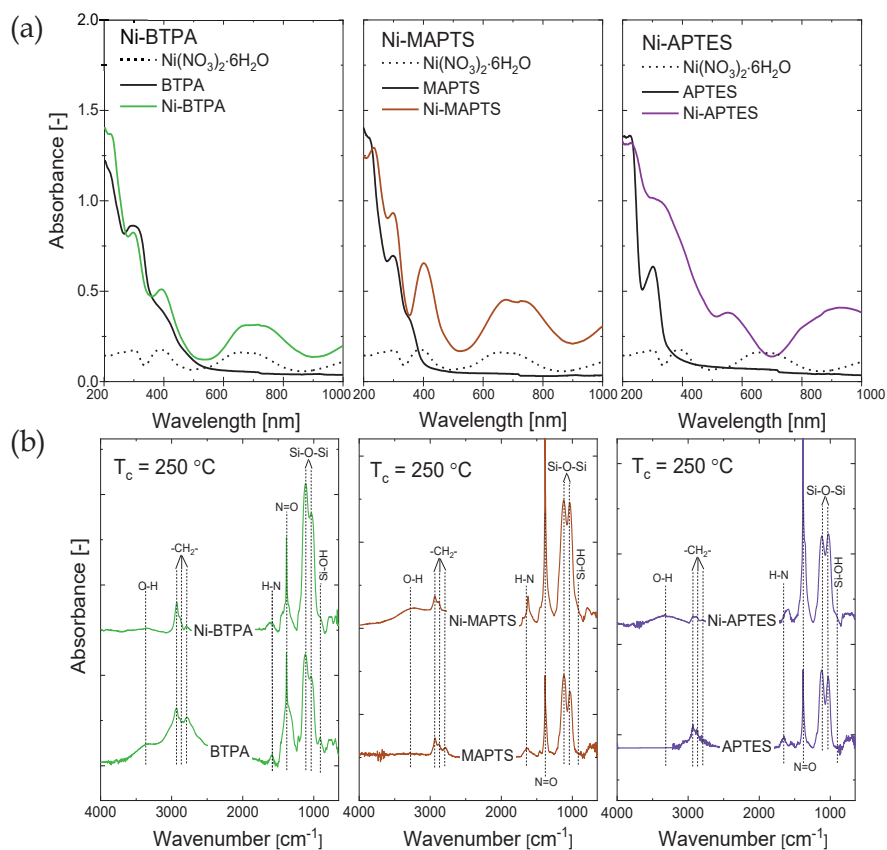
Fig. 4-2. UV-Vis diffuse reflectance absorption spectra (a), and wide range FT-IR spectra (b) for pristine aminosilica (BTPA, MAPTS, APTES) and the resultant nickel-doped aminosilica (Ni-BTPA, Ni-MAPTS, Ni-APTES) xerogel powders obtained at calcination temperature of 250 ℃.

We observed the appearance of two absorption peaks that were detected at wavelengths of approximately 200 (n → σ^*) and 300 nm (n → π^*) for all three aminosilica xerogel powders, which corresponds to the intraligand free-electron transition of amine groups (N-H) and the electron transfer between nitrate ions (N=O), respectively [48]. With the addition of nickel ions at a Ni/NH mole ratio of 0.25 mol mol^{-1}, the color of the mixture turned to yellow, bright green, and dark green for Ni-BTPA, Ni-MAPTS, and Ni-APTES, respectively. The n → σ^* electronic transition was shifted to a higher wavelength, confirming the ligand-to-metal charge transfer (LMCT) transition, which further indicated the formation of a stable coordination of amine groups as a ligand to the nickel-metal ions with lower energy levels [56]. In addition, significant changes in the spectrum of nickel-doped aminosilica composites were discovered in the visible range with the appearance of two new bands, which are summarized in Table 4-2. Similar to those previous reports, the formation of nickel-amine coordination was confirmed via the d-d

transition and further demonstrated characteristics of the tetrahedral environment nearby nickel ions [56, 57]. These results are consistent with our previous findings that nickel ions can be coordinated with four amines in an organosilica solution [49].

The characteristics of the FT-IR peaks were examined in terms of the chemical bonding environment, and the shift of peaks was an indication of the establishment of coordination, as shown in Fig. 4-2(b). All samples showed intense absorption peaks at 1,000-1,100 cm^{-1}, which is attributed to the vibration of the siloxane network (Si-O-Si), accompanied by an amine (N-H) deformation band at approximately 1,600 cm^{-1}.

Table 4-2. The spectroscopy characterization results of UV-vis diffuse reflectance, FT-IR, and powder XRD spectra

Membrane	Peak transition-visible range [nm][a]	ν N-H [cm^{-1}][b]	Periodic chain distance position [2θ/degree][c]
BTPA	-	1588	9.0
Ni-BTPA	391, 704	1583 and 1623	6.5
MAPTS	-	1626	7.1
Ni-MAPTS	406, 735	1622	6.8
APTES	-	1649	7.1
Ni-APTES	554, 925	1593	5.8
Values in parentheses are collected from UV-vis [a], FT-IR [b], XRD [c] characterization.			

A comparison of each nickel-doped amino composite shows that the relative intensity of their Si-O-Si bonds is similar, while the intensity and wavenumber position of the amine-deformation band showed an increased absorbance that featured a red-shift, which is listed in Table 4-2. Wang et al. [58] reported a strong shift for the secondary amine bond after the adsorption of metal ions, which indicated a robust coordination interaction between both components. Behaviors such as intensification and red-shifting verify the incorporation of nickel ions that act as lewis-acids that are capable of inducing the formation of coordination bonds with amine groups as lewis-base molecules [48, 49].

Fig. 4-3(a) shows the X-ray diffraction patterns of pristine aminosilica xerogel powder and nickel-composite materials calcined at 250 °C. The details of the peak positions are tabulated in Table 2. All three aminosilica compounds show two amorphous diffractions patterns centered at 2θ of 7-9° (peak A) and 20-22° (peak B), which reflects the distance of intermolecular periodic linking unit chains in polysisesquioxane and the average spacing in the siloxane framework, respectively (schematic images as shown in Fig. S4-3) [59]. After doping with nickel ions, a distortion into a lower degree of 2θ was

generated around the intermolecular periodic chain consisting of an amine moiety. Instead of that, Ni-MAPTS showed only small structural changes at 2θ of 7°. This finding suggests that the formation of partial nickel-amine coordination on Ni-MAPTS was due to the existence of non-hydrolyzable methyl groups subsequent to the amine functional groups at the calcination temperature of 250 °C. The methyl substituent in the pendant structure of the secondary amine structure of MAPTS increased the steric hindrance for the coordination between nickel ions and amine groups, which consequently prevented the construction of a coordinated framework. In accordance with the present results, previous studies demonstrated that the methylated-pendant chain of organosilica precursors was able to aggregate within the silica network and produced a relatively large volume of steric hindrance, which thereby enforced the nickel-metal center to move away from amine ligands, and resulted in a weakened affinity for coordination [42, 60, 61].
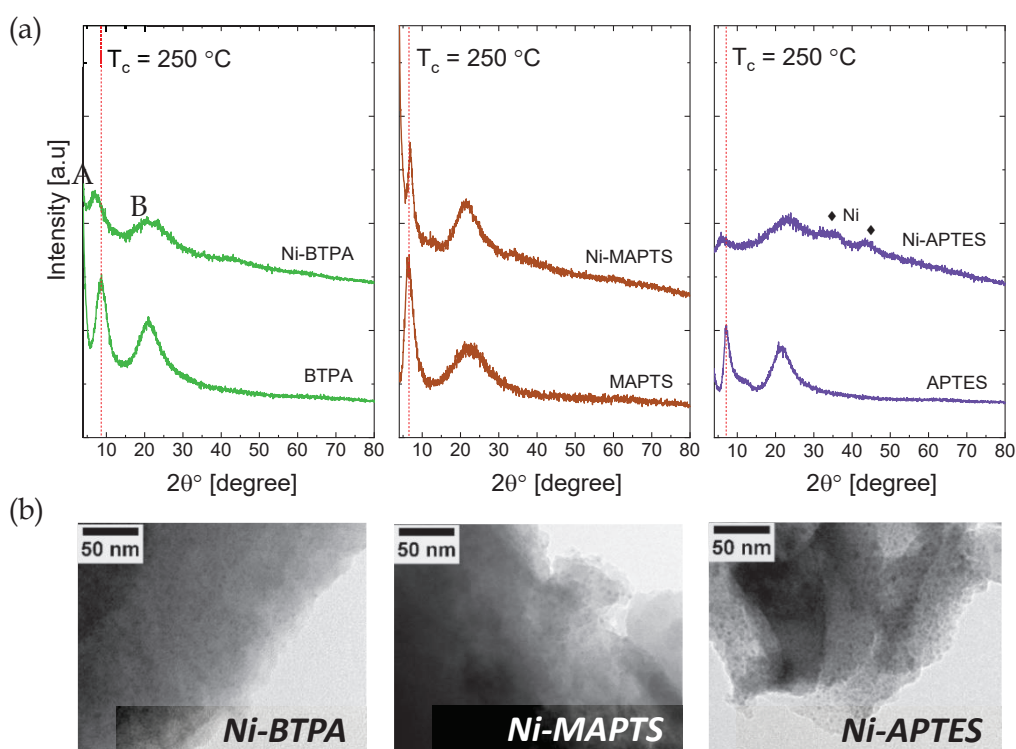
Fig. 4-3. The XRD petterns for aminosilica (BTPA, MAPTS, APTES) and nickel-doped aminosilica (Ni-BTPA, Ni-MAPTS, Ni-APTES) xerogel powders (a), and representative TEM images for nickel-composites material (Ni-BTPA, Ni-MAPTS, Ni-APTES) calcined at 250 °C

The coordination of APTES with nickel exclusively resulted in a moderate affinity because hydrogen substitution on the primary alkyl-amines structure reduced the steric hindrance of the metal center for the approach of ligand precursors, while the basicity of APTES was lower than that of the secondary amines in both bridge and pendant structures. Yu et al. [62] also reported a higher level of basicity secondary aminosilica precursors compared with the primary amine structure due to the balance between the electronic donating effect of alkyl groups, steric hindrance, and a solvation effect in the aqueous phase. Hence, the moderate affinity of APTES is likely to induce a shifting of the X-ray diffraction peak at 2θ from 7.1º to 5.8º while simultaneously generating the formation of nickel nanoparticles.

Moreover, the second diffraction peak at 2θ of 20-22º showed a slight shift to a higher degree for Ni-BTPA and Ni-APTES, while the opposite trend was observed for Ni-TMAPS. The shifting of correlated peak positions corresponds to a change in d-spacing values that reflect the estimated network distance of materials [63-65]. The peak shifts to a higher degree of 2θ for Ni-BTPA and Ni-APTES are likely to be related to a decrease in the interplane distance of the siloxane network (Si-O-Si), which was confirmed by the peak broadening after doping with nickel ions. In contrast with Ni-BTPA and Ni-APTES, however, Ni-MAPTS showed a slight shift to a lower degree of 2θ, which meant that a larger level of steric hindrance from the non-hydrolyzable methyl groups had slightly enlarged the Si-O-Si network and restricted the nickel ion to modify the framework via coordination.

In order to confirm the role of nickel-dopant in different types of aminosilica precursors, a TEM microphotograph was examined for three different samples of nickel-composites, as presented in Fig. 4-3(b). As the TEM images show, the nickel-dopant was fully incorporated within the bridge structure of the BTPA matrix, which resulted in a finer dispersion of the dopant. Conversely, the incorporation of nickel into the pendant structures of MAPTS and APTES shows an increased amount of metal dispersion (darker colors and round shapes), which supports the evidence in the XRD results that nickel nanoparticle reflection peaks increase with lower basicity and from an affinity for amine precursors. The amine surface of different types of precursors represents an important role in controlling the growth and dispersion of metal via catalyzing partially coordinated

networks and in the reduction of metal nitrate into well-dispersed nanoparticles, as reported by Anggarini et al. [66].

Fig. 4-4 shows the N_2 and CO_2 adsorption-desorption isotherms of bare aminosilica and nickel-doped aminosilica samples, and the corresponding textural properties are summarized in Table 3. All aminosilica samples (Fig. 4-4(a))-left side Fig.) exhibited low surface area and pore volume, which suggests extremely dense materials. The high flexibility of the organic chain incontrovertibly occupies the siloxane network, thus reducing porosity [39, 47]. The doping of nickel ions into different types of aminosilica precursors clearly shows the significant enhancement of both the surface area and the pore volume (Fig. 4-4(b)-right side Fig.), with the exception of the Ni-MAPTS composite.
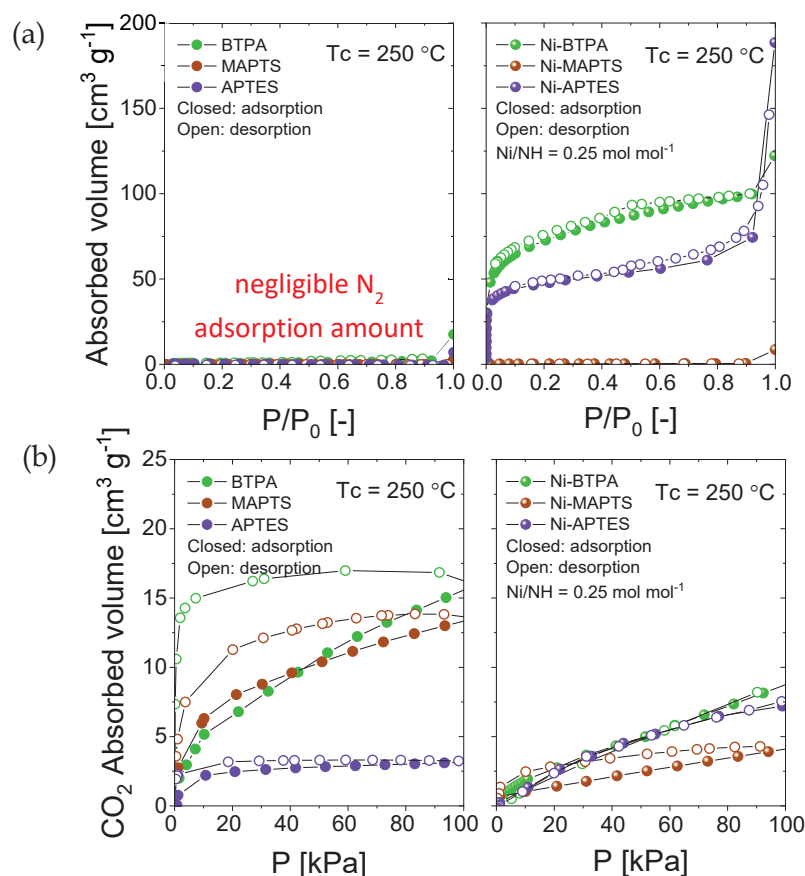
Fig. 4-4. N_2 sorption isotherms at -196 ^{o}C (a) and CO_2 uptake isotherms at 25 ^{o}C (b) of pristine aminosilica powders (left-side Fig.: BTPA, MAPTS, APTES) and Nickel-doped aminosilica materials (right-side Fig.: Ni-BTPA, Ni-MAPTS, Ni-APTES) calcined at 250 ^{o}C.

Anggarini et al. [48] discovered that microporosity could be controlled via the coordination affinity between a metal-dopant and an amine ligand, where a higher level of affinity enables an increased number of cross-linking interactions and an arrangement into a three-dimensional framework.

Table 4-3. Textural properties of pristine aminosilica and modified nickel-doped samples obtained in this study

Membrane	S_{BET} [m^2 g^{-1}][a]	Pore volume [cm^3 g^{-1}][a]	CO_2 sorption capacity [cm^3 g^{-1}][b]
BTPA	2.36	0.024	16.7
MAPTS	0.49	0.007	13.8
APTES	0.18	0.006	3.23
Ni-BTPA 0.25	162	0.124	8.14
Ni-MAPTS 0.25	1.18	0.026	3.91
Ni-APTES 0.25	173	0.271	7.53

[a] Values in parentheses are calculated based on the results of N_2 sorption isotherms
[b] Values in parentheses are CO_2 sorption capacities at 25 ℃ and 100 kPa.

Moreover, to examine the Lewis basicity strength of the relevant aminosilica precursors, CO_2 sorption isotherms were measured, as shown in Fig. 4-4(b). Based on sorption behavior, the CO_2 capacity followed the order of BTPA > MAPTS > APTES, which suggested the order of affinity for aminosilica materials. BTPA as a secondary amine precursor with a bridge structure conferred the highest Lewis-base nature (the highest CO_2 capacity with pronounced hysteresis loop), which allowed strong coordination with nickel ions, and resulted in a high surface area of 162 m^2 g^{-1} with a pore volume of 0.124 cm^3 g^{-1}. The development of the microporosity of Ni-MAPTS was influenced by the steric hindrance of non-hydrolyzable methyl groups and by the higher flexibility of the pendant-organic chain compared with that of the bridge type. Instead, Ni-APTES exhibited a high surface area (173 m^2 g^{-1}) and pore volume (0.271 cm^3 g^{-1}) that compared favorably with that of Ni-BTPA due to the unhindered pendant structure of the primary amine that allowed easy coordination with nickel ions. However, the lowest basicity properties of APTES (the lowest level of CO_2 sorption, as shown in Fig. 4(b)) indicates that the increases in pore volume and surface area following the introduction of nickel-dopant were due to the partially coordinated network and to the establishment of nanoparticles.

Hiroshima University Doctoral Dissertation

Compared with pristine materials, Ni-BTPA and Ni-APTES (Fig. 4-4(b)-right side Fig.) show a lower capacity for CO_2 with a reversible sorption trend and no saturation plateaus, which reflects the amine saturation level as an active site for the adsorption of CO_2. These results prove that most nickel ions are covalently coordinated with the amine ligands of BTPA and APTES precursors. On the other hand, Ni-MAPTS showed the lowest CO_2 sorption capacity with a small hysteresis loop, confirming that the pendant structure of the secondary amine precursor provided only partial coordination due to the steric hindrance of non-hydrolyzable methyl groups, which markedly reduced the reactivity. Pitteri et al. [67] found that steric hindrance by alkyl-amines promotes a retardation effect that limits the free-rotation movement around metal-amine bonds. Taken together, these findings suggest the roles of basicity, flexibility, and the steric hindrance of aminosilica precursors in promoting the formation of coordinated compounds in the following order: Ni-BTPA > Ni-APTES > Ni-MAPTS.

4.3.2 Structural transformation, textural properties, and porosity induced via nickel-amine coordination: The effect of calcination temperature and nickel mole ratio

Microporous networks were formed via the coordination between nickel ions and the amines of the organosilica precursors. In previous studies, we established the critical temperature required for the metamorphosis of dense structures into microporous versions. This temperature is also restricted to the decomposition temperature of amines as organic linkers [50]. To investigate the transformation together with the thermal stabilities of nickel-doped aminosilica membranes, FT-IR characterization was performed, and the results are summarized in Fig. 4-5. The absorbance of the amine deformation band for pristine materials (Fig. 4-5(a)) was observed at calcination temperatures as high as 300 ºC, but the band almost disappeared after calcination at 350 ºC. This result indicates the decomposition of amine groups could be minimized at a lower calcination temperature of 300 ºC, while higher temperatures accelerated the complete degradation.
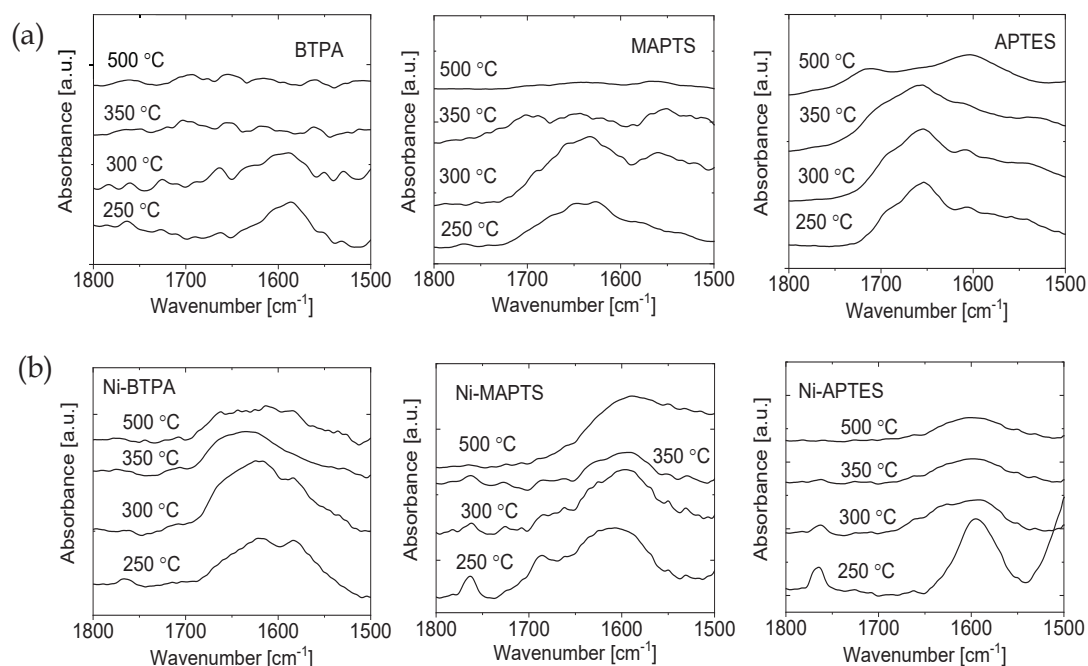
Fig. 4-5. The narrow FT-IR spectra for pristine aminosilica films of BTPA, MAPTS, APTES (a) and Ni-BTPA 0.25, Ni-MAPTS 0.25, and Ni-APTES 0.25 (b) at different calcination temperature

According to the narrow FT-IR spectra (Fig. 4-5(b)) for Ni-BTPA, Ni-MAPTS, and Ni-APTES, moderate absorption peaks from the NH deformation band of amine moieties were observed at a pyrolysis temperature of 250 $^\circ$C, while at higher calcination temperatures the peak intensity was gradually decreased until complete thermal degradation of amine groups was observed at 350 $^\circ$C.

In line with FT-IR characterizations, diffractograms of Ni-BTPA (Fig. 4-6.-left side Fig.) and Ni-MAPTS (Fig. 4-6.-middle side Fig.) showed amorphous phases at 250 $^\circ$C, and the formation of nickel nanoparticles was observed when the calcination temperature was increased to 300 $^\circ$C. By contrast, the diffractogram of Ni-APTES (Fig. 4-6-right side Fig.) shows the formation of nickel nanoparticles at 250 $^\circ$C, which indicates lower stability of the metal-dopant to withstand the ion phase, which resulted in the formation of phase separation. Anggarini et al. [48] reported that a high degree of coordination affinity induced the formation of a stable compound in the metal-ion state, while weak coordination led to the partial incorporation of metal into the aminosilica network. Calcination at 350 $^\circ$C caused a complete decomposition of the amine groups, which resulted in a reduction of nickel-amine coordination stability followed by the formation of nanoparticles.
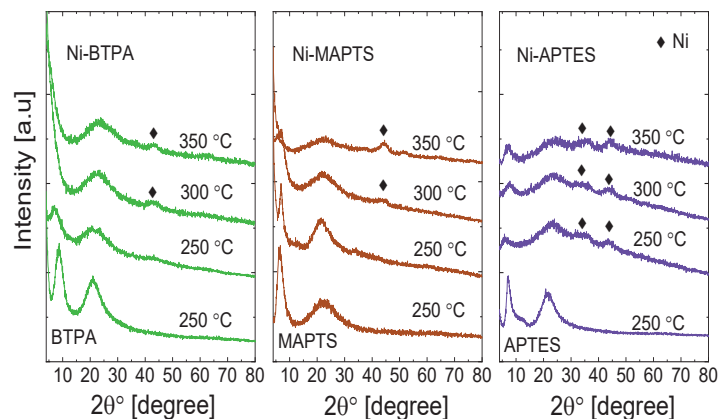
Fig. 4-6. Wide angle XRD patterns for Ni-BTPA 0.25, Ni-MAPTS 0.25, and Ni-APTES 0.25 at different calcination temperature

N₂ adsorption isotherms for nickel composites were performed to analyze their transformation and to determine the appropriate temperature for the conversion of the microporous network. As shown in Fig. 4-7, the nickel loading at higher calcination temperatures has an influence on increasing the N_2 sorption capacity for Ni-BTPA and Ni-MAPTS, while a slight decrease was observed for Ni-APTES (the pore size distribution for related materials, as shown in SI-(4-4), Fig. S4-4). During thermal treatment above 250 ⁰C, the Ni-BTPA composite showed an increase in N_2 adsorption at low relative pressure due to enhanced coordination, and at high relative pressure due to an increased number of mesopores that likely were formed via nanoparticles. That result further indicates higher calcination temperatures encourage the formation of bimodal pore structures of intraparticle and interparticle pores that originated from the coordinated organosilica network and the void spaces between packed nickel particles, respectively, as was confirmed by XRD. Further examination of Ni-MAPTS suggested that microporosity formed at the calcination temperature of 300 ⁰C, rather than at 250 ⁰C.

According to the thermogravimetric analysis curve and the differential thermogravimetric profile of Ni-MAPTS (Fig. 4-7(b)), the sample showed weight loss between 300 and 350 ⁰C due to the partial decomposition of the propylamine chain (based on the mass signal at m/z of 30 – Fig. 4-7(c)), and the non-hydrolyzable methyl groups (m/z = 15 – Fig. 4-7(c)).
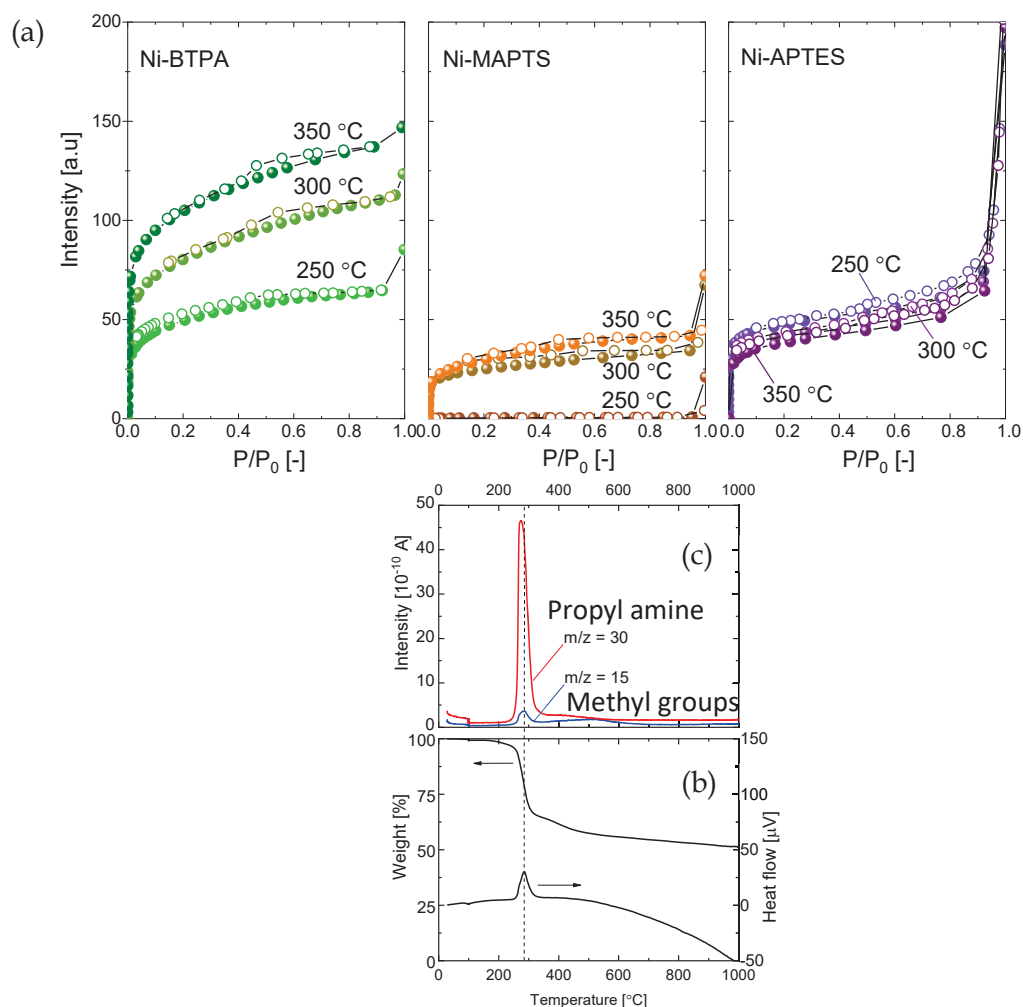
Fig. 4-7. The nitrogen adsorption-desorption isotherms (at -196 ºC) of Ni-BTPA 0.25 (left-side figure), Ni-MAPTS 0.25 (middle-side figure), and Ni-APTES 0.25 (right-side figure) calcined at different temperature (a), TGA-DTA curve of Ni-MAPTS composite in helium with a heating rate 10 ºC min^{-1} (b), and the mass signal of methyl groups (m/z = 15) together with propyl amine (m/z = 30) as a function of thermal treatment (c).

Therefore, after the progressive removal of methyl groups (at 300 ºC) from the MAPTS structure, the reduction in steric hindrance allowed nickel ions to freely coordinate with amine, which yielded a higher level of network connectivity and surface area. In contrast to secondary amine precursors, however, Ni-APTES with primary amine fragments display a decrease in N_2 adsorption capacity at higher calcination temperatures. The viability of primary amines promoted a rapid degradation of organic linkers due to their weaker basicity and lack of steric hindrance. This finding corroborates the FT-IR (Fig. 4-5) and XRD (Fig. 4-6) characterization that showed complete degradation of amine groups and the formation of nickel particles at 300 ºC. Zeleňák et al. [68] found that the

----

basicity of secondary amines is relatively higher than that of primary amines. This difference was influenced by the steric constraints, number of amine centers, and amine surface density. In general, therefore, the optimized calcination temperature for nickel-doped aminosilica membranes was determined to be 250 °C for Ni-BTPA and Ni-APTES, whereas a higher calcination temperature of 300 °C was required for Ni-MAPTS.

According to our previous study evaluating the effect of the mole ratio of nickel, the incorporation of different amounts of metal ions increased the specific surface area with high pore volume [49]. Interestingly, the existence of metal in two-phase structures as ions coordinated with amines and nanoparticles promoted a high level of flux with a superior separation factor. Therefore, in this section, the effect of the metal ratio on the different types of aminosilica precursors was discussed. The powder XRD patterns of nickel-doped aminosilica composites prepared at various Ni/NH mole ratios are depicted in Fig. 4-8(a) along with the diffractions of pristine materials. The diffractograms of coordinated compounds were characterized by a shifting in the first peak around 2θ of 7° into a lower degree on the order of Ni-BTPA > Ni-APTES >>Ni-MAPTS, which corresponds to the change in the periodic linking unit distance [48, 49, 66]. As expected, the first peak shifted significantly with an increase in the nickel concentration due to a strong coordination level for all nickel composites. However, at a higher nickel mole ratio of 0.50, an observable amount of Ni nanoparticles was generated, particularly for Ni-APTES, which clearly showed the high intensity of metal segregation. In addition, another part of diffraction at a 2θ of 20° showed a broader peak compared with that of pure materials, which suggested that the randomly oriented amorphous structure of the organosilica network could be maintained.
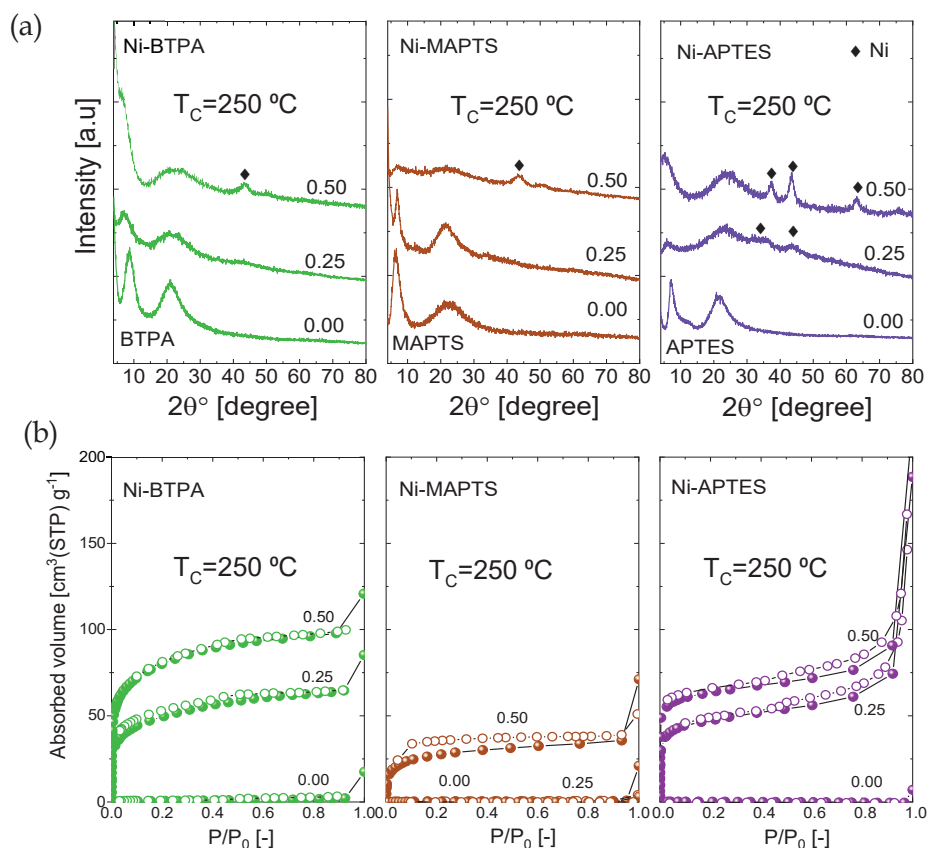
Fig. 4-8. XRD diffraction patterns (a), and N_2 sorption isotherms at -196 °C (b) for nickel-doped aminosilica (Ni/NH mole ratio = 0-0.50 mol mol^{-1}; calcination temperature = 250 °C) prepared from BTPA (left-side Fig.), MAPTS (middle-side Fig.), and APTES (right-side Fig.) precursors.

In order to deepen our understanding of the previous observation, porosity analysis of the nickel-doped aminosilica composites was performed. Fig. 4-8(b) summarizes the nitrogen sorption properties for tunable feeding mole ratios of Ni/NH at a calcination temperature of 250 °C. Ni-BTPA and Ni-APTES displayed type I isotherms after the addition of nickel in a ratio of 0.25 mol mol^{-1}, which showed the microporous structural ordering. Moreover, Ni-APTES also shows adsorption above $P/P_0 = 0.8$ due to the condensation of adsorbed gas into interparticle voids, which were possibly generated from nickel nanoparticles, as observed via XRD characterization [69]. The preparation of nickel-doped aminosilica composites with a higher mole ratio of Ni/NH shows an increase in the N_2 adsorption capacity, which suggested a higher metal content was also effective in developing the microstructure, as reported by Anggarini et al. [49]. A representative N_2 sorption isotherm of Ni-MAPTS showed the smallest formation of a

micropore structure under similar conditions, which could be attributed to the existence of non-hydrolyzable methyl groups that inhibited the coordination of the nickel metal-center with amines. Nobakht et al. [70] reported the formation of a coordinated compound with a methyl substituent, which resulted in a lower-dimension structure (1D), whereas a ligand without steric hindrance showed the formation of a 3D network. Li et al. [71] observed pendant groups of methyltriethoxysilane (MTES) occupying the free space of an organosilica network and becoming a barrier among silica pores. In that study, after the removal of the pendant chain via pyrolysis at high temperatures, more pore space was available for N_2 sorption. As a consequence, the occupation of methyl groups in the pendant structure of the MAPTS ligand resulted in a lack of coordination ability, which sterically reduced the free-volume surface area. It is plausible that modification of the aminosilica network via nickel-coordination exhibited a blended structure of partial crystallization that surrounded with the amorphous phase of polysilsesquioxane framework, which would be expected to display comparable properties as well as a metal-organic framework (MOF) structure.

4.3.3 Evaluating the establishment of microporosity in modified nickel-aminosilica membranes via single-gas permeation

Fig. 4-9(a) shows the molecular-diameter dependence on single-gas permeance for pristine aminosilica membranes and nickel composites with a Ni/NH mole ratio of 0.25 mol mol^{-1} prepared at 250 $^{\circ}$C. The decreasing order for the permeation of gases through pristine aminosilica membranes was BTPA (d_P = 0.46 nm) > MAPTS (d_P = 0.44 nm) > APTES (d_P = 0.41 nm), which indicated that greater free volume was created by increasing the organic chain in the dual flexible-rigid structure, as confirmed by N_2 and CO_2 adsorption [62]. More importantly, the membranes fabricated with a nickel dopant possess higher permeance compared with that of pristine versions, and nickel doping produced molecular sieving properties on the order of Ni-BTPA (d_P = 0.57 nm) > Ni-APTES (d_P = 0.54 nm) > Ni-MAPTS (d_P = 0.48 nm). It should be noted that membrane pore size, d_P, was determined via the normalized Knudsen-based permeance (NKP) method [72-74], as shown in SI-7. It should be noted that there is no clear and constant

relationship between N_2 sorption isotherms at -196 ℃ of the membrane materials and gas permeation properties at 200 ℃ for membrane films. Even though pristine aminosilica materials with high flexible organic chains may result in a nonporous structure (Fig. 4-4(a)), the gas permeation mechanism of the membrane thin layer at 200 ℃ (Fig. 4-9(a)) was influenced by the existence of free-volume pores (dual flexible-rigid network) instead of rigid pores. Ni-BTPA showed increased H_2 permeance that was approximately 5-fold greater, from 8.6×10^{-7} to 4.5×10^{-6} mol m^{-2} s^{-1} Pa^{-1}, while maintaining selectivity for H_2/SF_6 of > 10,000 (Fig. 4-9(a)).
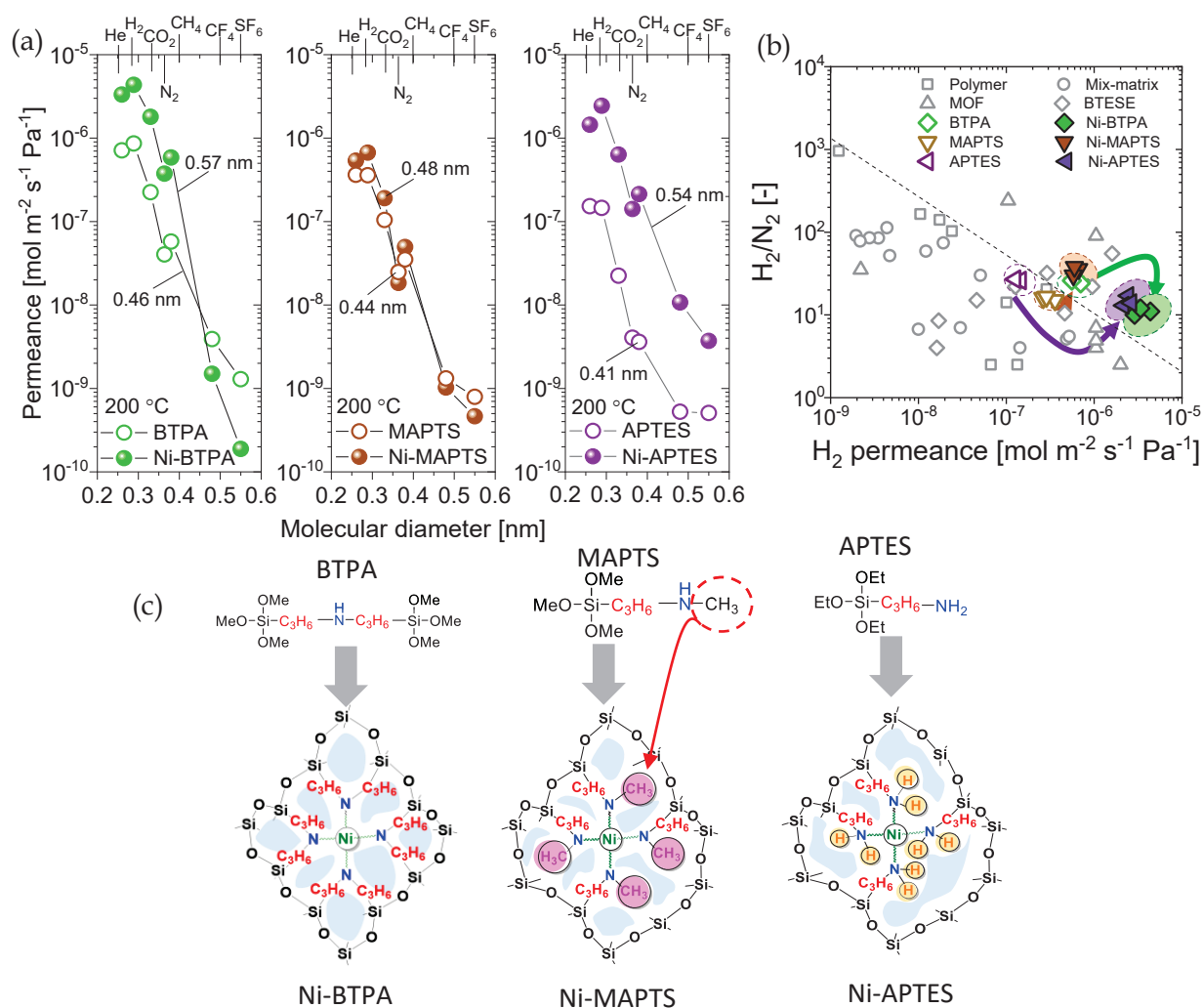
Fig. 4-9. Kinetic diameter dependence of single-gas permeance at 200 ℃ for pristine aminosilica membrane along with nickel composites prepared from BTPA (left-side Fig.), MAPTS (middle-side Fig.), and APTES (right-side Fig.) (a), H_2/N_2 permeance ratio as a function of H_2 permeation for different types of membranes (b), and schematic images of the formation of a nickel-amine coordinated network affected by different structure of aminosilica precursors (c).

The observed higher permeance of gases could be ascribed to the formation of the microporous network that was induced via nickel-amine coordination, which resulted in higher levels of surface area and pore volume (Fig. 4-4(a)). A higher H_2/SF_6 permeance ratio also was observed for Ni-composites membranes, which suggested that the contribution of nickel-amine coordination resulted in the formation of pore sizes that were more uniform and narrower with defect-free quality. By contrast, the change in Ni-MAPTS was insignificant by comparison with that of Ni-BTPA and Ni-APTES, which could be ascribed to the existence of non-hydrolyzable methyl groups as an 'arm' that prevented coordination. The features of the methyl pendant arm on the amine moiety occupied the free volume sites and further prohibited the formation of coordination [75].

In addition, we compared the corresponding network pore sizes of the membranes following the coordination process, and the H_2/N_2 permeance ratio as a function of H_2 permeance for different types of membranes is summarized in Fig. 4-9(b). Pristine aminosilica membranes exhibited low H_2 permeance with moderate to high selectivity, while nickel-doped aminosilica membranes showed higher permeance with moderate to low selectivity of H_2/N_2. For example, in the case of nickel-doping into the BTPA structure, the permeance of H_2 was significantly increased from 8.6×10^{-7} to 4.5×10^{-6} mol m^{-2} s^{-1} Pa, and the H_2/N_2 permeance ratio was decreased from 30 to 10 while maintaining a high H_2/SF_6 selectivity of more than 10,000. This result agreed well with the characterization results showing that flexible amine precursors tend to generate a dense structure in membranes, whereas the incorporation of nickel ions tunes the rigidity of the amine segment and increases network connectivity, which results in membranes with greater permeability. These results could be rationally interpreted from the viewpoint of membrane performances, as represented in Fig. 4-9(c). The presence of a bridged-secondary amine structure on BTPA with high basicity and low steric hindrance generated a strong level of coordination. Likewise, a small hindrance from the primary amine structure of APTES led to the facile development of a microporous network, while the non-hydrolyzable methyl groups on MAPTS lowered the probability of coordination and prevented the nickel ions from migrating closer to the amine coordination sites.

In order to further elucidate the transport mechanism through the undoped and nickel-doped aminosilica membranes, the temperature dependence of each permeating

----

gas for different types of membranes was compared, and the results appear in Fig. 4-10. Also, the quantitatively calculated activation energy values are tabulated in Table 4-4.

Table 4-4. The calculated values of activation energy, Ep (kJ mol^{-1}), for pristine aminosilica- and nickel-doped aminosilica-derived membranes

Membrane	H_2	N_2
BTPA	16.1	21.8
Ni-BTPA 0.25	13.6	10.0
MAPTS	8.87	9.39
Ni-MAPTS 0.25	10.5	12.7
APTES	11.6	20.7
Ni-APTES 0.25	10.3	11.4

Generally, the permeance of H_2 and N_2 was increased at the higher permeation temperature, which suggests an activated transport mechanism [76]. After coordination with nickel ions, the activation energy was significantly decreased as an indication of the enlargement of the pore sizes and higher levels of membrane connectivity via nickel-amine crosslinking that built a highly permeable sub-nanoporous framework [66]. Specifically, the activation energy of N_2 followed the sequence of Ni-MAPTS >> Ni-APTES > Ni-BTPA, which further confirms the higher ability of each amine for the development of a coordinated framework. Ni-MAPTS and MAPTS exhibited comparable H_2 permeance of 6.3×10^{-7} and 3.8×10^{-7} mol m^{-2} s^{-1} Pa^{-1}, respectively. Moreover, Ni-MAPTS showed no significant change in the activation energy compared with that of the pure MAPTS membrane. The steric hindrance of methyl groups effectively weakens the ability of secondary amine groups to interact with nickel ions. The consistent connection between membrane performance and the microstructure of materials (Fig. 4-4(a)) suggests that the steric hindrance of non-hydrolyzable methyl groups has a substantial effect to prevent further coordination of amine ligands with a metal center. In this case, Ni-MAPTS failed to construct a microporous framework at the calcination temperature of 250 ºC.
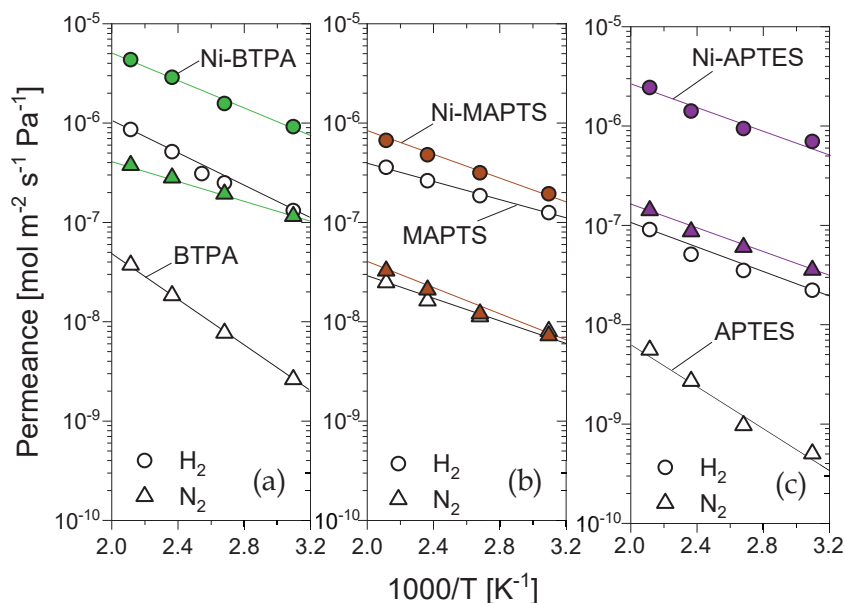
Fig. 4-10. Temperature dependence of single-gas permeance for pristine aminosilica membranes compared with nickel-doped aminosilica membranes calcined at 250 ℃: BTPA and Ni-BTPA (a), MAPTS and Ni-MAPTS (b), APTES and Ni-APTES (c).

A coordination bond was formed by reacting amine-functionalized organosilica precursors as organic linkers with nickel ions in the liquid phase, and this was explicitly confirmed via the microstructure characterization of gelled powders. A previous study revealed that the thermal degradation of amine linkers could generate a network collapse of the coordinated framework [66]. Herein, the fabrication of different types of nickel-coordinated, amine-functionalized, organosilica precursors was also evaluated at calcination temperatures of 250, 300, and 350 ℃. Fig. 4-11 shows the gas permeance at 200 ℃ for all types of membranes as a function of the molecular diameters of permeated gases. The gas permeance of pristine membranes was slightly increased at higher calcination temperatures with maintained selectivity for pristine membranes (Fig. 4-11(a)). H_2 permeance was slightly increased from 0.86×10^{-6} to 1.3×10^{-6} mol m^{-2} s^{-1} Pa^{-1} for BTPA, while the permeance ratio of H_2/N_2 was slightly decreased from 21 to 17 as the temperature was increased from 250 ℃ to 350 ℃. Generally, the permeance of non-functionalized silica membranes was decreased as the calcination temperature increased because higher temperatures facilitated the further condensation of silanol groups (Si-OH) and the hydrolyzable groups of Si-OR to form a siloxane (Si-O-Si) network. However, the enhanced gas permeance on aminosilica membranes could be attributed to

194

the partial degradation of amine groups, the liberation effect of organic groups, and a lower reaction rate for the condensation process [77, 78].
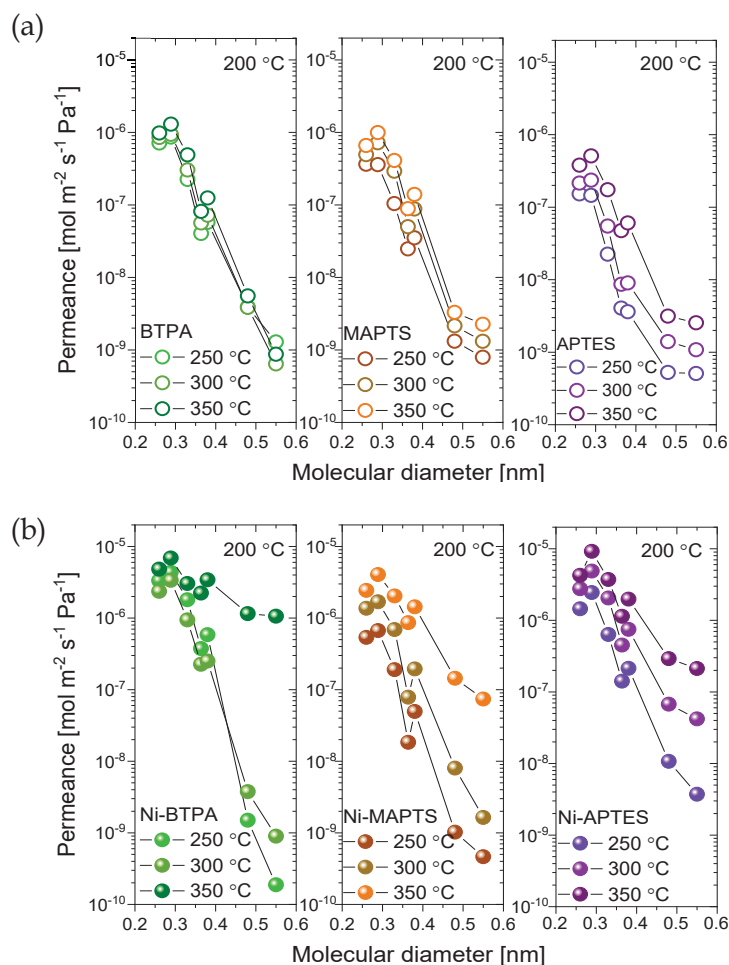
Fig. 4-11. Molecular diemeter dependency of permeance (measured at 200 ºC) for pristine aminosilica membrane of BTPA, MAPTS, and APTES (a), and nickel-doped aminosilica membranes at Ni/NH mole ratio of 0.25 for Ni-BTPA, Ni-MAPTS, and Ni-APTES prepared at various calcination temperature

Nickel-composite membranes showed that gas permeances increased considerably as the preparation temperature was increased from 250 to 300 ºC (Fig. 4-11(b)). As the temperature of calcination was increased from 250 ºC to 300 ºC, the H_2 permeance for Ni-APTES was increased from 2.4×10^{-6} to 4.9×10^{-6} mol m^{-2} s^{-1} Pa^{-1} with the H_2/N_2 permeance ratio maintaining values that ranged from 17 to 13 and with a significant decrease in the H_2/SF_6 permeance ratio ranging from 700 to 100, which indicated the presence of defects. APTES is the simplest primary amine precursor with basicity that is lower than that of the secondary amine precursors [79, 80]. Due to weak coordination with Ni, higher calcination temperatures led to the formation of interparticle

pores that were associated with the formation of nickel particles (Fig. 4-6). Moreover, the calcination of membranes at 350 ^oC resulted in the formation of a loose network with a dominant Knudsen diffusion transport, which is not feasible for the separation of both gases and liquid mixtures. Anggarini et al. [66] reported that the hybrid structure of metal-coordinated aminosilica membranes demonstrated a partially crystallized structure that was consistent with that of MOF structures that are surrounded by an amorphous siloxane network phase that derives from alkoxysilane precursors. The thermal degradation of amine linkers causes the fragmentation of nickel-amine coordination, which results in the collapse of the microporous framework [81]. On the other hand, Ni-MAPTS-300 showed increased H_2 permeance compared with that of Ni-MAPTS-250 from 0.63×10^{-6} to 1.7×10^{-6} mol m^{-2} s^{-1} Pa^{-1}, respectively, while maintaining H_2/SF_6 selectivity of as high as 1,000. This finding confirms the textural properties of Ni-MAPTS that were explained in Fig. 4-7(a) where a higher calcination temperature was required to get a microporous network and remove non-hydrolyzable methyl groups (as confirmed by TG-DTA results – Fig. 4-7(b) and (c)). Based on membrane performances in line with the characterization of the materials, we proposed a possible mechanism for microporous framework transformations under different calcination temperatures, as shown in Fig. 4-12. A coordinated network was established at 250 ^oC, while nickel-amine cleavage was detected at an amine decomposition temperature of 350 ^oC. Therefore, the optimized calcination temperature for Ni-BTPA and Ni-APTES is 250 ^oC, while for the Ni-MAPTS structure is 300 ^oC.
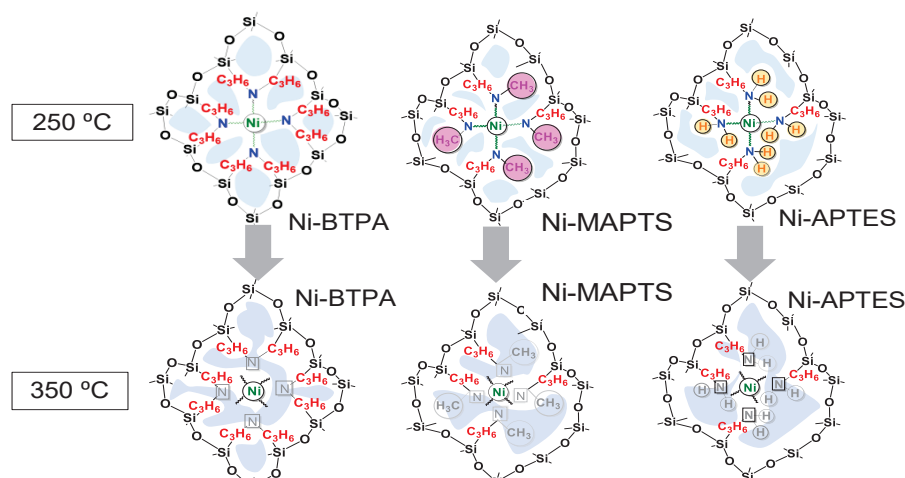
Fig. 4-12. Schematic image of the effect of different stage of calcination temperature on nickel-doped aminosilica framework structure

The synthesis strategy of a microporous coordinated nickel-amine framework can be rationally controlled by modifying the stoichiometric nickel/amine mole ratios to maximize the formation of the microporous network coupled with the formation of open metal sites for preferential transport properties. Fig. 4-13(a) shows the gas permeance for Ni-BTPA-, Ni-MAPTS-, and Ni-APTES-derived membranes at varying nickel ratios prepared at a calcination temperature of 250 °C. As the higher nickel content generated higher microporosity and greater surface area of the materials (Fig. 4-8), enhanced gas permeation with lower resistance from the enlarged membrane pore size was obtained. The improvement in gas permeance followed the order of Ni-BTPA 0.5 > Ni-BTPA 0.25 > BTPA; Ni-MAPTS 0.5 > Ni-MAPTS 0.25 > MAPTS; and Ni-APTES 0.5 > Ni-APTES 0.25 > APTES.
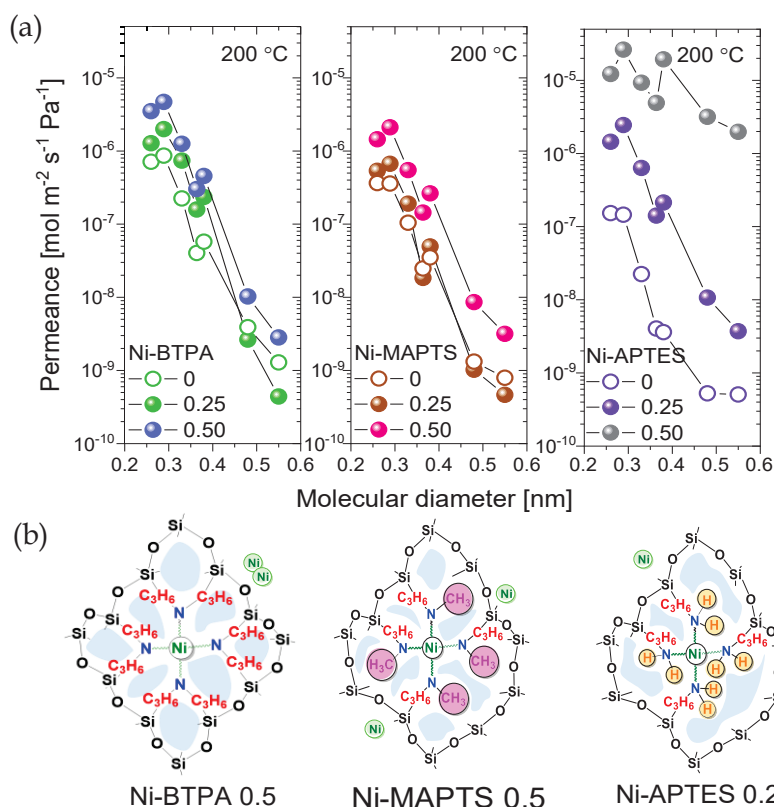
Fig. 4-13. Single-gas permeance at 200 °C as a function of the permeated gas sizes for nickel-doped aminosilica membranes (Ni-BTPA, Ni-MAPTS, Ni-APTES) with different nickel/amine mole ratio (a), and schematic image of nickel coordinated aminosilica network jointly with an excess of nickel nanoparticles (b).

In the case of Ni-APTES 0.5, the permeation of most gases was high due to the contribution of the Knudsen diffusion mechanism through non-selective large pore sizes

or defect voids that originated from large-sized nickel particles (Fig. 4-8(a)). In addition, the pendant structure of Ni-MAPTS 0.5 showed higher gas permeance with a reduced H_2/SF_6 permeance ratio of from > 1,000 to 600. Schematic illustrations of the network structure for different types of membranes appear in Fig. 4-13(b). The stability of the coordinated network derived from the bridge-structured precursor (BTPA) was higher compared with the pendant-structured versions (MAPTS, APTES) since lower basicity and larger steric hindrance of the pendant chain significantly perturbed the coordination bond. Accordingly, the higher metal content of the dopants in the pendant types of precursors allowed a larger phase separation for metal particles; thus, the optimal nickel mole ratios for the bridge (Ni-BTPA) and pendant precursors (Ni-MAPTS and Ni-APTES) were 0.5 and 0.25, respectively.

4.3.4 Selective methanol removal from organic solvents via pervaporation using nickel-doped aminosilica membranes

Our past work showed that combining the microporosity with an excess of nickel ions creates high-flux membranes and facilitates the transport of methanol [49]. Our strategy for the development of hybrid metal-coordinated amine-functionalized organosilica membranes is to assemble their structures as organic linkers in ways that will facilitate the removal of methanol from different types of solvents. In Fig.4-14, we compare the pervaporation time course for different types of hybrid nickel-doped aminosilica membranes under different types of mixtures at 50 °C (permeance values, permeance ratio, flux, and separation factors are shown in Table 4-5). Ni-BTPA composite membranes boost the transport of MeOH with a permeate concentration higher than 99 wt% with respect to Toluene (Tol), which results in a high flux of 1.42 kg m^{-2} h^{-1} with the highest separation factor of 5,000. Based on the pore size distribution, the permeance of Ni-MAPTS membranes is largely affected by calcination temperatures and by the concentration of nickel ions due to the existence of non-hydrolyzable methyl groups (The gas permeance and pervaporation performances for Ni-MAPTS 0.25-300 and Ni-MAPTS 0.50-250, as shown in Figs. S(4-10) and S(4-11), respectively).
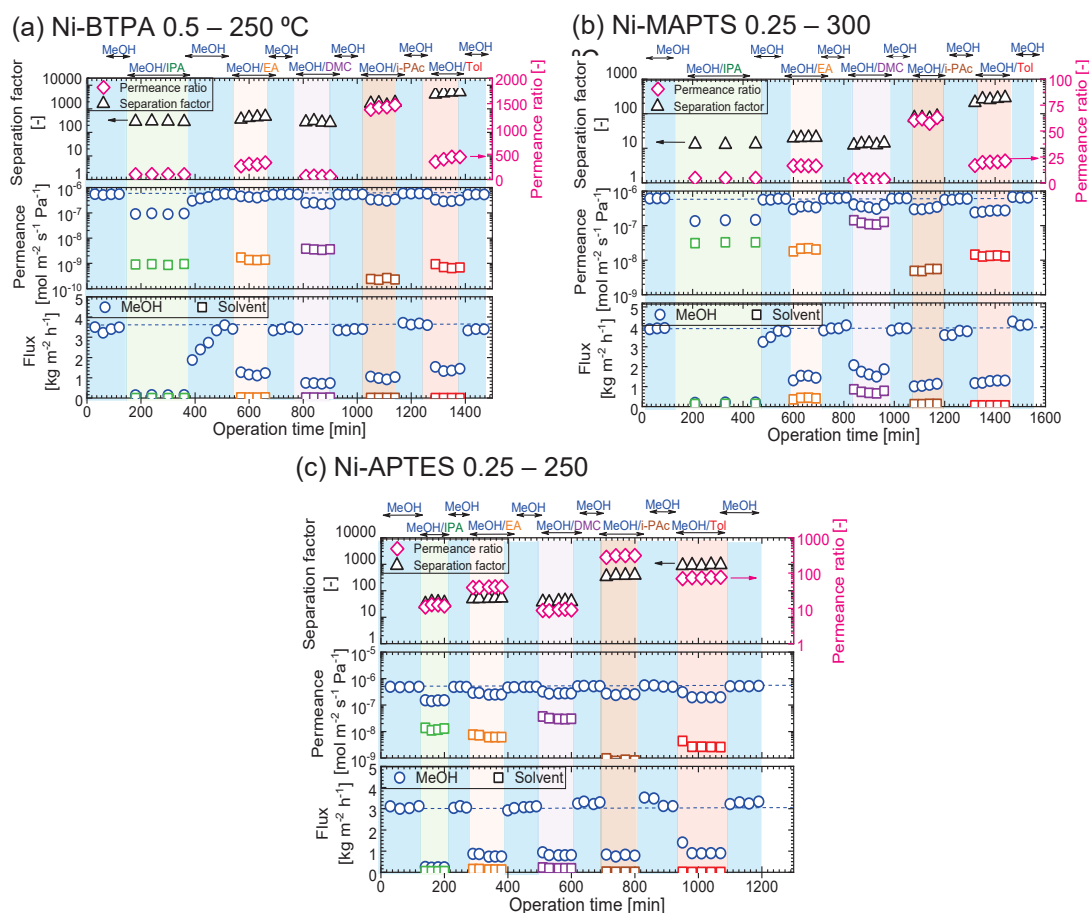
Fig. 4-14. The time courses for pervaporation performance of MeOH-solvents mixtures at 50 ºC for Ni-BTPA 0.5 – 250 ºC (a), Ni-MAPTS 0.25 – 300 ºC (b), and Ni-APTES 0.25 – 250 ºC (c) (methanol/solvents = 10 wt%/ 90 wt%; solvents used were IPA, EA, DMC, i-Pac, and Tol; pure MeOH was examined to confirm th stable PV performance before each PV separation of MeOH-solvent mixture.)

Ni-MAPTS 0.50-250 shows a lower flux and separation factor compared with that of Ni-BTPA 0.50 due to smaller pore size and the contribution of methyl groups that dramatically reduced the transport of MeOH. Moreover, the calcination of Ni-MAPTS 0.5-300 at a higher temperature (300 ºC) generated a greater amount of nickel nanoparticles instead of removing the non-hydrolyzable methyl groups, which degraded the performance (Figs. S(4-10) and S(4-11)). A higher level of performance was attained by the pervaporation of Ni-MAPTS 0.25-300 with a high flux of 1.24 kg m^{-2} h^{-1} and a separation factor for MeOH/Tol of 258. This improvement happened because the appropriate calcination temperature removed the non-hydrolyzable methyl groups, and the low concentration of nickel tended to control the formation of interparticle pores.

The low level of steric hindrance generated by the amine precursors of Ni-APTES 0.25 composite membranes showed an attractive performance with a high flux of 1 kg m^{-2} h^{-1} and a separation factor of 1,000. A comparison with the pervaporation results for the undoped-APTES membrane (Fig. S4-12(a)) shows a small flux of 0.35 kg m^{-2} h^{-1} with moderate selectivity for MeOH/Tol of 360, which indicates preferential sorption for MeOH into polar amine functional groups, as reported by Anggarini et al. [49]. With a higher nickel mole ratio, Ni-APTES 0.5 (Fig. S4-12(c)) failed to separate MeOH from different types of solvents due to the generation of large interparticle pores by nickel nanoparticles. The pore structure of the membrane exhibited the presence of a significant number of defects between the nanoparticles, which enhanced the contribution by Knudsen diffusion (Fig. S4-7). The separation performance for MeOH/solvents was in the following order: Ni-BTPA 0.5-250 > Ni-APTES 0.25-250 > Ni-MAPTS 0.25-300. In each case, the permeance of MeOH was comparable to the pure system and approximately constant for different types of mixtures, with the exception of the mixture of the MeOH/IPA (separation mechanism for alcohol mixture as explained in SI-(4-12)). These results indicated the preferential sorption of methanol and a high level of rejection for solvents even at high concentrations. The pervaporation of MeOH/IPA shows the historical effect proven by the gradual increase of MeOH flux in the pure system after the separation of IPA. Partial pore blockages by adsorbed IPA molecules result in the inability of pure MeOH to quickly transport through the membrane pore wall. The observed results can be explained by the fact that the hydrophilic surface of nickel-crosslinked amine membranes facilitates the sorption of polar alcohol components. In addition, the separation performance of nickel-doped aminosilica membranes showed an increase behavior when a non-polar solvent was applied to the mixture. The permeance of MeOH in different types of solvents was decreased as follows: in Tol ≈ i-Pac > DMC > EA >>> IPA. The extremely low flux of non-polar solvents such as i-Pac and Tol through nickel-coordinated aminosilica membranes was experimentally explained via the reluctance of nonpolar molecules to pass through the hydrophilic surface region, which is responsible for the enhanced separation between MeOH over non-polar solvents such as DMC, i-Pac, and Tol [27, 82].

Table 4-5. Comparison of methanol separation performance via pervaporation between nickel-doped aminosilica membranes and different types of membranes

Membrane	System	T_{PV} [°C]	MeOH feed conc [wt%]	Total flux [kg m² h⁻¹]	MeOH perm. ×10⁻⁷ [mol m⁻² s⁻¹ Pa⁻¹]*	Sep. factor [-]	Perm. ratio [-]*	Ref.
Ppy-PF	MeOH/IPA	57.5	10	0.50	0.51	2	0.7	[83]
LPS/pDMAEMA/PAI	MeOH/IPA	50	15	3.39	11.4	9	3	[84]
Ni-BTPA 0.50	MeOH/IPA	50	10	0.15	0.92	300	100	
Ni-MAPTS 0.50	MeOH/IPA	50	10	0.25	0.87	32	10	
Ni-APTES 0.25	MeOH/IPA	50	10	0.28	1.47	35	12	
Ni-APTES 0.50	MeOH/IPA	50	10	5.00	0.64	2	1	This work
Ni-BTPA 0.50	MeOH/EA	50	10	1.22	4.32	415	300	
Ni-MAPTS 0.50	MeOH/EA	50	10	0.61	1.60	45	36	
APTES	MeOH/EA	50	10	0.17	0.49	38	28	
Ni-APTES 0.25	MeOH/EA	50	10	0.86	2.63	51	40	
Ni-APTES 0.50	MeOH/EA	50	10	25.3	1.69	2	2	
BTESA	MeOH/DMC	50	10	3.13	11.3	118	26	[14]
BTESE	MeOH/DMC	50	10	0.45	1.40	235	59	[14]
GA-STA-CS	MeOH/DMC	50	10	1.03	3.23	91	21	[85]
PAA/PVA	MeOH/DMC	60	10	0.61	0.12	0.8	0.2	[86]
STA/CS	MeOH/DMC	50	10	1.16	3.53	67	16	[87]
Nafion	MeOH/DMC	40	10	0.93	2.67	11	2	[88]
Ni-BTPA 0.50	MeOH/DMC	50	10	0.75	2.36	280	66	
Ni-MAPTS 0.25	MeOH/DMC	50	10	1.75	3.6	13	3	
Ni-MAPTS 0.50	MeOH/DMC	50	10	0.57	0.99	11	3	
Ni-APTES 0.25	MeOH/DMC	50	10	0.98	2.82	39	9	This work
Ni-APTES 0.50	MeOH/DMC	50	10	24.1	1.88	2.57	0.6	
Ni-BTPA 0.50	MeOH/i-PAc	50	10	1.00	3.28	1700	1350	
Ni-MAPTS 0.50	MeOH/i-Pac	50	10	0.55	1.67	110	82	
Ni-APTES 0.25	MeOH/i-Pac	50	10	0.81	2.55	373	300	
Ni-APTES 0.50	MeOH/i-Pac	50	10	15.5	1.31	4	3	
Ppy-PF	MeOH/Tol	50	10	0.28	0.59	441	39	[83]
TiPCS	MeOH/Tol	50	10	0.64	1.35	410	36	[89]
Chitosan	MeOH/Tol	35	10	0.80	3.22	162	14	[26]
Cellulose acetate	MeOH/Tol	30	10	1.80	8.79	80	7	[25]
PA/UiO-66(NH₂)-EDTA/cellulose	MeOH/Tol	22	72	1.55	9.51	5	5	[90]
SPI	MeOH/Tol	50	10	0.79	1.43	49	4	[91]
TEOS-CS	MeOH/Tol	30	10	0.18	0.93	396	35	[28]
BTPA	MeOH/Tol	50	10	0.07	0.14	382	34	[49]
Ni-BTPA 0.50	MeOH/Tol	50	10	2.81	5.95	907	80	[49]
Ni-BTPA 0.50	**MeOH/Tol**	**50**	10	**1.42**	**3.03**	**5000**	**410**	
Ni-MAPTS 0.25	MeOH/Tol	50	10	2.63	5.34	420	37	
Ni-MAPTS 0.50	MeOH/Tol	50	10	0.81	1.51	70	6	This work
APTES	MeOH/Tol	50	10	0.36	0.75	368	30	
Ni-APTES 0.25	MeOH/Tol	50	10	0.90	2.16	919	73	
Ni-APTES 0.50	MeOH/Tol	50	10	11.2	0.64	5	0.3	

*MeOH permeance and the permeance ratios were calculated based on Eqs. (3) and (4)

4.3.5 Permeation and separation mechanism through nickel-doped aminosilica membranes

Fig. 4-15(a) gives an overview of the molecular sieving properties of nickel-doped aminosilica membranes and the polarity of the organic mixtures that affected the separation performance. Permeance (P) is the product of the diffusivity (D) and solubility (S) of permeated molecules across the membrane barrier, where the diffusivity value is affected by the pore dimensions, and the solubility is affected by the critical temperature of the solvent and the interaction between membrane surface (organic phase) and permeated solvent [62, 73, 92].
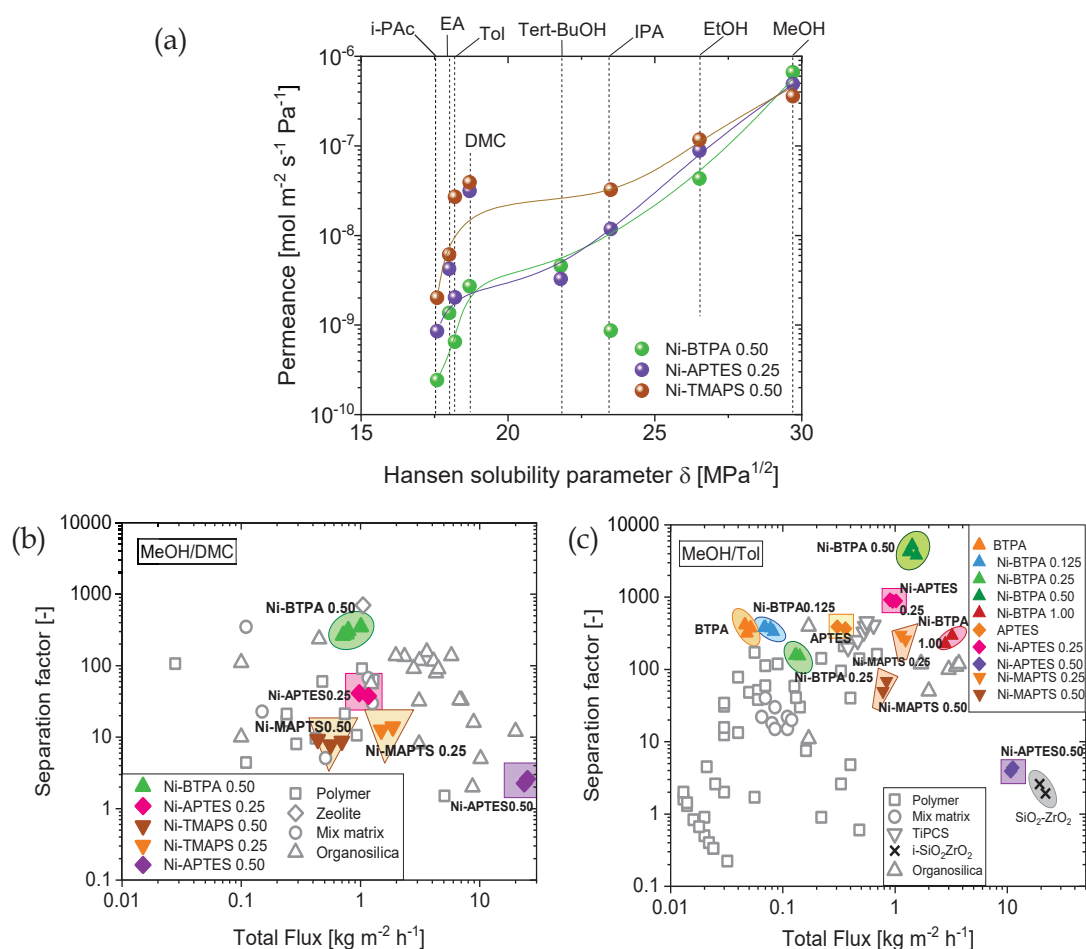
Fig. 4-15. The correlation between Hansen solubility parameter and permeance for Ni-BTPA, Ni-MAPTS, and Ni-APTES (a), comparison pervaporation performance for the separation of methanol/dimetil carbonate (MeOH/DMC) (b) and methanol/toluene (MeOH/Tol) mixture (c) between nickel-doped aminosilica membranes and different types of membranes.

Sridhar et al. [93] reported that the performance of pervaporation-based membranes for a specified mixture would depend on the solubility parameters and the free volume, which reflects the interactions between the permeated molecules, the membrane materials, and the pore structure that is available for adsorption. In this study, the Hansen solubility parameter including the partial parameters of dispersion, dipole, and hydrogen bonding was used to describe the relationship between the structure and the interaction strength of solvents [93, 94]. Fig. 4-15(a) shows a clear correlation between the Hansen solubility parameter and the permeance (P) values. MeOH as a polar solvent showed the highest solubility parameter with the highest value of permeance, while DMC, Tol, and i-Pac are less-polar solvents that showed the lowest solubility parameters, as well as permeance, which resulted in high separation performance for both mixtures. The results reported here support the assumption that MeOH freely interacts with a large quantity of metal-crosslinked groups that makes the surface properties of these membranes very hydrophilic.

The solubility parameters for DMC, Tol, and i-Pac through hydrophilic membranes show much lower values compared with MeOH due to their relatively hydrophobic nature. Permselectivity is determined by the combination of molecular sieving properties (diffusivity) and the affinity for separation (solubility) since the separation performance of nickel-doped aminosilica membranes in organic mixtures followed the order of Ni-BTPA > Ni-APTES > Ni-MAPTS, and the bridge amine structure (BTPA) generated a stable and highly coordinated network. The pendant structure (MAPTS and APTES), on the other hand, showed moderate-to-low coordination levels due to steric hindrance that worsened the coordination ability and affected the membrane performance.

Fig. 4-15(b) shows the trade-off curve between total flux and the separation factor of MeOH/DMC mixtures for different types of membranes at 50 $^{\circ}$C. Each plotted point represents the experimental data of a different membrane, as tabulated in Table S1. Commercial polymeric membranes are simply indicative of a trade-off trend where a more permeable membrane shows a high flux of 8 kg m^{-2} h^{-1} with a low separation ability for MeOH/DMC of 2, while another membrane could show an extremely small flux of 0.03 kg m^{-2} h^{-1} with a moderate selectivity of 100. The hybrid structure from nickel-

coordinated amine-functionalized organosilica precursors breaks through the original trade-off where the flux of the membranes was increased to approximately 1 kg m^{-2} h^{-1} with a separation factor higher than 200. Each plotted point for several nickel-doped aminosilica membranes prepared under similar conditions showed a comparable performance, which confirmed the reproducibility of membrane fabrication and the measurement accuracy with standard deviations of less than 20%.

Fig. 4-15(c) summarizes the pervaporation performance for MeOH/Tol separation by the hybrid nickel-doped aminosilica membranes fabricated in this study, along with different types of membranes. Compared with membranes such as polymeric, MOFs, and TiPCS, the Ni-BTPA showed the highest separation performance with a high flux of 1.42 kg m^{-2} h^{-2} and the highest separation factor of 5,000. Other nickel-composites of Ni-APTES and Ni-MAPTS also exhibited high potential for the separation of MeOH/Tol, with a high flux that was approximately > 1 kg m^{-2} h^{-1} and a separation factor higher than 300. The enhancement of membrane flux and the separation factor can be ascribed to the balance between higher levels of interconnected micropores generated from nickel-amine coordination, and the existence of uncoordinated nickel ions that acted as active sites for the diffusion of methanol [11, 50]. The pervaporation findings are consistent with materials characterization obtained from instrumental interpretations and the pore structure estimation from single-gas permeation results, which suggested beneficial modification through the precise control of the pore structure and the hydrophilic surface. As far as we could ascertain, this study introduces the first high-flux membrane that has demonstrated a methanol-selective performance that could be applied to industrial-scale purifications.

4.4 Conclusions

Microporous nickel-doped aminosilica membranes were successfully synthesized via a sol-gel process that was followed by a coordination reaction. The nickel-composite membranes show attractive separation performance with methanol-selective properties and high flux.

(1) The optimal nickel/amine mole ratio and appropriate calcination temperature for the development of high porosity, facilitated the high diffusion of methanol as follows.

    a. Bridge-structure amine precursor (Ni-BTPA) = 0.50 – 250 ^{o}C

    b. Pendant-structure amine precursors = Ni-APTES = 0.25 – 250 ^{o}C; Ni-MAPTS = 0.25 – 300 ^{o}C

(2) The permeation mechanism for nickel-doped aminosilica membranes was influenced by the pore size distribution of the membranes and by the affinity between the hydrophilic surface of the membranes and the permeating molecules.

(3) Competitive adsorption was observed for alcohol mixtures (MeOH/EtOH, MeOH/IPA, and MeOH/tert-BuOH), which then resulted in pore blockage via hydrogen bonding interactions.

(4) The nickel-doped aminosilica membranes show high levels of flux and separation factors on the order of Ni-BTPA > Ni-APTES > Ni-MAPTS. The Ni-BTPA membrane recorded the most outstanding performance with a high flux of 1.42 kg m^{-2} h^{-1} and a superior separation factor for MeOH/Tol of 5,000.

References

[1] Y.K. Ong, G.M. Shi, N.L. Le, Y.P. Tang, J. Zuo, S.P. Nunes, T.-S. Chung, Recent membrane development for pervaporation processes, Prog. Polym. Sci., 57 (2016) 1-31.

[2] B. Smitha, D. Suhanya, S. Sridhar, M. Ramakrishna, Separation of organic–organic mixtures by pervaporation—a review, J. Membr. Sci., 241 (2004) 1-21.

[3] T. Tsuru, T. Shibata, J. Wang, H.R. Lee, M. Kanezashi, T. Yoshioka, Pervaporation of acetic acid aqueous solutions by organosilica membranes, J. Membr. Sci., 421 (2012) 25-31.

[4] J.G. Villaluenga, A. Tabe-Mohammadi, A review on the separation of benzene/cyclohexane mixtures by pervaporation processes, J. Membr. Sci., 169 (2000) 159-174.

[5] K.-Y. Hsu, Y.-C. Hsiao, I.-L. Chien, Design and control of dimethyl carbonate−methanol separation via extractive distillation in the dimethyl carbonate reactive-distillation process, Ind. Eng. Chem. Res., 49 (2010) 735-749.

[6] J.s.A. Jaime, G. Rodríguez, I.n.D. Gil, Control of an optimal extractive distillation process with mixed-solvents as separating agent, Ind. Eng. Chem. Res., 57 (2018) 9615-9626.

[7] K. Mishra, N. Kaistha, Synthesis, design, and control of an azeotropic distillation system for methanol–isopropyl acetate separation, Ind. Eng. Chem. Res., 58 (2018) 1229-1243.

[8] H.-M. Wei, F. Wang, J.-L. Zhang, B. Liao, N. Zhao, F.-k. Xiao, W. Wei, Y.-H. Sun, Design and control of dimethyl carbonate–methanol separation via pressure-swing distillation, Ind. Eng. Chem. Res., 52 (2013) 11463-11478.

[9] Z. Zhang, Q. Zhang, G. Li, M. Liu, J. Gao, Design and control of methyl acetate-methanol separation via heat-integrated pressure-swing distillation, Chin. J. Chem. Eng., 24 (2016) 1584-1599.

[10] X. Feng, R.Y. Huang, Liquid separation by membrane pervaporation: a review, Ind. Eng. Chem. Res., 36 (1997) 1048-1066.

[11] U. Anggarini, L. Yu, H. Nagasawa, M. Kanezashi, T. Tsuru, Microporous Nickel-Coordinated Aminosilica Membranes for Improved Pervaporation Performance of Methanol/Toluene Separation, ACS Appl. Mater. Interfaces, (2021).

[12] S.D. Bhat, T.M. Aminabhavi, Zeolite K-LTL-loaded sodium alginate mixed matrix membranes for pervaporation dehydration of aqueous–organic mixtures, J. Membr. Sci., 306 (2007) 173-185.

[13] B. Bolto, M. Hoang, Z. Xie, A review of membrane selection for the dehydration of aqueous ethanol by pervaporation, Chemical Engineering and Processing: Process Intensification, 50 (2011) 227-235.

[14] G. Dong, H. Nagasawa, L. Yu, Q. Wang, K. Yamamoto, J. Ohshita, M. Kanezashi, T. Tsuru, Pervaporation removal of methanol from methanol/organic azeotropes using organosilica membranes: Experimental and modeling, J. Membr. Sci., 610 (2020) 118284.

[15] A. Ghoreyshi, M. Jahanshahi, K. Peyvandi, Modeling of volatile organic compounds removal from water by pervaporation process, Desalination, 222 (2008) 410-418.

[16] G.O. Yahaya, Separation of volatile organic compounds (BTEX) from aqueous solutions by a composite organophilic hollow fiber membrane-based pervaporation process, J. Membr. Sci., 319 (2008) 82-90.

[17] R. Castro-Muñoz, F. Galiano, O. de la Iglesia, V. Fíla, C. Téllez, J. Coronas, A. Figoli, Graphene oxide–Filled polyimide membranes in pervaporative separation of azeotropic methanol–MTBE mixtures, Sep. Purif. Technol., 224 (2019) 265-272.

[18] Q. Zhang, J. Peng, K. Zhang, Separation of an azeotropic mixture of dimethyl carbonate and methanol via partial heat integration pressure swing distillation, Asia‐Pacific Journal of Chemical Engineering, 12 (2017) 50-64.

[19] W. Huang, D. Xiang, Optimal design framework and techno-economic-environmental assessment for efficient solvent recovery separation of ethyl acetate and methanol, Sep. Purif. Technol., 260 (2021) 118210.

[20] G.L. Han, Q.G. Zhang, A.M. Zhu, Q.L. Liu, Pervaporation separation of methanol/methyl tert-butyl ether mixtures using polyarylethersulfone with cardo membranes, Sep. Purif. Technol., 107 (2013) 211-218.

[21] M.A. Pacheco, C.L. Marshall, Review of dimethyl carbonate (DMC) manufacture and its characteristics as a fuel additive, Energy & Fuels, 11 (1997) 2-29.

[22] D. Delledonne, F. Rivetti, U. Romano, Developments in the production and application of dimethylcarbonate, Applied Catalysis A: General, 221 (2001) 241-251.

[23] Y. Ono, Catalysis in the production and reactions of dimethyl carbonate, an environmentally benign building block, Applied Catalysis A: General, 155 (1997) 133-166.

[24] B. Elvers, Ullmann's encyclopedia of industrial chemistry, Verlag Chemie, 1991.

----

[25] A.A. Bhat, V.G. Pangarkar, Methanol-selective membranes for the pervaporative separation of methanol–toluene mixtures, J. Membr. Sci., 167 (2000) 187-201.

[26] R. Huang, G. Moon, R. Pal, N-acetylated chitosan membranes for the pervaporation separation of alcohol/toluene mixtures, J. Membr. Sci., 176 (2000) 223-231.

[27] S. Mandal, V.G. Pangarkar, Separation of methanol–benzene and methanol–toluene mixtures by pervaporation: effects of thermodynamics and structural phenomenon, J. Membr. Sci., 201 (2002) 175-190.

[28] S. Moulik, V. Bukke, S.C. Sajja, S. Sridhar, Chitosan-polytetrafluoroethylene composite membranes for separation of methanol and toluene by pervaporation, Carbohydrate polymers, 193 (2018) 28-38.

[29] S.M. Pal, V.G. Pangarkar, Acrylonitrile‐based copolymer membranes for the separation of methanol from a methanol–toluene mixture through pervaporation, J. Appl. Polym. Sci., 96 (2005) 243-252.

[30] G. Polotskaya, T. Meleshko, I. Sushchenko, A. Yakimansky, A.Y. Pulyalina, A. Toikka, Z. Pientka, Membranes based on polyimide–polyaniline nanocomposites for pervaporation of organic mixtures, J. Appl. Polym. Sci., 117 (2010) 2175-2182.

[31] N. Singha, S. Kuila, P. Das, S. Ray, Separation of toluene–methanol mixtures by pervaporation using crosslink IPN membranes, Chemical Engineering and Processing: Process Intensification, 48 (2009) 1560-1565.

[32] W.F. Yong, H. Zhang, Recent advances in polymer blend membranes for gas separation and pervaporation, Prog. Mater Sci., 116 (2021) 100713.

[33] Y. Cui, H. Kita, K.-I. Okamoto, Zeolite T membrane: preparation, characterization, pervaporation of water/organic liquid mixtures and acid stability, J. Membr. Sci., 236 (2004) 17-27.

[34] X. Chen, M. Zhu, S. Xiang, T. Gui, T. Wu, Y. Li, N. Hu, I. Kumakiri, X. Chen, H. Kita, Growth process and short chain alcohol separation performance of fluoride-containing NaY zeolite membrane, Chin. J. Chem. Eng., 29 (2021) 154-159.

[35] A. Msahel, F. Galiano, M. Pilloni, F. Russo, A. Hafiane, R. Castro-Muñoz, V.B. Kumar, A. Gedanken, G. Ennas, Z.e. Porat, Exploring the effect of iron metal-organic framework particles in polylactic acid membranes for the azeotropic separation of organic/organic mixtures by pervaporation, Membranes, 11 (2021) 65.

[36] J. Gascon, F. Kapteijn, B. Zornoza, V. Sebastian, C. Casado, J. Coronas, Practical approach to zeolitic membranes and coatings: state of the art, opportunities, barriers, and future perspectives, Chem. Mater., 24 (2012) 2829-2844.

[37] J. Caro, Hierarchy in inorganic membranes, Chem. Soc. Rev., 45 (2016) 3468-3478.

[38] K. Li, Ceramic membranes for separation and reaction, John Wiley & Sons, 2007.

[39] T. Tsuru, Silica-based membranes with molecular-net-sieving properties: development and applications, J. Chem. Eng. Jpn., 51 (2018) 713-725.

[40] K. Yamamoto, J. Ohshita, Bridged polysilsesquioxane membranes for water desalination, Polym. J., 51 (2019) 1103-1116.

[41] N. Moriyama, H. Nagasawa, M. Kanezashi, T. Tsuru, Pervaporation dehydration of aqueous solutions of various types of molecules via organosilica membranes: Effect of membrane pore sizes and molecular sizes, Sep. Purif. Technol., 207 (2018) 108-115.

[42] I. Agirre, P.L. Arias, H.L. Castricum, M. Creatore, E. Johan, G.G. Paradis, P.H. Ngamou, H.M. van Veen, J.F. Vente, Hybrid organosilica membranes and processes: Status and outlook, Sep. Purif. Technol., 121 (2014) 2-12.

[43] H.L. Castricum, G.G. Paradis, M.C. Mittelmeijer‐Hazeleger, R. Kreiter, J.F. Vente, J.E. Ten Elshof, Tailoring the separation behavior of hybrid organosilica membranes by adjusting the structure of the organic bridging group, Adv. Funct. Mater., 21 (2011) 2319-2329.

[44] N. Raman, C. Brinker, Organic "template" approach to molecular sieving silica membranes, J. Membr. Sci., 105 (1995) 273-279.

[45] C.-F. Cheng, Z. Luan, J. Klinowski, The role of surfactant micelles in the synthesis of the mesoporous molecular sieve MCM-41, Langmuir, 11 (1995) 2815-2819.

[46] M. Kanezashi, K. Yada, T. Yoshioka, T. Tsuru, Organic–inorganic hybrid silica membranes with controlled silica network size: preparation and gas permeation characteristics, J. Membr. Sci., 348 (2010) 310-318.

[47] M. Kanezashi, Y. Yoneda, H. Nagasawa, T. Tsuru, K. Yamamoto, J. Ohshita, Gas permeation properties for organosilica membranes with different Si/C ratios and evaluation of microporous structures, AlChE J., 63 (2017) 4491-4498.

[48] U. Anggarini, L. Yu, H. Nagasawa, M. Kanezashi, T. Tsuru, Metal-induced microporous aminosilica creates a highly permeable gas-separation membrane, Mat. Chem. Front., 5 (2021) 3029-3042.

[49] U. Anggarini, L. Yu, H. Nagasawa, M. Kanezashi, T. Tsuru, Microporous Nickel-Coordinated Aminosilica Membranes for Improved Pervaporation Performance of Methanol/Toluene Separation, ACS Appl. Mater. Interfaces, 13 (2021) 23247-23259.

[50] U. Anggarini, H. Nagasawa, M. Kanezashi, T. Tsuru, Structural two-phase evolution of aminosilica-based silver-coordinated membranes for increased hydrogen separation, J. Membr. Sci., (2021) 119962.

[51] W. Puthai, M. Kanezashi, H. Nagasawa, K. Wakamura, H. Ohnishi, T. Tsuru, Effect of Firing Temperature on The Water Permeability Of SiO_2–ZrO_2 Membranes for Nanofiltration, J. Membr. Sci., 497 (2016) 348-356.

[52] S.-J. Ahn, A. Takagaki, T. Sugawara, R. Kikuchi, S.T. Oyama, Permeation properties of silica-zirconia composite membranes supported on porous alumina substrates, J. Membr. Sci., 526 (2017) 409-416.

[53] M. Van Leeuwen, Derivation of Stockmayer potential parameters for polar fluids, Fluid Phase Equilib., 99 (1994) 1-18.

[54] M. Wang, M. Li, N. Chang, L. Gao, M. Wang, Y. Zhang, Vapor separation of methanol-dimethyl carbonate mixture on SAPO-34 zeolite membrane, J. Membr. Sci., 565 (2018) 311-321.

[55] Y. Marcus, The sizes of molecules—revisited, J. Phys. Org. Chem., 16 (2003) 398-408.

[56] A.A.A. Aziz, A.N.M. Salem, M.A. Sayed, M.M. Aboaly, Synthesis, structural characterization, thermal studies, catalytic efficiency and antimicrobial activity of some M (II) complexes with ONO tridentate Schiff base N-salicylidene-o-aminophenol (saphH2), J. Mol. Struct., 1010 (2012) 130-138.

[57] J.R. Hartman, R.W. Vachet, J.H. Callahan, Gas, solution, and solid state coordination environments for the nickel (II) complexes of a series of aminopyridine ligands of varying coordination number, Inorg. Chim. Acta, 297 (2000) 79-87.

[58] Z. Wang, M. Wang, G. Wu, D. Wu, A. Wu, Colorimetric detection of copper and efficient removal of heavy metal ions from water by diamine-functionalized SBA-15, Dalton transactions, 43 (2014) 8461-8468.

[59] S.S. Choi, A.S. Lee, H.S. Lee, H.Y. Jeon, K.Y. Baek, D.H. Choi, S.S. Hwang, Synthesis and characterization of UV‐curable ladder‐like polysilsesquioxane, J. Polym. Sci., Part A: Polym. Chem., 49 (2011) 5012-5018.

[60] A. Panja, Exclusive selectivity of multidentate ligands independent on the oxidation state of cobalt: influence of steric hindrance on dioxygen binding and phenoxazinone synthase activity, Dalton Transactions, 43 (2014) 7760-7770.

[61] Y.-P. Ren, X.-J. Kong, X.-Y. Hu, M. Sun, L.-S. Long, R.-B. Huang, L.-S. Zheng, Influence of steric hindrance of organic ligand on the structure of Keggin-based coordination polymer, Inorg. Chem., 45 (2006) 4016-4023.

[62] L. Yu, M. Kanezashi, H. Nagasawa, T. Tsuru, Fabrication and CO_2 permeation properties of amine-silica membranes using a variety of amine types, J. Membr. Sci., 541 (2017) 447-456.

[63] S.S. Hosseini, M.R. Omidkhah, A.Z. Moghaddam, V. Pirouzfar, W.B. Krantz, N.R. Tan, Enhancing the properties and gas separation performance of PBI–polyimides blend carbon molecular sieve membranes via optimization of the pyrolysis process, Sep. Purif. Technol., 122 (2014) 278-289.

[64] L. Lei, F. Pan, A. Lindbråthen, X. Zhang, M. Hillestad, Y. Nie, L. Bai, X. He, M.D. Guiver, Carbon hollow fiber membranes for a molecular sieve with precise-cutoff ultramicropores for superior hydrogen separation, Nature communications, 12 (2021) 1-9.

[65] H.B. Park, Y.K. Kim, J.M. Lee, S.Y. Lee, Y.M. Lee, Relationship between chemical structure of aromatic polyimides and gas permeation properties of their carbon molecular sieve membranes, J. Membr. Sci., 229 (2004) 117-127.

[66] U. Anggarini, H. Nagasawa, M. Kanezashi, T. Tsuru, Structural two-phase evolution of aminosilica-based silver-coordinated membranes for increased hydrogen separation, J. Membr. Sci., 642 (2022) 119962.

[67] B. Pitteri, G. Marangoni, L. Cattalini, Reactivity of neutral nitrogen donors in planar d8 metal complexes. Part 2. The system [2, 6-bis (methylsulfanyl-methyl) pyridine] chloroplatinum (II) with pyridines and amines in methanol. Effect of basicity, π-acceptor capacity and steric hindrance, J. Chem. Soc., Dalton Trans., (1994) 3539-3543.

[68] V. Zeleňák, M. Skřínska, A. Zukal, J. Čejka, Carbon dioxide adsorption over amine modified silica: effect of amine basicity and entropy factor on isosteric heats of adsorption, Chem. Eng. J., 348 (2018) 327-337.

[69] F.J. Sotomayor, K.A. Cychosz, M. Thommes, Characterization of micro/mesoporous materials by physisorption: concepts and case studies, Acc. Mater. Surf. Res, 3 (2018) 34-50.

[70] V. Nobakht, A. Beheshti, D.M. Proserpio, L. Carlucci, C.T. Abrahams, Influence of the counter anion and steric hindrance of pyrazolyl and imidazolyl flexible ligands on the structure of zinc-based coordination polymers, Inorg. Chim. Acta, 414 (2014) 217-225.

[71] G. Li, M. Kanezashi, T. Tsuru, Preparation of organic–inorganic hybrid silica membranes using organoalkoxysilanes: The effect of pendant groups, J. Membr. Sci., 379 (2011) 287-295.

[72] H.R. Lee, M. Kanezashi, Y. Shimomura, T. Yoshioka, T. Tsuru, Evaluation and fabrication of pore‐size‐tuned silica membranes with tetraethoxydimethyl disiloxane for gas separation, AlChE J., 57 (2011) 2755-2765.

[73] H. Nagasawa, T. Niimi, M. Kanezashi, T. Yoshioka, T. Tsuru, Modified gas‐translation model for prediction of gas permeation through microporous organosilica membranes, AlChE J., 60 (2014) 4199-4210.

[74] T. Yoshioka, M. Kanezashi, T. Tsuru, Micropore size estimation on gas separation membranes: A study in experimental and molecular dynamics, AlChE J., 59 (2013) 2179-2194.

[75] L.A. Lesikar, A.F. Gushwa, A.F. Richards, Synthesis, characterization, and steric hindrance comparisons of selected transition and main group metal β-ketoiminato complexes, J. Organomet. Chem., 693 (2008) 3245-3255.

[76] M. Kanezashi, T. Shioda, T. Gunji, T. Tsuru, Gas permeation properties of silica membranes with uniform pore sizes derived from polyhedral oligomeric silsesquioxane, AlChE J., 58 (2012) 1733-1743.

[77] X. Ren, M. Kanezashi, M. Guo, R. Xu, J. Zhong, T. Tsuru, Multiple Amine-Contained POSS-Functionalized Organosilica Membranes for Gas Separation, Membranes, 11 (2021) 194.

[78] L. Yu, M. Kanezashi, H. Nagasawa, N. Moriyama, T. Tsuru, K. Ito, Enhanced CO2 separation performance for tertiary amine‐silica membranes via thermally induced local liberation of CH3Cl, AlChE J., 64 (2018) 1528-1539.

[79] R.J. Ouellette, J.D. Rawn, Organic chemistry: structure, mechanism, synthesis, Academic Press, 2018.

[80] L. Yu, M. Kanezashi, H. Nagasawa, T. Tsuru, Role of amine type in CO2 separation performance within amine functionalized silica/organosilica membranes: a review, Applied Sciences, 8 (2018) 1032.

[81] M.Z. Hussain, M. Bahri, W.R. Heinz, Q. Jia, O. Ersen, T. Kratky, R.A. Fischer, Y. Zhu, Y. Xia, An in situ investigation of the thermal decomposition of metal-organic framework NH2-MIL-125 (Ti), Microporous Mesoporous Mater., 316 (2021) 110957.

[82] W.-J. Chen, C.R. Martin, Highly methanol-selective membranes for the pervaporation separation of methyl t-butyl ether/methanol mixtures, J. Membr. Sci., 104 (1995) 101-108.

[83] M. Zhou, M. Persin, J. Sarrazin, Methanol removal from organic mixtures by pervaporation using polypyrrole membranes, J. Membr. Sci., 117 (1996) 303-309.

[84] S.V. Kononova, Y.P. Kuznetsov, R. Apostel, D. Paul, H.H. Schwarz, New polymer multilayer pervaporation membrane, Die Angewandte Makromolekulare Chemie: Applied Macromolecular Chemistry and Physics, 237 (1996) 45-53.

[85] J.H. Chen, X.F. Dong, Y.S. He, Investigation into glutaraldehyde crosslinked chitosan/cardo-poly-etherketone composite membrane for pervaporation separation of methanol and dimethyl carbonate mixtures, RSC advances, 6 (2016) 60765-60772.

[86] L. Wang, J. Li, Y. Lin, C. Chen, Separation of dimethyl carbonate/methanol mixtures by pervaporation with poly (acrylic acid)/poly (vinyl alcohol) blend membranes, J. Membr. Sci., 305 (2007) 238-246.

----

[87] J.H. Chen, Q.L. Liu, A.M. Zhu, Q.G. Zhang, J. Fang, Pervaporation separation of MeOH/DMC mixtures using STA/CS hybrid membranes, J. Membr. Sci., 315 (2008) 74-81.

[88] M. Kludský, O. Vopička, P. Matějka, Š. Hovorka, K. Friess, Nafion® modified with primary amines: chemical structure, sorption properties and pervaporative separation of methanol-dimethyl carbonate mixtures, Eur. Polym. J., 99 (2018) 268-276.

[89] Q. Wang, L. Yu, H. Nagasawa, M. Kanezashi, T. Tsuru, High‐performance molecular‐separation ceramic membranes derived from oxidative cross‐linked polytitanocarbosilane, J. Am. Ceram. Soc., 103 (2020) 4473-4488.

[90] A.V. Penkova, A.I. Kuzminova, M.E. Dmitrenko, V.A. Surkova, V.P. Liamin, D.A. Markelov, A.V. Komolkin, D.Y. Poloneeva, A.V. Laptenkova, A.A. Selyutin, Novel pervaporation mixed matrix membranes based on polyphenylene isophtalamide modified by metal–organic framework UiO-66 (NH2)-EDTA for highly efficient methanol isolation, Sep. Purif. Technol., 263 (2021) 118370.

[91] D. Sapegin, S. Kononova, G. Gubanova, E. Kruchinina, N. Saprykina, E. Popova, E. Vlasova, Selective facilitated fixed-site carrier transport of methanol through sulfonated copolyimide pervaporation membranes for the separation of methanol/toluene mixtures, Sep. Purif. Technol., 236 (2020) 116274.

[92] N. Moriyama, Y. Kawano, Q. Wang, R. Inoue, M. Guo, M. Yokoji, H. Nagasawa, M. Kanezashi, T. Tsuru, Pervaporation via silicon‐based membranes: Correlation and prediction of performance in pervaporation and gas permeation, AlChE J., 67 (2021) e17223.

[93] S. Sridhar, B. Smitha, A. Shaik, Pervaporation‐based separation of methanol/MTBE mixtures—A review, Separation and Purification Reviews, 34 (2005) 1-33.

[94] A. Buekenhoudt, F. Bisignano, G. De Luca, P. Vandezande, M. Wouters, K. Verhulst, Unravelling the solvent flux behaviour of ceramic nanofiltration and ultrafiltration membranes, J. Membr. Sci., 439 (2013) 36-47.

Supporting Information

----------SI-(4-1)----------

1. Gas cylinder
2. Pressure controller
3. Stop valve
4. Temperature controller
5. Furnace
6. Membrane module
7. Membrane
8. Pressure gauge
9. Back pressure valve
10. Three way valve
11. Vacuum pump
12. Soap film flow meter
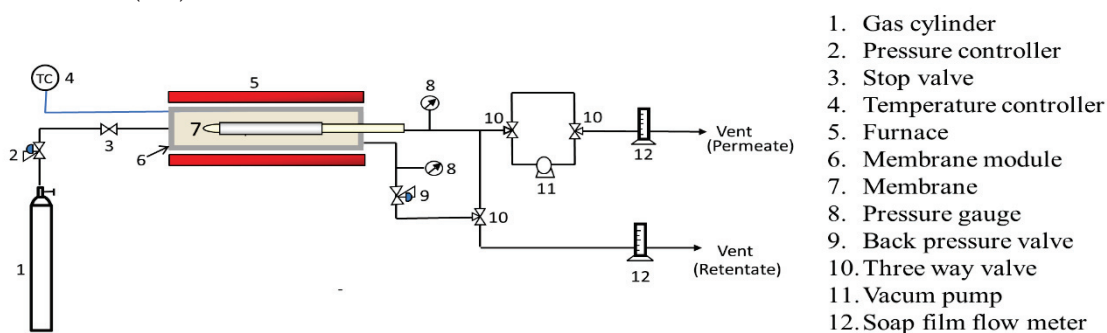
Fig. S4-4. Experimental set-up of single-gas permeation apparatus

----------SI-(4-2)----------

1. Membrane
2. Heater
3. Screw
4. Cold trap
5. Thermocontroller
6. Thermocouple
7. Motor
8. Vacuum pump
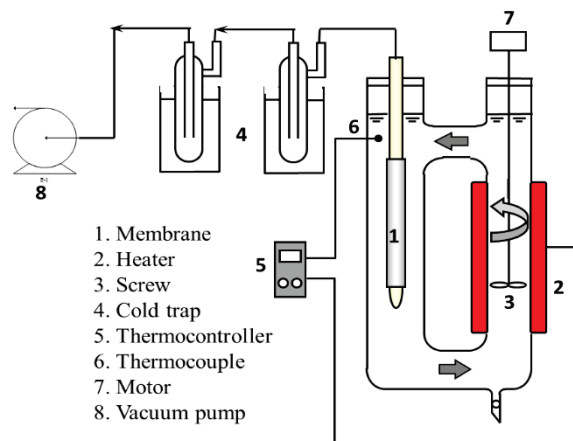
Fig. S4-5. Schematic diagram of pervaporation experiment

----------SI-(4-3)----------

Fig. S4-3. Overview of the intermolecular periodic linking unit chain distance (A) and the average spacing in the siloxane network (B) for Ni-BTPA (a), Ni-MAPTS (b), and Ni-APTES (c).

--- --

----------SI-(4-4)----------
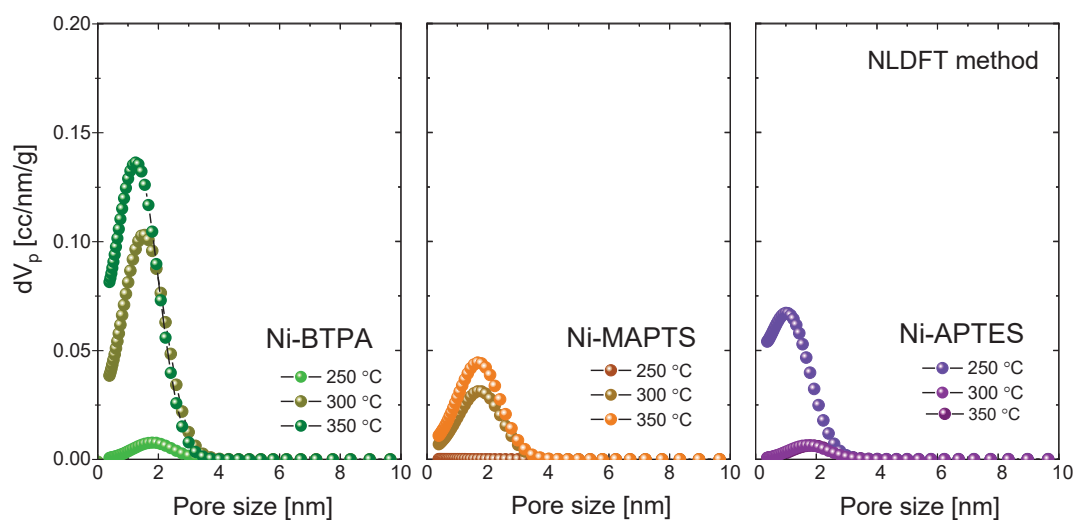
Fig. S4-4. Pore size distribution (calculated with NLDFT method) for Ni-BTPA, Ni-MAPTS, and Ni-APTES calcined at different temperatures

----

----------SI-(4-5)----------
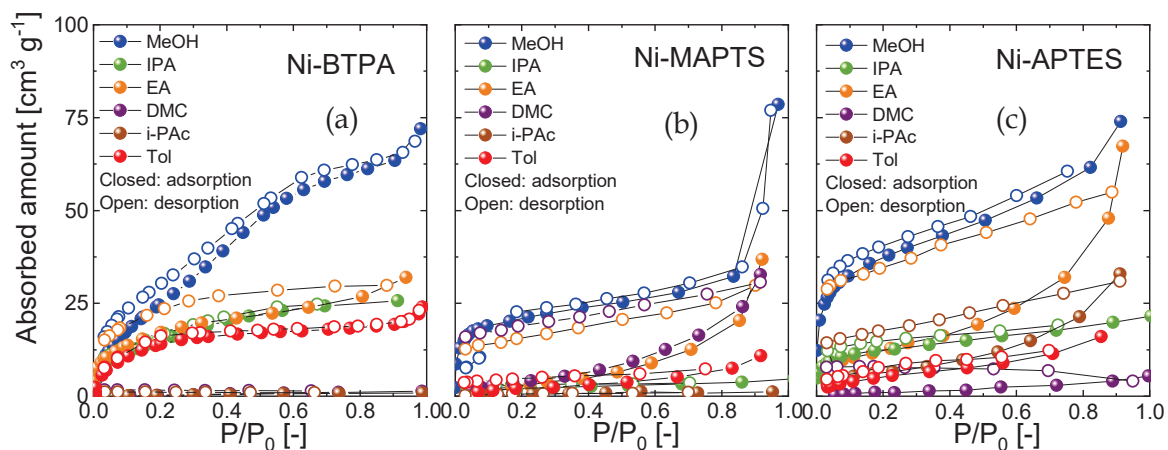
Fig. S4-5. Vapor sorption isotherms at 25 ºC of methanol-MeOH, isopropyl alcohol-IPA, ethyl acetate-EA, dimethyl carbonate-DMC, isopropyl acetate-i-Pac, and toluene-Tol for Ni-BTPA (a), Ni-MAPTS (b), and Ni-APTES (c) (Ni/NH = 0.25 mol mol^{-1}) composites calcined at 250 ºC under inert atmosphere of N_2.

--- --

----------SI-(4-6)----------
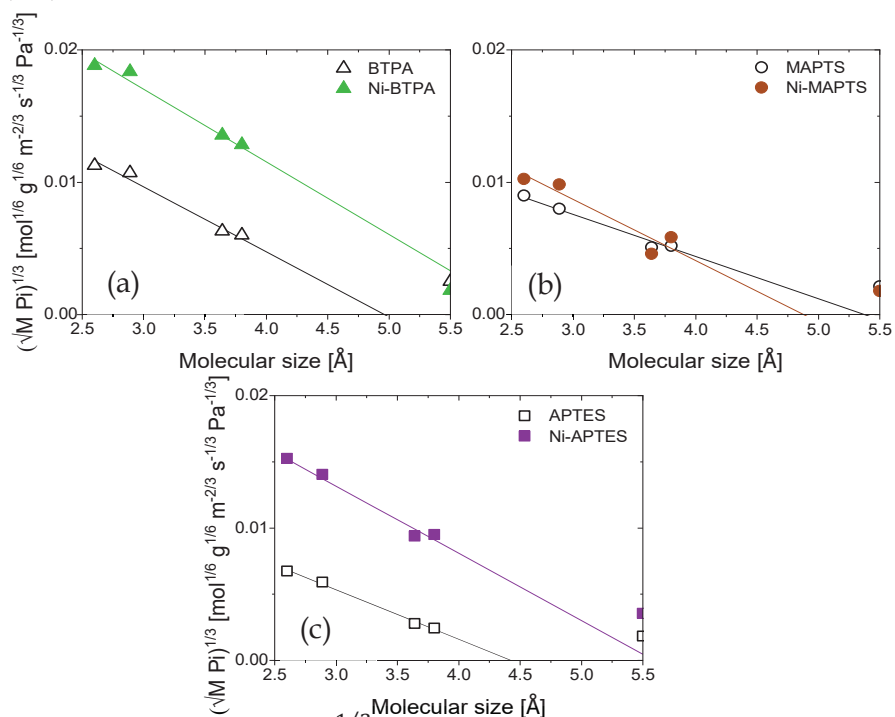
Fig. S4-6. The correlation of $\left(\sqrt{M_i}P_i\right)^{1/3}$ as a function of molecular size of permeating gases (points and lines are experimentally and theoritically calculated, respectively, for BTPA and Ni-BTPA (a), MAPTS and Ni-MAPTS (b), APTES and Ni-APTES (c)

----------SI-(4-7)----------
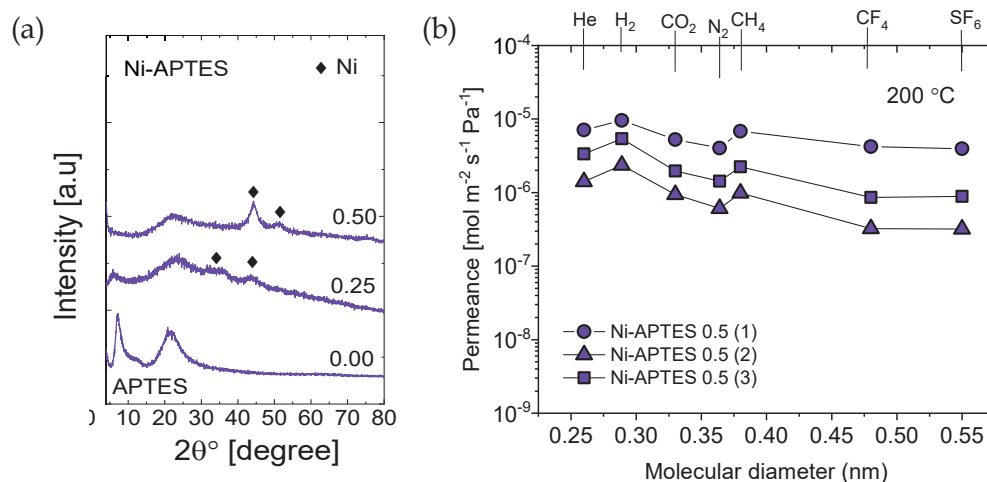
Fig. S4-7. The XRD diffractogram for APTES and Ni-APTES at different amount of nickel calcined at 250 °C (a), and the reproducible data of single-gas permeance at 200 °C for Ni-APTES 0.50 (b)

--- --

----------SI-(4-8)----------

Table S4-1. The calculated values of activation energy, Ep (kJ mol^{-1}), for pristine aminosilica- and nickel-doped aminosilica-derived membranes

Membrane	He	H$_2$	CO$_2$	N$_2$	CH$_4$
BTPA	15.7	16.1	31.1	21.8	21.3
Ni-BTPA 0.25	12.2	13.6	8.92	10.0	8.73
MAPTS	10.2	8.87	4.47	9.39	8.67
Ni-MAPTS 0.25	11.4	10.5	9.50	12.7	13.2
APTES	12.6	11.6	14.7	20.7	17.8
Ni-APTES 0.25	9.70	10.3	0.47	11.4	10.7
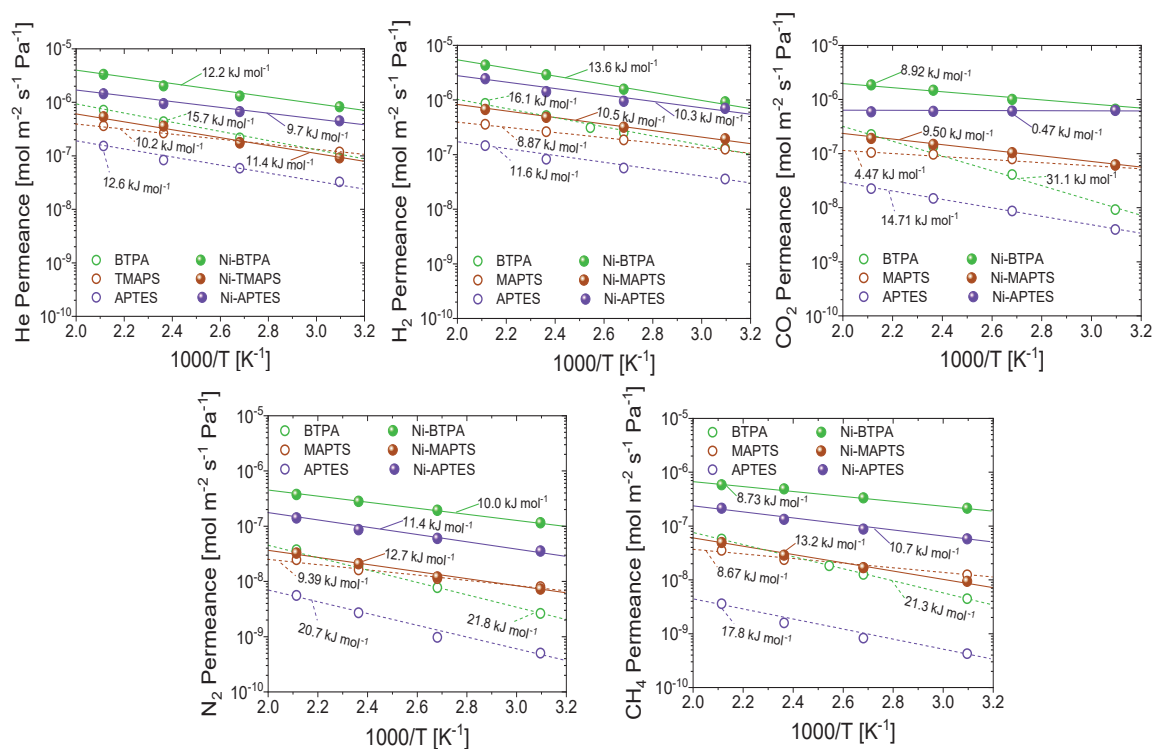
Fig. S4-8. Temperature dependence of single-gas permeance for pristine aminosilica membranes (BTPA, MAPTS, APTES) compared with nickel-doped aminosilica membranes (Ni-BTPA, Ni-MAPTS, Ni-APTES) calcined at 250 ⁰C.

--- --

----------SI-(4-9)----------

(a)

(b)
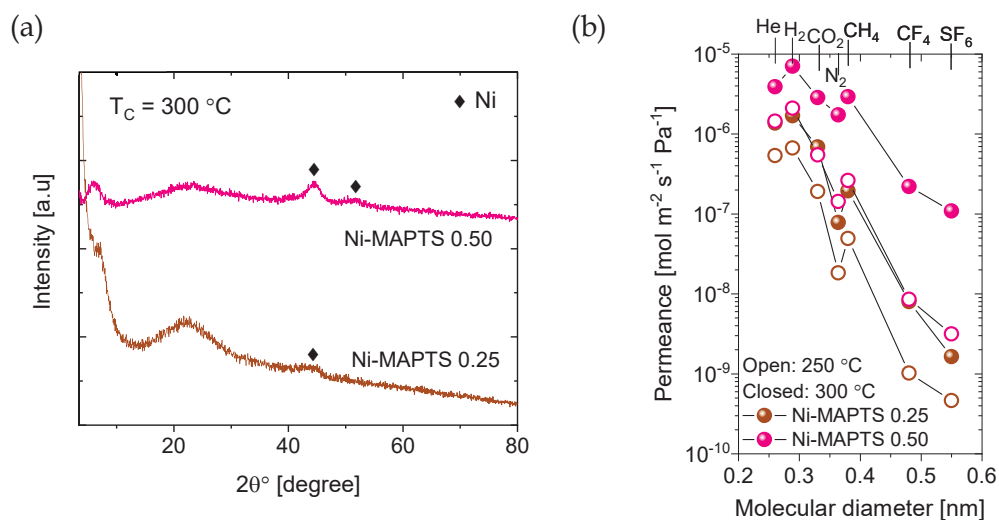
Fig. S4-9. The XRD diffractogram for Ni-MAPTS 0.25 and 0.50 calcined at 300 ºC (a), and kinetic diameter dependence of single-gas permeance at 200 ºC for Ni-MAPTS 0.25 and Ni-MAPTS 0.50 calcined at 250 ºC and 300 ºC (b)

----------SI-(4-10)----------
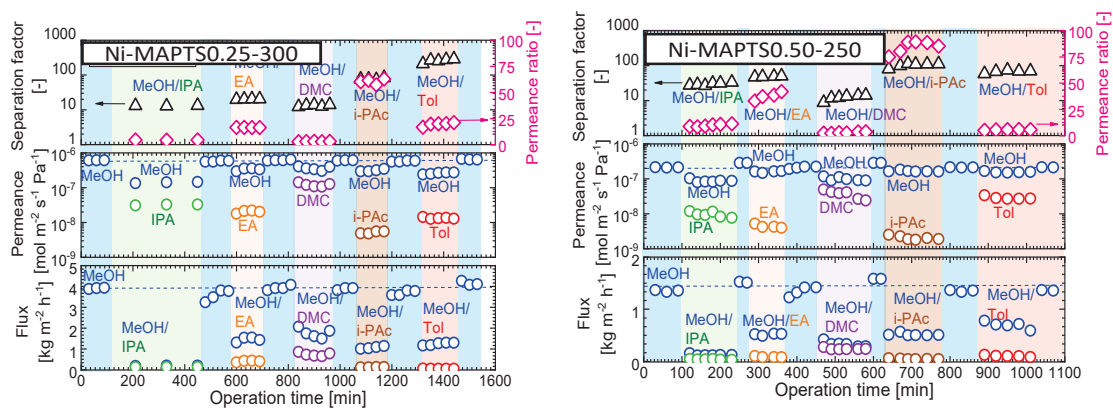
Fig. S4-10. Effective practical time courses of pervaporation performance through Ni-MAPTS0.25-300 and Ni-MAPTS0.50-250 for the methanol removal systems at 50 ºC

--- --

----------SI-(4-11)----------
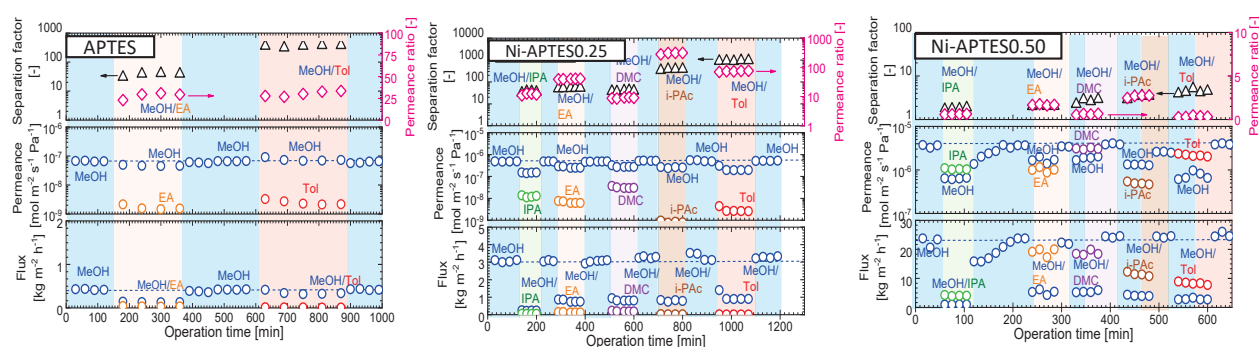
Fig. S4-11. Effective practical time courses of pervaporation performance through APTES, Ni-APTES 0.25, and Ni-APTES 0.50 for the methanol removal systems at 50 ºC (methanol/solvents = 10 wt%/ 90 wt%)

----------SI-(4-12)----------

Separation of alcohol mixtures through nickel-doped aminosilica membranes

In the previous section of 3.3 (main article), the pervaporation performance for MeOH/IPA in all types of membranes showed a lower permeance and separation factor compared with other types of solvents (Figure 14). This result might be explained by the fact that IPA (polarity index = 3.9) is a polar solvent with a polarity index comparable to that of MeOH (polarity index = 5.1). To further ascertain the permeation mechanism of alcohol mixtures through the hybrid membranes, the separation systems of MeOH/EtOH and MeOH/tert-BuOH (10 wt%/90 wt%) were also performed at 50 ºC. Before measuring the pervaporation of the alcohol mixtures, the membrane was soaked in pure methanol overnight to remove the component that was adsorbed on the membrane pore wall and reduce the history effect. Separation of MeOH with different types of alcohol mixtures had low performance, especially when the polarity indexes of the component were similar. The other reason for poor selectivity is related to the small difference in the molecular sizes between the separating molecules. As summarized in Figure S4-12, the polarity of solvents directly affected the separation ability of crosslinked nickel-aminosilica membranes.

-- --

---------------- Fig. S(4-12). -----------------
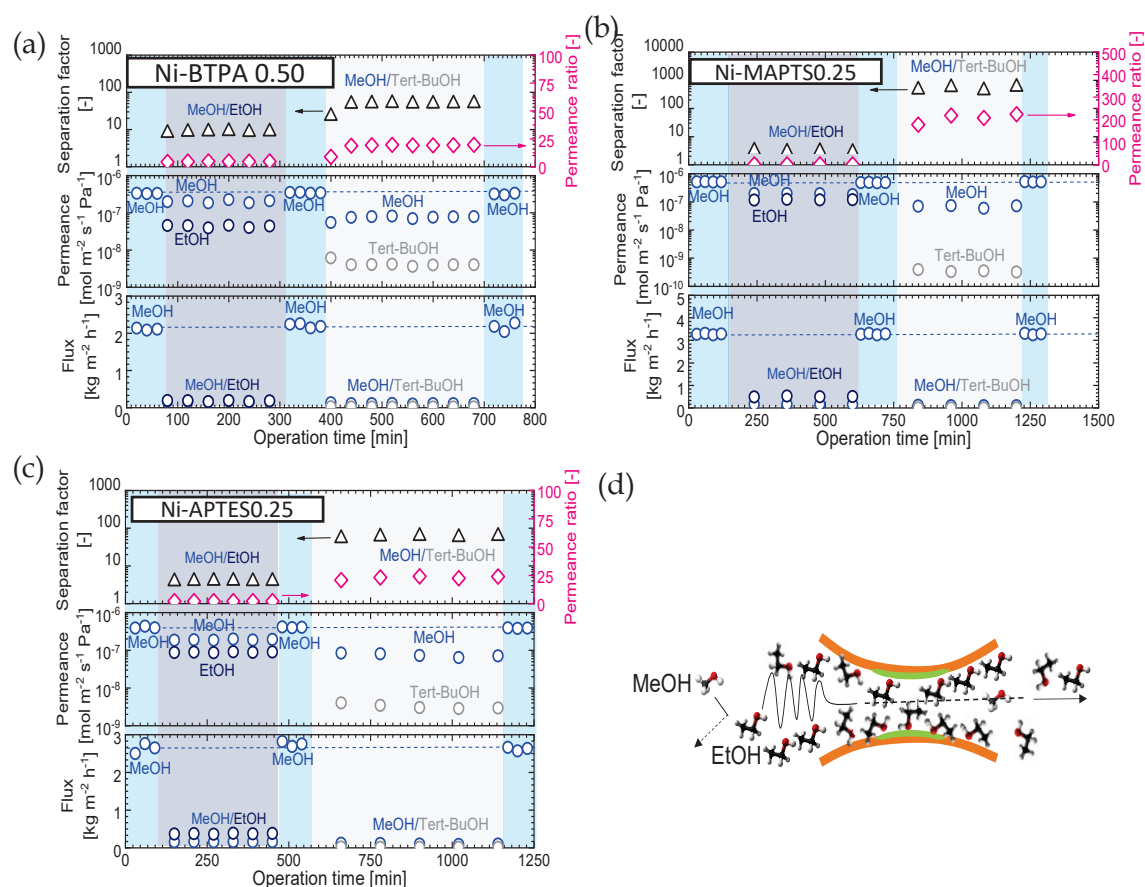
Fig. S4-12. Time courses for the pervaporation performance of methanol/ alcohol mixture (ethanol and tert-butanol) at 50 °C through the Ni-BTPA 0.50-250 (a), Ni-MAPTS 0.25-300 (b), Ni-APTES 0.25-250 (c) membranes, and schematic representation of an alcohol competitive sorption on coordinated nickel-amine based silica membrane

----

The optimized nickel-doped aminosilica membranes such as Ni-BTPA 0.50 showed high flux and high separation factors for MeOH/Tol , but were found to be unselective for the MeOH/alcohol mixture. The Ni-BTPA (Figure S4-12(a)) membrane exhibited a low flux of 0.13 kg m^{-2} h^{-1} with a separation factor of less than 50 for MeOH/tert-BuOH. Similarly, Ni-MAPTS (Figure S12(b)) and Ni-APTES(Figure S12(c)) exhibited low performance for the separation of alcohol mixtures. The permeance of methanol always became lower compared with the pure systems, and the flux of both components was largely decreased as an indication of high competitive adsorption between alcohol mixtures.

A higher concentration of alcohol compounds with a larger size than MeOH could have entered the pores of nickel-doped aminosilica membranes and interrupted the diffusion of MeOH inside the pores structure as schematically shown in Figure S12(d). Anggarini et al. reported the uncoordinated nickel nanoparticles acted as Lewis-acid and could interact with hydroxyl groups from alcohol Lewis-base molecules which then increased the diffusivity of higher concentrations of alcohol components via larger pores. In addition, most alcohol mixtures could interact with hydrophilic functional groups presented in nickel-doped aminosilica composites via the physical interaction of hydrogen bonding, which then blocks the available free volumes.

Chapter 5

Structural two-phase evolution of aminosilica-based silver-coordinated membranes for increased hydrogen separation

5.1 Introduction

Gas separation membrane technology has grown significantly throughout the years due to lowered costs, simpler operations, improvements in compactness, and improvements in performance that include higher levels of permeability and selectivity [1]. Microporous organosilica is one of the inorganic membranes that has shown a high potential for gas separation processes under chemically harsh environments. Other advantages of microporous organosilica membranes include excellent mechanical and thermal stability and highly tunable pore sizes for specific gas-separation applications [2-4]. Adequately prepared organosilica membranes show high permeability for smaller gases such as helium (He, kinetic diameter-KD = 0.26 nm), H_2 (KD = 0.29 nm), and carbon dioxide (CO_2, KD = 0.33 nm) with significant selectivity of larger gases such as carbon tetrafluoride (CF_4, KD = 0.48 nm) and sulfur hexafluoride (SF_6, KD = 0.55 nm), and of hydrocarbons such as propene (C_3H_6, KD = 0.45 nm) and C_3H_8 (KD = 0.48 nm). Kanezashi et al. [5] evaluated the performance of silica membranes with tetraethoxysilane (TEOS) as the precursor at different calcination temperatures. A TEOS membrane calcined at 550 ^{o}C showed high H_2 permeance of 1.3×10^{-7} mol m^{-2} s^{-1} Pa^{-1} with high H_2/N_2 selectivity of 80. Labropoulos et al. [6] also reported high performance of organosilica membranes fabricated via chemical vapor deposition (CVD) with the highest permeance for He of 5.2×10^{-7} mol m^{-2} s^{-1} Pa^{-1} and a selectivity for He over N_2 that reached 164.1. Moreover, Nagasawa et al. [7] developed a high-performance organosilica membrane via plasma-enhanced chemical vapor deposition (PECVD) of hexamethyldisiloxane (HMDSO)-derived membranes, and with it they reported He permeance of 1×10^{-7} mol m^{-2} s^{-1} Pa^{-1} with a permeance ratio for He/N_2 that reached 7,800. The molecular sieving properties of organosilica membranes with high permeability and high selectivity represent the most valued qualities for applications in

the industrial, scientific, and medical sectors [8].

The concept of tailoring the micropore structure was developed to enhance the separation ability in order to produce higher levels of gas permeance. The highest separation ability of organosilica membranes has been achieved when the characteristic pore dimensions of the membrane are capable of separating penetrants that differ in kinetic diameter via molecular sieving [9, 10]. Hence, the critical pore size of the membrane must be determined to achieve a high level of molecular sieving performance. The microporous structure of organosilica membranes can be tailor-made via various techniques that include burning out the organic compounds during the post-synthesis process and adjusting the structure of the linking units between bi-silyl precursors (spacer method) [11, 12]. Raman and Brinker [12] introduced an organic template method to create a pore structure by using the organic component as a template that can be incorporated into an inorganic matrix, which then can be removed via thermal treatment without collapsing the original matrix. Another process, the spacer method, refers to the modification of silsesquioxane with different lengths of linking units between two silicon atoms [11, 13]. The pore size and structure of the resultant material were strongly influenced by the organic functional groups. Most organosilica precursors with higher carbon numbers between a bi-silyl structure, however, tend to produce a flexible structure that fails to generate the microporosity of a highly permeable membrane.

The industrial application of H_2 purification technology has developed rapidly over the decades in the forms of water-gas shift processing, coal gasification, steam reforming, and the dehydrogenation of hydrocarbons [14-17]. Most H_2 separation membranes encounter obstacles to gas permeation accompanied by a desirable level of separation, and vice versa. Because it is the smallest molecule, H_2 can be separated by solution-diffusion in non-porous membranes or by molecular sieving in porous membranes [4]. Well-known examples of hydrogen-selective membranes originated from metal-organic frameworks (MOFs) [18], two-dimensional lamellar nanomaterials [19], zeolites [20, 21], covalent organic frameworks (COFs) [22], Pd and its composite alloys [23, 24], and carbon molecular sieving membranes [25]. Ma et al. [26] reported that nano-sheets seeds for the secondary growth of a Zeolite imidazolate framework-95 (ZIF-95) could control the thickness of the membrane and improve the H_2 permeance of 1.96×10^{-7} mol m^{-2} s^{-1}

Pa^{-1} with the highest selectivity of H_2/CO_2 of 49.4 via a narrow pore size of 0.37 nm and huge cavities of 2.4 nm. Wen et al. [27] showed that graphene oxide (GO)-based membranes make up a class that is derived from graphene with a laminar network and adjustable nanochannels that exhibit excellent molecular sieving features for the separation of H_2 isotopic water with high selectivity. However, the large oxygen content in the GO structure degrades the selective diffusion properties of the membrane via specific interactions with water (H_2O) molecules, and this results in large pore sizes and swelling of the GO lamella. Carbon molecular sieving (CMS) membranes show a bimodal pore size distribution of ultramicropores and micropores that provides high levels of gas separation performance and permeability [28]. The pore structure of the membrane was developed via carbonization of polymeric precursors at high temperatures, which resulted in a tightening of the micropores and a resultant higher level of selectivity. Moreover, energy consumption during the carbonization process continued to present an economical problem for large-scale industrial applications.

High purity of H_2 gases (99%) is attainable by separation via the dense structure of metallic membranes, in particular, this applies to composite palladium (Pd)-alloy types. Several varieties of metals such as pure types (Pd, niobium-Nb, and titanium-Ti), binary alloys (Pd-silver/Ag, Pd-copper/Cu, Pd-yttrium/Y), and complex alloys (Pd with more than 3 types of metal alloys) have been investigated for their use in H_2 separation [29-32]. Most metallic alloy membranes, however, form thicknesses larger than 0.1 mm, which makes them unattractive due to low permeance, low stability, and high cost. Porous membranes, on the other hand, have generally demonstrated the promise of high flux with thermal stability at temperatures ranging from 200 to 600 ^oC. The synthesis of MOF materials has been widely elaborated due to their attractive properties for the separation and purification of gases [22, 29]. MOF membranes have shown high flux performance due to ultra-high porosity with highly dimensional interconnected structures. A rigid framework of porous coordinated materials, however, tends to generate interfacial defects in their crystal structures, which results in a reduction in the separation performance of the membranes [33, 34].

Based on these findings, we first proposed a new concept for controlling the microporosity of organosilica ceramic membranes via a sol-gel process that follows a

coordination reaction to obtain significantly higher levels of permeance and selectivity. Coordination is facilitated via cross-linking reactions between the amine groups in the linking units of bis[3-trimethoxysilyl) propyl] amine (BTPA) as a Lewis base molecule with a silver ion act as a Lewis acid. A pair of nonbonding electrons from an amine moiety donated to the empty d orbitals of a silver ion induces the formation of a more rigid linking unit structure of BTPA, which gives rise to a higher surface area and high permeating flux of small molecules. In addition, the flexible amorphous phase of pristine BTPA ensures a high level of separation ability.

Previous study by our group has shown that silver dopants with a weak affinity for coordination easily generate metal segregation as a product of uncoordinated silver nanoparticles following calcination at 250 $^{\circ}$C [35]. Ag is commonly used as metal alloyed with Pd to increase the permeability of H_2 and reduce the brittle effect of the membranes [36, 37]. We expected the existence of metallic Ag nanoparticles to facilitate the transport of H_2 through an inorganic silica membrane and result in a higher permeance of H_2. Yang and Chen [38] showed that the introduction of metallic silver into TEOS and methyltriethoxysilane (MTES) increased the flux of H_2 by increasing the pressure difference. This result was explained as Ag enhancing the surface diffusion of hydrogen through a silica network. The experimental work presented in this study is one of the first investigations into how a two-phase structure that includes silver-amine coordination and silver nanoparticles could facilitate the diffusion of H_2 as a smaller-sized gas and how the amorphous properties of a silica-based framework tends to reject larger-sized gases such as hydrocarbons. Therefore, the present research offers the first explanation of the effect that a silver-dopant concentration exerts on the formation of microporous aminosilica membranes for the separation of H_2.

5.2 Experimental

5.2.1 Preparation of bis[3-(trimethoxysilyl)propyl] amine (BTPA) and silver-modified bis[3-(trimethoxysilyl)propyl] amine (Ag-BTPA)

BTPA was used as a precursor and hydrolyzed under a mole composition of BTPA/H_2O/HNO_3 at 1/300/1. The weight percent of the precursor was maintained to 5% by the addition of ethanol (C_2H_5OH) as a solvent agent. The hydrolysis and condensation reactions were conducted at room temperature for 12 hours under vigorous stirring. After synthesis of the BTPA sol, a certain amount of silver nitrate ($AgNO_3$) was added into the solution as a dopant with different mole ratios of silver/amine ranging from 0.1 to 0.5 mol/mol. Finally, the mixtures were further stirred continuously at room temperature for 1 hour. The resultant sols without and with silver content will herein be referred to as BTPA, Ag-BTPA 0.1, Ag-BTPA 0.2, Ag-BTPA 0.3, and Ag-BTPA 0.5. The silver-doping process was also conducted using bis-(trimethoxysilyl)-hexane (BTMSH) precursor with the same mole ratio for comparison between coordinated and uncoordinated species.

5.2.2 Structural characterization of Ag-BTPA films and xerogels

Silver-doped organosilica gel powders were prepared via a slow solvent evaporation process at 50 ^{o}C under an air atmosphere [39]. The coordinated (Ag-BTPA) and non-coordinated (Ag-BTMSH) compounds were confirmed using a UV-Vis diffuse reflectance spectrophotometer (Shimadzu UV-3600 plus). The thermal properties of silver-doped BTPA powder were determined using a thermogravimetric mass spectrometer (TG-MS, TGA-DTA-PIMS 410/S, Rigaku, Japan). The formation of a two-phase structure to produce silver-amine coordination and silver nanoparticles was studied using powder X-ray diffraction (XRD D2 PHASER, Bruker, Germany) in the 2θ range of 5-80°. All the xerogel samples of Ag-BTPA with different contents of silver were calcined at 250 ^{o}C under a nitrogen (N_2) atmosphere. The morphologies and the formation of the nanoparticle structure were confirmed using a transmission electron microscope (TEM JEOL2010 Ltd., Japan). The samples for TEM evaluation were prepared by

suspending the silver-doped organosilica gel powder in a volatile solvent, which then was deposited onto a copper mesh grid. Such pretreated samples were then submitted to vacuum conditions for 12 hours.

The chemical structure of Ag-doped aminosilica was examined using Fourier Transform Infrared Spectroscopy (FT/IR-4100, JASCO, Japan) over a wavenumber range of 500-4000 cm^{-1}. The Ag-BTPA-derived films were coated onto a potassium bromide (KBr) plate and then calcined at 250 ^{o}C under a N_2 flow for 30 minutes. The chemical environment of pristine BTPA and Ag-BTPA was also studied using XPS elemental analysis (Shimadzu ESCA-3400HSE spectrometer).

The textural characteristics of each powder were evaluated via N_2 sorption isotherms at -196 ^{o}C and CO_2 adsorption-desorption isotherms at 25 ^{o}C in a BELMAX (BELJAPAN Inc.). The specific surface area was calculated based on the Brunauer-Emmett-Teller (BET) technique in a P/P_0 range of 0.05-0.20. All samples were pretreated by heating at 200 ^{o}C under vacuum conditions for 12 hours prior to measurement.

5.2.3 Preparation of Ag-BTPA membranes and the evaluation of membrane performance

Porous α-alumina tubes were used as a membrane support with 50% porosity and an average pore size of 1 μm (length 100 mm; inner diameter 8 mm; outer diameter 10 mm), as supplied by the Nikkato Corporation (Japan) [40]. The α-alumina tubes were connected with non-porous alumina (Al_2O_3) tubes via a highly thermal sintering process before membrane preparation. α-Al_2O_3 particles with average particle sizes of 2 μm and 0.2 μm were dispersed into a silica-zirconia (SiO_2-ZrO_2) sol as a binder with a solid concentration of 10 wt% and subsequently coated onto the outer surface of a porous α-Al_2O_3 support followed by calcination at 550 ^{o}C under an air atmosphere for 15 minutes. These procedures were repeated three times for each of the types of particles to smooth the surface of the membrane. The intermediate layer was made from a 0.5 wt% SiO_2-ZrO_2 sol that was coated onto the surface of the particle layer and fired under an air atmosphere at 550 ^{o}C. These procedures were repeated several times until the average pore size of the

Hiroshima University Doctoral Dissertation

----

support reached approximately 1 nm. Finally, the topmost layer was obtained by two coatings of 0.1 wt% Ag-BTPA sols onto the intermediate layer followed by calcination at 250 °C under a flow of N_2 for 30-60 minutes.

Single-gas permeation experiments were conducted using high-purity components of He, H_2, CO_2, N_2, CH_4, CF_4, and SF_6 under conventional constant pressure at temperatures ranging from 50-200 °C. Each permeation gas was fed to the outside of the membrane with an upstream pressure of 200 – 400 kPa. The pressure inside the system was maintained at atmospheric levels, and the flow rate of the permeate was measured using a film flow meter (Horiba, Co. Ltd., Japan). The permeation measurement was recorded after the membrane reached a steady state with respect to the pressure difference between the shell and the inner side of the membrane and flux. The permeance of each gas (P_i) and the ideal selectivity for the $i-th$ and $j-th$ components ($\alpha_{i/j}$) were calculated using the following equations.

$$P_i = {F_i}/{A \Delta p_i} \tag{5-1}$$

$$\alpha_{i/j} = \frac{P_i}{P_j} \tag{5-2}$$

where P_i is the permeance of the $i-th$ component (mol m^{-2} s^{-1} Pa^{-1}), F_i is the molar flow rate of the ith component (mol s^{-1}), A is the effective cross-sectional area of the membrane (m^2), and Δp_i is the partial pressure difference of component i between the feed and the permeate of the membrane (Pa). The permeate flow rate was evaluated with errors of less than 5 and 20% for the permeance value larger than 10^{-7} and smaller than 10^{-7} mol m^{-2} s^{-1} Pa^{-1}, respectively.

5.3 Results and discussion

5.3.1 Structural analysis of silver-modified amine- and non-functionalized organosilica

The amine groups in the linking units of BTPA molecules have the ability to covalently bind to the transition metal of Ag(I) [35]. To compare the difference between

----

coordinated and uncoordinated compounds, Ag(I) was added into two types of organoalkoxysilane: bis [3-(trimethoxysilyl) propyl] amine (BTPA) and bis (trimethoxysilyl) hexane (BTMSH). In our previous study, we discovered that the coordinated compound of Ag-BTPA showed no absorption peak in the range of visible light since the resultant solution was colorless. However, the UV-Vis diffuse reflectance spectra of powdered materials for pristine organosilica precursors, Ag-BTPA and Ag-BTMSH, were collected, as shown in Fig. 5-1. BTPA (Fig. 5-1(a)) showed the characteristic absorption peak at approximately 193 nm, which represents the free-electron transition (n $\longrightarrow \sigma^*$) from the amine groups. After the coordination with Ag (Fig. 5-1(a)), the absorption peak shifted to a higher wavelength of 236 nm, which revealed a shifting into a lower energy level that was defined by a spectral red shift [41, 42]. The red shift is thought to be due to the coordination that led to stabilization into a lower energy level for the Ag-BTPA network. As a non-coordinated compound, however, Ag-BTMSH (Fig. 5-1(b)) displays an absorption peak that is similar to that of BTMSH.
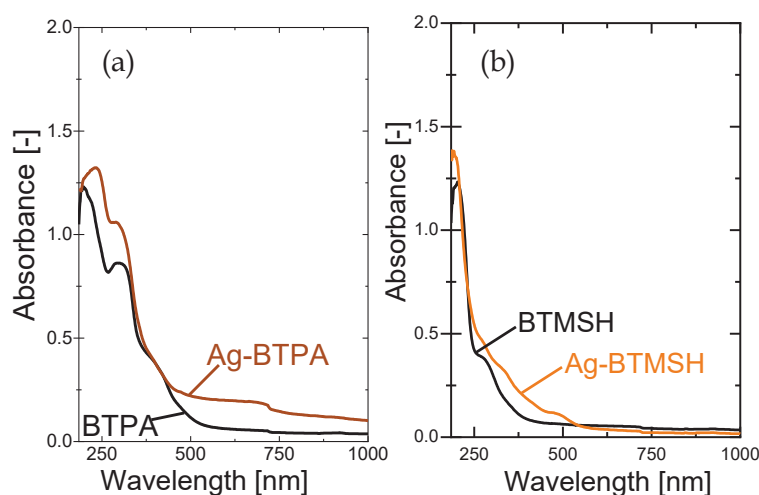
Fig. 5-1. UV-vis diffuse reflectance absorption spectra of BTPA and Ag-BTPA (a) compared with non-functionalized BTMSH and Ag-BTMSH (b)

Based on the UV-Vis spectra of the powders, a coordinated level of high density was later confirmed in silver-doped aminosilica powder via XRD, FT-IR, and N_2 sorption isotherms. Manna et al. have explained how $AgNO_3$ reacts with N-hexadecyl ethylenediamine to generate a coordinated compound of Ag(hexadecyl ethylenediamine)$_2NO_3$ that protects the metal cores of silver nanoparticles from aggregation into floc particles [43].

In order to deepen understanding of the effect of the silver-amine modification, the microstructural and adsorption isotherms properties were compared between amine-functionalized (BTPA) and non-functionalized (BTMSH) alkoxysilane structures. Both types of precursors have an extremely flexible chain with six carbons between the linking units that definitely exhibit a textural structure of non-porosity (Fig. 5-2(a)). Yu et al. [44] reported that the intrinsic flexible properties of organic-rich alkoxysilane allow free movement that creates free volume, but occupies the rigid siloxane skeleton, and reduces the number of porosity. After the incorporation of silver metal, however, the amount of adsorbed N_2 gradually increased for Ag-BTPA, while a small capacity for adsorption was observed with Ag-BTMSH. This is due to the porosity created by the coordination between the electron receptors of silver and the electron donors of the amine moieties, which results in a higher level of rigidity for the linking units of the BTPA structure as well as a greater amount of surface area [35].
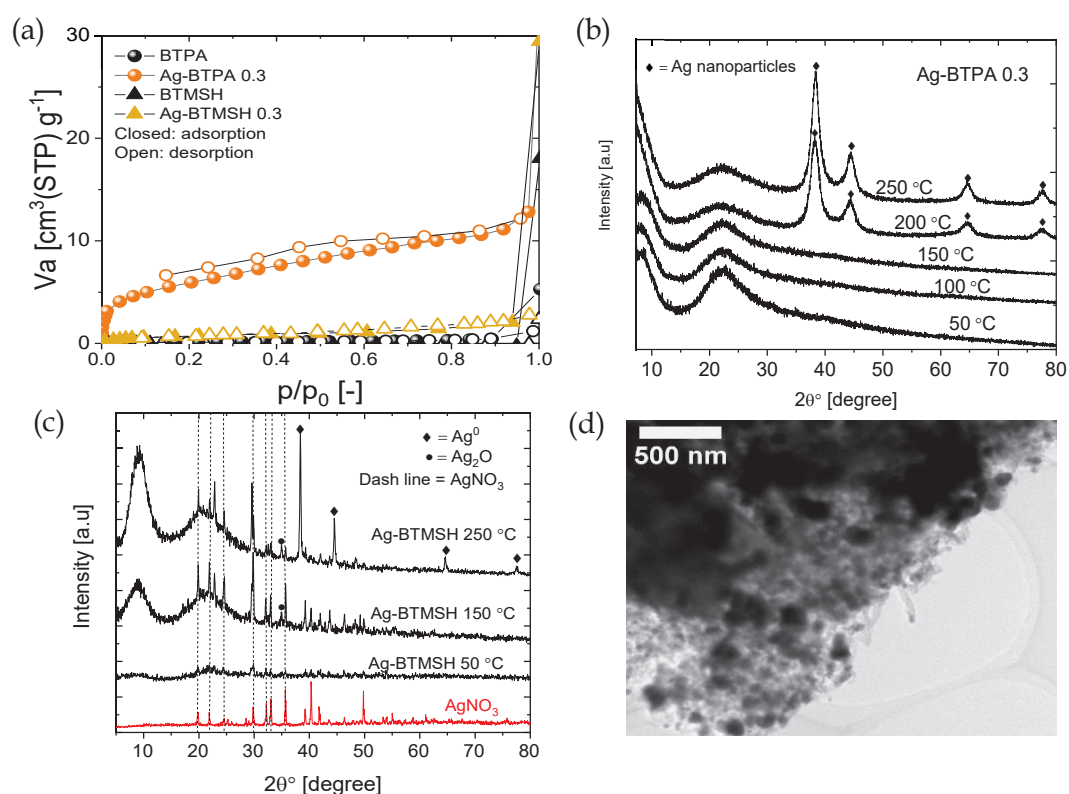
Fig. 5-2. Comparison of N_2 adsorption/desorption isotherms for both type of silver doped organosilica precursors (a), powder XRD pattern of silver doped amino-silica precursors/Ag-BTPA (b) and amine-free silica precursor/Ag-BTMSH (c) xerogel powder at different calcination temperature, and representatives TEM image of Ag-BTMSH at calcination of 250 ºC (d)

As Fig. 5-2(b) illustrates, the XRD pattern of Ag-BTPA showed an amorphous phase at lower calcination temperatures, which confirmed a full incorporation of silver ions into the BTPA matrix. When the calcination temperature was raised to 200 ^{o}C, the formation of a face-centered cubic (fcc) silver phase was detected. By contrast, the impregnation of silver into non-functionalized alkoxysilane resulted in unreacted AgNO$_3$, Ag$_2$O, and a heterogeneous distribution of metallic silver (Ag^0) with crystal sizes larger than 30 nm that were possibly deposited on the surface of BTMSH as confirmed by XRD measurement (Fig. 5-2(c)) and TEM (Fig. 5-2(d)).

AgNO$_3$ as a metal dopant was stable under acid conditions and promoted thermal decomposition to produce Ag$_2$O at 170 ^{o}C followed by Ag^0 at 440 ^{o}C [45]. The appearance of a silver metallic phase after the calcination temperature of 200 ^{o}C on Ag-BTPA further confirmed that amine groups on the surface play an important role in catalyzing partially coordinated compounds and in the reduction of AgNO$_3$ to produce well-dispersed silver nanoparticles.

5.3.2 The effect of preparation temperature on the Ag-BTPA structure

Optimization of the calcination temperature is an essential parameter in the fabrication of silver-modified aminosilica membranes. The thermal treatment of organosilica-derived membranes generally enhances the condensation of silanol (Si-OH) groups leading to the formation of a siloxane network via crosslinking of the Si-O-Si backbone, which results in higher connectivity and the establishment of molecular sieving [46, 47]. Nevertheless, the calcination of aminosilica membranes at high temperatures could be restricted to the degradation of amine moieties [48]. Fig. 5-3(a) shows the FT-IR analysis for Ag-BTPA 0.5 films coated onto KBr plates at different calcination temperatures: 150, 250, and 350 ^{o}C. Ag-BTPA 0.5 samples displayed the characteristic vibrational peaks of Si-O-Si at 1,025 – 1,110 cm^{-1}, which was increased in intensity according to increases in the calcination temperature. On the other hand, the existence of Si-OH at a wavenumber of 909 cm^{-1} was observed at a calcination temperature of 150 ^{o}C, which was gradually decreased by increasing the temperature of heat treatment.
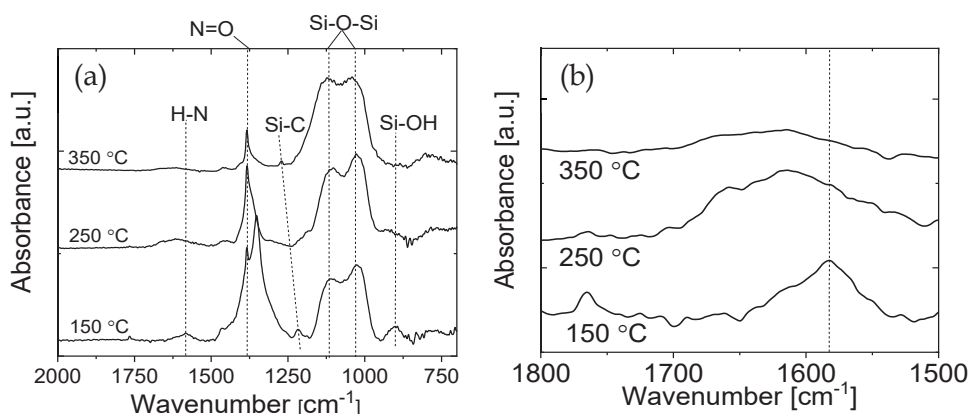
Fig 5-3. FT-IR spectra for Ag-BTPA 0.5 in wavenumber range of 2000-700 cm^{-1} (a), and the deformation NH mode range of 1800-1500 cm^{-1} (b)

These findings suggested that higher thermal treatment induces the condensation of Si-OH groups to establish the Si-O-Si framework [49]. The NH deformation band of secondary amine groups in the linking units of BTPA (1600 cm^{-1}) was shifted to a higher wavenumber (1,616 cm^{-1}) at 250 °C as an indication of coordination (Fig. 5-3(b)). Simultaneously, at a high calcination temperature of 350 °C, Ag-BTPA 0.5 showed reductions in the NH deformation band, indicating a complete decomposition of amine moieties.

This result was validated by the TG-MS measurement shown in Fig. 5-4. Ag-BTPA 0.5 showed two stages of weight loss. The first weight loss of 14% occurred at temperatures ranging from 110-300 °C, and was related to the condensation of -OH groups (m/z = 18). The second weight loss was observed at approximately 350 °C (20%), and was ascribed to a significant removal of amine groups and organic chains. These losses were based on the mass signals (Fig. 5-4-upper figure) at m/z = 30 (alkyl-amine molecules) and m/z = 44 (CO_2 molecules), respectively.
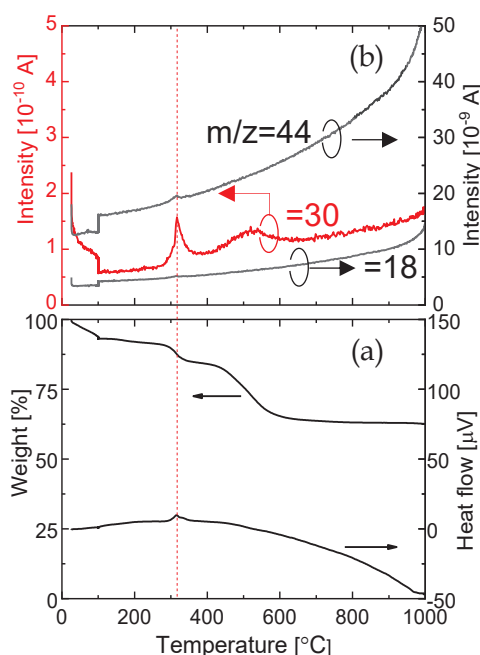
Fig 5-4. Thermal properties of Ag-BTPA 0.5 confirmed by thermogravimetric (TG) and heat-flow curve (a) accompanied by mass signal peaks (b)

5.3.3 The silver doping ratio and its effect on the construction of the Ag-BTPA network

The microstructural properties of silver-doped BTPA xerogel powders were analyzed, and the results are presented in Fig. 5-5(a). Both pristine BTPA and Ag-BTPA exhibited an XRD pattern with two amorphous peaks. The first sharp peak below 10⁰ reflected the distance from the intermolecular periodic chain to a chain in the polysisesquioxane structure, and the second diffraction peak at around 20⁰ demonstrated the average distance in the siloxane backbone [50]. The XRD patterns of Ag-BTPA powders show broader peaks at 2θ of 8⁰ and 20⁰ with higher concentrations of silver, which represent the more disordered network structure that is induced by doping with silver. The formation of face-centered cubic (fcc) planes of silver nanoparticles were observed at higher 2θ degrees of 38⁰ (1 1 1), 44⁰ (2 0 0), 64⁰ (2 2 0), and 78⁰ (3 1 1) [35, 51, 52]. The intensity of the silver nanoparticles was gradually increased by increases in the silver content in the matrix. This can be explained by silver acting as a metal dopant with a weak affinity to the amine groups that are theoretically known to be coordinated

with two amines creating a one-dimensional arrangement [53]. At a low concentration of Ag/NH = 0.1, silver existed as an ion in an amorphous metallic phase. With a higher silver ratio, however, the weak coordination between the silver and amine interaction tended to produce an unstable complex, and phase separation was confirmed by the formation of high-intensity fcc silver nanoparticles.
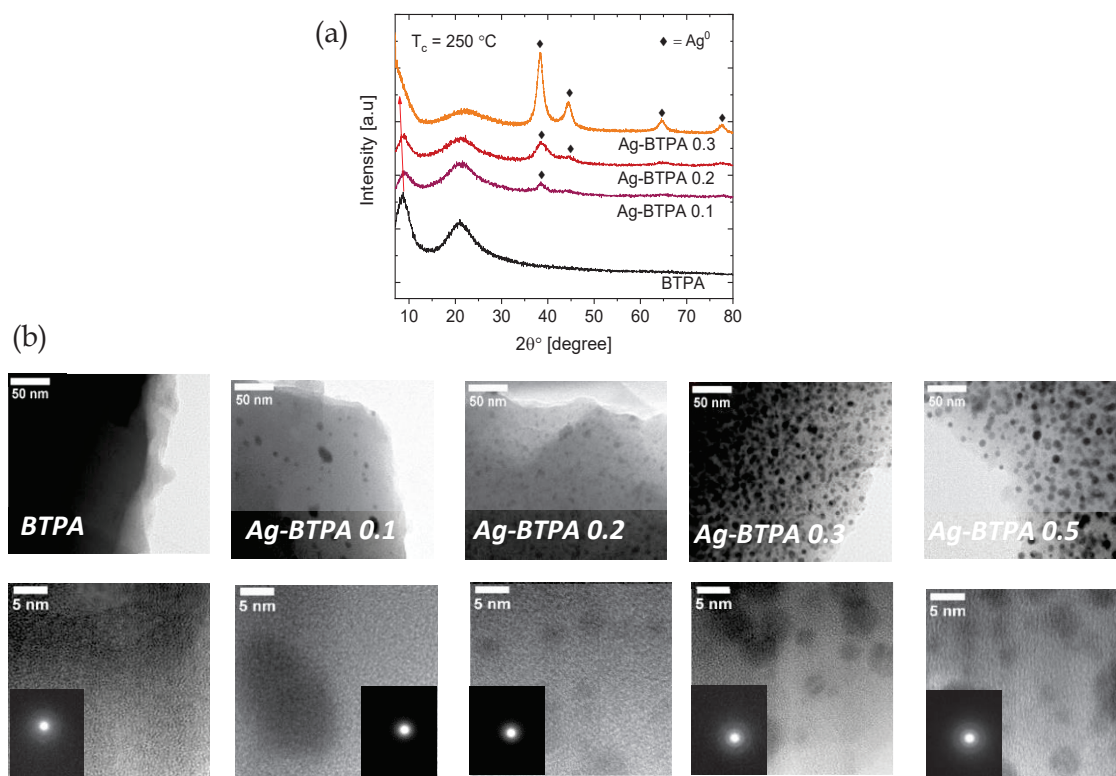
Fig. 5-5. XRD patterns (a) and TEM images (b) of BTPA and Ag-BTPA xerogel powders with different silver content calcined at 250 ⁰C

In order to confirm the formation of a coordinated compound and the dispersion of ordered silver nanoparticles on the surface of the BTPA matrix, TEM imaging was conducted for the xerogel powders obtained at a calcination temperature of 250 ⁰C (Fig. 5-5(b)). The amorphous nature of the aminosilica precursor was observed as a uniform morphology with a diffuse electron-diffraction pattern (the insert shows the lower layer). With greater amounts of metal doping the dispersion of the metallic silver phase (darker color with a spherical shape) tended to uniformly increase. Anggarini et al. [54] found that amounts of metal doping that exceeded saturation conditions tended to generate uncoordinated species that easily formed metallic nanoparticles. At low silver mole ratios of 0.1 and 0.2, coordinated compounds were dominant, which resulted in the formation

--- --

of silver in the amorphous phase. The mean particle sizes of the silver nanoparticles in the Ag-BTPA 0.3 and 0.5 samples agreed well with the Scherrer equation from the XRD spectra, at 6.22, and 13.3 nm, respectively.

The transformation of the chemical environment of the silver element for Ag-BTPA films during the coordination was investigated using XPS, as shown in Fig. 5-6(a). The Ag $3d_{3/2}$ and Ag $3d_{5/2}$ peaks for Ag-BTPA heat treatment at 250 °C appeared at approximately 375 and 369 eV, respectively. The first peak for a higher level of binding energy indicates the photoelectron excitation probability in the inner orbital shell, and is known to be influenced by the silver particle size.
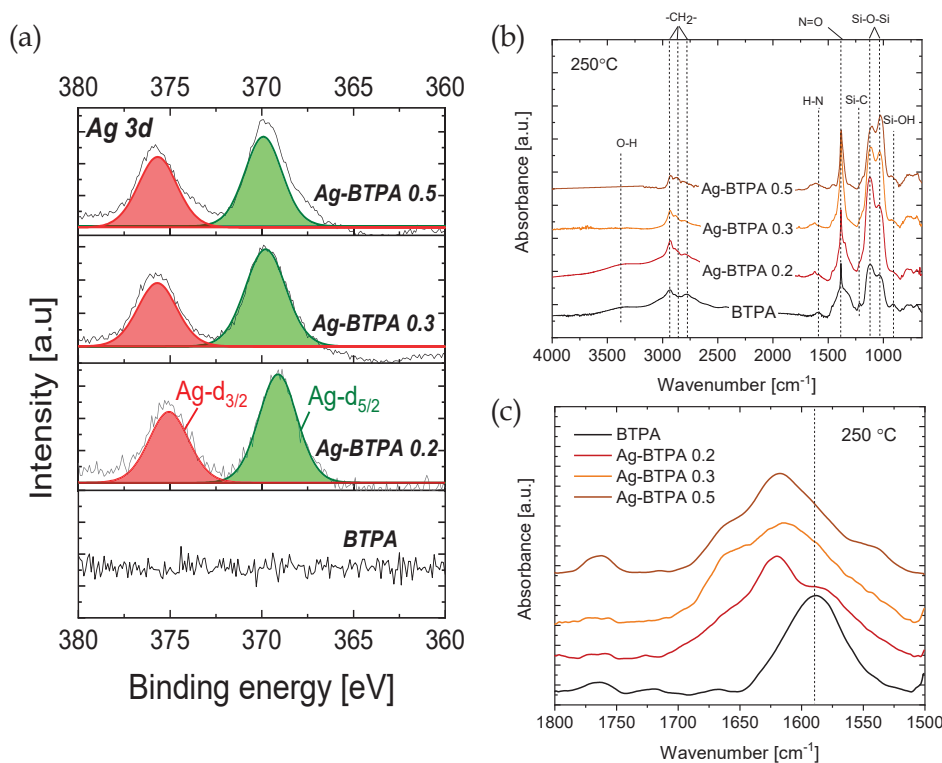
Fig. 5-6. XPS high-resolution spectra of Ag (3d) binding energy (a), FTIR wide-range spectra (b) and FT-IR narrow-range spectra (c) for BTPA and Ag-BTPA films heat treated at 250 °C under an inert atmosphere

The slight shift in the Ag $3d_{3/2}$ core level towards higher binding energy upon the incorporation of silver could be attributed to the formation of silver nanoparticles smaller than 20 nm [52, 55]. Salido et al. [55] also found that the core levels of the energy for Ag$3d_{3/2}$ shifts to a higher level of binding energy for silver with a small particle crystal size of 10 nm. Therefore, the establishment of the small-sized and well-dispersed silver

nanoparticles in Ag-BTPA is consistent with the XRD and TEM characterizations. Another core level spectrum of Ag $3d_{5/2}$ was attributed to excitation of the photoelectrons in the outer orbital shell, and indicated the existence of different oxidation states for silver [56]. We noted that at a low silver concentration of 0.2 (mol mol^{-1}), the main characteristic peak was centered at a lower binding energy of 369 nm, which meant that most of the silver had remained in an ion phase (Ag$^+$) rather than being reduced as in the silver metallic phase (Ag^0). As the covalence coordination interaction between the silver and amine groups increased, the binding energy of the core levels of the electrons were decreased for the silver ions [57]. However, when the mole ratio of silver was increased to higher than 0.3, this peak was shifted to a higher binding energy, which confirmed the formation of a high portion of silver nanoparticles (Ag^0) as verified via XRD and TEM characterization.

The establishment of coordinated silver-amine was also confirmed via FT-IR measurement with high magnification in the range of 1,800-1,500 cm^{-1}, which is related to the N-H deformation vibrational mode (Fig. 5-6(c)). By comparing the FT-IR spectra, it is clear that the monodentate amines coordinated to silver (I) ions could be observed via a gradual shifting of the N-H deformation band into a higher wavenumber, which suggests the involvement of a dynamic process that includes three types of reactions: hydrolysis, condensation, and coordination [35, 58].

To assess the modification of silver into an aminosilica structure via coordination leading to an increase in the surface area, textural analysis of Ag-BTPA xerogel powders was performed via N_2 adsorption/desorption isotherms at -196 ⁰C, as summarized in Fig. 5-7(a). As already discussed in Fig. 5-2(a), pristine BTPA with organic-rich properties displayed a negligible amount of N_2 adsorption, which indicates a nonporous structure that is due to the high flexibility of the linking units that consequently occupy the siloxane network. Kanezashi et al. [39] reported that the nonporous structure of organosilica membranes could be ascribed to the increased flexibility of the linking units between the bi-silyl structure. Ag-BTPA 0.1 shows the comparable adsorption capacity of pristine BTPA, which indicates that a low metal ratio of silver exhibits a weak effect to generate a transformation in the coordinated network of Ag-BTPA. During the silver modification, a gradual increase in N_2 uptake was observed. This result suggested that the formation of

microporosity could be achieved with a higher mole ratio of silver (Fig. 5-7(c)), where a two-phase structural evolution from silver-amine coordination to silver nanoparticles was developed.

CO$_2$ adsorption was measured to confirm the formation of coordinated compounds between silver-amine sites under different mole ratios of silver, because the chemisorption activity of CO$_2$ on amine-functionalized organosilica materials has been established [48, 59, 60].
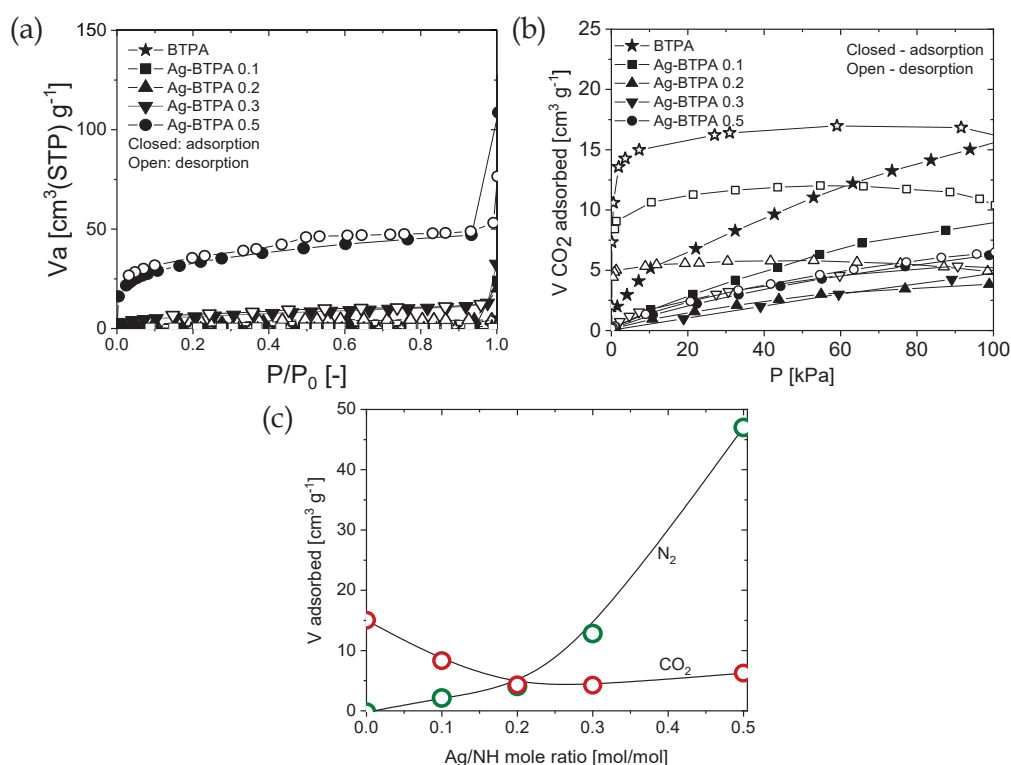
Fig 5-7. N$_2$ sorption isotherms curve (a), CO$_2$ adsorption/desorption isotherms (b), and the gas sorption capacity (N$_2$ at P/P$_0$ = 0.5, and CO$_2$ at P = 100 kPa) as a function of silver/amine mole ratio (c) originated from BTPA and Ag-BTPA xerogel powders at calcination temperature of 250 °C

Although BTPA shows a low surface area according to the Brunauer-Emmett-Teller (BET) calculation based on N$_2$ sorption isotherms, its secondary amine structure showed a greater CO$_2$ uptake capacity than that of Ag-BTPA samples (Fig. 7(b)). A broad hysteresis loop was also observed in BTPA as an indication that the adsorbed molecules of CO$_2$ were trapped within the abundant active sites of amine moieties [61]. After the addition of silver ions, the CO$_2$ adsorption capacity was decreased with the increased

silver content (Fig. 7(c)), and the hysteresis loops were narrowed to Ag/NH = 0.1-0.3 and even linear sorption isotherms were achieved at Ag/NH = 0.5 in Ag-BTPA samples. These results indicated that the saturation level of -NH groups for CO_2 adsorption was achieved after the formation of a coordinated compound from the silver-amine interaction where fewer amine active sites were accessible for CO_2 sorption.

5.3.4 The effect of membrane preparation temperature

To further explore the effect of calcination temperature on the pore structure evolution of Ag-BTPA, three membranes were prepared by firing at 150, 250, and 350 ⁰C, as presented in Fig. 5-8. The permeance of Ag-BTPA 0.5 was increased when calcination temperature was increased from 150 to 250 ⁰C. Interestingly, the membrane calcined at a higher temperature of 250 ⁰C showed higher H_2 permeance of 1.46×10^{-6} mol m^{-2} s^{-1} Pa^{-1} with high H_2/CO_2 selectivity of 12, while the membrane calcined at 150 ⁰C showed lower H_2 permeance and selectivity.
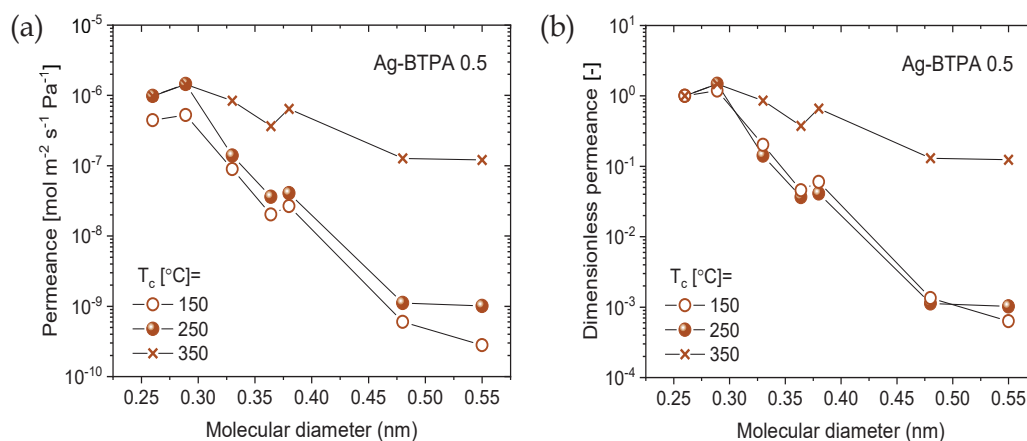
Fig 5-8. Molecular size dependence of single-gas permeance at the measurement test of 200 ⁰C (a), and dimensionless permeance based on He permeance for Ag-BTPA 0.5 calcined at a temperature range of 150 - 350 ⁰C

This result indicated that calcination at 250 ⁰C was required to produce coordination. As reported by Anggarini et al., [35] a lower temperature for hydrolysis and condensation was predominated by the existence of H_2O and HNO_3. After the evaporation of those components at a higher temperature, the formation of coordination was more dominant. This finding is also supported by the FTIR characterization shown in Fig. 5-3(a). Si-OH

groups are known to reduce gas permeation properties due to low levels of dehydroxylation of the silica network and to occupy the pore spaces in aminosilica membranes [49, 62].

Furthermore, thermal treatment at 350 $^{\circ}$C of Ag-BTPA membranes promoted the formation of a loose framework similar to that of corresponding Knudsen-like permeation properties (Fig. 5-8), which can be ascribed to a complete degradation of the amine groups of Ag-BTPA 0.5 following calcination at 350 $^{\circ}$C (Fig. 5-3(a) and 5-3(b)). After the decomposition of amine groups, the fragmentation of silver-amine coordination could result in a collapse of the microporous network structure. Hussain et al. [63] have reported thermal decomposition in a MOF following the decomposition of organic linkers, which then resulted in cleavage of the coordination between metal and organic linkers. In the coordinated phase, Ag-BTPA exhibited a hybrid structure that could have been partially crystallized and would have surrounded the amorphous phase of the alkoxysilane network where it would have been expected to show characteristics similar to that of a MOF. Hence, the optimized calcination temperature for the development of Ag-BTPA was 250 $^{\circ}$C, which allowed the development of a well-coordinated silver-amine network by avoiding the thermal degradation of amine groups.

5.3.5 The effect of the silver doping ratio

The gas-permeation performance of hybrid Ag-BTPA membranes with different mole ratios of silver are shown in Fig. 5-9(a). All Ag-BTPA membranes were developed at 250 $^{\circ}$C under a N_2 atmosphere. Single-gas permeation results revealed that increases in the silver content resulted in slightly higher levels of gas permeance. Ag-BTPA 0.5 showed the highest H_2 permeance, which was 65-fold higher than that of BTPA, with a high H_2/SF_6 permeance ratio of 1,700. The enhanced performance of metal-doped silica membranes was also reported by Uhlmann et al. [64] via the existence of a cobalt (Co) phase that promoted a higher level of stability for the TEOS membrane and enabled the higher permeation of smaller gases such as He while maintaining low permeance for larger gases such as N_2, which favors high selectivity for the membranes. In that work, the Co dopant strongly inhibited the rate of the condensation process by creating a less-

rigid and weakly branched silica matrix. In the same way, the condensation reaction rate for Ag-BTPA membranes was controlled via coordination between the metal- and organosilica-based amino functional groups. Fig. 5-9(b) shows that the permeance of smaller-sized gases such as He and H_2 was slightly increased by increasing the silver content, whereas the permeation of larger-sized gases was constant or even decreased after the doping process. Based on the membrane performance and the results of spectroscopy characterization, the formation of silver nanoparticles very possibly generated interparticle pores as the product of voids among packed particles [65], which then affected the diffusion of larger-sized gases. On the other hand, the formation of a coordinated compound was also confirmed for all Ag-BTPA samples. Therefore, the two phases of the structural evolution of silver ions contributed to a transformation of the gas-permeation behavior of the membranes.
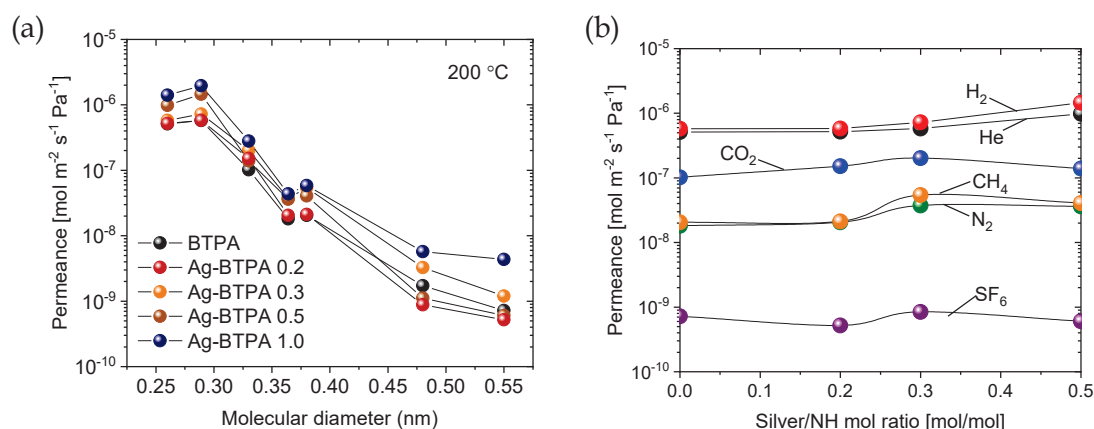
Fig 5-9. Single gas permeance as a function of permeating molecule-sizes at 200 ºC(a), the permeance of gases as a function of silver/amine mole ratio (b)

In accordance with the spectroscopy characterization results and membrane pore structure evaluation, we proposed schematic illustrations for the silver-modified aminosilica network structure as a result of changes in calcination temperature and in the silver/amine mole ratio, and these appear in Figs. 5-10(a) and 5-10(b), respectively. Silver facilitates a porosity transformation of the amine-functionalized alkoxysilane network via sol-gel followed by coordination at different calcination temperatures (Fig. 5-10(a)). At a low temperature of 150 ºC, low levels of gas permeance and selectivity of the membrane were attributed to the existence of Si-OH groups and to the remaining nitrate ions(NO_3^-),

which was confirmed by FT-IR and TG-MS results (Figs. 5-3 and 5-4). An optimized balance between the coordinated network and the silver nanoparticles of Ag-BTPA was successfully obtained at 250 ℃ with higher gas permeation, while a disjointed network was present after the decomposition (at 350 ℃) of amine groups, which facilitated a linkage to the silver ions.
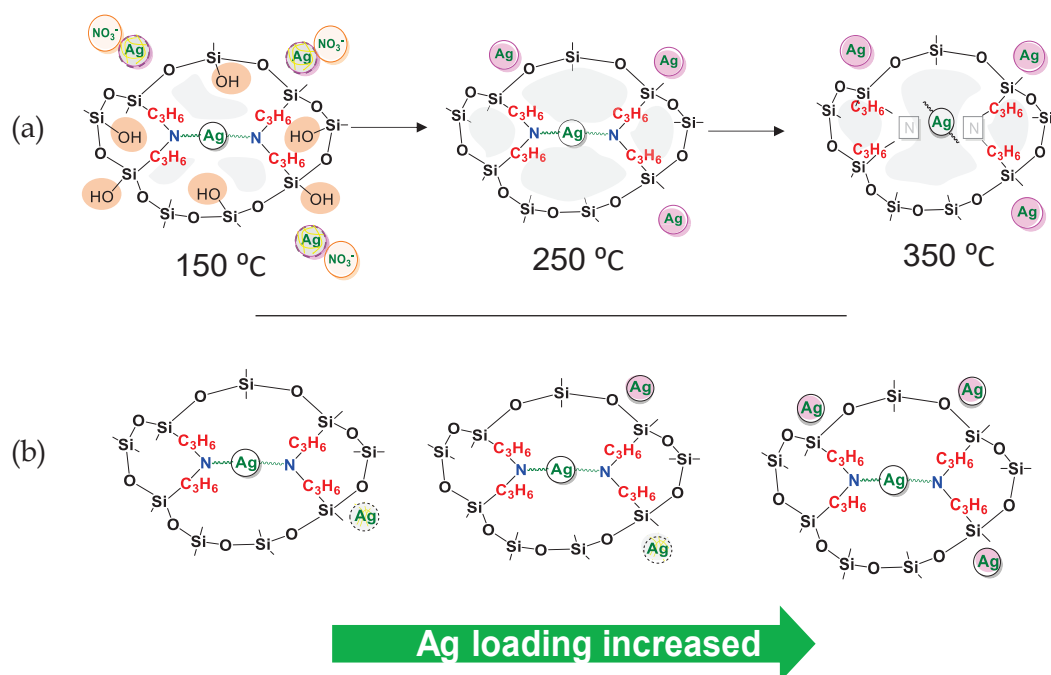
Fig. 5-10. Schematic illustration of the establishment of Ag-BTPA 0.5 network at different calcination temperatures (a), and proposed mechanism for the formation of silver-amine coordination and silver growth on the surface of aminosilica membranes (b)

The effect that various silver/amine mole ratios exert on the formation of the Ag-BTPA network is shown in Fig. 5-10(b). The addition of silver dopant into the amino-silica precursor (BTPA) tended to generate the formation of silver nanoparticles, even at the lowest concentration. The amine groups in the linking units of BTPA acted as colloidal suspension stabilizers that modified the surface properties of $AgNO_3$ by avoiding the agglomeration of metal particles [66]. Moreover, the amine groups possibly reduced the Ag^+ ions into Ag^0 via the electronic transfer of lone pairs of electrons from the nitrogen atoms into the partially empty d orbitals of the silver ions. This process led to a decrease in the potential of Ag^+/Ag which then promoted the reduction of Ag^+ [66]. In addition,

the reduction of Ag^+ into Ag^0 was accelerated via heat treatment at 250 ºC [45], which then simultaneously resulted in silver growth to produce smaller-sized nanoparticles.

5.3.6 H_2 transport through Ag-BTPA membranes: the temperature dependence of gas permeance

H_2 permeation enhancement of Ag-BTPA was achieved since the two-phase structure of silver facilitated the molecular sieving and surface diffusion processes. To further analyze the effect of silver on H_2 permeation, the permeance of a particular gas was compared with inert gases such as He and N_2 in terms of temperature dependence, as shown in Fig. 5-11. The activation energy value of each gas was calculated based on the slope of the regression curve obtained by using the modified gas translation (m-GT) model as expressed in Eq. 5-3.

$$P_{m-GT,i} \;=\; \sqrt{\frac{k_{0,i}}{M_i RT}}\; \exp\left(-\frac{E_{P,i}}{RT}\right) \qquad\qquad (5\text{-}3)$$

The estimated activation energy values of He, H_2, and N_2 for BTPA and Ag-BTPA 0.5 are summarized in Table 5-1. BTPA with a flexible structure of organic linking units between Si atoms showed a large value of activation energy for permeation that ranged from $10 - 20$ kJ mol^{-1}, which can be ascribed to the dense structure of the membrane. Meanwhile, the activation energies of He and N_2 in Ag-BTPA were decreased with a slight increase in the gas permeance. This suggests that the formation of silver-amine coordination improved the membrane connectivity and porosity as evidenced in Fig. 5-6 via the crosslinking between network layers that formed highly permeable sub-nanoporous networks. The permeance of all gases was decreased with decreasing temperatures, indicating an activated permeation mechanism. The slopes of temperature dependency for He and H_2 in the pristine BTPA membrane showed identical trends, suggesting similar transport for both types of gases. Conversely, the permeance of the smaller-sized H_2 in Ag-BTPA 0.5 was greatly decreased with decreasing temperature, which is similar to the larger-sized N_2 (Fig. 5-11(c)), which resulted in a high level of activation energy. The larger level of activation energy indicated that higher energy was

required for H_2 to travel through the Ag-BTPA membranes, particularly at a lower temperature of 50 °C.
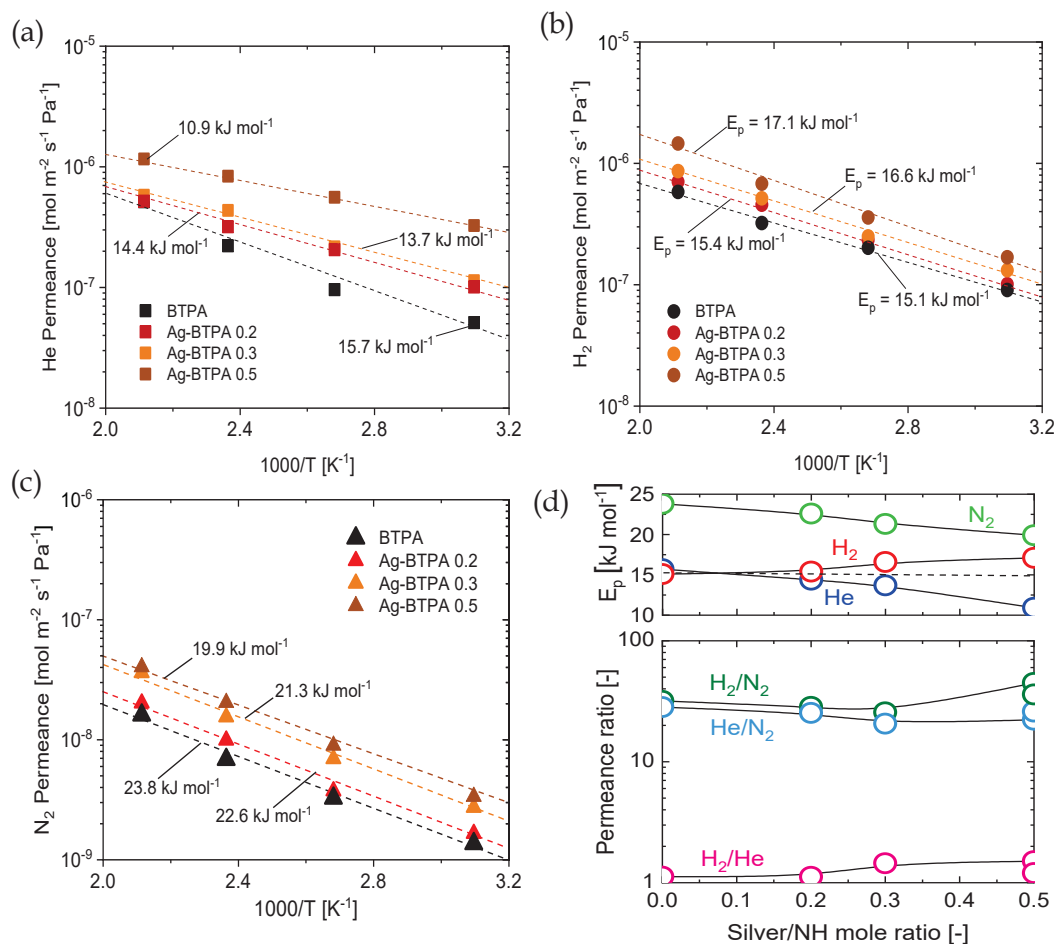
Fig. 5-11. Effect of the temperature measurement in the range of 50 – 200 °C on He (a) and H_2 (b), N_2 (c), and the effect of silver addition on the permeance ratio (lower figure) and the activation energy (upper figure) of He, H_2 and N_2 for BTPA and Ag-BTPA membranes (d)

Table 5-1. The estimated values of activation energy, Ep (kJ mol^{-1}), for BTPA- and Ag-BTPA-derived membranes

Membrane	He	H_2	N_2
BTPA	15.7	15.1	23.8
Ag-BTPA 0.2	14.4	15.4	22.6
Ag-BTPA 0.3	13.7	16.6	21.3
Ag-BTPA 0.5	10.9	**17.1**	19.9

For organosilica membranes, permeation occurs through the adsorption process (ΔH_S), which then accompanies the diffusion of permeating molecules (ΔE_D) that generates the activation energy of permeation (ΔE_p), as shown by Equation (5-4).

$$\Delta E_p = \Delta H_S + \Delta E_D \tag{5-4}$$

The heat of adsorption (ΔH_S) is related to the interaction between the permeating molecules that pass through the membrane pore wall. In this analysis, He and H_2 were compared since both gases have similar smaller-sized kinetic diameters of 0.26 and 0.28 nm, respectively. Fig. 5-11(a) shows the temperature dependence of He for pristine BTPA and Ag-BTPA membranes calcined at 250 °C under an inert atmosphere. The activation energy of He was decreased with increases in the silver content, which suggested larger pore sizes in the membrane network layers. The activation energy of H_2 for different amounts of silver-doped BTPA membranes is compared in Fig. 5-11(b). The H_2 permeation rate was increased with a silver mole ratio between 0.1 and 0.5. In line with this finding, the activation energies were gradually increased with an increase in the silver content. Ag-BTPA 0.5 exhibited the lowest He activation energy of 10.9 kJ mol^{-1} but showed the highest H_2 activation energy at 17.1 kJ mol^{-1}. The existing silver nanoparticles on the Ag-BTPA network facilitate intermolecular attractive interaction between H_2 and the membrane pore wall. For this reason, the heat of adsorption for H_2 was increased with a higher silver mole ratio, which resulted in a higher level of activation energy for diffusion. He showed a different trend, however, where the estimated heat of adsorption equaled zero due to non-specific interactions that resulted in a smaller level of activation energy for diffusion (ΔE_D). The permeation of He occurs mostly through the pores of the membrane network layers that are obtained at higher levels of the silver mole ratio. At an elevated temperature of 200 °C, silver nanoparticles possess a specific surface interaction that enhances the diffusion of H_2 by substantially reducing its permeance at a lower temperature. Zhao et al. [67] reported that silver modification through Pd-type membranes changes the surface transport, which impacts the H_2 permeation rate, the temperature dependency, and increases the activation energy at low temperatures. The higher diffusion rate of H_2 at 200 °C through the Ag-BTPA membranes could possibly be correlated with the higher connectivity of a coordinated network and with the free movement of molecules inside the crystalline face-centered (fcc) cubic silver lattice.

Fig. 5-11(d) shows the permeance ratio for different pairs of gases as a function of the silver/amine mole ratio. With an increase in the Ag/NH mole ratio, Ag-BTPA membranes exhibit almost a constant, or at least a slightly decreased, permeance ratio of $30 - 20$ for He/N_2, which suggests that the average pore size of the membranes was unchanged, or possibly only slightly increased, following modification with silver. On the other hand, the permeance ratios of H_2/He and H_2/N_2 showed a clear increase with increases in silver doping. In addition, the activation energies of He and N_2 as inert gases were decreased with increases in the silver content while H_2 activation energy showed an opposite trend. These findings suggest that a higher silver content promotes specific diffusion for H_2 while maintaining the same level of rejection for other gases, which is induced by specific interactions between the silver nanoparticles and H_2. Yang and Chen [45] also reported that metallic silver accelerated the transport of H_2 through silica membranes, which resulted in high separation performance.

5.3.7 H_2 separation for Ag-BTPA membranes

The commercialization of membranes for industrial application has gained much attention during the past few decades in efforts to explore the opportunity for obtaining more permeable and selective membranes [68]. The correlation between the selectivity and permeability of polymer membranes is referred to as the upper boundary, as reported by Roberson [69, 70]. Based on this correlation, more-permeable polymers have shown lower levels of selectivity, and vice versa. Since doping a BTPA network with silver enhanced the permeance of H_2 (Fig. 5-9(a) and (b)) in this study, silver doping was examined for its potential to improve the separation of H_2 via specific interactions through the two-phase structural evolution of silver-amine coordination and silver nanoparticles. Fig. 5-12 compares the trade-off between H_2 permeance and the permeance ratio for H_2/X ($X = CO_2$, and C_3H_8) in an effort to analyze the separation performance of Ag-BTPA-derived membranes. In Fig. 5-12, the permeance ratio is plotted as a function of permeance rather than permeability that was used for the Robeson plot, because levels of permeance are primarily obtained from experiments, which makes them more practical for real applications.

Fig. 5-12(a) provides the experimental data on the separations of H_2/CO_2 for different types of membranes. Fig. 5-12 confirms the reproducibility of Ag-BTPA membranes since each plotted point represents a different membrane (details of the reproducibility of Ag-BTPA appear in SI-(5-2), Fig. S5-2. Fig. S5-2 demonstrates the results of the permeation measurements and the standard deviations for three different Ag-BTPA 0.5 membranes prepared under identical conditions was less than 20%. Ag-BTPA membranes showed an improvement in both permeance and selectivity that surpasses the trade-off lines. The permeance of H_2 was increased by 1.46×10^{-6} mol m^{-2} s^{-1} Pa^{-1} for Ag-BTPA 0.5, which is larger than the corresponding pristine BTPA (5.76×10^{-7} mol m^{-2} s^{-1} Pa^{-1}). Ag-BTPA showed separation performance that was higher than that of polymer membranes such as polyimide, polyaniline, etc.
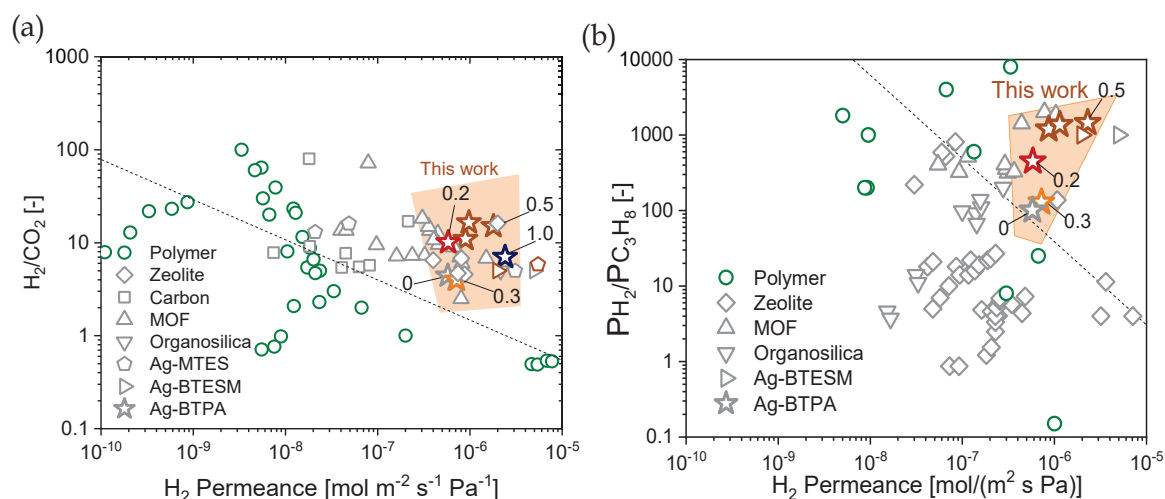
Fig 5-12. Gas permeation plots of H_2/CO_2 (a), and H_2/C_3H_8 (b) for hybrid silver-doped aminosilica membranes (Ag-BTPA) containing different metal in coordinated and metallic crystals compared with various type of membranes

Yang and Chen [38] provided an in-depth analysis of the contribution of the methyl ligands of methyltriethoxysilane (MTES), and doping with silver was investigated for its effect on the enlargement of average pore size and total pore volume of the membranes for H_2/CO_2 separation. As discussed in section 5.3.6, silver crystalline structures with an estimated average size of 28 nm promoted the surface diffusion of H_2 through a silica network, which resulted in a high permeance of H_2 at 5.5×10^{-6} mol m^{-2} s^{-1} Pa^{-1} with an

----

elevated value in the permeance ratio to 6 at an operating temperature of 200 °C with a pressure difference of 0.35 MPa. The increase in H_2 permeance with increases in the silver content was due to the formation of a rigid segment caused by the silver-amine coordination, which led to an increase in microporosity, whereas a higher permeance ratio of H_2/CO_2 was generated by the dual-network structure of Ag-BTPA that reduced the free volume for the diffusion of larger-sized gases. In addition, an increase in the silver content tended to enhance the surface diffusion of H_2, which is similar to reports by Xiao et al. [71]. The results of that study indicated an enhancement of gas-pair selectivity as an outcome of higher levels of interconnecting micropores that were formed by the migration of the smaller-sized disintegrated silver particles and by growth from the larger-sized carbon particles during the pyrolysis process. This finding supports evidence that the coordination following the sol-gel process possessed a tunable pore size of the membrane with increases in network connectivity, which is promising for hydrogen separation via molecular sieving properties.

Moreover, the dual flexible-rigid network of Ag-BTPA demonstrated impressive separation of H_2 over C_3H_8, as shown in Fig. 5-12(b). The performance of the membrane was remarkably enhanced with high H_2 permeance at 1.46×10^{-6} mol m^{-2} s^{-1} Pa^{-1} and H_2/C_3H_8 selectivity of 1,500. The conversion yield of C_3H_6 from propane dehydrogenation is strongly restricted by the equilibrium reaction, as demonstrated by Eq. 5-5 [17]. The removal of coexistent H_2 as a product of the reaction could purify C_3H_8. The pore sizes of Ag-BTPA membranes averaged 0.45 nm, whereas the kinetic diameter of C_3H_8 (0.506 nm) was much larger than the membrane pore size. Hence, the design of Ag-BTPA pore size allows H_2 to pass through the network while rejecting C_3H_8 molecules.

$$C_3H_8 \rightleftharpoons C_3H_6 + H_2 \qquad\qquad (5\text{-}5)$$

Fig. 5-13(a) shows the temperature dependencies of H_2 and C_3H_8 permeance and the permeance ratio of H_2/C_3H_8 at temperatures ranging from 50-200 °C for an Ag-BTPA 0.5 membrane calcined at 250 °C under a N_2 atmosphere. The activation energies of H_2 and C_3H_8 through an Ag-BTPA 0.5-derived membrane were 17.1 and 0.35 kJ mol^{-1},

respectively. The permeance of H_2 was increased with increases in temperature, which suggests an activated diffusion mechanism.
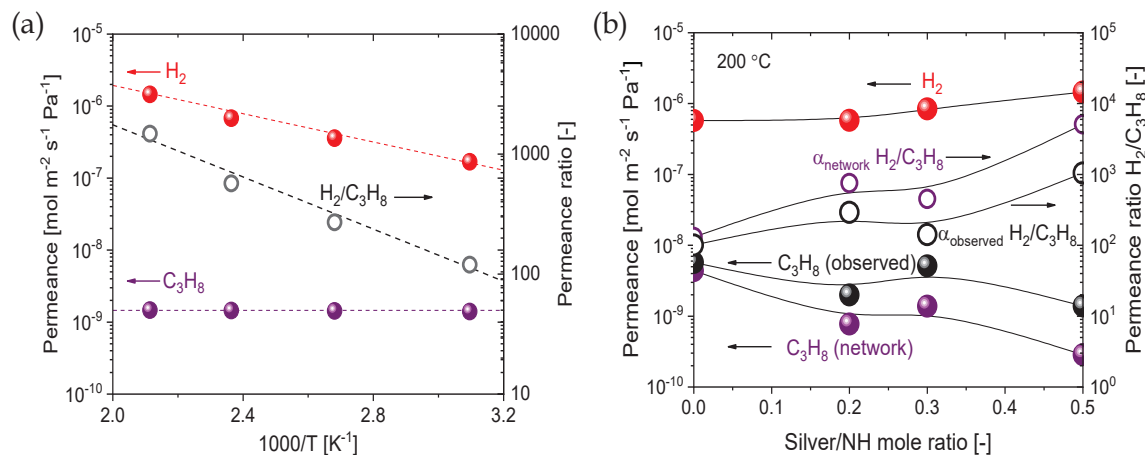
Fig 5-13. Temperature dependence of H_2 and C_3H_8 permeation for Ag-BTPA 0.5 membrane calcined at 250 ℃ (a), and permeation performance as a function of silver/NH mole ratio of Ag-BTPA membranes for the separation of H_2 and C_3H_8 at 200 ℃ (b)

Contrary to this, the permeation of C_3H_8 was increased at a lower temperature, which indicated a surface diffusion mechanism. It should be noted that the surface diffusion transport of C_3H_8 was different from the facilitated diffusion of H_2 via silver nanoparticles. Most of the H_2 molecules permeated through the network of Ag-BTPA membranes, while the larger-sized molecules of C_3H_8 could only permeate via surface diffusion through an affinity with the membrane pore wall. This finding confirms the contribution of silver ions and nanoparticles in facilitating the transport of H_2 while retaining C_3H_8 molecules through an affinity with the membrane pore wall, which has resulted in a higher permeance ratio for H_2/C_3H_8 at a higher temperature of 200 ℃.

To develop a better understanding of the permeation mechanism of C_3H_8 through the membrane pore structure of Ag-BTPA, the C_3H_8 permeance through the network is defined by Eq. (5-6).

$$P_{C_3H_{8\,network}} = P_{C_3H_8} - \left(P_{SF_6} \sqrt{\frac{MW_{SF_6}}{MW_{C_3H_8}}} \right) \qquad (5\text{-}6)$$

A bulky molecule of SF_6 was used as an indication of the permeation through cracks and the extra crystalline pores or defects [72]. The practical development of organosilica

Hiroshima University Doctoral Dissertation

-- --

membranes has always favored the development of a distribution of pore sizes rather than a single-sized pore structure. Consequently, the permeation of C_3H_8 could be classified into two different mechanisms: molecular sieving through network pores, and Knudsen diffusion through the defects in a membrane. As Fig. 5-13(b) shows, the permeance of H_2 was increased with an increase in the silver content, while the permeance of C_3H_8 through network pores revealed a sharp decrease in the higher content of silver. These findings suggest that the increase in silver content resulted in a greater degree of crosslinking with the amine moiety and a higher rate of smaller-sized silver nanoparticle development. The formation of defects in Ag-BTPA 0.5 was minimized through the coordination of the linking unit chain that led to the formation of more uniform network pores, thereby reducing the permeance of C_3H_8 and increasing the selectivity of the H_2/C_3H_8 that could diffuse through the network pores of Ag-BTPA.

5.4 Conclusions

The present study was designed to determine the effect of a two-phase structural evolution of silver: the Ag^+ ion state with amine coordination and Ag^0 nanoparticles that developed from reduction when exposed to the aminosilica surface. This investigation shows that a gradual increase in the formation of microporosity could be achieved with a high silver/amine mole ratio of 0.5 that produced a high surface area of 115 m^2 g^{-1} and a pore volume of 0.149 cm^3 g^{-1}. Spectroscopy study revealed that the dynamic processes of hydrolysis and condensation were followed by coordination that generated silver covalently bonded with monodentate-amine moieties. In addition, amine groups promoted the reduction of Ag^+ into Ag^0 which then simultaneously became a smaller-sized nanoparticle. The two-phase structural evolution of silver was confirmed to contribute to the transformation of gas permeation behavior. Ag-BTPA 0.5 showed high H_2 permeance of 1.46×10^{-6} mol m^{-2} s^{-1} Pa^{-1} and a high selectivity for H_2/C_3H_8 separation of 1,500. The partial structure of the silver-amine coordination with respect to the silver nanoparticles facilitated the diffusion of a smaller-sized gas such as H_2 and the amorphous nature of a silica-based framework that rejected a larger-sized gas such as C_3H_8, resulting in high selectivity by the membrane.

References

[1] R.W. Baker, Future directions of membrane gas separation technology, Ind. Eng. Chem. Res., 41 (2002) 1393-1411.

[2] A.J. Burggraaf, Important characteristics of inorganic membranes, in: Membrane Science and Technology, Elsevier, 1996, pp. 21-34.

[3] N.K. Kanellopoulos, Recent advances in gas separation by microporous ceramic membranes, (2000).

[4] T. Tsuru, Silica-based membranes with molecular-net-sieving properties: development and applications, J. Chem. Eng. Jpn., 51 (2018) 713-725.

[5] M. Kanezashi, T. Sasaki, H. Tawarayama, T. Yoshioka, T. Tsuru, Hydrogen Permeation Properties and Hydrothermal Stability of Sol－Gel‐Derived Amorphous Silica Membranes Fabricated at High Temperatures, J. Am. Ceram. Soc., 96 (2013) 2950-2957.

[6] A. Labropoulos, C. Athanasekou, N. Kakizis, A. Sapalidis, G. Pilatos, G. Romanos, N. Kanellopoulos, Experimental investigation of the transport mechanism of several gases during the CVD post-treatment of nanoporous membranes, Chem. Eng. J., 255 (2014) 377-393.

[7] H. Nagasawa, H. Shigemoto, M. Kanezashi, T. Yoshioka, T. Tsuru, Characterization and gas permeation properties of amorphous silica membranes prepared via plasma enhanced chemical vapor deposition, J. Membr. Sci., 441 (2013) 45-53.

[8] J. Sunarso, S.S. Hashim, Y. Lin, S. Liu, Membranes for helium recovery: An overview on the context, materials and future directions, Sep. Purif. Technol., 176 (2017) 335-383.

[9] B. Freeman, Y. Yampolskii, Membrane gas separation, John Wiley & Sons, 2011.

[10] K.M. Steel, W.J. Koros, Investigation of porosity of carbon materials and related effects on gas separation properties, Carbon, 41 (2003) 253-266.

[11] H.L. Castricum, G.G. Paradis, M.C. Mittelmeijer‐Hazeleger, R. Kreiter, J.F. Vente, J.E. Ten Elshof, Tailoring the separation behavior of hybrid organosilica membranes by adjusting the structure of the organic bridging group, Adv. Funct. Mater., 21 (2011) 2319-2329.

[12] N. Raman, C. Brinker, Organic "template" approach to molecular sieving silica membranes, J. Membr. Sci., 105 (1995) 273-279.

[13] D.A. Loy, K.J. Shea, Bridged polysilsesquioxanes. Highly porous hybrid organic-inorganic materials, Chem. Rev., 95 (1995) 1431-1442.

[14] J.A. Ritter, A.D. Ebner, State‐of‐the‐art adsorption and membrane separation processes for hydrogen production in the chemical and petrochemical industries, Sep. Sci. Technol., 42 (2007) 1123-1193.

[15] R. Sanz, J.A. Calles, D. Alique, L. Furones, H2 production via water gas shift in a composite Pd membrane reactor prepared by the pore-plating method, Int. J. Hydrogen Energy, 39 (2014) 4739-4748.

[16] S. Smart, C. Lin, L. Ding, K. Thambimuthu, J.D. Da Costa, Ceramic membranes for gas processing in coal gasification, Energy Environ. Sci., 3 (2010) 268-278.

[17] Z. Wang, J. Xu, S. Pati, T. Chen, Y. Deng, N. Dewangan, L. Meng, J.Y. Lin, S. Kawi, High H2 permeable SAPO‐34 hollow fiber membrane for high temperature propane dehydrogenation application, AlChE J., 66 (2020) e16278.

[18] Y. Peng, Y. Li, Y. Ban, H. Jin, W. Jiao, X. Liu, W. Yang, Metal-organic framework nanosheets as building blocks for molecular sieving membranes, Science, 346 (2014) 1356-1359.

[19] L. Ding, Y. Wei, L. Li, T. Zhang, H. Wang, J. Xue, L.-X. Ding, S. Wang, J. Caro, Y. Gogotsi, MXene molecular sieving membranes for highly efficient gas separation, Nature communications, 9 (2018) 1-7.

[20] M.Y. Jeon, D. Kim, P. Kumar, P.S. Lee, N. Rangnekar, P. Bai, M. Shete, B. Elyassi, H.S. Lee, K. Narasimharao, Ultra-selective high-flux membranes from directly synthesized zeolite nanosheets, Nature, 543 (2017) 690-694.

[21] W. Mei, Y. Du, T. Wu, F. Gao, B. Wang, J. Duan, J. Zhou, R. Zhou, High-flux CHA zeolite membranes for H2 separations, J. Membr. Sci., 565 (2018) 358-369.

[22] H. Fan, M. Peng, I. Strauss, A. Mundstock, H. Meng, J.r. Caro, High-flux vertically aligned 2D covalent organic framework membrane with enhanced hydrogen separation, J. Am. Chem. Soc., 142 (2020) 6872-6877.

[23] L. Shi, A. Goldbach, H. Xu, High-flux H2 separation membranes from (Pd/Au) n nanolayers, Int. J. Hydrogen Energy, 36 (2011) 2281-2284.

[24] P.M. Thoen, F. Roa, J.D. Way, High flux palladium–copper composite membranes for hydrogen separations, Desalination, 193 (2006) 224-229.

[25] H. Richter, H. Voss, N. Kaltenborn, S. Kämnitz, A. Wollbrink, A. Feldhoff, J. Caro, S. Roitsch, I. Voigt, High‐flux carbon molecular sieve membranes for gas separation, Angew. Chem. Int. Ed., 56 (2017) 7760-7763.

[26] X. Ma, Y. Li, A. Huang, Synthesis of nano-sheets seeds for secondary growth of highly hydrogen permselective ZIF-95 membranes, J. Membr. Sci., 597 (2020) 117629.

[27] M. Wen, M. Chen, G.-K. Ren, P.-L. Li, C. Lv, Y. Yao, Y.-K. Liu, S.-J. Deng, Z. Zheng, C.-G. Xu, Enhancing the selectivity of hydrogen isotopic water in membrane distillation by using graphene oxide, J. Membr. Sci., 610 (2020) 118237.

[28] L. Lei, A. Lindbråthen, X. Zhang, E.P. Favvas, M. Sandru, M. Hillestad, X. He, Preparation of carbon molecular sieve membranes with remarkable CO2/CH4 selectivity for high-pressure natural gas sweetening, J. Membr. Sci., 614 (2020) 118529.

[29] S. Adhikari, S. Fernando, Hydrogen membrane separation techniques, Ind. Eng. Chem. Res., 45 (2006) 875-881.

[30] Z.Y. Li, H. Maeda, K. Kusakabe, S. Morooka, H. Anzai, S. Akiyama, Preparation of palladium-silver alloy membranes for hydrogen separation by the spray pyrolysis method, J. Membr. Sci., 78 (1993) 247-254.

[31] S.-E. Nam, K.-H. Lee, Hydrogen separation by Pd alloy composite membranes: introduction of diffusion barrier, J. Membr. Sci., 192 (2001) 177-185.

[32] S. Yun, S.T. Oyama, Correlations in palladium membranes for hydrogen separation: A review, J. Membr. Sci., 375 (2011) 28-45.

[33] J. Duan, W. Jin, S. Kitagawa, Water-resistant porous coordination polymers for gas separation, Coord. Chem. Rev., 332 (2017) 48-74.

[34] Y. Wang, H. Jin, Q. Ma, K. Mo, H. Mao, A. Feldhoff, X. Cao, Y. Li, F. Pan, Z. Jiang, A MOF glass membrane for gas separation, Angew. Chem. Int. Ed., 59 (2020) 4365-4369.

[35] U. Anggarini, L. Yu, H. Nagasawa, M. Kanezashi, T. Tsuru, Metal-induced microporous aminosilica creates a highly permeable gas-separation membrane, Mat. Chem. Front., 5 (2021) 3029-3042.

[36] S. Nayebossadri, J. Speight, D. Book, Effects of low Ag additions on the hydrogen permeability of Pd–Cu–Ag hydrogen separation membranes, J. Membr. Sci., 451 (2014) 216-225.

[37] M. Vadrucci, F. Borgognoni, A. Moriani, A. Santucci, S. Tosti, Hydrogen permeation through Pd–Ag membranes: Surface effects and Sieverts' law, Int. J. Hydrogen Energy, 38 (2013) 4144-4152.

[38] J. Yang, J. Chen, Hydrophobic modification and silver doping of silica membranes for H2/CO2 separation, J. CO2 Util., 3 (2013) 21-29.

[39] M. Kanezashi, Y. Yoneda, H. Nagasawa, T. Tsuru, K. Yamamoto, J. Ohshita, Gas permeation properties for organosilica membranes with different Si/C ratios and evaluation of microporous structures, AlChE J., 63 (2017) 4491-4498.

[40] W. Puthai, M. Kanezashi, H. Nagasawa, K. Wakamura, H. Ohnishi, T. Tsuru, Effect of Firing Temperature on The Water Permeability Of SiO_2–ZrO_2 Membranes for Nanofiltration, J. Membr. Sci., 497 (2016) 348-356.

[41] A. Kumar, H. Joshi, R. Pasricha, A. Mandale, M. Sastry, Phase transfer of silver nanoparticles from aqueous to organic solutions using fatty amine molecules, J. Colloid Interface Sci., 264 (2003) 396-401.

[42] F. Yang, S. Gao, C. Xiong, H. Wang, J. Chen, Y. Kong, Coordination of manganese porphyrins on amino-functionalized MCM-41 for heterogeneous catalysis of naphthalene hydroxylation, Chinese Journal of Catalysis, 36 (2015) 1035-1041.

[43] A. Manna, T. Imae, M. Iida, N. Hisamatsu, Formation of silver nanoparticles from a N-hexadecylethylenediamine silver nitrate complex, Langmuir, 17 (2001) 6000-6004.

[44] L. Yu, M. Kanezashi, H. Nagasawa, J. Oshita, A. Naka, T. Tsuru, Pyrimidine-bridged organoalkoxysilane membrane for high-efficiency CO2 transport via mild affinity, Sep. Purif. Technol., 178 (2017) 232-241.

[45] J. Yang, J. Chen, Silver-Doped Organic-Inorganic Hybrid Silica Membranes by Sol-Gel Method: Preparation and Hydrothermal Stability, Sep. Sci. Technol., 46 (2011) 2128-2137.

[46] M. Kanezashi, T. Sasaki, H. Tawarayama, H. Nagasawa, T. Yoshioka, K. Ito, T. Tsuru, Experimental and theoretical study on small gas permeation properties through amorphous silica membranes fabricated at different temperatures, J. Phys. Chem. C, 118 (2014) 20323-20331.

[47] M. Kanezashi, K. Yada, T. Yoshioka, T. Tsuru, Organic–inorganic hybrid silica membranes with controlled silica network size: preparation and gas permeation characteristics, J. Membr. Sci., 348 (2010) 310-318.

[48] L. Yu, M. Kanezashi, H. Nagasawa, T. Tsuru, Fabrication and CO2 permeation properties of amine-silica membranes using a variety of amine types, J. Membr. Sci., 541 (2017) 447-456.

[49] H. Song, Y. Wei, H. Qi, Tailoring pore structures to improve the permselectivity of organosilica membranes by tuning calcination parameters, Journal of Materials Chemistry A, 5 (2017) 24657-24666.

Hiroshima University Doctoral Dissertation

----

[50] S.S. Choi, A.S. Lee, H.S. Lee, H.Y. Jeon, K.Y. Baek, D.H. Choi, S.S. Hwang, Synthesis and characterization of UV‐curable ladder‐like polysilsesquioxane, J. Polym. Sci., Part A: Polym. Chem., 49 (2011) 5012-5018.

[51] B.A. Khan, V.S. Chevali, H. Na, J. Zhu, P. Warner, H. Wang, Processing and properties of antibacterial silver nanoparticle-loaded hemp hurd/poly (lactic acid) biocomposites, Composites Part B: Engineering, 100 (2016) 10-18.

[52] P. Prieto, V. Nistor, K. Nouneh, M. Oyama, M. Abd-Lefdil, R. Díaz, XPS study of silver, nickel and bimetallic silver–nickel nanoparticles prepared by seed-mediated growth, Appl. Surf. Sci., 258 (2012) 8807-8813.

[53] D. Depuydt, N.R. Brooks, S. Schaltin, L. Van Meervelt, J. Fransaer, K. Binnemans, Silver-containing ionic liquids with alkylamine ligands, ChemPlusChem, 78 (2013) 578.

[54] U. Anggarini, L. Yu, H. Nagasawa, M. Kanezashi, T. Tsuru, Microporous Nickel-Coordinated Aminosilica Membranes for Improved Pervaporation Performance of Methanol/Toluene Separation, ACS Appl. Mater. Interfaces, (2021).

[55] I. Lopez-Salido, D.C. Lim, Y.D. Kim, Ag nanoparticles on highly ordered pyrolytic graphite (HOPG) surfaces studied using STM and XPS, Surf. Sci., 588 (2005) 6-18.

[56] E. Sumesh, M. Bootharaju, T. Pradeep, A practical silver nanoparticle-based adsorbent for the removal of Hg2+ from water, J. Hazard. Mater., 189 (2011) 450-457.

[57] T. Ivanova, A. Naumkin, A. Sidorov, M. Kiskin, V. Novotortsev, I. Eremenko, X-Ray Photoelectron Spectra and Structure of Polynuclear Nickel Complexes, Russ. J. Inorg. Chem., 52 (2007) 1781-1785.

[58] C.L. Phillips, T.Z. Regier, D. Peak, aqueous Cu (II)–organic complexation studied in situ using soft X-ray and vibrational spectroscopies, Environ. Sci. Technol., 47 (2013) 14290-14297.

[59] C.Y. Chuah, W. Li, S. Samarasinghe, G. Sethunga, T.-H. Bae, Enhancing the CO2 separation performance of polymer membranes via the incorporation of amine-functionalized HKUST-1 nanocrystals, Microporous Mesoporous Mater., 290 (2019) 109680.

[60] T. Jafari, E. Moharreri, P. Toloueinia, A.S. Amin, S. Sahoo, N. Khakpash, I. Noshadi, S.P. Alpay, S.L. Suib, Microwave-assisted synthesis of amine functionalized mesoporous polydivinylbenzene for CO2 adsorption, J. CO2 Util., 19 (2017) 79-90.

[61] D.-M. Chen, X.-J. Zhang, Stepwise and hysteretic sorption of CO 2 in polycatenated metal–organic frameworks, CrystEngComm, 21 (2019) 4696-4700.

[62] M. Kanezashi, S. Miyauchi, H. Nagasawa, T. Yoshioka, T. Tsuru, Gas permeation properties through Al-doped organosilica membranes with controlled network size, J. Membr. Sci., 466 (2014) 246-252.

[63] M.Z. Hussain, M. Bahri, W.R. Heinz, Q. Jia, O. Ersen, T. Kratky, R.A. Fischer, Y. Zhu, Y. Xia, An in situ investigation of the thermal decomposition of metal-organic framework NH2-MIL-125 (Ti), Microporous Mesoporous Mater., 316 (2021) 110957.

[64] D. Uhlmann, S. Liu, B.P. Ladewig, J.C.D. da Costa, Cobalt-doped silica membranes for gas separation, J. Membr. Sci., 326 (2009) 316-321.

[65] T. Tsuru, Development of metal-doped silica membranes for increased hydrothermal stability and their applications to membrane reactors for steam reforming of methane, J. Jpn. Pet. Inst, 54 (2011) 277-286.

[66] A. Frattini, N. Pellegri, D. Nicastro, O. De Sanctis, Effect of amine groups in the synthesis of Ag nanoparticles using aminosilanes, Mater. Chem. Phys., 94 (2005) 148-152.

[67] L. Zhao, A. Goldbach, C. Bao, H. Xu, Structural and permeation kinetic correlations in PdCuAg membranes, ACS Appl. Mater. Interfaces, 6 (2014) 22408-22416.

[68] H.B. Park, J. Kamcev, L.M. Robeson, M. Elimelech, B.D. Freeman, Maximizing the right stuff: The trade-off between membrane permeability and selectivity, Science, 356 (2017).

[69] L.M. Robeson, Correlation of separation factor versus permeability for polymeric membranes, J. Membr. Sci., 62 (1991) 165-185.

[70] L.M. Robeson, The upper bound revisited, J. Membr. Sci., 320 (2008) 390-400.

[71] Y. Xiao, M.L. Chng, T.-S. Chung, M. Toriida, S. Tamai, H. Chen, Y.J. Jean, Asymmetric structure and enhanced gas separation performance induced by in situ growth of silver nanoparticles in carbon membranes, Carbon, 48 (2010) 408-416.

[72] D.M. Ruthven, S. Brandani, Sorption and diffusion of SF6 in silicalite crystals, Adsorption, 5 (1999) 369-372.

Supporting Information

----------SI-(5-1)----------
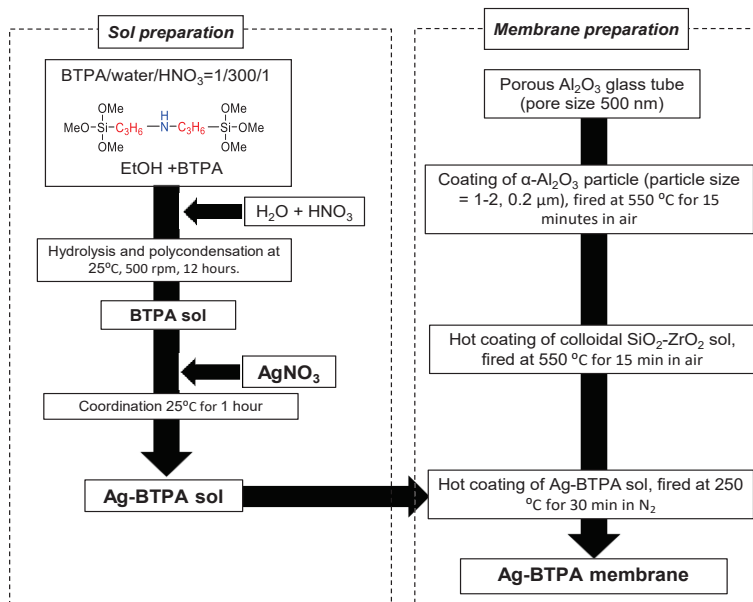
Fig. S5-1. The flowchart of experimental study for the processes of sol preparation and membrane fabrication of Ag-BTPA

----------SI-(5-2)----------
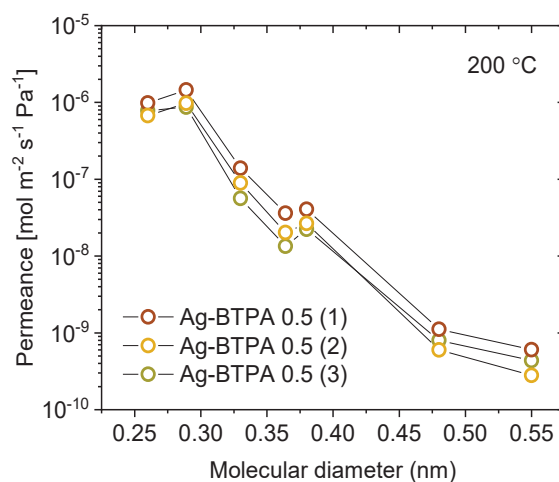
Fig. S5-2. Reproducible data of single-gas permeance for Ag-BTPA 0.5 as a function of the kinetic diameter size of gases measured at 200 ⁰C

Chapter 6
Conclusions

This dissertation is dedicated to the development of metal-induced microporous aminosilica via the crosslinking between donor pairs of electrons in the amine moiety and electron acceptors in the empty "d" orbital of the transition metal for highly permeable membranes and selective transport of specified components. The structural transformation of the coordinated network and surface chemistry have been clearly confirmed and illustrated via a series of characterizations. To further improve the membrane performance, the microstructure of metal-doped aminosilica membranes was tailored via the optimization of metal with different affinity, the effect of metal mole ratio, and the evaluation of coordination affinity via different types of amine-functionalized organosilica precursors. The present research highlights the novel strategy to modify the dense framework of aminosilica network into microporous membranes, which favorable for the development high flux and selective membranes for gas and liquid mixtures separations. The main conclusions and outlook of this thesis were summarized as follows:

6.1 Conclusions

The main conclusions in this thesis were summarized according to each chapter as follows:

[1]. The present research was focused on examining the affinity of different metals for the formation of coordinated compounds with the amine moiety of an amorphous silica matrix. The characterization of metal-doped BTPA has shown evidence of a metal-amine interaction that is induced by the reorganization of bridges in the amine-silsesquioxane network that allow maximum coordination to generate a more rigid structure. In this investigation, we found that the surface area and pore volume of a metal-doped BTPA composite was increased by increasing the metal coordination affinity on the order of Ni-BTPA > Cu-BTPA > Ag-BTPA > BTPA. An evaluation of single-gas permeance showed higher values for gas permeation, which corresponded to transformations in the membrane structure following the metal-doping process and

255

simultaneously generated a defect-free membrane. The activation energy of permeated gas was decreased by increases in membrane pore size and in the network connectivity on the order of Ni-BTPA < Cu-BTPA < Ag-BTPA < BTPA. The Ni-BTPA membrane revealed excellent separation performance with permeance and selectivity of N_2 that reached 3.75×10^{-7} mol m^{-2} s^{-1} Pa^{-1} and 1,900, respectively.

[2]. Ordered microporous nickel-doped BTPA membranes were fabricated via different nickel loadings to create coordination with nitrogen-enriched BTPA precursors. Spectroscopic characterization consistently showed a linear correlation between material properties and membrane performance, where a higher nickel content generated a higher surface area of Ni-BTPA powders on the order of Ni-BTPA 0.50 > Ni-BTPA 0.25 > Ni-BTPA 0.125 > BTPA. The pore size of the Ni-BTPA membranes also increased with Ni-doping with a higher gas flux of the membrane. Afterward, a higher nickel content (1.00) tended to generate phase separation that reduced the separation factor of the membrane, thus further confirming that the optimal point for a nickel mole ratio is 0.50. Ni-BTPA exhibited superior performance for gas separation ($N_2/SF_6 > 100 - 1,000$, N_2 permeance $> 10^{-7}$ mol m^{-2} s^{-1} Pa^{-1}) and methanol/toluene separation with high flux and separation factors of 2.8 kg m^{-2} h^{-1} and 907, respectively, for a 10 wt% methanol concentration in the feed solution.

[3]. Microporous nickel-doped aminosilica membranes were successfully synthesized via a sol-gel process that was followed by a coordination reaction. The nickel-composite membranes show attractive separation performance with methanol-selective properties and high flux. The optimal nickel/amine mole ratio and appropriate calcination temperature for the development of high porosity, facilitated the high diffusion of methanol as follows: Bridge-structure amine precursor (Ni-BTPA) = 0.50 – 250 ℃; and Pendant-structure amine precursors = Ni-APTES = 0.25 – 250 ℃; Ni-MAPTS = 0.25 – 300 ℃. The permeation mechanism for nickel-doped aminosilica membranes was influenced by the pore size distribution of the membranes and by the affinity between the hydrophilic surface of the membranes and the permeating molecules. Competitive adsorption was observed for alcohol mixtures (MeOH/EtOH, MeOH/IPA, and MeOH/tert-BuOH), which then resulted in pore blockage via hydrogen bonding interactions. The nickel-doped aminosilica membranes show high levels of flux and separation factors on the order of Ni-BTPA >

Ni-APTES > Ni-MAPTS. The Ni-BTPA membrane recorded the most outstanding performance with a high flux of 1.42 kg m^{-2} h^{-1} and a superior separation factor for MeOH/Tol of 5,000.

[4]. The present study was designed to determine the effect of a two-phase structural evolution of silver: the Ag$^+$ ion state with amine coordination and Ag^0 nanoparticles that developed from reduction when exposed to the aminosilica surface. This investigation shows that a gradual increase in the formation of microporosity could be achieved with a high silver/amine mole ratio of 0.5 that produced a high surface area of 115 m^2 g^{-1} and a pore volume of 0.149 cm^3 g^{-1}. Spectroscopy study revealed that the dynamic processes of hydrolysis and condensation were followed by coordination that generated silver covalently bonded with monodentate-amine moieties. In addition, amine groups promoted the reduction of Ag$^+$ into Ag^0 which then simultaneously became a smaller-sized nanoparticle. The two-phase structural evolution of silver was confirmed to contribute to the transformation of gas permeation behavior. Ag-BTPA 0.5 showed high H$_2$ permeance of 1.46×10^{-6} mol m^{-2} s^{-1} Pa^{-1} and a high selectivity for H$_2$/C$_3$H$_8$ separation of 1,500. The partial structure of the silver-amine coordination with respect to the silver nanoparticles facilitated the diffusion of a smaller-sized gas such as H$_2$ and the amorphous nature of a silica-based framework that rejected a larger-sized gas such as C$_3$H$_8$, resulting in high selectivity by the membrane.

6.2 Recommendations

This thesis has contributed to an interesting topic about the formation of metal-coordinated amine-functionalized organosilica membranes through the coordination of covalent bonding between the transition metal and amine moieties. The formation of coordinated networks with more rigid frameworks features a high-dimensional framework, a tailorable pore structure, and a large specific surface area. Based on the studies in Chapters 2 and 4, both ligand and metal affinity largely affected the formation of microporosity, thus resulting in membrane material with different properties compared to the pristine aminosilica membranes. Pristine aminosilica membrane with a highly flexible linking unit is commonly known to generate a dense structure with high activation

energy for permeating molecules, while metal-coordinated aminosilica membranes show an interesting property of high permeating flux and high selectivity. This finding suggested the existence of the partially crystalline structure from metal-amine coordination and the amorphous nature of the silica networks could beneficially improve membrane performance that surpasses the trade-off trend. In the other discussion in Chapters 3 and 5, we found that the existence of metal in two different phases as ions and nanoparticles can facilitate the formation of coordinated networks and act as open metal sites for facilitated transport, respectively. However, some more in-depth studies should also be done to further evaluate the role of the formation of coordinated networks as well as its synergistic effect on the material structure and membrane performance in the development of highly permeable membranes.

Based on the results and the conclusions derived from this thesis, the particular recommendations were suggested for future works are given as follows:

[1]. More studies should be devoted to the reaction rate estimation and the order of reactions since the development of a coordinated network involves three steps reaction of hydrolysis, condensation, and coordination. The optimized condition can be used to predict the formation of a microporous structure in relation to the membrane separation performance.

[2]. Metal-coordinated aminosilica membranes contain a certain amount of metal ions that are connected to the amine moieties. The crosslinking degree of these membranes was high, thus increasing the hydrophilic properties of the membranes. The existence of weak coordination bonding between metal and amine groups results in a material that is stable in an organic system but unstable in an aqueous solution. Therefore, an investigation for improving the stability of coordinated membranes in an aqueous system can be considered.

[3]. Based on the discussion in chapter 3, the saturation point for the development of the coordinated network was at a metal/amine mole ratio of 0.25 mol mol^{-1}, which means one metal ion can be coordinated with a maximum of four amine ligand molecules. Studies on the utilization of extended linkers for increasing the coordinated network as well as the microporosity on amorphous aminosilica membranes are also significant to direct the preparation of highly permeable membranes.

List of Publications

Peer-reviewed journal articles:

1. **Ufafa Anggarini**, Liang Yu, Hiroki Nagasawa, Masakoto Kanezashi, Toshinori Tsuru*, Metal-induced microporous aminosilica creates a highly permeable gas-separation membrane. Mat. Chem. Front. 2021: 5, 3029-3042.

2. **Ufafa Anggarini**, Hiroki Nagasawa, Masakoto Kanezashi, Toshinori Tsuru*, Microporous Nickel-Coordinated Aminosilica Membranes for Improved Pervaporation Performance of Methanol/Toluene Separation. ACS Appl. Mater. 2021: 13, 23247-23259.

3. **Ufafa Anggarini**, Liang Yu, Hiroki Nagasawa, Masakoto Kanezashi, Toshinori Tsuru*, Structural transformation of the nickel coordination-induced subnanoporosity of aminosilica membranes for methanol-selective, high-flux pervaporation. J. Membr. Sci. 2022:

4. **Ufafa Anggarini**, Hiroki Nagasawa, Masakoto Kanezashi, Toshinori Tsuru*, Structural two-phase evolution of aminosilica-based silver-coordinated membranes for increased hydrogen separation. J. Membr. Sci. 2022: 642, 119962.

Proceedings:

1. **Ufafa Anggarini,** Liang Yu, Hiroki Nagasawa, Masakoto Kanezashi, Toshinori Tsuru*, A novel design of metal coordinated aminosilica for highly permeable membrane, SCEJ 86th Annual Meeting 2021, March 21-22, 2021, Japan. (Oral)

-- --

2. **Ufafa Anggarini**, Hiroki Nagasawa, Masakoto Kanezashi, Toshinori Tsuru*, Aminosilica-based metal coordinated membranes: Tailoring the microporosity for advanced molecular separation, MRM2021 Materials Research Meeting, December 13-17, 2021, Yokohama, Japan. (Poster)

3. **Ufafa Anggarini**, Hiroki Nagasawa, Masakoto Kanezashi, Toshinori Tsuru*, Hybrid nickel-coordinated aminosilica membranes for the selective pervaporation of methanol: tuning coordinated structure by a variety of amine types, SCEJ 87th Annual Meeting 2021, March 16-18, 2022, Kobe, Japan. (Oral)

Acknowledgments

First and foremost, all praise to Allah SWT, I praise and thank Allah the Almighty for His grace, love, mercy, and guidance throughout my life. With Allah's will and mercy, I have been able to undertake this research study and complete it. Without the blessing from Allah, this achievement would not have been possible.

I would like to express my sincere gratitude to my advisor Prof. Toshinori Tsuru, for his continued guidance, inspiration, great support, and encouragement in every stage of my Ph.D. study. Prof. Toshinori Tsuru is a distinguished expert in both chemical engineering and membrane separation technology. I am always touched and learn a lot from his professional dedication, profound knowledge, and perseverance in scientific research which will provide me with lifetime benefits for my future research career.

I am very grateful to Prof. Masakoto Kanezashi and Prof. Hiroki Nagasawa for their kind assistance in my experiment, insightful discussion of my research work, and valuable suggestions for the organization of journal articles. I also would like to express my sincere gratitude to Prof. Joji Ohshita and Prof. Toru Ishigami on my dissertation committee for reviewing my thesis in their busy schedule.

I would like to appreciate the help and guidance from Dr. Liang Yu who always support and give kind assistance to my research work. He gave me constructive advice when I started the experimental work and helped to understand through the discussion.

I am also grateful to my tutor, Mr. Keita Nakahiro, for his warm-hearted assistance in my early daily life in Japan. I would like to thank all other group members, past and present in the Separation Engineering Lab., for their sustained help and for all the good moments we spent together.

I am also grateful to Japan Government for the financial support under Monbukagakusho Scholarship that enabled this work to be successfully completed.

Lastly, I would like to thank my family member, especially my parents (Setyo Suwarno and Sunarsih), my husband (Ndaru Candra Sukmana), and my son (Athala Dzaky Sukmana) for their endless support, understanding, and encouragement, which motivated me to insist on my study. I cannot acknowledge them enough and I love them for the sake of Allah.

July 2022
Ufafa Anggarini